Correlating Nanoscale Grain Boundary Composition with Electrical Conductivity in Ceria

by

William John Bowman

A Dissertation Presented in Partial Fulfillment
of the Requirements for the Degree
Doctor of Philosophy

Approved September 2016 by the
Graduate Supervisory Committee:

Peter A. Crozier, Chair
Candace K. Chan
Martha McCartney
Karl Sieradzki

ARIZONA STATE UNIVERSITY

December 2016

ABSTRACT

Because of their favorable ionic and/or electronic conductivity, non-stoichiometric oxides are utilized for energy storage, energy conversion, sensing, catalysis, gas separation, and information technologies, both potential and commercialized. Charge transport in these materials is influenced strongly by grain boundaries, which exhibit fluctuations in composition, chemistry and atomic structure within Ångstroms or nanometers. Here, studies are presented that elucidate the interplay between macroscopic electrical conductivity, microscopic character, and local composition and electronic structure of grain boundaries in polycrystalline ceria-based (CeO_2) solid solutions. AC impedance spectroscopy is employed to measure macroscopic electrical conductivity of grain boundaries, and electron energy-loss spectroscopy (EELS) in the aberration-correction scanning transmission electron microscope (AC-STEM) is used to quantify local composition and electronic structure. Electron diffraction orientation imaging microscopy is employed to assess microscopic grain boundary character, and links these macro- and nanoscopic techniques across length scales.

A model system, $Ca_xCe_{1-x}O_{2-x-\delta}$, is used to systematically investigate relationships between nominal Ca^{2+} concentration, grain boundary ionic conductivity, microscale character, and local solute concentration. Grain boundary conductivity varied by several orders of magnitude over the composition range, and assessment of grain boundary character highlighted the critical influence of local composition on conductivity. Ceria containing Gd^{3+} and $Pr^{3+/4+}$ was also investigated following previous theoretical work predicting superior ionic conductivity relative to state-of-the-art $Gd_xCe_{1-x}O_{2-x/2-\delta}$. The grain boundary conductivity was nearly 100 times greater than expected and a factor four

enrichment of Pr concentration was observed at the grain boundary, which suggested electronic conduction that was cited as the origin of the enhanced conductivity. This finding inspired the development of two EELS-based experimental approaches to elucidate the effect of Pr enrichment on grain boundary conductivity. One employed ultra-high energy resolution (~10 meV) monochromated EELS to characterize Pr inter-bandgap electronic states. Alternatively, STEM nanodiffraction orientation imaging coupled with AC-STEM EELS was employed to estimate the composition of the entire grain boundary population in a polycrystalline material. These compositional data were the input to a thermodynamic model used to predict electrical properties of the grain boundary population. These results suggest improved DC ionic conduction and enhanced electronic conduction under AC conditions.

This is dedicated to

Peter, my mentor, teacher and friend—without whom this work wouldn't exist,
my parents, family and friends, for their genes and generosity,
and my society, which paved my way here.

ACKNOWLEDGMENTS

I would like to thankfully acknowledge the many individuals and funding agencies who have enabled my work. Most importantly, I recognize Peter Crozier, who let me to join his research group at the start of my third undergraduate year; perhaps because I hadn't yet taken his courses. His guidance and instruction in the time since have without doubt shaped my future, and for that, I am thankful.

I acknowledge too the past and present members of my research group, who've helped me in innumerable ways, tangible and not. In particular, I'd like to recognize Dr. Vaneet Sharma, who, as a senior doctoral student, supervised my early work. I also thank Dr. Renu Sharma, of the National Institute of Standards and Technology, who supervised me as a part of the Summer Undergraduate Research Fellowship program, and has been a supportive colleague and friend since. I must also thank Karl Weiss, who, after teaching me to load a specimen holder into ASU's Topcon TEM during the fall of my last undergraduate year, proceeded to watch me dump its column vacuum. His continuous support and encouragement since was invaluable in my endeavor into (read: *struggles with*) electron microscopy; I would also like to recognize Toshihiro Aoki, who has passed along much practical and general knowledge to me.

Throughout this research I've had the pleasure of collaborating with outstanding scientists, who I'd like to acknowledge here. Prof. Jennifer Rupp of the Swiss Federal Institute of Technology (ETH) in Zürich was kind enough to welcome me into her research group for nine months, and gave me an opportunity to work and interact with the students and postdocs in her group. I'd also like to thank Jiangtao Zhu, Cruz Hernandez, Kimberly McGuinness, Christy Sennavongsa, David Wright, Ken Mossman, and John Mardinley, who worked with me throughout my time at ASU. For their

various contributions to my doctoral work and experience, I also would like to thank Katia March, Amith Darbal, Madeleine Kelly and Gregory Rohrer, Jay Sheth, Brian Sheldon and Sean Bishop, Martha MeCartney, Jason Nicolas, Andrea Lassenberger, Alla Sologubenko, and Duncan Alexander.

Finally, I thankfully acknowledge the funding supplied by the National Science Foundation's Graduate Research Fellowship Program (DGE-1311230), and Department of Materials Research. (DMR-1308085), as well as ASU Graduate College's Doctoral Enrichment Fellowship. I'd like to recognize the NSF's Graduate Research Opportunities Worldwide Grant, and thank the State Secretariat for Education, Research and Innovation of Switzerland via the Swiss Government Excellence Scholarship (ESKAS No. 2015.1183) for their financial and logistical (particularly Ms. Sandra Zweifel) support during my stay at ETH Zürich. Additionally, I thank ASU's Fulton Undergraduate Research Initiative for their financial, research and travel support, and the National Institute of Standards and Technology's Summer Undergraduate Research Fellowship. I acknowledge travel and conference support provided by the Microscopy Society of America, the Microscopy and Microanalysis Meeting, the International Microscopy Congress, and the Gordon Research Conferences.

TABLE OF CONTENTS

Page

LIST OF TABLES x

LIST OF FIGURES xi

CHAPTER Page

1 INTRODUCTION 1

1.1 Motivation 1

1.2 Solid Oxide Cells 4

1.3 CeO_2 7

1.3.1 Fluorite Structure 8

1.3.2 Phase Stability 9

1.4 Electrical Conductivity 10

1.4.1 Small Polarons 14

1.4.2 Ceria Solid Solutions 15

1.4.3 Polycrystalline Solids 21

1.5 Grain Boundaries 25

1.5.1 Conductivity 31

1.5.2 Space Charge Formalism 34

1.6 Goals and Objectives 38

2 METHODS 41

2.1 Material Preparation 41

2.1.1 Spray Drying Synthesis 41

2.1.2 Pellet Fabrication 43

CHAPTER Page

2.2 Electrical Characterization 44

2.2.1 AC Impedance Spectroscopy (ACIS) 45

2.2.2 Migration Activation Energy 54

2.3 Physical Characterization 54

2.3.1 Transmission Electron Microscopy (TEM) 54

2.3.2 Scanning Transmission Electron Microscopy (STEM) 60

2.3.3 Energy-Dispersive X-Ray Spectroscopy (EDX) 64

2.3.4 Electron Energy-Loss Spectroscopy (EELS) 65

2.3.5 X-Ray Diffraction (XRD) 85

2.3.6 Scanning Electron Microscopy (SEM) 85

2.3.7 Electron Backscatter Diffraction (EBSD) 85

2.3.8 Precession-Enhanced Nanodiffraction (PEND) 88

3 GRAIN BOUNDARY IONIC CONDUCTIVITY MODULATED BY LOCAL SOLUTE CONCENTRATION IN $Ca_xCe_{1-x}O_{2-x/2-\delta}$ 91

3.1 Motivation 91

3.2 Experimental 93

3.3 Results and Discussion 95

3.3.1 Microstructure and Phase Purity 95

3.3.2 Ionic Conductivity 97

3.3.3 Grain Boundary Character 100

3.3.4 Nanocharacterization 102

3.3.5 Grain Boundary Composition and Conductivity 108

CHAPTER Page

3.4 Summary 110

4 CONDUCTIVITY AND COMPOSITION OF $Pr_{0.04}Gd_{0.11}Ce_{0.85}O_{1.95-\Delta}$ 112

4.1 Motivation 112

4.2 Experimental 113

4.2.1 Material Synthesis and Sample Fabrication 113

4.2.2 TEM 113

4.3 Results and Discussion 115

4.3.1 Electrical Characterization 115

4.3.2 Nanocharacterization 119

4.4 Summary 130

5 MONOCHROMATED STEM EELS OF BANDGAP STATES IN $Pr_{0.1}Ce_{0.9}O_{2-\Delta}$ 132

5.1 Motivation 132

5.2 Experimental 134

5.2.1 Material Synthesis and Fabrication 134

5.2.2 TEM 134

5.3 Results and Discussion 135

5.3.1 EELS 135

5.3.2 Spectral Modelling 140

5.4 Summary 145

6 THE DISTRIBUTION OF GRAIN BOUNDARY COMPOSITION AND CONDUCTIVITY 147

6.1 Motivation 147

CHAPTER Page

6.2 Experimental 148
6.2.1 Precession-enhanced Nanodiffraction (PEND) 148
6.2.2 TEM 149
6.3 Results & Discussion 150
6.3.1 Grain Boundary Character 150
6.3.2 Grain Boundary Composition via Targeted STEM EELS 152
6.3.3 Correlating Grain Boundary Character and Composition 154
6.3.4 Grain Boundary Polaron Hopping and Ionic Conductivity 157
6.4 Summary 168
7 CONCLUSIONS AND OUTLOOK 170
8 APPENDIX 175
8.1 Dielectric Data for Relevant Oxides 175
8.2 Impedance Data 175
8.3 Comparing Calculation Methods for Conductivity 193
9 REFERENCES 196

LIST OF TABLES

Table Page

3.1. EELS Spectral Processing Windows 94

3.2. CCO Particle and Pellet Grain Size 97

3.3. Summary of CCO Electrical Data 99

3.4. CCO Grain Boundary Composition from STEM EELS 108

4.1. EELS Spectral Processing Windows 114

4.2. Summary of Data for 20GCO and PGCO 119

6.1. EELS Spectral Processing Windows 150

6.2. Grain and Grain Boundary Composition Data for PGCO 156

6.3. Constants Used for Poisson-Cahn Simulation 160

6.4. Polynomial Coefficients for Fits of Grain Boundary Properties 164

8.1. Dielectric Constants Derived from Refractive Index 175

8.2. Grain Size vs. Capacitance Method 195

LIST OF FIGURES

Figure Page

1.1. Schematic of Solid Oxide Fuel Cell Operating Principles 5

1.2. Ionic Conductivity of Various Oxygen Conducting Solids 7

1.3. The Cubic Fluorite Structure 8

1.4. Phase Diagram of Ceria, CeO_x 10

1.5. Ionic Transference Number vs. Oxygen Partial Pressure 12

1.6. Schematic of Aliovalent Solute and Vacancy in Fluorite 16

1.7. Ionic Conductivity vs. Solute Concentration for Fluorite Electrolytes 18

1.8. Predicted Ionic Conductivity in Ceria with Gd^{3+} and/or Pr^{3+} 20

1.9. The Grain Boundary Conductivity Effect in Ceria 22

1.10. Amorphous Impurity Phase at Triple Grain Junction 23

1.11. Grain and Grain Boundary Conductivity in $Gd_xCe_{1-x}O_{2-x/2-\delta}$ 24

1.12. Effect of Grain Size on Electrical Properties of Ceria 25

1.13. SEM Image of the Surface of a Dense Polycrystalline Ceria Solution 26

1.14. Dillon-Harmer Grain Boundary Complexions in Alumina (Al_2O_3) 29

1.15. TEM Images of Bicrystal Grain Boundaries in Yttria-Stabilized Zirconia 30

1.16. Mott-Schottky and Guoy-Chapman Charge Density Profiles 36

2.1. Schematic Illustrating the Spray Drying Apparatus 42

2.2. As-Sprayed CeO_2 Nanoparticles 43

2.3. “Brick Layer Model” of Polycrystalline Solid 45

2.4. Idealized Nyquist Plot for Polycrystalline Conductor 48

2.5. Equivalent Circuit Model for a Brick Layer Model 49

Figure Page

2.6. Equivalent Circuit Model for a Brick Layer Model 49

2.7. Classical View of Electron Scattering by a C Atom 57

2.8. Schematic Illustrating TEM and STEM Basic Operating Principles 59

2.9. Operating Principles of STEM Imaging 63

2.10. STEM Spherical Aberration Correction 64

2.11. Schematic of TEM Interaction Volume 65

2.12. Schematic Illustrating Basic Operating Principle of STEM EELS 68

2.13. Energy-Loss Spectrometer Design Schematic 68

2.14. Schematic Illustrating Origin of Energy-Loss Spectrum 70

2.15. First-Principles Calculation of the TiO_2 Electronic Structure 70

2.16. EELS Spectrum Acquisition and Features 71

2.17. Ultra-High Energy Resolution EELS 73

2.18. Effect of Specimen Thickness on Low-Loss and Core-Loss Signal 76

2.19. EELS Fine Structure Evolution in CeO_2 78

2.20. EELS Spatial Resolution 79

2.21. Inverse Power Law Background Fit and Subtraction 80

2.22. Two-Window Background Fitting Procedure Applied to Pr M_5 Peak. 81

2.23. EBSD Inverse Pole Figure Showing 5CCO 87

2.24. Schematic of Precession-Enhanced Nanodiffraction 89

3.1. CCO Pellet Microstructure 96

3.2. XRD of CCO 96

3.3. Impedance Analysis of CCO 98

Figure Page

3.4. EBSD Inverse Pole Figures of CCO and MADs 101

3.5. CCO Grain Boundary Plane Distributions 102

3.6. Phase Contrast TEM Images of CCO Grain Boundaries 103

3.7. Grain Boundary STEM EELS of 10CCO 104

3.8. Grain Boundary STEM EELS of 5CCO and Line Scans 107

3.9. CCO Grain Boundary Conductivity and Composition 109

4.1. Microstructure of PGCO 115

4.2. Nyquist Data from 20GCO and PGCO 116

4.3. Conductivity of 20GCO and PGCO 117

4.4. Spectroscopic Data from 20GCO and PGCO 120

4.5. TEM Images of 20GCO Grain Boundaries 121

4.6. Grain Boundary STEM EELS of 20GCO 122

4.7. EELS Overlap Correction in 20GCO 123

4.8. STEM EELS Maping at 20GCO Triple Junction 125

4.9. STEM EELS Mapping at PGCO Grain Boundary 127

4.10. Proposed Band Diagram for PCO 130

5.1. TEM and STEM Images of 10PCO Particles 136

5.2. Valence-Loss EELS from 10PCO and CeO_2 137

5.3. Core-Loss EELS from 10PCO 140

5.4. DOS Modeling of 10PCO 143

5.5. Proposed DOS for Oxidized and Reduced 10PCO 145

6.1. Grain Boundary Character Analysis of PGCO 151

Figure Page

6.2. AC-STEM and EELS of PGCO 153

6.3. Compositional Distribution of PGCO Grain Boundaries 155

6.4. Schematic Illustrating Grain Boundary Chemical Polarization 158

6.5. Grain Boundary Solute Segregation Simulation Results 163

6.6. Grain Boundary Ionic Conductivity Distribution 166

8.1. Comparison of Conductivity Calculation Methods 194

1 Introduction

1.1 Motivation

Electricity consumption is strongly correlated with human quality of life; thus, as global quality of life has continued to increase, so too has the consumption of electricity (Gaye, 2007). Most of the commonly-available energy sources are fossil fuels (e.g. coal, crude oil, natural gas, etc.) and biomass (e.g. wood, animal excrement, etc.), whose combustion produces usable energy in the form of heat, but also carbonaceous gasses including CO_2 and soot (incomplete combustion byproducts). While biomass combustion does not contribute additional atmospheric CO_2, the result of increasing the atmospheric concentration of these 'greenhouse' gasses has been the gradual warming of the planet (Pachauri, Mayer, & Intergovernmental Panel on Climate Change, 2015). This notion supported widely by the climate science community, which published approximately 11,640 of 12,000 (*97%*) peer reviewed journal articles endorsing anthropogenic global warming (AGW)—that originating from human activity—between 1991 and 2011 (Cook *et al.*, 2013).

The impacts of AGW are believed to include increased global surface temperature, more frequent heat waves with longer duration, more intense and frequent extreme precipitation events, and ocean warming and acidification, which, in aggregate, are expected to lead to increased socioeconomic and geopolitical unrest associated with mass population displacement and resource scarcity. Thus, addressing AGW—in part by

reducing greenhouse gas emissions stemming from electricity generation, is likely one of the seminal challenges facing humanity (Pachauri *et al.*, 2015).

The share of consumed electricity derived from renewable energy sources such as wind, geothermal and solar has increased considerably in recent decades, but still only accounts for approximately 20% of generated power. According to the International Energy Agency, an estimated 5,070 TWh electricity was generated globally by renewables, accounting for 22 % of total power generation (International Energy Agency, 2014). Renewable sources also face the very considerable challenge of intermittency, so supplemental energy storage technologies, such as batteries and electrolysis cells, are widely pursued. Additionally, it is important to consider use of transitional technologies capable to converting currently-available fuels (i.e. fossil fuels) and future fuels (e.g. synthetic hydrocarbons, hydrogen gas, etc.) into electricity with optimal efficiency. Hence, *fuel-flexible* solid oxide fuel cells (discussed below) have been the subject of considerable fundamental research and technological development over the last decades (Fergus, 2007; Fuel Cell Today, 2013; Wachsman & Lee, 2011).

A popular class of materials employed in these devices is electroceramics, which, broadly speaking, are glasses, single- and polycrystalline ceramics, or ceramic-based composites with desirable optical, magnetic, electrical and/or electrochemical properties (Kingery, Bowen, & Uhlmann, 1976; Moulson & Herbert, 2003). Readers interested in the breadth of electroceramics research areas are also referred to the Journal of Electroceramics. Common electroceramic materials include fluorite, perovskite and garnet structured oxides, which are the focus of considerable research and development due to

their wide-ranging applications as solid electrolytes and electrodes in energy storage (Rawlence, Garbayo, Buecheler, & Rupp, 2016; van den Broek, Afyon, & Rupp, 2016), conversion (Wachsman & Lee, 2011), gas separation (Sunarso *et al.*, 2008), and information (Schweiger, Kubicek, Messerschmitt, Murer, & Rupp, 2014) technology.

In many cases, solid electrolytes with high ionic and/or electronic conductivity are desired to maximize device performance. Though, a persistent challenge to maximizing ionic conductivity has been the presence of highly resistive grain boundaries in polycrystalline electrolytes (Bauerle & Hrizo, 1969; Wang & Nowick, 1980; Christie & van Berkel, 1996; Haile, West, & Campbell, 1998; Ma *et al.*, 2014), which comprise the majority of manufactured electrolytes. In commonly-used oxygen conducting ceria (CeO_2) and zirconia (ZrO_2) solid solutions, for example, grain boundary conductivity can be 10^2 – 10^8 times lower than that of grains (Avila-Paredes, Choi, Chen, & Kim, 2009; Bowman, Zhu, Sharma, & Crozier, 2015; Guo, Sigle, & Maier, 2003). The issue of high grain boundary resistance has also been identified in other systems, such as lithium ion conductors for all-solid-state batteries (Ma *et al.*, 2014) and proton conductors (Haile *et al.*, 1998).

The selection of materials investigated in the present work was motivated by an overarching goal of enhancing the oxygen ionic conductivity of ceria-based polycrystalline electrolytes, like those used in solid oxide fuel and electrolysis cells. However, ceria, its many solid solution formulations, and polycrystalline materials in general have been employed widely in ceramic sciences and technology (Kingery *et al.*, 1976; Trovarelli, 2002), so the experimental approach(es) and results presented here—namely correlating

measured and predicted grain boundary properties over a range of length scales, may be relevant to other fields. Moreover, the development and implementation of advanced TEM techniques described here may be generally relevant to researchers working on electroceramics, polycrystalline materials, grain boundaries, transmission electron microscopy and electron spectroscopy.

Nevertheless, as the materials selection here was motivated by electrolytes for solid oxide cells, and because of their considerable relevance to the current and future energy landscape, a brief description of the technology is provided, with an emphasis on some of the materials involved. That is followed by a more extensive discussion of relevant properties of ceria and ceria-based solid solutions, which, as previously mentioned, were investigated here for their technological relevance and as model materials.

1.2 Solid Oxide Cells

Solid oxide fuel cells are electrochemical devices that directly convert chemical energy into electrical energy with efficiency ranging from 45% to 65% in stand-alone applications (based on lower heating value (LHV) of the fuel). When integrated into a combined heat-and-power cycle, potential efficiencies >85 % LHV are possible (Haile, 2003; Wachsman & Lee, 2011). The basis for solid oxide fuel cell operation (Figure 1.1) is fuel oxidation at the anode to produce electrons which flow through an external circuit to the cathode where they reduce gaseous oxygen to oxygen ions. Between these electrodes is an oxygen ion conducting electrolyte, whose ionic conductance directly influences cell power output. As the choice of fuel is only limited in that it must react with ionic oxygen,

there is a considerable number of possible fuels, including hydrogen gas (K. T. Lee *et al.*, 2012), methane (Timmermann *et al.*, 2006), various higher hydrocarbons (Boaro *et al.*, 2010; Costa-Nunes, Vohs, & Gorte, 2003), alcohols (T.-J. Huang & Chen, 2010) and even biomass (Mermelstein, Millan, & Brandon, 2010). This *fuel-flexibility* makes solid oxide fuel cells an attractive transition technology due to their ability to accept some of today's most common fuel streams, as well as those of the future. Furthermore, the cell can operate essentially in reverse as a solid oxide *electrolysis* cell, using electricity to produce fuel or chemical intermediates and molecular oxygen (Ebbesen & Mogensen, 2009). In this way, solid oxide (fuel/electrolysis) cells can help to address issues of intermittency in electricity production.

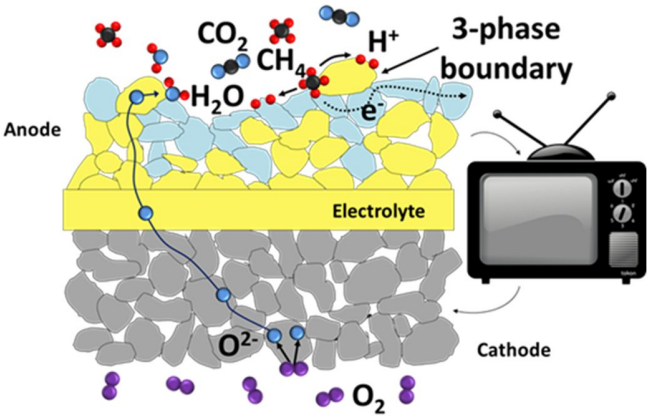

Figure 1.1. Schematic of Solid Oxide Fuel Cell Operating Principles.

Currently-available solid oxide cells typically use a porous ceramic-metal composite for the anode. This *cermet* contains a metallic phase (e.g. Ni) capable of catalyzing the decomposition of the fuel molecule (Sharma, Crozier, Sharma, & Adams, 2012) while also enabling electronic diffusion to an external circuit. The oxide phase (e.g. yttria-stabilized zirconia (ZrO_2) or a ceria (CeO_2) solid solution such as $Gd_xCe_{1-x}O_{2-x/2}$)

facilitates oxygen ion migration from the electrolyte to three-phase boundaries—the reactive sites where the fuel molecules are oxidized. The electrolyte phase, typically a dense polycrystalline oxide membrane of composition similar to those aforementioned, allows rapid oxygen ion diffusion from cathode to anode while (ideally) blocking entirely the counter diffusion of electrons from anode to cathode. The cathode material is commonly a perovskite (e.g. $La_{1-x}Sr_xMnO_{3-\delta}$ (Haile, 2003)) that must facilitate mixed ionic-electronic conduction and rapid oxygen ion absorption and transport.

Zirconia-based solid oxide fuel cells operate at ~950 °C to maximize oxygen ion conductivity in the electrolyte, and to optimize electrode catalytic activity. However, such high operating temperature results in material instability and severely restricts the use of low cost component materials (Wachsman & Lee, 2011). In light of this design constraint, efforts to lower device operating temperatures via reducing electrolyte resistance have been explored. For example, reducing electrolyte thickness using advanced oxide fabrication techniques such as atomic layer deposition (Chao, Hsu, Cui, & Prinz, 2011) and spray pyrolysis (Rupp & Gauckler, 2006) have been demonstrated. Alternatively, cerium and bismuth (Wachsman & Lee, 2011) based oxides that exhibit higher oxygen ion conductivity than YSZ are also a topic of considerable fundamental research and commercial development. Figure 1.2 illustrates the higher conductivity of a selection of these ceria and bismuth oxides relative to YSZ.

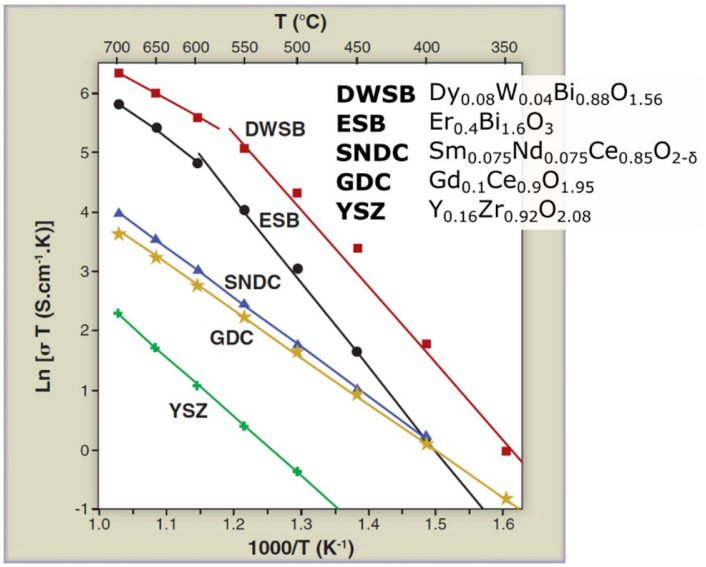

Figure 1.2. Ionic Conductivity of Various Oxygen Conducting Solids. Image adapted from (Wachsman & Lee, 2011).

1.3 CeO_2

Ceria is widely used in industrial applications including chemical-mechanical polishing, self-cleaning ovens, and most notably three-way catalysts used in automotive catalytic convertors (Shelef & McCabe, 2000), and has been the focus of many decades of fundamental research due to its ability to form oxygen-deficient solids with a wide range of electrical, optical and catalytic properties (Zintl & Croatto, 1939; Trovarelli, 2002). Oxygen vacancies form under reducing conditions, at elevated temperatures, and/or to charge compensate substitutional aliovalent cations such as La^{3+}, Ca^{2+} and Gd^{3+}, offering a high degree of extrinsic control over the material's properties. The ability to readily tune the properties of ceria and its solid solutions has led to its incorporation in mature and emerging applications, such as fuel cell electrolytes and electrodes (Steele, 2000; Haile, 2003), hydrogen production catalysts (Chueh & Haile, 2010) and resistance-switching

integrated circuit components (Schweiger *et al.*, 2014). The direct and indirect bandgaps of ceria have been reported to be 3.66 eV and 3.33 eV, respectively (Ruiz-Trejo, 2013).

1.3.1 Fluorite Structure

Ceria crystallizes in the cubic fluorite ($Fm\bar{3}m$) structure (Trovarelli, 2002), shown in Figure 1.3. The unit cell comprises four cations and eight anions, with a face-centered cubic array of cations tetrahedrally coordinated about the oxygen anions (see Figure 1.3a), which are octahedrally coordinated about the cations (see Figure 1.3b). A number of solid state ionic conductors share this structure, including urania (UO_2), thoria (ThO_2) and praseodymia (PrO_2). Zirconia, one of the most commonly used solid oxide electrolytes can also assume the fluorite structure upon addition of stabilizing acceptor cation dopants, most notably Yttrium.

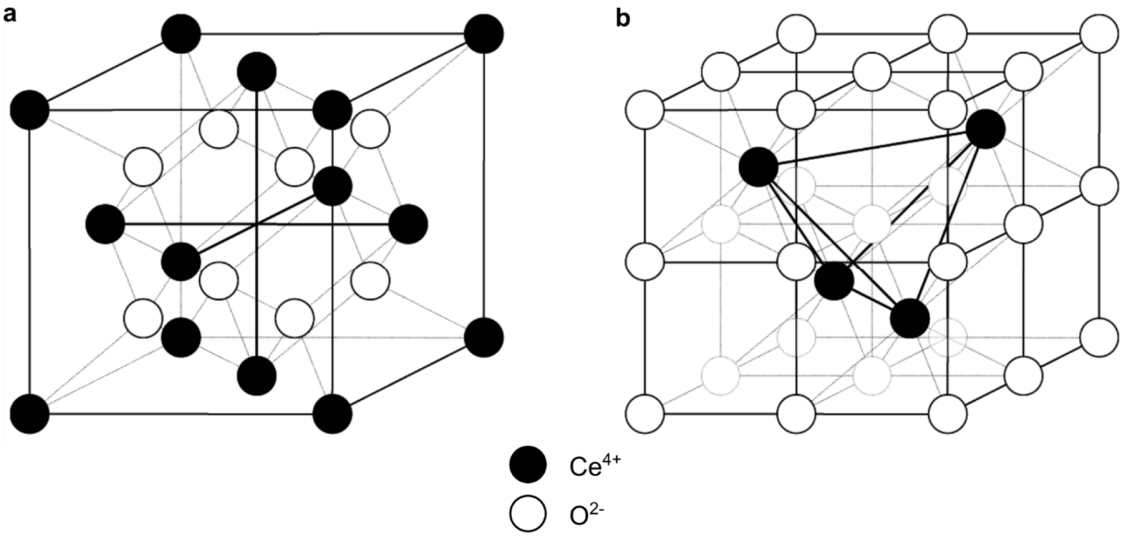

Figure 1.3. The Cubic Fluorite Structure. (a) and (b) are equivalent, but with different unit cell origins. Image from (Stefanik, 2004).

1.3.2 Phase Stability

Ceria releases oxygen to form anion vacancies, which is accommodated via reduction of tetravalent Ce ions to trivalent Ce (Bevan, 1955). The oxygen release process is described using the defect chemical equation (1.1), wherein oxygen nonstoichiometry, δ (or x), yields gaseous oxygen. This is reiterated in Equation (1.2), which employs Kröger-Vink notation to indicate the charge of each ionic defect relative to the ionic species under the condition of net charge neutrality (Kröger & Vink, 1956). For instance, a Ce cation located on a Ce cationic site, Ce_{Ce}^{x}, carries no charge (indicated by x) relative to the host lattice site. An oxygen vacancy, $V_O^{\bullet\bullet}$, carries a charge of +2 (indicated by ••) relative to an occupied oxygen lattice site, and its formation necessitates the existence of two trivalent Ce ions, $Ce_{Ce}^{/}$, under the condition of net charge neutrality.

$$CeO_2 \leftrightarrow CeO_{2-\delta} + \frac{\delta}{2} O_2(gas) \tag{1.1}$$

$$Ce_{Ce}^{x} + 2O_O^{x} \leftrightarrow Ce_{Ce}^{/} + \frac{1}{2} V_O^{\bullet\bullet} + O_O^{x} + \frac{1}{2} O_2\,(gas) \tag{1.2}$$

Oxygen release may result in several intermediate ordered phases of CeO_x (Bevan, 1955; Kang & Eyring, 1997), shown in the phase diagram in Figure 1.4. The α phase, fluorite-type $CeO_{2-\delta}$, dominates the phase diagram when $x > 1.72$. For $1.5 < x < 1.7$ the σ bixbyite $Ce_2O_{3+\delta}$ phase—related to C-type sesquioxide structure—dominates (Kang & Eyring, 1997). At lower temperatures, various disordered α phases order and form oxygen-deficient fluorite-related phases α′, δ, etc. As discussed below in §1.4, this order-disorder transition is detectable as a change in the effective migration activation energy for oxygen

ions. Because the work presented here is performed in air (oxygen partial pressure of 0.21 atm), only the disordered and ordered fluorite-related α phases are of concern. At oxygen partial pressure of 10^{-2} atm, the oxygen deficient fluorite phase was shown to persist to 1200 °C (Tuller & Nowick, 1979).

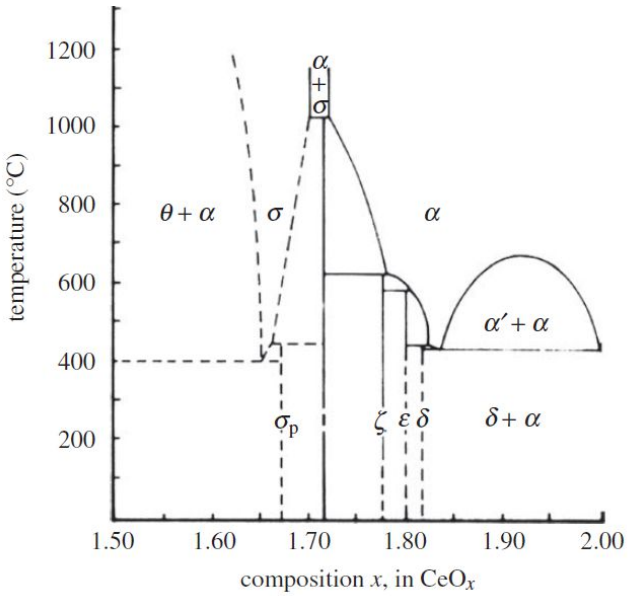

Figure 1.4. Phase Diagram of Ceria, CeO_x. Image presented by Kang and Eyring (1997) and Trovarelli (2002).

The solubility limit for metal oxides in ceria varies considerably, from around 5 mole% (e.g. SrO and BaO) up to about 40 mole% for rare-earth oxides (e.g. La_2O_3, Sm_2O_3) and yttria (Y_2O_3) (Zintl & Croatto, 1939; Yahiro, Eguchi, Arai, & others, 1988; Eguchi, Setoguchi, Inoue, & Arai, 1992; Mogensen, Sammes, & Tompsett, 2000).

1.4 Electrical Conductivity

Electrical conductivity in pure ceria occurs primarily via thermally activated migration of oxygen ions/vacancies and electrons via small polaron hopping (discussed

below), making it a mixed-ionic-electronic conductor (Tuller & Nowick, 1977). In pure ceria, electronic and ionic charge carriers are produced by reduction of cerium ions and formation of oxygen vacancies according to Equations (1.1) and (1.2). The degree of mixed ionic-electronic conductivity depends on the temperature and ambient oxygen partial pressure, which defines the oxygen nonstoichiometry and thus concentration of mobile carriers. Ion conduction is thermally activated motion of oxygen ions into oxygen vacancies, and is the minority contribution to total conductivity in reduced pure ceria. For example, at 1000 °C ionic conduction comprises less than 3 % of the total conductivity when the oxygen partial pressure (pO_2) is 10^{-6} atm (Trovarelli, 2002). In air ($pO_2 \approx 10^{-1}\ atm$) the degree of oxygen non-stoichiometry, x in CeO_{2-x}, was shown to be below 10^{-3} at temperatures below 1200 °C (Tuller & Nowick, 1979).

To utilize ceria as an oxygen electrolyte, however, the fraction of ionic contribution to total conductivity (the ionic transference) must far exceed that of the electronic contribution, i.e. the ionic transference number must be approach unity. This is typically achieved by increasing the concentration of oxygen vacancies through formation of solid solutions containing di- and/or trivalent substitutional cations, discussed below. For example, Figure 1.5 shows the transference number of $Y_{0.05}Ce_{0.95}O_{1.98-\delta}$ at 800 °C is unity down to (i.e. the *electrolytic domain* extends to) $pO_2 \approx 10^{-5}\ atm$ before appreciable electronic current is detected (Tuller & Nowick, 1975). Assuming one is familiar with the defect chemistry and defect formation equations for mobile carrier species (e.g. Equation (1.2)), it is possible to determine ionic transference via conductivity measurements performed as a function of the oxygen partial pressure, which dictates the carrier concentration via mass balance relationships such as Equation (1.2).

The total electrical conductivity, σ_{Total}, is the sum of all mobile species contributing to conduction following

$$\sigma_{Total} = \sum_i n_i q_i \mu_i \tag{1.3}$$

where n, q and μ are the concentration, charge ($= |z_i|e$), and mobility of the ith species, respectively, and e is the charge of an electron.

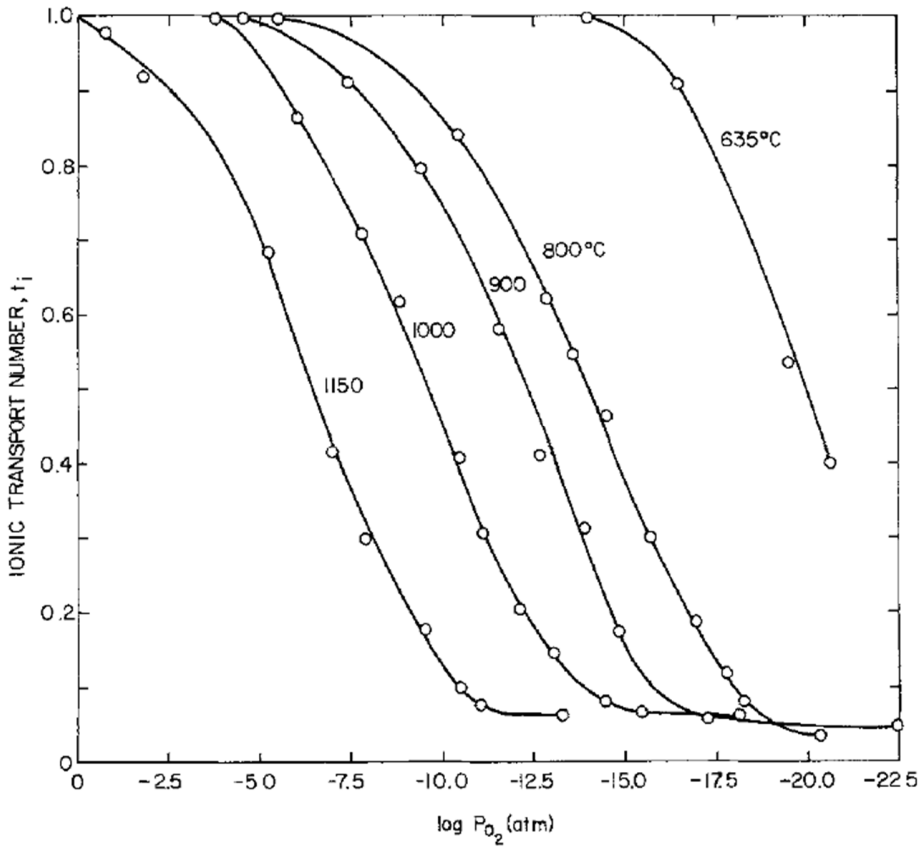

Figure 1.5. Ionic Transference Number vs. Oxygen Partial Pressure. Ionic transference ('transport number') t_i of $Y_{0.05}Ce_{0.95}O_{1.98-\delta}$ at various oxygen partial pressures and temperatures. Image from (Tuller & Nowick, 1975).

The mobility of a particular species which undergoes thermally activated migration in the presence of an electric field (e.g. an ion/vacancy or polaron) is defined as

$$\mu_i = \frac{\nu\alpha^2 q}{kT} exp\left(-\frac{\Delta G_i}{kT}\right) \tag{1.4}$$

where ν in the lattice vibrational frequency ($\approx 10^{13}\ sec^{-1}$), α is the migration jump distance, and ΔG_i is the free energy of activation for motion (Kingery *et al.*, 1976), which can be defined in terms of the migration activation enthalpy, ΔH_i, and entropy, ΔS_i as

$$\Delta G_i = \Delta H_i - T\Delta S_i \tag{1.5}$$

Substituting Equation (1.5) into (1.4) yields

$$\mu_i = \frac{\nu\alpha^2 q}{kT} exp\left(-\frac{\Delta H_i - T\Delta S_i}{kT}\right) \tag{1.6}$$

which can be rewritten as

$$\mu_i = \frac{\nu\alpha^2 q}{kT} exp\left(\frac{\Delta S_i}{k}\right) exp\left(-\frac{\Delta H_i}{kT}\right) \tag{1.7}$$

Taking Equation (1.3) for a single mobile species, and inserting into it Equation (1.7) produces

$$\sigma_i = n_i \frac{\nu\alpha^2 q_i^2}{kT} exp\left(\frac{\Delta S_i}{k}\right) exp\left(-\frac{\Delta H_i}{kT}\right) \tag{1.8}$$

which can be simplified to

$$\sigma_i = \frac{\sigma_i^0}{T} exp\left(-\frac{E_a}{kT}\right) \tag{1.9}$$

where σ_i^0 is the carrier-concentration-dependent pre-exponential factor

$$\sigma_i^0 = n_i \frac{\nu \alpha^2 q_i^2}{k} exp\left(\frac{\Delta S_i}{k}\right) \tag{1.10}$$

and E_a is the effective activation energy for migration (Bauerle & Hrizo, 1969; Kilner & Waters, 1982). This quantity reflects the dual contributions of the migration enthalpy, ΔH_m, and defect association enthalpy, ΔH_a, as

$$E_a = \Delta H_m + \Delta H_a \tag{1.11}$$

At lower temperatures, the aliovalent solutes and charge-compensating oxygen vacancies form defect associates. As demonstrated theoretically by Kilner and Waters, as temperature increases, the contribution of the defect association enthalpy to E_a decreases or becomes insignificant (Kilner & Waters, 1982; Nowick & Park, 1976), thus lowering E_a. It is thought that an order-to-disorder transition occurs above a certain temperature that liberates mobile oxygen vacancies. The drop in E_a is detectable as a gradual decrease in slope of the conductivity Arrhenius plot at high temperatures, exemplified in Figure 1.11, below. In the high temperature regime, wherein defect association effects are insignificant, the conductivity is controlled by the concentration of mobile charge carriers, defined by the extrinsic solute concentration.

1.4.1 Small Polarons

Charge carriers (electrons and holes) in ionic solids are coupled to optical phonon modes of the lattice, which impacts charge mobility. As the carrier moves through the lattice it is accompanied by a lattice distortion, or a cloud of phonons. This combination of

charge carrier and associated distortion, or polarized configuration, of the lattice is a polaron. If the coupling strength is sufficient to stabilize the carrier to a lattice site, it is referred to a small polaron, implying that the size of the lattice distortion is comparable to the lattice parameter (Agullo-Lopez, Catlow, & Townsend, 1988).

As mentioned above, thermally activated small polaron hopping gives rise to significant n-type electronic conductivity in pure ceria which strongly influences transport properties (Tuller & Nowick, 1977). In $Pr_xCe_{1-x}O_{2-\delta}$ (PCO), small polarons localized on mixed-valent $Pr^{3+/4+}$ serve as both mobile charge carriers (Bishop, Stefanik, & Tuller, 2011, 2012) and absorption color centers (Bowman, March, Hernandez, & Crozier, 2016; J. J. Kim, Bishop, Thompson, Chen, & Tuller, 2014; J. J. Kim, Bishop, Thompson, Kuru, & Tuller, 2012), and will be discussed in detail in the results chapters.

1.4.2 Ceria Solid Solutions

Ionic conductivity occurs in ceria via oxygen vacancy hopping, whereby oxygen ion diffusion is facilitated by the counter diffusion of oxygen vacancies (Trovarelli, 2002). Vacancies can form thermodynamically at high temperatures or under reducing conditions (see Equations (1.1) and (1.2)), or to maintain charge neutrality upon the addition of aliovalent solute cations such as Gd^{3+}, Sm^{3+}, Ca^{2+}, etc (For examples of other solutes see (Omar, Wachsman, Jones, & Nino, 2009)). This process is illustrated schematically in Figure 1.6, which shows a fluorite half unit cell with an aliovalent solute cation and oxygen vacancy.

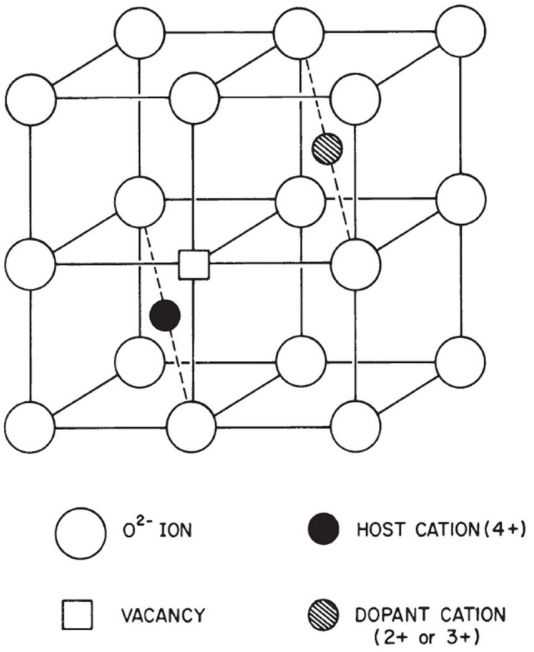

Figure 1.6. Schematic of Aliovalent Solute and Vacancy in Fluorite. A half unit cell with tetravalent host cation, aliovalent solute cation, and oxygen anionic vacancy. Image from (Nowick & Park, 1976)

Equation (1.11) describes the defect chemical reaction for the formation of $Ca_xCe_{1-x}O_{2-x}$ ('CCO'). This reaction produces an oxygen vacancy and gaseous oxygen upon substitution of Ce^{4+} by Ca^{2+} (i.e. $Ca_{Ce}^{//}$ in Kröger-Vink notation, Equation (1.13)).

$$CeO_2 + x\,CaO \leftrightarrow Ca_xCe_{1-x}O_{2-x} + \frac{x}{2}O_2(gas) \tag{1.12}$$

$$CaO \overset{CeO_2}{\longleftrightarrow} Ca_{Ce}^{//} + V_O^{\bullet\bullet} + O_O^x + \frac{1}{2}O_2(gas) \tag{1.13}$$

Like pure ceria, oxygen ionic conductivity in solid solutions depends on both temperature and ambient environment, but also the solute concentration which in part defines the concentration of oxygen vacancies. Figure 1.7 shows the influence of solute concentration on ionic conductivity in several ceria and fluorite solutions (Bishop *et al.*,

2012; Eguchi, Kunisaki, & Arai, 1986). For each material, conductivity isotherms are broad peaks with maxima situated at solute concentrations of ca. 10 mole% – 20 mole%. The broad peak shape results from low carrier concentration at low solute concentration, and increasingly significant defect-vacancy interactions at high solute concentration (Blumenthal, Brugner, & Garnier, 1973). There is also considerable spread in the maximum conductivity for the various solutes, with Gd^{3+} and Sm^{3+} exhibiting the highest conductivity.

It has been shown experimentally and using simulation that optimal ionic conductivity occurs when the solute ionic radius and valence are close to that of Ce^{4+}. As the solute radius and valence deviate from that of Ce^{4+}, defect interactions such as clustering and vacancy ordering (Ou *et al.*, 2008) are increasingly impactful and deleterious to ionic conductivity (Andersson, Simak, Skorodumova, Abrikosov, & Johansson, 2006; Gerhardt-Anderson & Nowick, 1981; Kilner & Waters, 1982). Hence, while solutes of lower valence, such Ca^{2+}, do induce the formation of more mobile oxygen vacancies per solute ion, their impact on the effective activation energy for vacancy migration yields lower ionic conductivity than Gd^{3+}, for example. Nevertheless, it is informative to investigate material properties as a function of solute valence, so Ca^{2+} was employed in this work in addition to Gd^{3+} and mixed valence $Pr^{3+/4+}$.

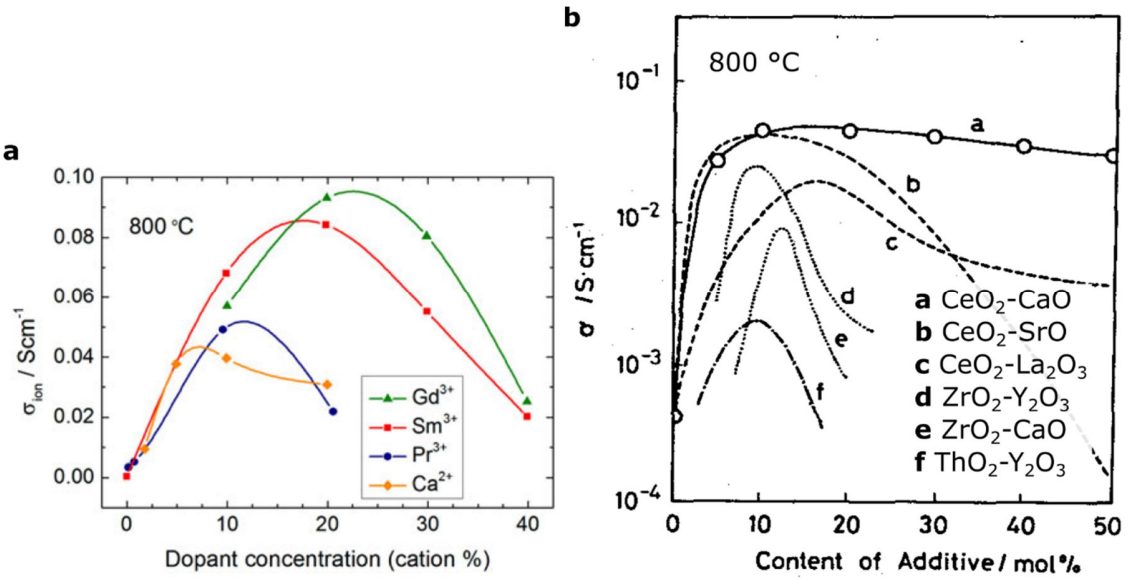

Figure 1.7. Ionic Conductivity vs. Solute Concentration for Fluorite Electrolytes. Ionic conductivity isotherms for various ceria and fluorite solutions at 800 °C. Image (a) from (Bishop *et al.*, 2012); Image (b) adapted from (Eguchi *et al.*, 1986).

Beyond modulating ionic conductivity via solute concentration, researchers have also demonstrated the ability to increase/decrease conductivity using interfacial elastic strain at thin film heterolayer interfaces. It is possible to alter the ionic migration activation energy via compressive and tensile strain in the conduction direction (Jiang, Hu, Shen, Ni, & Hertz, 2013; Korte, Peters, Janek, Hesse, & Zakharov, 2008; Schweiger *et al.*, 2014).

Multiple Solute Solutions

Motivated to improve ionic conductivity via lowering the effective activation energy for ionic conduction, researchers have successfully employed an approach of incorporating two solute cations in ceria solutions. The rationale behind this involves lowering ΔH_a (Equation (1.11)), the component of the effective activation energy related to solute-vacancy association, which stems from the Coulombic interaction between oppositely-charged point defects, the elastic strain field surrounding each solute, and the

strain fields around defect-defect associates (Kilner & Brook, 1982). Omar and coworkers showed that $(Lu^{3+},Nd^{3+})_xCe_{1-x}O_{2-x/2-\delta}$ exhibited higher grain ionic conductivity than either $Lu_xCe_{1-x}O_{2-x/2}$ or $Nd_xCe_{1-x}O_{2-x/2}$, attributing the increase to the fact that the solutes were combined in the appropriate ratio to yield the optimal *weighted average* solute radius, thus zero net elastic strain was measured in the solid solution (Omar, Wachsman, & Nino, 2006). Using DFT to calculate effective migration activation energies for oxygen in ceria solutions, Andersson *et al.* screened candidate solutes and concluded that the ideal solute would have an effective atomic number between 61 (Pm^{3+}) and 62 (Sm^{3+}). They also recommended the solute combinations of Nd^{3+}/Sm^{3+} and Pr^{3+}/Gd^{3+} to maximize ceria ionic conductivity (Andersson *et al.*, 2006).

Motivated by these theoretical findings, Omar and colleagues showed that indeed the grain ionic conductivity measured in $(Sm^{3+},Nd^{3+})_xCe_{1-x}O_{2-x/2-\delta}$ exceeded that of $Gd_xCe_{1-x}O_{2-x/2}$, the ceria solution oft cited as the fastest oxygen conductor. Consistent with predictions, they were also able to explain this behavior based on a decrease the number of solute-vacancy associates known to trap mobile vacancies (Omar, Wachsman, & Nino, 2008). This reduction in the concentration of defect associates, i.e. the number of ordered vacancies, in ceria with two solutes was later corroborated by Ou *et al.* using selected area electron diffraction in the TEM. They showed that diffraction spots (superlattice reflections) associated with ordered oxygen vacancy domains were absent in solutions with two solutes when compared to single solute solutions (Ou, Ye, & Mori, 2011).

Dholabhai *et al.* also used DFT to predict the activation energies for various hopping pathways for an oxygen vacancy in the vicinity of Gd^{3+} and Pr^{3+} solutes in ceria,

and then used kinetic lattice Monte Carlo simulations to predict ionic conductivity. Selected results of this work are presented in Figure 1.8, which shows that the material containing both Pr and Gd solutes outperformed the material containing either solute alone. (Dholabhai, Adams, Crozier, & Sharma, 2011). This result motivated the experimental study described in Chapter 3, and further discussion of this particular solute combination is provided there. It is worth noting here, though, that these predictions have been qualitatively confirmed experimentally (Bowman *et al.*, 2015).

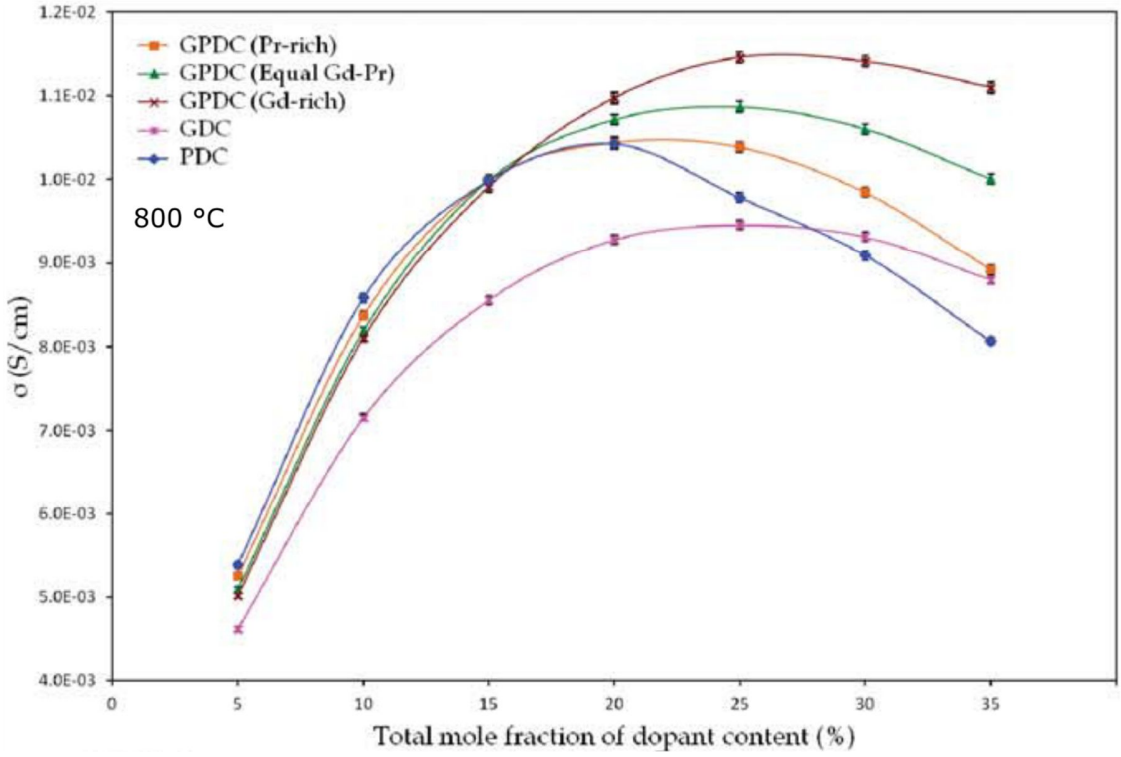

Figure 1.8. Predicted Ionic Conductivity in Ceria with Gd^{3+} and/or Pr^{3+}. Conductivity of $Gd_xCe_{1-x}O_{2-x/2}$ (*GDC*), $Pr_xCe_{1-x}O_{2-x/2}$ (*PDC*) and combinations of Gd^{3+}/Pr^{3+} (*PGCO*) as a function of total solute concentration. Image from (Dholabhai *et al.*, 2011).

Beyond improving ionic conductivity, dual-solute ceria solutions have shown other advantageous electrolytic properties. For example, Dudek *et al.* showed experimentally that adding Ca^{2+} to $Sm_xCe_{1-x}O_{2-x/2}$ and $Gd_xCe_{1-x}O_{2-x/2}$ could reduce electronic conductivity

(i.e. increase ionic transference) without affecting ionic conductivity (Dudek, Rapacz-Kmita, Mroczkowska, Mosiałek, & Mordarski, 2010). This is particularly significant for the performance of solid oxide fuel cells with ceria-based electrolytes, which is degraded by electronic leakage through the electrolyte layer (Jang, Hyun, & Kim, 2002; K. T. Lee *et al.*, 2012; Park & Wachsman, 2006; Wachsman & Lee, 2011). Moreover, replacing expensive or scarce solutes with inexpensive or abundant ones may provide economic and/or ecological advantageous. Cho and colleagues showed that adding CaO and MgO to $Gd_xCe_{1-x}O_{2-x/2}$ effectively improved total conductivity by lowering the grain boundary resistivity. They cited the ability of Ca and Mg to mitigate the accumulation of Si impurities at grain boundaries, reducing the impact of ionically-blocking siliceous grain boundary films (P.-S. Cho *et al.*, 2006, 2008; Y. H. Cho *et al.*, 2007). This particular effect is elaborated upon in the subsequent section on the conductivity of polycrystalline oxide conductors.

1.4.3 Polycrystalline Solids

The total conductivity of a polycrystalline ion conductor like ceria and zirconia comprises conduction through grains and across grain boundaries. Total ionic conductivity is degraded by the presence of highly resistive grain boundaries, which can be as much as eight orders of magnitude more resistive than grains. Using AC impedance spectroscopy (see Methods chapter), Brauerle reported early evidence for this grain boundary effect in yttria-zirconia (Bauerle, 1969), while Wang and Nowick reported similar observations for ceria solutions (see Figure 1.9), and demonstrated that the migration activation energy for grain boundaries was greater than that of grains (Wang & Nowick, 1980). Additional

discussion of conductivity in polycrystalline materials is provided during the discussion of AC impedance spectroscopy in the Methods chapter (see §2.2.1).

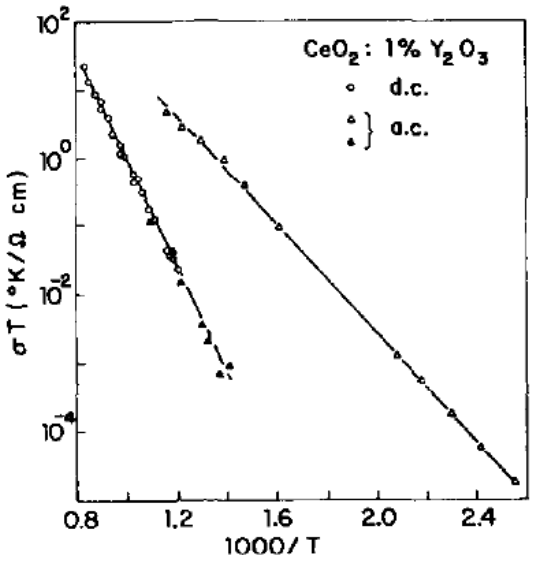

Figure 1.9. The Grain Boundary Conductivity Effect in Ceria. Grain (top curve) and grain boundary (bottom curve) conductivity of $Y_{0.01}Ce_{0.99}O_{2-\delta}$. Image from (Wang & Nowick, 1980).

Using TEM imaging and X-ray spectroscopy (discussed in the Methods chapter), early researchers found that highly resistive impurity phases can be present at grain boundaries. As shown in Figure 1.10, these resistive second phases comprised silica and other alkali impurities, and were thought to be constricting the flow of oxygen across grain boundaries (Gerhardt, Nowick, Mochel, & Dumler, 1986). Subsequent efforts were made to fabricate 'clean' grain boundaries by employing high purity precursors or by adding scavenging solutes such as Ca^{2+} (P.-S. Cho *et al.*, 2006, 2008) or Mg^{2+} (Y. H. Cho *et al.*, 2007), that formed stabile compounds with impurities, thus mitigating their segregation to grain boundaries.

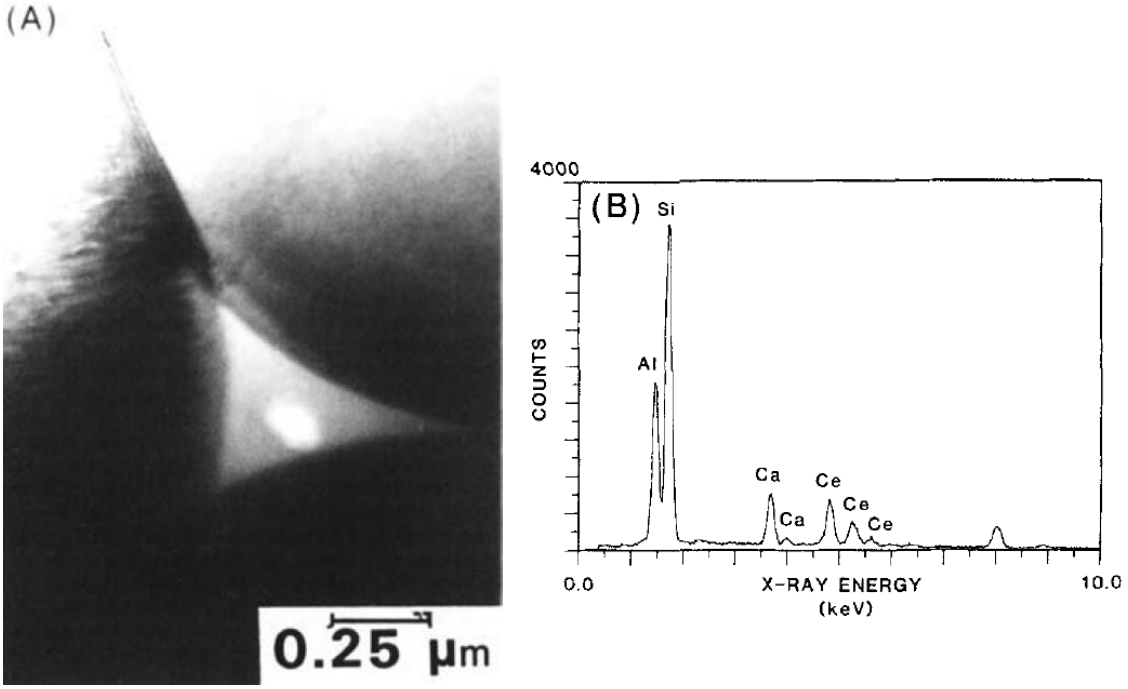

Figure 1.10. Amorphous Impurity Phase at Triple Grain Junction. (a) Bright field TEM micrograph showing amorphous impurity phase wetting a triple grain junction in CeO_2. (b) Energy-dispersive X-ray spectrum acquired from triple grain junction indicating the presence of alkali earth elements. Image from (Gerhardt *et al.*, 1986).

Despite efforts to fabricate high-purity polycrystalline samples with minimal amorphous intergranular phases (Guo *et al.*, 2003), high grain boundary resistivity persisted and is now attributed to grain boundary space charge effects. Exemplary data reported by Avila-Paredes *et al.* for a high purity polycrystalline $Gd_xCe_{1-x}O_{2-x/2-\delta}$ are presented in Figure 1.11 (Avila-Paredes *et al.*, 2009). Discussed in subsequent sections, an intrinsic space charge double-layer potential barrier is believed to be localized at the grain boundary interface, and induces local redistribution of charge carriers in the vicinity of grain boundaries. This redistribution results in depletion of the concentration of charge carriers, degrading conductivity.

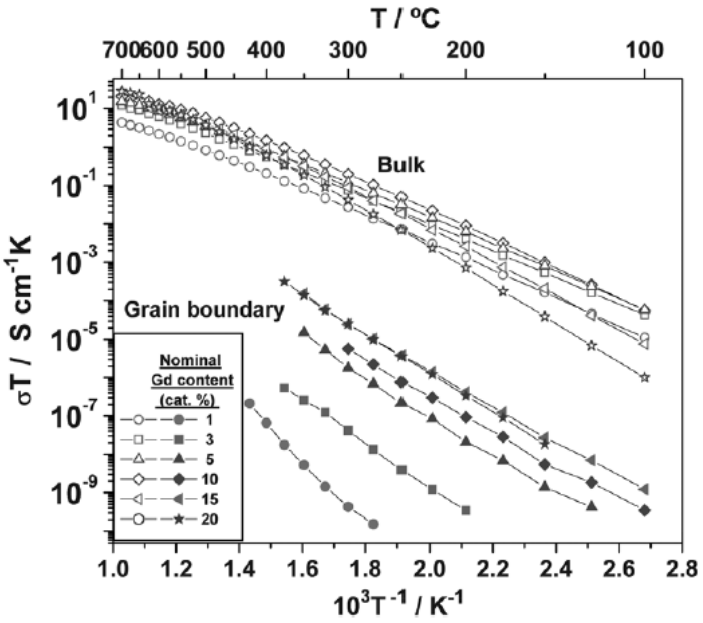

Figure 1.11. Grain and Grain Boundary Conductivity in $Gd_xCe_{1-x}O_{2-x/2-\delta}$ Arrhenius plots of grain (*Bulk*) and grain boundary ionic conductivity in $Gd_xCe_{1-x}O_{2-\delta}$. Image from (Avila-Paredes *et al.*, 2009).

For polycrystalline ceria, grain size is an important parameter when considering the total conductivity and the conduction mechanism. Tschöpe and colleagues showed that as the grain size decreases, the grain boundary volume fraction—and that of the space charge regions—increases (Tschöpe, 2001; Tschöpe & Birringer, 2001). As will be shown below, grain boundary space charge regions in ceria exhibit higher electron concentration than grains, making them more electronically conducting than the grains. With decreasing grain size, electronic conduction in the space charge regions results in an increase in the overall conductivity and a decrease in the effective activation energy, both resulting from electronic conduction. These effects are demonstrated in Figure 1.12.

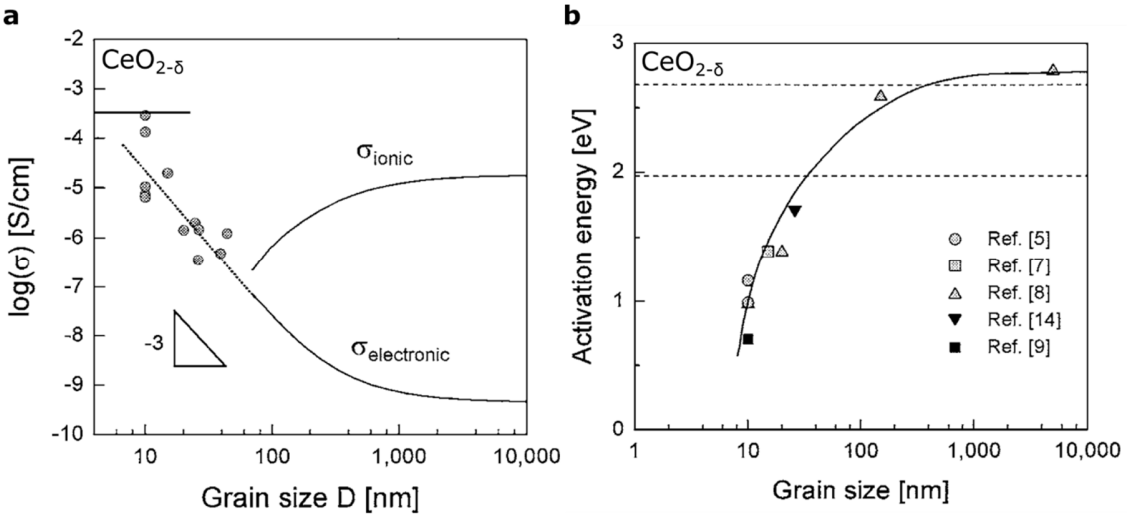

Figure 1.12. Effect of Grain Size on Electrical Properties of Ceria. (a) Dependence of measured electrical conductivity and predicted ionic/electronic conductivity on grain size in ceria. (b) Effect of grain size on effective activation energy in ceria. Images adapted from (Tschöpe & Birringer, 2001).

1.5 Grain Boundaries

Grain boundaries are structural features in solids where adjacent grains meet to form an interface. Grains are typically crystalline, though the boundary between two distinct phases in a solid, regardless of their crystallinity, may also be referred to as a grain boundary (Sutton & Balluffi, 1995). Figure 1.13 shows the microstructure of a dense polycrystalline ceramic with highlighted grain boundaries. Grain boundaries strongly affect the processing and service properties of polycrystalline solids, and have thus been an area of active fundamental research and technological development for many decades (Brandon, 1966; Donald & Craven, 1979; Wang & Nowick, 1980; Cantwell *et al.*, 2014). Many bulk materials properties are influenced by the presence and nature of grain boundaries, such as mechanical strength, optical transparency, electrical conductivity and catalytic activity.

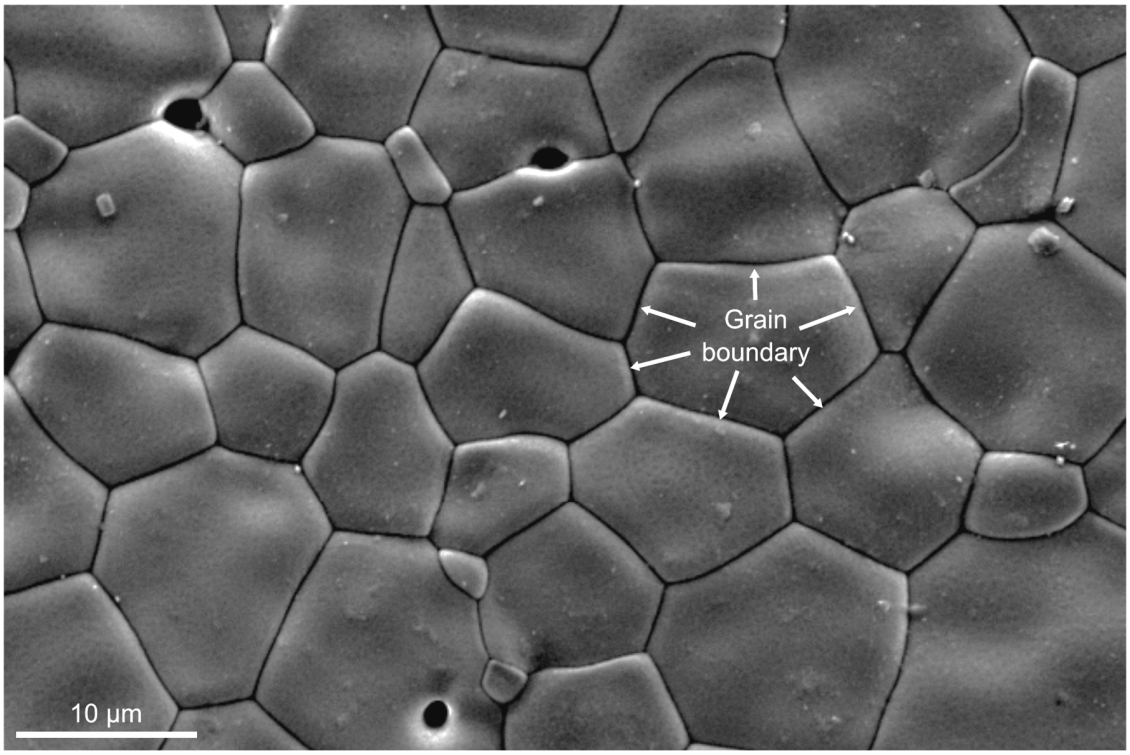

Figure 1.13. SEM Image of the Surface of a Dense Polycrystalline Ceria Solution. Grain boundaries are indicated with arrows. Data acquired following sintering and coating with carbon conductive layer; courtesy of Cruz Hernandez; FEI XL30 FEG SEM.

The energy per unit area of grain boundary is the fundamental thermodynamic quantity which characterizes grain boundaries, and represents the work required to form a unit area of grain boundary. This is the excess free energy in the system resulting from the presence of grain boundaries. A grain boundary is often described using a geometric convention based on five macroscopic degrees of freedom: three parameters specifying the misorientation vector between adjacent grains, and two describing the average orientation, or plane inclination, of the grain boundary plane normal. These parameters can be determined using a stereological technique applied to grain orientation data acquired using automated electron diffraction methods in the SEM via electron backscatter diffraction, or in the TEM using the transmitted diffraction pattern (Rohrer *et al.*, 2004; Darbal *et al.*,

2013). Grain boundaries have generally been classified based on their misorientation angle as ‘low angle’ or ‘high angle’ (a single parameter description). Additionally, grain boundaries may be of coincident site lattice type (also referred to as ‘special’ grain boundaries), where the angle-axis relationship of the adjacent grains is such that their lattice sites coincide partially. As will be demonstrated, in Chapter 3, these occur relatively infrequently, hence their ‘special’ label.

The size and dimensionality of grain boundaries varies considerably, from two-dimensional, atomically abrupt and structurally coherent interfaces, to amorphous intergranular films with thickness on the order of tens of nanometers. Relatively recently, Dillon *et al.* introduced the term “grain boundary complexion” to describe the equilibrium grain boundary state (Cantwell *et al.*, 2014; Dillon, Tang, Carter, & Harmer, 2007). Figure 1.14 illustrates the diversity of grain boundaries, and shows the structure of several grain boundaries observed in alumina (Al_2O_3) by these authors using atomic-resolution TEM imaging. Aspects of these images that are pertinent to this introductory discussion on grain boundaries will be discussed here, with details regarding TEM image formation and contrast mechanisms detailed in the Methods chapter. The images in the top row (a-c) were acquired using annular dark field STEM imaging, which is sensitive to the crystallographic orientation of grains (via diffraction) as well as atomic number of the individual atoms in the image. Images (a) and (c) reveal the presence of relatively heavy Nd atoms adsorbed in a monolayer and bi-layer configuration, respectively. The grain boundary shown in (b) is considered to be ‘clean’, i.e. it is free of adsorbed Nd. The difference in image intensity between the grains on the left and right of the grain boundary arise from differences in the

diffracting condition established in each grain by their respective orientations relative to the incident electron beam.

Images in the bottom row (d-f) are phase contrast TEM images, which are capable of differentiating crystalline and amorphous phases. Again, differences in the relative diffracting conditions of the grains visible in (d) and (e) give rise to differences in their image intensity. The grain boundary in (d) can be described as having a 0.6 nm intergranular disordered layer stemming from multi-layer adsorption, whereas the disordered intergranular phase visible (e) is attributed to an intergranular film. The ~20 nm thick disordered intergranular phase in (f) is attributed to a wetting film which is amorphous (shows uniform mass-thickness image contrast, see Methods chapter).

Grain boundaries exhibit atomic structure, composition, chemistry, phase behavior and properties that are markedly different or unique from adjacent grains, but their limited size, and significant diversity in local crystallography and chemistry make them difficult to characterize, fully describe, and ultimately optimize. The extensive grain boundary diversity in polycrystalline materials, and the considerable difficulty in characterizing them at the nanoscale and atomic level has motivated many researchers to investigate bicrystal model samples, formed by fusing two single crystals (Dimos, Chaudhari, Mannhart, & LeGoues, 1988; Shibata, Oba, Yamamoto, & Ikuhara, 2004; Ye, Yin, Ou, & Mori, 2014). This approach makes it possible to control the character of the grain boundary, and has yielded significant insights into the nature and behavior of grain boundaries.

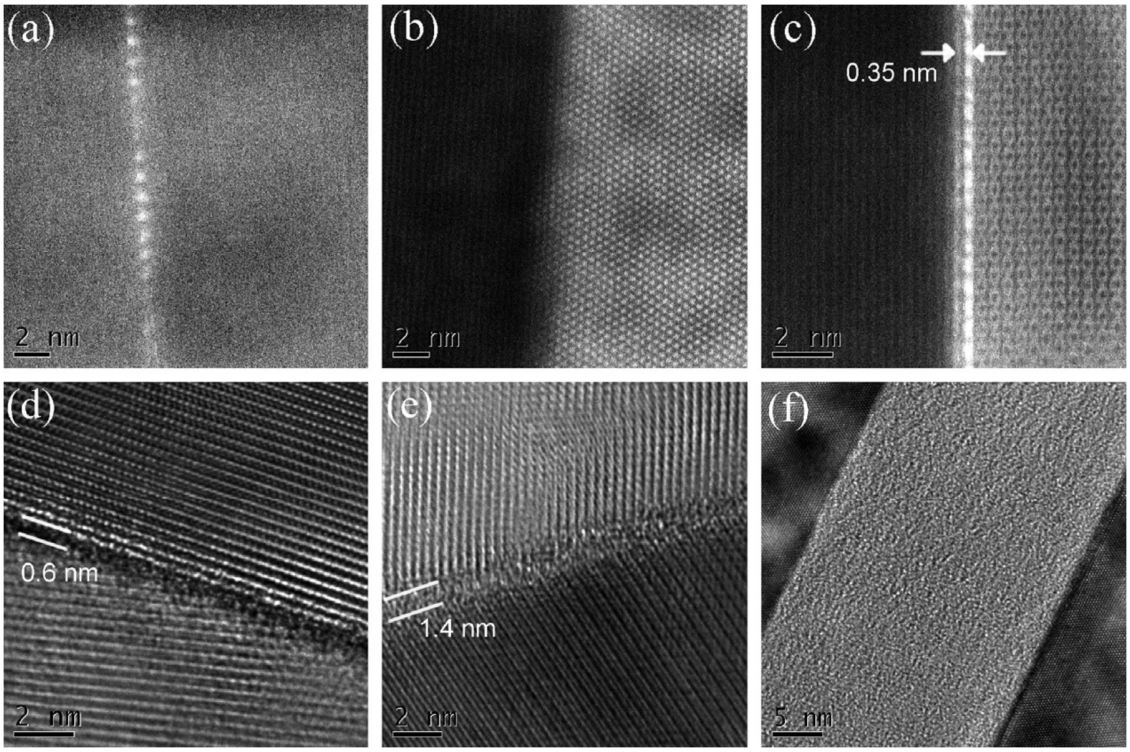

Figure 1.14. Dillon-Harmer Grain Boundary Complexions in Alumina (Al_2O_3). (a-c) annular dark field STEM and (d-f) bright-field TEM images of alumina doped with CaO, MgO, SiO_2 or Nd_2O_3. Image from (Dillon *et al.*, 2007).

Figure 1.15 presents a series of TEM images of yttria-stabilized zirconia bicrystals observed by Shibata *et al.* A number of repeating crystallographic motifs were observed, for instance (a) shows a line of edge dislocations spaced equally along the grain boundary, whereas (g) indicates a faceted array of dislocation cores forming the grain boundary. Model data like these are vital for improving the robustness of grain boundary theoretical models, though it should be noted that the prevalence of such special grain boundaries in polycrystalline material of practical application is limited. This point is discussed further in Chapter 6.

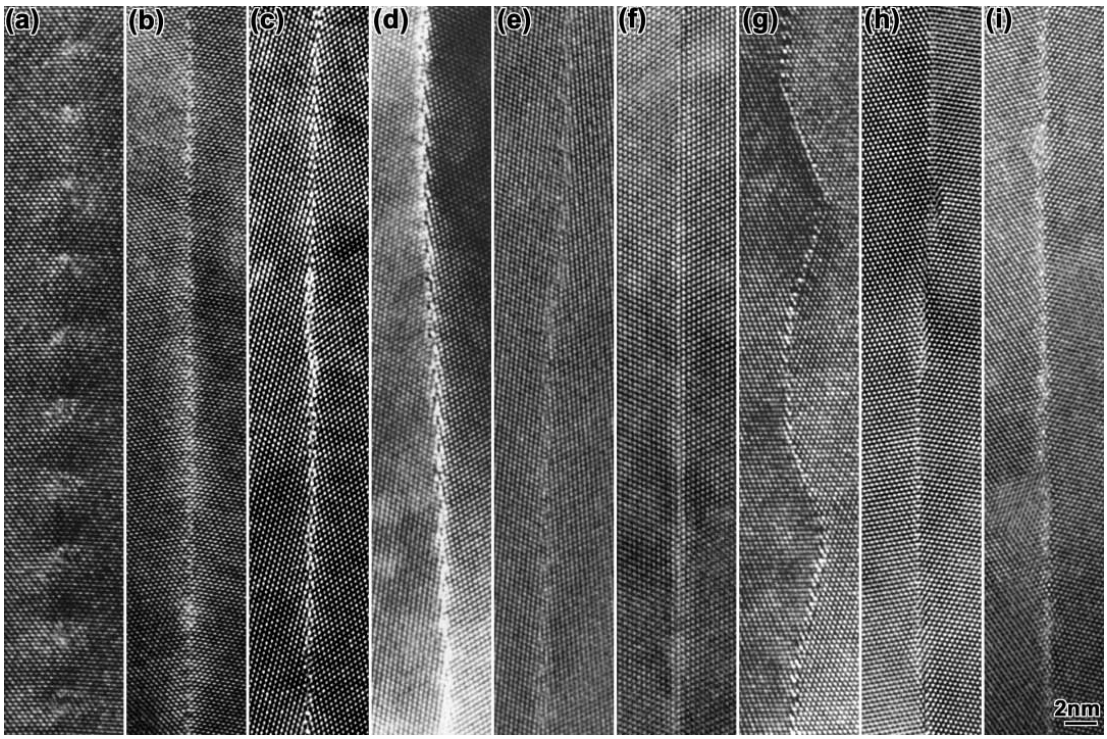

Figure 1.15. TEM Images of Bicrystal Grain Boundaries in Yttria-Stabilized Zirconia. Atomic resolution bright field TEM micrographs of bicrystal interfaces in YSZ. Image from (Shibata *et al.*, 2004).

Considering the minute length scales involved in elucidating the nature of grain boundaries, there has been a significant contribution to the field by TEM investigations. A range of imaging and spectroscopic techniques have been applied to oxide grain boundaries, with a selection reviewed here. TEM phase contrast imaging was used to identify an amorphous impurity phase wetting grain boundaries and constricting oxygen ion conduction paths (Gerhardt *et al.*, 1986), and was used to characterize repeating atomic structure motifs in polycrystalline ceria (Tong, Yang, Moeck, Nandasiri, & Browning, 2013). Direct imaging of oxygen atoms via annular bright field STEM has added robustness to direct quantification of boundary stoichiometry (Findlay, Azuma, Shibata, Okunishi, & Ikuhara, 2011), and the concentration of oxygen vacancies has also been

investigated via negative-spherical-aberration (negative-Cs) imaging in the aberration-corrected TEM (An *et al.*, 2013).

Electron energy-loss spectroscopy (EELS) and energy-dispersive X-ray spectroscopy (EDX) in the TEM and STEM have been used to measure the composition of grain boundaries (Lei, Ito, Browning, & Mazanec, 2002), and of segregated second phases at grain boundaries (Gerhardt *et al.*, 1986). STEM EELS and EDX measurements of ceria and YSZ by our group and others have also served to illustrate the very significant compositional variations localized within nanometers of boundaries; and electronic structure variations observed via STEM EELS revealed abrupt changes in cation valence and oxygen bonding at boundaries and interfaces in ceria (Bowman *et al.*, 2015; Lei *et al.*, 2002).

Addressing the challenges associated with TEM-based characterization, statistically relevant sampling, and the correlation of nanoscale and atomic level grain boundary chemical properties and electronic structure with bulk electrical conductivity is a primary motivation of the research program described herein.

1.5.1 Conductivity

The total conductivity in polycrystalline materials arises from charge transport through grains and along and/or across grain boundaries. Grain boundaries can, in general act as fast conduction pathways or as blocking layers, whose mass and charge transport properties may be independent from that of the grains. The high resistivity for oxygen ion conduction across grain boundaries in zirconia and ceria results from an intrinsic

electrostatic space charge double layer situated at grain boundaries such oxides (M. Kim *et al.*, 2001; S. Kim & Maier, 2002; Guo & Waser, 2004; Mebane & De Souza, 2015). This space charge potential is positive relative to the electroneutral grains and stems from the relatively high intrinsic concentration of oxygen vacancies (charged positive relative to divalent oxygen anions) at the grain boundary. In the space charge region there is a redistribution of charges resulting in the depletion of oxygen vacancies, and often resulting in the accumulation of solute cations. These effects both reduce the mobile carrier concentration in the vicinity of the grain boundary, and increase solute-vacancy interaction effects which increase the effective activation energy for vacancy motion. To elucidate this effect in ceria solutions, theoretical and experimental work, has focused sharply on the electrical properties of extended nanoscale and atomic-level features such as dislocations, grain boundaries and interfaces (Avila-Paredes *et al.*, 2009; Schweiger *et al.*, 2014; Sun, Marrocchelli, & Yildiz, 2015; Mebane & De Souza, 2015; Bowman *et al.*, 2015; Diercks *et al.*, 2016).

As mentioned previously, scavenging solutes have been employed to mitigate segregation of impurities to grain boundaries, improving conductivity overall. Efforts have also been made to optimize conductivity via alteration of the space charge potential barrier, by modifying the concentration and/or species of solute cations deliberately segregated to grain boundaries. This intentional solute decoration of grain boundaries was employed by Avila-Paredes *et al.*, who introduced various divalent transition metal solute species (TM) into $TM_xGd_{0.01}Ce_{0.99-x}O_{2-\delta}$ precursor material prior to the sintering of bulk polycrystalline pellets (Avila-Paredes & Kim, 2006). For select transition metal solutes they reported a drop in grain boundary resistivity and concluded that the space charge potential was

reduced via segregation of transition metal ions to grain boundaries, where they substituted for tetravalent Ce, thus reducing the net positive charge in the space charge region. A similar scheme to alter the space charge potential was implemented by Litzelman *et al.* in columnar-grained ceria thin films fabricated using puled laser deposition (Litzelman *et al.*, 2009). After depositing the ceria films, the authors deposited coating layers of gadolinia (Gd_2O_3) and Ni metal which were allowed to decorate grain boundaries via in-diffusion from the diffusion sources at elevated temperature. They concluded from in-plane conductivity measurements and elemental depth profiling that the presence of in-diffused cations yielded a measurable reduction in the grain boundary space charge potential.

In addition to compositional effects on grain boundary conductivity, grain orientation, the so-called grain boundary *character*, has also been shown to affect grain boundary transport. Researchers have fabricated bicrystal samples with systematically varied misorientation angles in order to demonstrate the influence of interface character on ionic resistivity (Dimos *et al.*, 1988; Ye *et al.*, 2014). Thus, considering the relatively large parameter space defining the grain boundary electrical properties in oxygen ion conductors, the use of correlated characterization across length scales is critical to elucidating the nature of these planar defects in the context of electrical properties. This illustrates the need to develop a fundamental understanding of the relationship between charge transport, grain-boundary structure and composition. Such an understanding may allow grain-boundary tailoring to be accomplished, leading to substantial improvements in ionic conductivity in polycrystalline electrolytes.

1.5.2 Space Charge Formalism

Kliewer and Koehler showed rigorously that the space charge region forms inherently at surfaces of ionic crystals under thermal equilibrium (Kliewer & Koehler, 1965), and Maier has detailed the influence of space charge on the conduction of polycrystalline ionic conductors (Maier, 1986). Kim and coworkers reported analytical solutions to the Poisson-Boltzmann equation to predict defect concentration profiles near grain boundaries under various space charge conditions (S. Kim, Fleig, & Maier, 2003).

An expression relating the space charge potential and the concentration of a charged defect, *j*, at a distance *x* from the grain boundary is derived below. The electrochemical potential of a species *j*, $\tilde{\mu}_j$, is defined in Equation (1.14), where μ_j^0 is the standard chemical potential, *a* is the activity, and ϕ is the electrostatic potential.

$$\tilde{\mu}_j = \mu_j^0 + kT \ln a_j + z_j e\phi \tag{1.14}$$

Under thermodynamic equilibrium, the electrochemical potential of *j* is assumed to be constant at any two points x_1 and x_2 (Kröger & Vink, 1956; Franceschetti, 1981).

$$\tilde{\mu}_j(x_1) = \tilde{\mu}_j(x_2) \tag{1.15}$$

When the concentration of *j* is assumed to be dilute, i.e. they are non-interacting point defects, activity can be approximated as the molar concentration (or site fraction), n (Kröger & Vink, 1956). Under this assumption, substitution of Equation (1.14) into Equation (1.15) yields

$$\mu_j^0(x_1) + kT \ln n_j(x_1) + z_j e\phi(x_1) = \mu_j^0(x_2) + kT \ln n_j(x_2) + z_j e\phi(x_2) \tag{1.16}$$

which simplifies to

$$\ln n_j(x_1) - \ln n_j(x_2) = \frac{z_j e}{kT}\left(\phi(x_2) - \phi(x_1)\right) \tag{1.17}$$

Taking x_2 to be located some distance away from the grain boundary in the neutral grain, $n_j(x_2)$ can be approximated as the nominal bulk concentration of j, n_j^{Bulk}, and Equation (1.17) can be expressed as

$$\frac{n_j(x_1)}{n_j^{Bulk}} = exp\left(-\frac{z_j e}{kT}\Delta\phi(x)\right) \tag{1.18}$$

where $\Delta\phi(x)$ is the grain boundary space charge potential if x_1 is taken to be the position of the grain boundary mid-plane.

Two solutions to Equation (1.18) are presented in Figure 1.16, which shows the predicted charge density distribution for electrons, n, oxygen vacancies, $V_O^{\bullet\bullet}$, and trivalent acceptor dopants, $A_{Ce}^{/}$, in ceria containing 1700 ppm of the acceptor dopant (Tuller & Bishop, 2011). One set of profiles (solid blue curves) was calculated under the so-called Mott-Schottky condition, whereby the acceptor concentration is assumed to be fixed at all locations in the space charge region, which may be a reasonable assumption depending on the thermal history of the material containing said space charge region. The other set of profiles (dashed red curves) was calculated under the Gouy-Chapman condition whereby

the acceptor concentration is allowed to vary spatially, resembling the segregation behavior commonly observed in oxides that have undergone high temperature processing such as sintering. In both cases, the concentration of oxygen vacancies decreases approaching the grain boundary, with the electron concentration increasing.

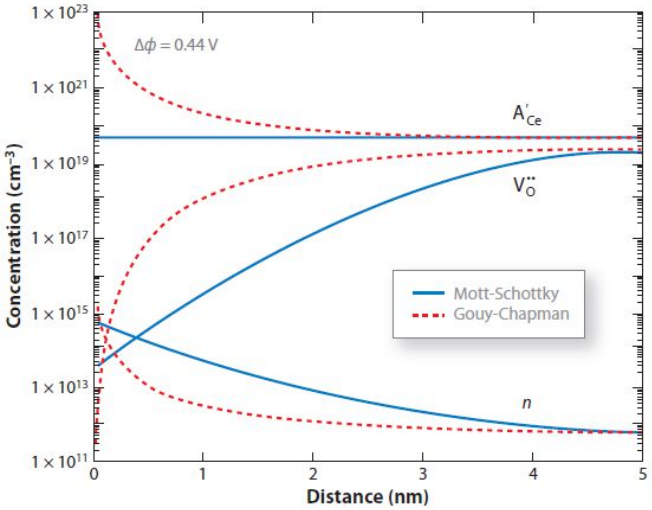

Figure 1.16. Mott-Schottky and Guoy-Chapman Charge Density Profiles. Example profiles for acceptor dopants, $A_{Ce}^{/}$, oxygen vacancies, $V_O^{\bullet\bullet}$, and electrons, n, in the space charge zone near a grain boundary under the Mott-Schottky (solid lines) and Gouy-Chapman (dashed lines) models. Simulation temperature is 500 °C, with space charge potential indicated on the plot. Image from (Tuller & Bishop, 2011).

Equation (1.18) relies on the assumption of non-interacting point defects, implying sufficiently dilute solute concentrations, i.e. < 1 mole% (Mebane & De Souza, 2015), which is about an order of magnitude less concentrated than commonly used ceria and zirconia solutions. Thus, recent efforts have focused on including defect-defect interactions in grain boundary space charge models to make them more applicable to such practical oxide conducting solid solutions. To this end, Mebane and De Souza have proposed a so-called 'Poisson-Cahn' thermodynamic framework which predicts the distribution of trivalent solutes and oxygen vacancies in the space charge region ceria (Mebane & De

Souza, 2015). As the name suggests, their framework combines the standard Poisson-Boltzmann model and the Cahn-Hilliard model for concentrated solid solutions, and includes an excess chemical potential term added to the expression for the electrochemical potential (Equation (1.14)).

$$\tilde{\mu}_j = \mu_j^0 + kT \ln n_j + z_j F\phi + \mu_j^{\text{excess}} \tag{1.19}$$

This excess term is divided into local (f) and non-local (β) terms, which together comprise an effective activity coefficient. The authors derived the electrochemical potentials for oxygen vacancies, v, and trivalent acceptor solutes, a, as shown below in Equation (1.20), which were then used to predict their concentrations, n_v and n_a, resepectively.

$$\begin{aligned} \tilde{\mu}_v &= \mu_v^0 + f_{vv} n_v + f_{av} n_a + RTln\frac{n_v}{1-n_v} + 2F\phi - \beta_v \nabla^2 n_v \\ \tilde{\mu}_a &= \mu_a^0 + f_{aa} n_a + f_{av} n_v + RTln\frac{n_a}{1-n_a} - F\phi - \beta_a \nabla^2 n_a \end{aligned} \tag{1.20}$$

Here f_{vv} and f_{aa} are defect self-interaction energies, and f_{av} is the acceptor-vacancy interaction energy (local interaction terms), and β_v and β_a are gradient energy coefficients (non-local terms); F is the Faraday constant ($F = N_A\, e$) This framework has been implemented in the Chapter 6 as a means to predict grain boundary transport properties, which is a key goal in this work.

1.6 Goals and Objectives

Very significant progress has been made in the optimization of solid oxides for ionic conductivity, primarily through minimization of the effective activation energy for oxygen ion migration. Efforts have focused predominantly on grains, while grain boundary conductivity has not been addressed as comprehensively (Wang & Nowick, 1980; Maier, 1986, 1995; S. Kim *et al.*, 2003; Browning, Klie, & Lei, 2004; S. Kim, Kim, Khodorov, Maier, & Lubomirsky, 2016). Considering the miniscule size and extensive diversity of grain boundaries, this is unsurprising, as elucidating the origin of their properties necessitates precise characterization at the nanoscale and atomic level, requiring specialized—and expensive—micro-analytical instrumentation such as modern aberration-correction TEMs. Moreover, to optimize conductivity, the role of grain boundary atomic structure, nanoscale composition and electronic structure must be correlated with electrical transport properties, assessed micro- or macroscopically using techniques such as AC impedance spectroscopy. However, even when suitable nanocharacterization techniques are applied, there exists an inherent limitation associated with the statistical relevance of such observations to a macroscopic system, so alternative techniques and more complex experimental approaches are required to bridge atomic-, micro- and macroscale observations.

Hence, exploring the interplay between local composition and electronic structure, microscopic character, and macroscopic electrical conductivity of grain boundaries in ceria solutions is a chief objective of this work. This interplay is complex, and still not well understood, so this research program employs macroscopic electrical transport

measurements, a range of electron microscopic characterization techniques, and novel experimental approaches to correlate grain boundary properties across length scales. Ultimately, the goal of this work is to elucidate fundamental relationships between local grain boundary composition and ionic conductivity using advanced TEM techniques and experimental approaches.

Open questions motivating this research program include:

- What is the role of the local grain boundary composition on ionic conductivity in a model system? Is solute segregation correlated with ionic conductivity?
- Can theoretical predictions of state-of-the-art oxygen ionic conductivity in a Pr/Gd dual-solute ceria solution be confirmed experimentally?
- How does local grain boundary composition influence the transport properties and mechanism in the above dual-solute system?
- Can high spatial resolution spectroscopy elucidate these transport properties?
- Can correlated TEM be employed to elucidate transport properties of an entire grain boundary population, and predict ionic conductivity?

To this end, a model system $Ca_xCe_{1-x}O_{2-x-\delta}$ was employed to systematically investigate the role of nominal Ca^{2+} solute concentration on the local grain boundary composition and grain boundary ionic conductivity. While $Ca_xCe_{1-x}O_{2-x-\delta}$ is not the most

conducting solution, Ca^{2+} is abundant, and there is relatively little data published on grain boundary conductivity in this system. It is also considered as a potential divalent solute for application to heterogeneous grain boundary doping schemes intended to modulate grain boundary space charge potential.

Following previous theoretical predictions of state-of-the-art ionic conductivity in Pr/Gd dual-solute solutions, a $Pr_xGd_yCe_{1-x-y}O_{2-y/2-\delta}$ material was fabricated to experimentally verify these predications. This work led to the discovery that grain boundary electrical conductivity was highly sensitive to the Pr concentration, and the hypothesis that the grain boundary transport mechanism was electronic via Pr polaron hopping facilitated by a localized Pr impurity bandgap electronic state. The enhancement of this Pr bandgap state localized at grain boundaries was confirmed using ultra-high energy resolution electron energy-loss spectroscopy in a monochromated STEM, a recently commercialized technique and presently bourgeoning research area in electron microscopy.

The objective of predicting the transport properties off *all* grain boundaries in a polycrystalline material using TEM was then addressed. A correlated approach combining STEM orientation imaging, targeted STEM electron energy-loss spectroscopy and a recently developed thermodynamic model for grain boundaries was employed. This approach ultimately enabled the determination of the DC ionic conductivity of all grain boundaries in the dual-solute solute solution mentioned above using the TEM.

2 Methods

2.1 Material Preparation

Ceria solutions have been synthesized in numerous ways to produce powders, coatings and thin films. Researchers have reported using a diverse set of synthesis approaches including co-precipitation (Avila-Paredes *et al.*, 2009), solid-state reactions (Omar *et al.*, 2009; Pikalova *et al.*, 2011), spray pyrolysis (Rupp & Gauckler, 2006), pulsed-laser deposition (Rupp *et al.*, 2014; Rupp & Gauckler, 2006), DC sputtering (H. Huang, Gür, Saito, & Prinz, 2006), electrostatic spray deposition (Rossignol, Roman, Benetti, & Djurado, 2011), combustion and microwave syntheses (Acharya, Singh, & Bhoga, 2010) and aerosol deposition (Bae, Choi, & Choi, 2013). Due to its simplicity, low cost, high yield, and ability to continuously produce nanoscale powders and deposit layers of tunable composition, spray drying has also garnered attention for use in the synthesis of several materials including rare-earth doped ceria (Blennow, Chen, Lundberg, & Menon, 2009; Bowman *et al.*, 2015; Lundberg, Wang, Blennow, & Menon, 2011; Sharma, Eberhardt, Sharma, Adams, & Crozier, 2010; Van Driessche, Schoofs, Bruneel, & Hoste, 2004; Wu, Tu, Yang, & Shi, 2006). Here, oxide nanoparticles were synthesized from hydrated-nitrate precursor salts (Alpha Aesar; Sigma Aldrich) of > 99.99 % purity.

2.1.1 Spray Drying Synthesis

Powders were synthesized using a spray-drying synthesis technique (Sharma *et al.* 2010). The spray drying apparatus is shown in Figure 2.1. During spray drying, pressurized

gas atomizes a 0.1 M aqueous solution of precursor ions into a fine mist, which enters a reaction vessel where it is introduced to a stream of air heated to approximately 300 °C to produce solid solution particles that are compositionally mixed at the nanometer scale.

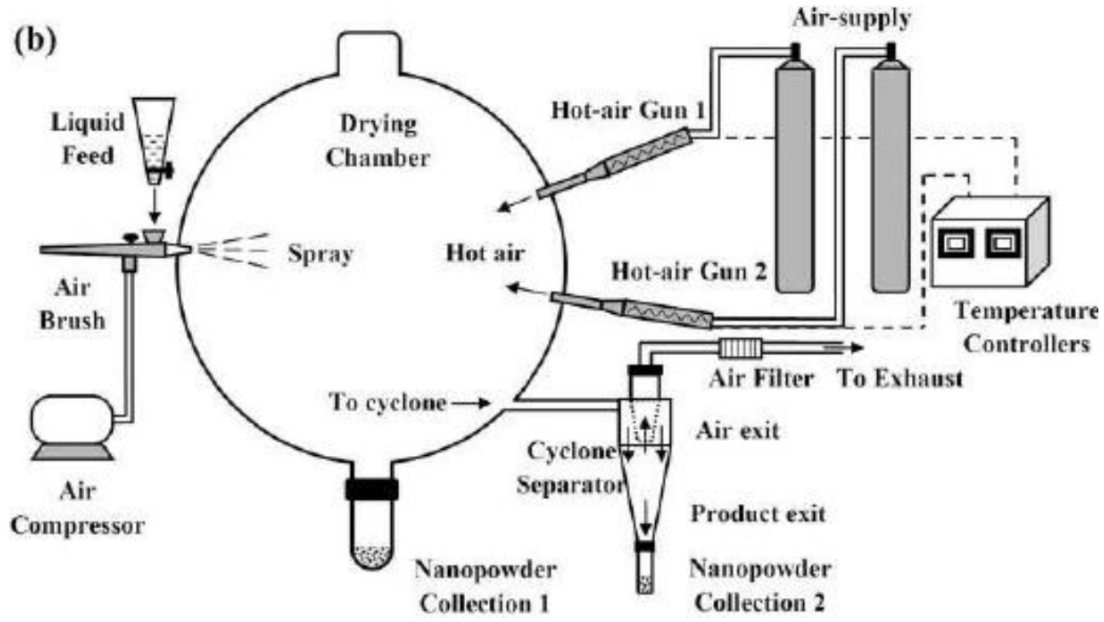

Figure 2.1. Schematic Illustrating the Spray Drying Apparatus.

The as-sprayed product was extracted from the cyclone separator using methanol and dried under air. The as-sprayed product is a combination of oxide crystallites approximately 5 nm – 15 nm in size and a disordered phase containing residual nitrate from the precursor solution. A TEM image is provided in Figure 2.2 showing the typically observed morphology of as-sprayed ceria.

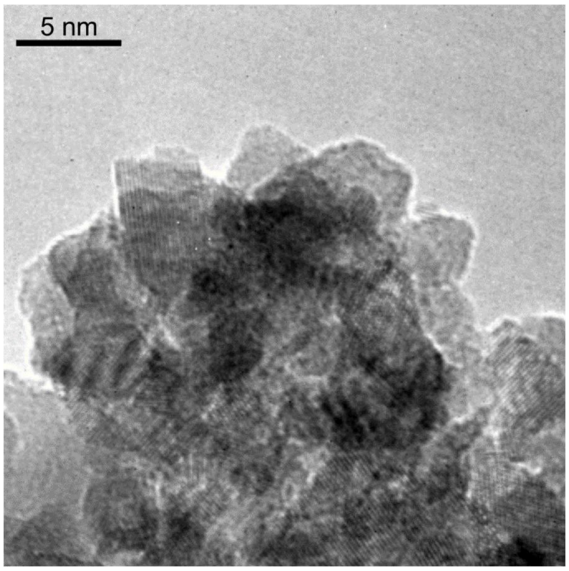

Figure 2.2. As-Sprayed CeO_2 Nanoparticles. 180 kV TopCon TEM, ASU.

The as-sprayed material was then calcined above 500 °C to fully decompose residual nitrate, crushed with a mortar and pestle, and calcined further to coarsen the oxide crystallites. Heating rates and soak temperatures are provided in subsequent chapters for each system investigated. All heat treatments were followed by furnace cooling. Typical particles used for further analysis and/or processing are shown in Figure 5.1.

2.1.2 Pellet Fabrication

Dense polycrystalline pellets (e.g. Figure 1.13) were fabricated by compacting 1.5 g – 2.5 g of calcined powders into cylindrical discs 18 mm in diameter and ~1 mm thick using a hardened steel die. Powders were compacted under uniaxial compression at room temperature using up to 180 MPa pressure. The compacts were pressed such that they could be handled gently without crumbling, and did not show signs of cracking as the result of pressing. Lower pressures were sometimes required to avoid cracking of the compact

during pressing. Compacts were sintered in air between 1300 °C and 1400 °C (see subsequent chapters for details) to densities > 90 % of their theoretical densities as determined using the Archimedes method. Heating rates were between 2.5 °C/min and 5 °C/min, soak times ranged from 12 h to 24 h (see subsequent chapters for details), and all heating procedures were followed by furnace cooling to room temperature. Heating was performed in clean glazed alumina crucibles with lids. Following sintering, the parallel faces of each pellet were polished to remove surface layers using 1 μm lapping film prior to further processing or analysis.

2.2 Electrical Characterization

Macroscopic electrical measurements were performed on pellets using AC impedance spectroscopy (ACIS). Grain and grain boundary conductivities (σ_{Grain} and σ_{GB}, respectively), and grain and grain boundary migration activation energies (E_a^{Grain} and E_a^{GB}, respectively) were determined and used to compare materials of different composition. Characterization of the electrical properties of polycrystalline ionic conductors is aided by the assumption that their microstructure can be approximated as a fully dense array of cubic grains separated by flat grain boundary layers. This formalism enables comparison of grain boundary electrical properties for materials of different grain size, and has been applied readily throughout the solid state ionics literature related to σ_{GB} (Avila-Paredes *et al.*, 2009; Guo & Maier, 2001; Jasper, Kilner, & McComb, 2008). This so called "brick layer model" was derived rigorously by Maier (1986) and summarized by Haile *et al.* (1998). The model, shown in Figure 2.3, assumes cubic grains with average diameter *G* are separated by grain boundaries with average thickness *g* (ca. $10^{-3} \cdot G$ for typical microstructures) arranged

parallel and perpendicular to the conduction direction. *Grain* and *grain interior* are henceforth used interchangeably.

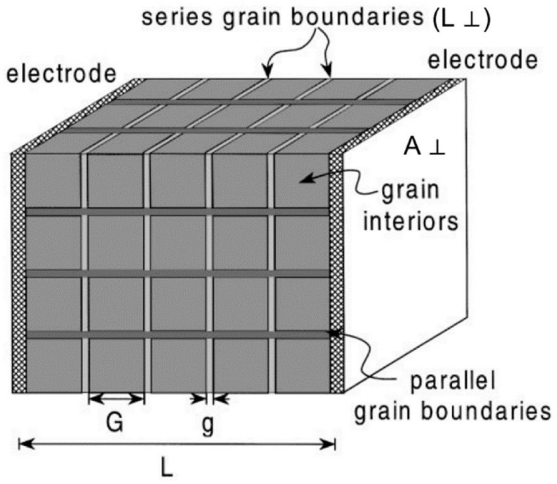

Figure 2.3. "Brick Layer Model" of Polycrystalline Solid; cubic grains (*grain interiors*) are separated by grain boundary layers. Image from (Haile *et al.*, 1998).

For typical ceria and zirconia solutions, σ_{Grain} is typically greater than σ_{GB} by several orders of magnitude at low and intermediate temperatures, so the subsequent discussion will focus on the application of the brick layer model when $\sigma_{GB} \ll \sigma_{Grain}$. The alternative scenarios have been discussed by Haile *et al.* (1998). As detailed below, application of the brick layer model relies on knowledge of—at the very least—the sample geometry, and the resistivity of grain and grain boundary, the latter of which can be measured using AC impedance spectroscopy.

2.2.1 AC Impedance Spectroscopy (ACIS)

ACIS is a technique capable of discerning the impedance response of a material's electrically distinct phases, e.g. grains and grain boundaries (Bauerle, 1969). A detailed

introduction to the technique is available as a book chapter by Lasia in a text edited by Conway, Bockris and White (Lasia, 1999). From knowledge of the sample's geometry, it is relatively straight forward to determine the resistivity of the grains, whose volumetric contribution to the sample is approximately unity. With slightly more information about the solid's microstructure, namely average grain diameter and grain boundary thickness, one can also estimate the grain boundary resistivity from the brick layer model.

During ACIS a time-variant voltage, E_t, with signal amplitude E_0 is applied with radial frequency, $\omega = 2\pi f$, where f is the frequency of the applied potential. This voltage induces a current, I_t, with amplitude I_0, which is out of phase with E_t by phase angle φ. The applied voltage and induced current are both functions of time, t, defined as

$$\begin{aligned} E_t &= E_0 \sin(\omega t) \\ I_t &= I_0 \sin(\omega t + \varphi) \end{aligned} \tag{2.1}$$

The sample impedance, Z, can then be defined as

$$Z = \frac{E_t}{I_t} = \frac{E_0 \sin(\omega t)}{I_0 \sin(\omega t + \varphi)} = Z_0 \frac{\sin(\omega t)}{\sin(\omega t + \varphi)} \tag{2.2}$$

where Z_0 is the magnitude of the impedance. Via Euler's relationship the applied potential and induced current can be expressed using complex functions as

$$\begin{aligned} E_t &= E_0 \exp(j\omega t) \\ I_t &= I_0 \exp(j\omega t - \varphi) \end{aligned} \tag{2.3}$$

where $j = \sqrt{-1}$, and the sample impedance, Z, can be defined as

$$Z(\omega) = \frac{E_t}{I_t} = Z_0\, exp(j\varphi) = Z_0(cos\,\varphi + j\, sin\,\varphi) \tag{2.4}$$

Plotting the imaginary, $Z_{Imaginary}$, and real, Z_{Real}, components of the impedance as a function of frequency yields a complex impedance spectrum, or Nyquist plot (after Harry Nyquist). An idealized Nyquist plot typically observed in studies of polycrystalline oxide conductors (Bauerle, 1969) is presented Figure 2.4; its use is justified below. The Nyquist plot consists of a series of arcs, each corresponding to the impedance response of an electrically discernable component of the sample. In this case the arcs are attributed to the grain, grain boundary, and electrode. ACIS is commonly performed using a porous Pt electrode which allows oxygen exchange with the measurement environment, hence it is 'non-blocking'. To determine electrical properties from a Nyquist plot, it is fit with an equivalent circuit model, which, in the case of polycrystalline oxide conductors, may comprise a series combination of subcircuits each with a resistor (R_i) and a constant phase element (Q_i) in parallel (Figure 2.4). An additional resistor and an inductor (L) are included in series to account for measurement artifacts associated with system resistance and lead inductance. The constant phase element is used to describe non-ideal capacitors, and has impedance

$$Z_Q = [(j\omega)^{\alpha} Y]^{-1} \tag{2.5}$$

where α and Y are constants (Haile *et al.*, 1998). α ranges between zero and one, and is experimentally found to be close to unity, demonstrating that these elements behave like capacitors.

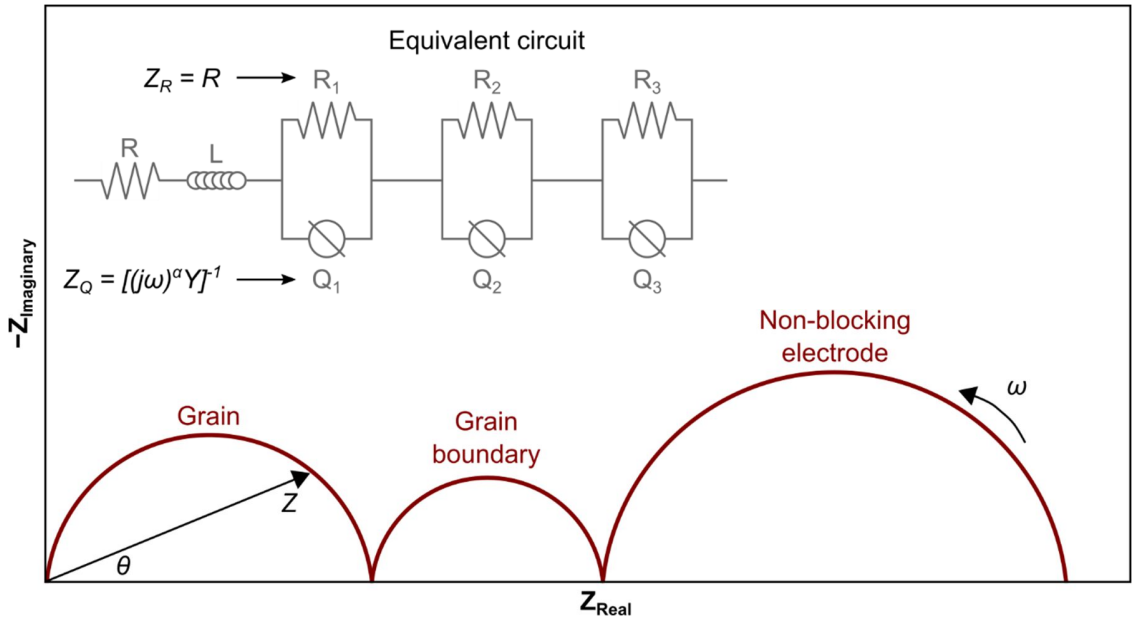

Figure 2.4. Idealized Nyquist Plot for Polycrystalline Conductor. The AC frequency, ω, of the applied voltage increases from right to left. An equivalent circuit model comprising a series combination of resistors, R, and constant phase elements, Q, is inset. Image adapted from (Tuller & Bishop, 2011).

Each RQ subcircuit has a characteristic frequency, ω_0, corresponding to the apex of the arc and defined as

$$\omega_0 = (Y^{-1}R)^{1/\alpha} \tag{2.6}$$

For each arc, if the constant α approaches unity, *and* the characteristic frequency differs sufficiently from that of the other arcs, the resistance of each subcircuit corresponds to the arc diameter measured along the real axis. The equivalent capacitance of an RQ subcircuit, C_{Eq}, is given as

$$C_{Eq} = (R^{(1-\alpha)}Y)^{1/\alpha} \tag{2.7}$$

According to the brick-layer model the resistances of the leftmost (highest frequency) arcs, R_1 and R_2 in the inset equivalent circuit model, explicitly include three impedance contributions: (1) the grain boundaries parallel to the current direction, (2) the perpendicular grain boundaries, and (3) the grains (see Figure 2.2). The contributions of the parallel grain boundaries and grains comprise a parallel subcircuit that is in series with the perpendicular grain boundary contribution, as shown in Figure 2.5.

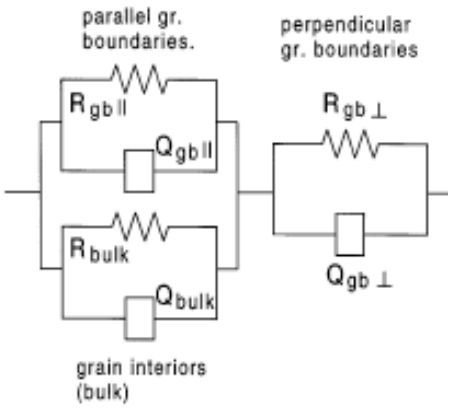

Figure 2.5. Equivalent Circuit Model for a Brick Layer Model. Parallel and perpendicular grain boundary components are explicitly included. Image from (Haile *et al.*, 1998).

By combining the parallel subcircuits, one can simplify the polycrystalline equivalent circuit to that shown in Figure 2.6.

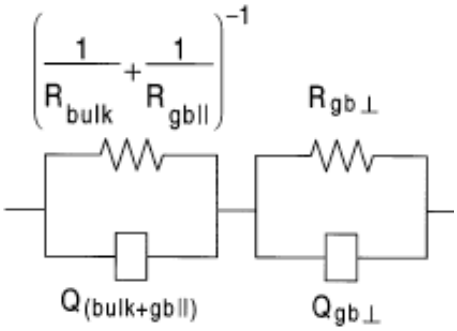

Figure 2.6. Equivalent Circuit Model for a Brick Layer Model. Grain ('bulk') and parallel grain boundary components are combined. Image from (Haile *et al.*, 1998).

Recalling the model diagram (Figure 2.3), the length, $L_{\perp}$, and area, $A_{\perp}$, of grain boundaries perpendicular to the direction of current flow are defined as

$$L_{\perp} = \left(\frac{g}{G}\right) L$$
$$A_{\perp} = A \tag{2.8}$$

With the grain boundary length, $L_{//}$, and area, $A_{//}$, parallel to the direction of current flow defined as

$$L_{||} = L$$
$$A_{||} = \left(\frac{2g}{G}\right) A \tag{2.9}$$

The resistances of each subcircuit in Figure 2.6 can be rewritten in terms of σ_{Grain} and σ_{GB}, where $\sigma_i = \left(\frac{L_i}{A_i}\right)\frac{1}{R_i}$, to yield Equations (2.10) and (2.11).

$$\frac{1}{R_1} = \frac{1}{R_{GB}^{||}} + \frac{1}{R_{Grain}} = \frac{A_{||}}{L_{||}}\sigma_{GB}^{||} + \frac{A}{L}\sigma_{Grain} = \left(\frac{A}{L}\right)\left[\frac{2g}{G}\sigma_{GB}^{||} + \sigma_{Grain}\right] \tag{2.10}$$

$$\frac{1}{R_2} = \frac{1}{R_{GB}^{\perp}} = \frac{A_{\perp}}{L_{\perp}}\sigma_{GB}^{\perp} = \left(\frac{A}{L}\right)\left[\frac{G}{g}\sigma_{GB}^{\perp}\right] \tag{2.11}$$

Assigning conductivities to arcs R_1 and R_2 in Figure 2.4a yields

$$\sigma_1 = \left(\frac{L}{A}\right)\frac{1}{R_1} = \left[\frac{2g}{G}\sigma_{GB}^{||} + \sigma_{Grain}\right] \tag{2.12}$$

$$\sigma_2 = \left(\frac{L}{A}\right)\frac{1}{R_2} = \left[\frac{G}{g}\sigma_{GB}^{\perp}\right] \tag{2.13}$$

This treatment demonstrates that the high frequency arc, *1*, is associated with the parallel grain boundaries and grains, while the lower frequency Nyquist arc, *2*, is associated with the perpendicular grain boundaries. For a material with typical microstructure where $g \ll G$, and $\sigma_{Grain} \gg \sigma_{GB}$, as is the case for typical oxygen ion conductors, Equation (2.12) approximates to

$$\sigma_1 = \left(\frac{L}{A}\right)\frac{1}{R_1} = \sigma_{Grain} \tag{2.14}$$

Equation (2.13) illustrates how $\sigma_{GB}^{\perp}$, henceforth called σ_{GB}, is determined from microstructural data *G* and *g*. Alternatively, if the grain size and grain boundary width is unknown, σ_{GB} can be estimated solely from impedance spectroscopy if one considers the geometric capacitances of the grain and grain boundary, C_{Grain} and C_{GB}, respectively. Capacitances measured using impedance spectroscopy are related to geometrical capacitances as

$$C_1 \approx C_{Grain} = \frac{A}{L}\varepsilon_{Grain}\varepsilon_0 \tag{2.15}$$

$$C_2 \approx C_{GB}^{\perp} = \frac{A_{\perp}}{L_{\perp}}\varepsilon_{GB}\varepsilon_0 = \left(\frac{G}{g}\right)\frac{A}{L}\varepsilon_{GB}\varepsilon_0 \tag{2.16}$$

where ε_{Grain} is ε_{GB} are the dielectric constants of the grain and grain boundary, respectively, and are assumed in the literature to be approximately equal, i.e. $\varepsilon_{Grain} \approx \varepsilon_{GB}$ (Bonanos, Steele, & Butler, 2005). Under this simplifying assumption, the ratio of

measured capacitances is used to approximate microstructural parameters via Equation (2.17), with an expected error of around a factor of two (Bonanos *et al.*, 2005).

$$\frac{C_1}{C_2} \approx \frac{g}{G} \tag{2.17}$$

Substituting Equation (2.17) into Equation (2.13) enables one to estimate grain boundary conductivity solely from impedance spectroscopy. The expressions used in the following chapters to determine σ_{Grain} and σ_{GB} are summarized in Equations (2.18) and (2.19), though the capacitance ratio in Equation (2.19) may be substituted according to Equation (2.17). These methods are compared in Appendix §8.2.

$$\sigma_{Grain} = \frac{L}{A}\frac{1}{R_1} \tag{2.18}$$

$$\sigma_{GB} = \frac{L}{A}\frac{1}{R_2}\left(\frac{C_1}{C_2}\right) \tag{2.19}$$

Pellets were prepared for impedance spectroscopy by polishing their parallel faces using 1 μm lapping film, and then coating with Pt ink (Fuel Cell Materials, Columbus, OH). The viscosity of the Pt ink was such that an ink droplet formed on the pellet surface would require between 10 and 30 minutes to fully wet the pellet's surface with an ink layer 1 – 2 mm thick. Once the droplet was applied, the end of a Pt or Au wire was submerged in the ink such that the wire could be left at rest. The entire assembly was left at room temperature for 24 – 48 h so the organic binder in the Pt ink could partially evaporate. The assembly was then placed in a 100 °C oven for 1 h, prior to firing at 1000 °C for 1 h (1 °C/min heating rate, furnace cooling). The electrode was used for impedance

measurements only if it was continuous, had not wetted the side of the pellet, and was without cracks following firing.

Impedance measurements were performed with the pellet in the center of a tube furnace under air using a Gamry Reference 3000 potentiostat operating in potentiostat (fixed applied voltage) EIS mode (Gamry Instruments, Westminster, PA). An excitation voltage of 50 mV was applied over the frequency range of 0.1 Hz to 1 MHz, and the sample temperature was monitored with a K-type thermocouple. Samples were heated in a stepwise manner between 150 °C and 700 °C in a quartz tube inside a tube furnace (Lindberg Blue), and impedance spectra were acquired at each dwell temperature.

Nyquist plots were fit with equivalent circuit models (e.g. Figure 2.4) using the Gamry E-Chem Analyst software package. Capacitance values were estimated from constant phase elements using Equation (2.7). Grain and grain boundary Nyquist arcs were differentiated based on the brick layer model, and further via comparison of their capacitance values with comparable ceria solutions reported in the literature (Esposito & Traversa, 2008; S. Kim & Maier, 2002). Grain and grain boundary capacitances measured in this work typically varied by two to three orders of magnitude; typical values are provided in subsequent chapters. At higher measurement temperatures, Nyquist plots shifted to lower impedance and the grain arc occasionally became inaccessible due to the 1 MHz upper frequency limit of the potentiostat and the reduced time constant of polarization relaxation at elevated temperatures (Zhan, Wen, Tu, & Lu, 2001). When the grain arc was not visible, σ_{Grain} was determined from fitting the grain boundary arc only. The parallel RQ component corresponding to the grain in the equivalent circuit in these

cases was replaced with a single resistor whose value was assumed to be that of the grain resistance, and σ_{GB} was not determined.

2.2.2 Migration Activation Energy

E_a^{Grain} and E_a^{GB} were calculated from Arrhenius slopes of $ln(\sigma T)\ vs.\ 1/T$ using Equation (2.20), where σ_0 is the conductivity pre-exponential, T is temperature, and k is the Boltzmann constant. Uncertainty in measured conductivities corresponds to the uncertainty in the equivalent model fitting. Uncertainty in activation energies stems from the variation in the Arrhenius slope possible within the error bars of conductivity data points.

$$\sigma T = \sigma_0 e^{\frac{-E_a}{kT}} \tag{2.20}$$

2.3 Physical Characterization

2.3.1 Transmission Electron Microscopy (TEM)

TEM was the primary technique used to characterize the various materials studied here. Imaging was used to access pellet microstructure, and to verify that the grain boundaries analyzed were free of any amorphous intergranular phases. Spectroscopic data were acquired using the TEM to characterize solute distribution and electronic structure of powders, grains and grain boundaries. Details of the development, fundamental physics, instrumentation, and capabilities of TEM are provided in texts by Williams and Carter (2008), Pennycook and Nellist (2011) and Egerton (2011), as well as the Nobel lecture of

Ruska (1987). A condensed introduction to the TEM concepts and techniques most relevant to this dissertation is provided below.

The TEM is a versatile instrument used in physical and biological sciences which employs electron illumination to produce atomic resolution images, and to perform micro- and nanocharacterization of solids, liquids and gases. In-depth, and often otherwise unobtainable, information about materials at the nanoscale and atomic level is accessible via characterizing the various electron-specimen interactions occurring in the TEM. The seminal feature of electron microscopes is their superior resolving power compared to other forms of microscopy. This is illustrated basically by considering Rayleigh's criterion for visible light microscopy, which states that the minimum resolvable distance, δ, is proportional to the wavelength of radiation employed, λ, and can be approximated as

$$\delta = \frac{0.61\,\lambda}{\mu\, sin\beta} \tag{2.21}$$

where μ is the refractive index of the viewing medium, and β the collection semi-angle of the magnifying lens. A similar expression can be derived to approximate the TEM resolution ($\delta \approx 1.22\ \lambda/\beta$), and it is thus apparent that a significant resolution enhancement is possible using electron radiation of wavelength on the order of picometers instead of visible light (Williams & Carter, 2008).

Its invention in 1931 by Max Knoll and Ernst Ruska earned Ruska the 1986 Nobel Prize in Physics, and it has since been an integral characterization tool to the research and development of many modern technologies (Ruska, 1987). At low magnification, TEM imaging provides sub-micrometer information about, for example, the microstructure of

bulk solids, or the morphology and size distribution of particles. A low magnification TEM image is presented in Figure 4.1. At high magnification, atomic resolution images can be utilized to measure interplanar spacing of crystals, or probe the atomic structure of interfaces, surfaces and other defects. An atomic resolution TEM image is presented in Figure 3.6b.

Electron-specimen interactions in the TEM are the basis for electron diffraction, emission of characteristic X-rays, electron energy-loss, etc. A subset of these interactions are illustrated schematically in Figure 2.7, which shows elastic and inelastic scattering of incident electrons by a single C atom (Egerton, 2011). As the incident, or 'fast', electron passes through a specimen it can interact with nuclei and electrons via electrostatic Coulomb forces. This will alter the trajectory and momentum of the fast electron, causing it to scatter, and an appreciable amount of energy may be transferred. Broadly speaking, scattering can be described as either *elastic*—implying a negligible transfer of energy, and *inelastic*—involving a non-negligible energy transfer. Elastic scattering results from attractive interaction with the nucleus, whose intense local electric field deflects the fast electron through high angles, referred to as Rutherford scattering (Figure 2.7a). Strictly speaking, an energy transfer of several or tens of meV can be expected even during elastic scattering, which, in a crystalline specimen may be thought of in terms of phonon excitation, or vibration of the array of atoms. Recent technological advances in TEM instrumentation, discussed below, have motivated pioneering work focused on such vibrational interactions. Elastic interactions in crystals also include diffraction, which considers the fast electron's wave nature and involves the interference of scattered waves

which causes the distribution of scattered intensity to peak sharply at angles characteristic of the atomic spacing.

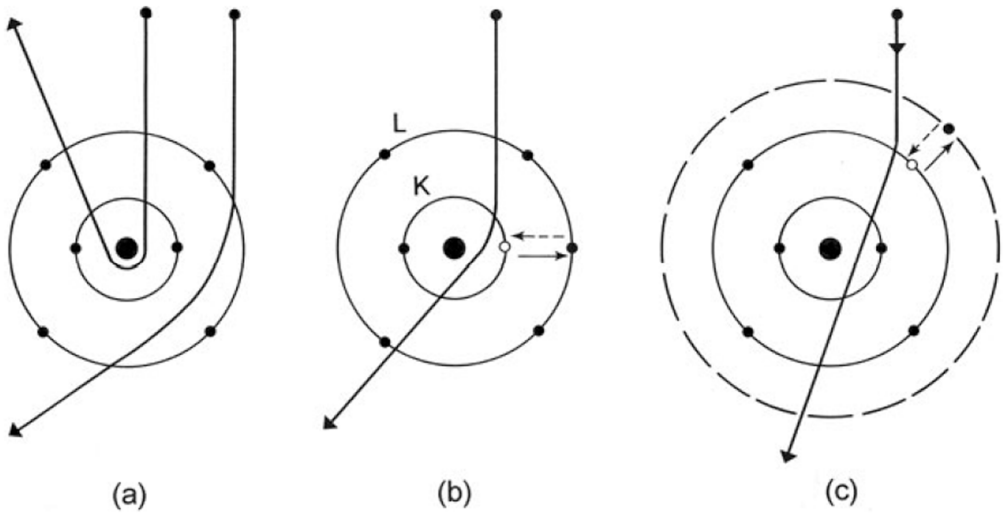

Figure 2.7. Classical View of Electron Scattering by a C Atom. (a) Elastic scattering via nuclear Coulomb attraction. Coulomb repulsion by inner- (b) and outer-shell (c) electrons causes inelastic scattering which excites (solid arrows) bound electrons to higher energy state. De-excitation of these electrons is indicated with dashed arrows. Image from (Egerton, 2011).

Inelastic scattering involves repulsive Coulomb interactions of the incident electron with bound electrons, rather than nuclei, in the specimen (Figure 2.7b-c). This can include single-electron interactions, involving in the transition of a bound electron into an unoccupied energy state above the Fermi level or ejection of the electron from the specimen, leaving behind an excited atom. The de-excitation of this atom can occur via downward transition of an electron to fill the hole, thus resulting in emission of electromagnetic radiation (e.g. visible light and/or X-rays), or the non-radiative transfer of the excess energy to heat. Outer-shell inelastic scattering can, as an alternative to single-electron excitation, involve many atoms and cause a collective oscillation of the valence

electron density, referred to as a plasmon. These electron-solid interactions form the foundation of TEM imaging and spectroscopy techniques described below.

Image contrast in conventional TEM images arises from change in amplitude and/or phase of the electron wave as it passes through the specimen. The basic operating principles of TEM imaging are illustrated schematically in Figure 2.8a, which shows scattering of a plane wave of illumination by a specimen, and the refocusing of the scattered electrons by the imaging lens to a point on the image plane of the microscope. Amplitude contrast can result from spatial variations in the local density or thickness of the specimen, referred to as *mass-thickness contrast*. Mass-thickness contrast is caused by Rutherford scattering, or incoherent elastic scattering, which depends strongly on the atomic number, of the scattering element. In non-crystalline materials, such as amorphous or biological materials, mass-thickness is the chief source of image contrast. The ability to differentiate amorphous phases and crystalline material at the nanoscale was particularly impactful on early microscopic studies of grain boundaries, which were found to serve as sinks for impurity segregation during high temperature ceramic processing. Si, Ca and other alkali earth elements were observed as glassy phases which wet grain surfaces and formed ionically blocking layers.

Amplitude contrast also results from Bragg scattering (coherent elastic scattering) of incident electrons from crystalline material in the specimen, and is thus referred to as *diffraction contrast*. Diffraction contrast is important in both TEM and STEM imaging (described) below, and relies on strong excitation of a single Bragg beam. When this Bragg beam and the unscattered direct beam are used to form an image, this is commonly referred

to as a two-beam condition. In TEM imaging, diffraction contrast results from the interference of the direct and Bragg scattered beam, which are in fact out of phase, making diffraction contrast a form of phase contrast imaging.

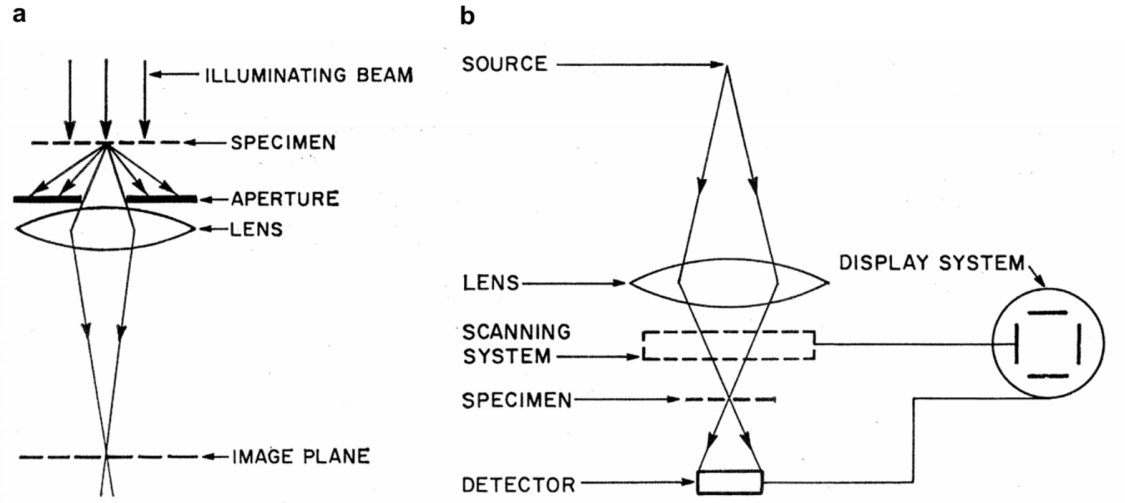

Figure 2.8. Schematic Illustrating TEM and STEM Basic Operating Principles. Comparison of the basic electron imaging system of a conventional TEM (a) and STEM (b). Image from (Crewe, 1966).

Phase contrast arises when scattered beams that are out of phase with one another interfere to form an image (i.e. an interference pattern). The typical distinction between diffraction and phase contrast is the number of scattered beams used to form an image. Phase contrast imaging relies on the interference of many beams and is highly sensitive to instrument and specimen parameters such as objective lens defocus and specimen thickness. Thus, image interpretation is notoriously complex, and it is often the case that image simulations are employed to verify the atomic-level origin (i.e. crystal structure, elemental composition, etc.) of contrast features visible in experimental image data.

2.3.2 Scanning Transmission Electron Microscopy (STEM)

Unlike in the TEM, the imaging (objective) lens of the STEM is positioned ahead of the specimen, and incident electrons are focused to a fine probe which is scanned laterally across the specimen as in an SEM (Figure 2.8b). The first STEM was developed by Baron Manfred von Ardenne in Berlin in 1937-38, around the same time as the TEM (von Ardenne, 1938). He was motivated by the idea that high resolution images could be formed merely via detection of scattered transmitted electrons. By eliminating the post-specimen imaging lens used to refocus transmitted electrons in the TEM, degradation of the image by chromatic aberrations caused by energy-loss in the specimen could be avoided in the STEM. Von Ardenne's instrument was capable of 40 nm lateral resolution, though high levels of image noise represented a key limitation to further instrumental development, and he soon turned his attention to TEM development following the design of Ruska. Nearly three decades later Albert Crewe began development of the modern STEM, incorporating into his design a high brightness unheated field emission source capable of producing a small probe with sufficient beam current (Crewe, 1966). This approach yielded an instrument with resolution of 5 nm, with subsequent designs capable of 5 Å resolution (Crewe, Wall, & Langmore, 1970) and 2.5 Å resolution (Wall, Langmore, Isaacson, & Crewe, 1974), thus making ADF imaging of single atoms in the electron microscope a reality. Today, STEM aberration correction enables the routine formation of 1 Å diameter electron probes.

The basic STEM operating principle is illustrated schematically in Figure 2.8, which compares operating principles of the TEM and STEM. Just like an SEM, electrons

in the STEM are focused to a probe which is scanned laterally over a region of interest in the specimen. Key distinctions between the TEM and STEM include the position of the imaging lens (objective) relative to the specimen plan and the (non-) convergence of the illuminating electrons. Transmitted electrons in the STEM are usually detected using an axial bright field (BF) detector, and/or an annular detector, typically referred to as an annular dark field (ADF) detector, illustrated by Figure 2.9a. The STEM BF detector can be used to produce phase contrast images similar to BF TEM, whereas the ADF detector is often configured with inner collection angle of ~30-100 mrad so as to avoid detection of the direct beam, thus producing a dark field image (e.g. Figure 2.9b). The outer collection angle of the ADF detector may be up to several hundreds of mrad, referred to as high-angle annular dark field imaging, which is particularly chemically sensitive because this incoherent scattered intensity is proportional to the atomic number, Z, of the scattering element (Treacy, Howie, & Wilson, 1978). Annular detectors with inner collection angles in range of ~10 mrad are increasingly common for annular *bright field* (ABF) imaging, a technique proposed originally by Rose (1974) to improve the efficiency of STEM phase contrast imaging. Recently, ABF STEM has been shown to be particularly robust for imaging light elements such as oxygen (Hojo *et al.*, 2010).

Aberration correction

The resolution of electron microscopes is limited ultimately by diffraction effects, but imperfections in current electron optical systems introduce spherical and chromatic beam aberrations that limit present day practical resolution. Relatively recently, spherical aberration correction systems developed by Rose and colleagues for the TEM (Urban,

Kabius, Haider, & Rose, 1999), and Krivanek and coworkers for the STEM (Krivanek, Dellby, & Lupini, 1999) have been commercialized. Basically, a spherical aberration corrector addresses an inherent deficiency of electron lenses, namely that the focusing strength of lens exhibits an angular distribution. In the case of a STEM probe, electrons would ideally be brought to focus at a single point; however, electrons that pass through the focusing lens at different distances from the optic axis are brought to focus at different positions along the optic axis.

The influence of aberration correction in the STEM is illustrated by Figure 2.10, which shows an ADF STEM image of a dislocation array in $SrTiO_3$ acquired (a) *without* and (b) *with* spherical aberration correction. The image recorded with aberration correction exhibits a higher signal-to-background ratio, evidenced by the improved contrast of the bright atomic columns against the dark background. The atomic column positions are also better resolved when compared to the image recorded without aberration correction. The inset images (b-c) show calculated probe intensity distributions for a STEM without a spherical aberration corrector (b) and with (c). It is apparent that the aberration corrected probe intensity is more strongly peaked and narrow, which gives rise to the improved imaging performance. While the enhanced intensity may induce more rapid specimen degradation, aberration corrected probes can be beneficial for spectroscopic applications which benefit from enhanced signal generation.

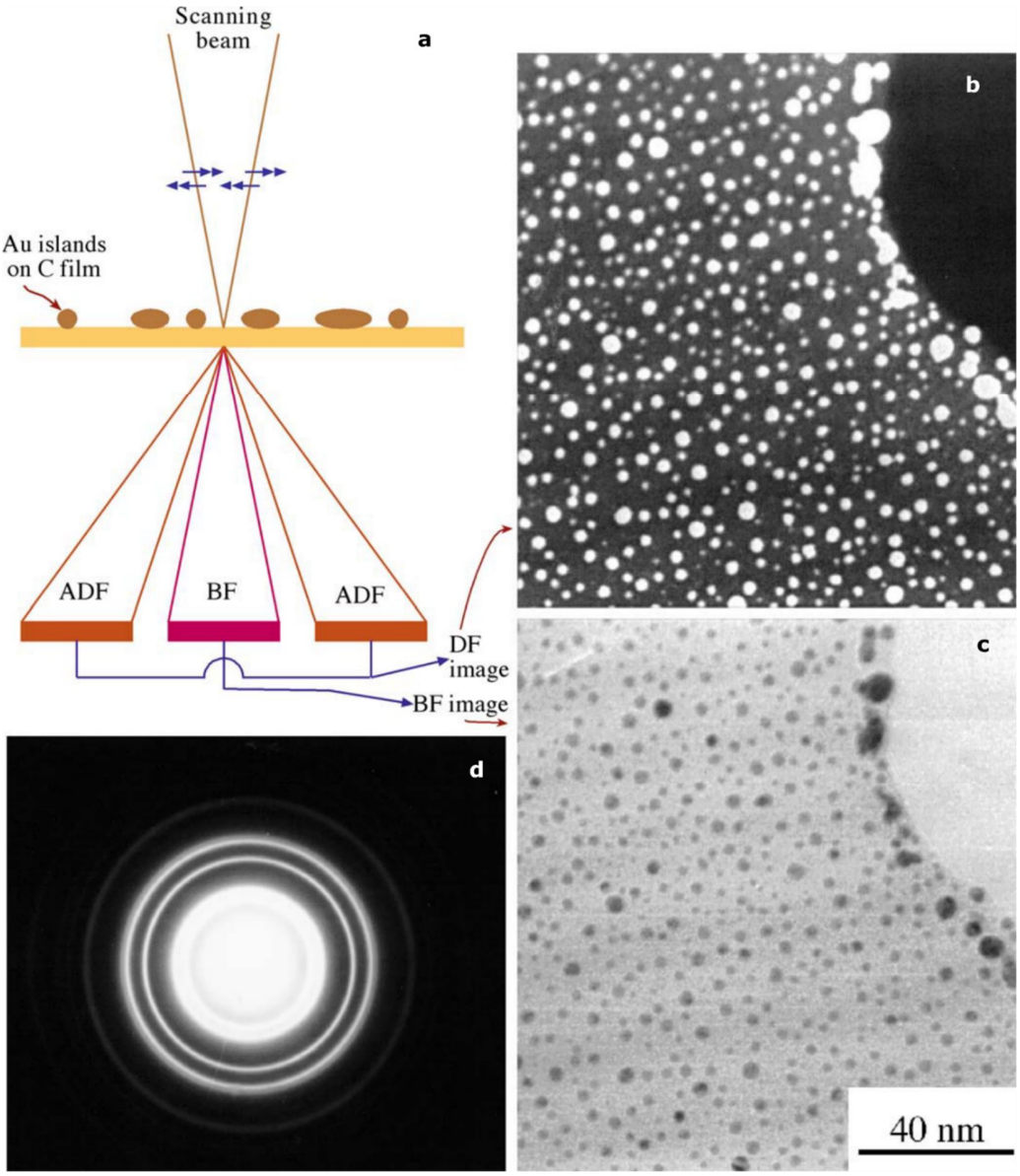

Figure 2.9. Operating Principles of STEM Imaging. (a) Schematic illustrating the basic operating principles of STEM bright field (BF) and annular dark field (ADF) image formation. (b,c) ADF and BF (respectively) STEM images of Au particles on a C film. (d) Selected area diffraction pattern showing the angular distribution of scattered intensity. Image from (Williams & Carter, 2008).

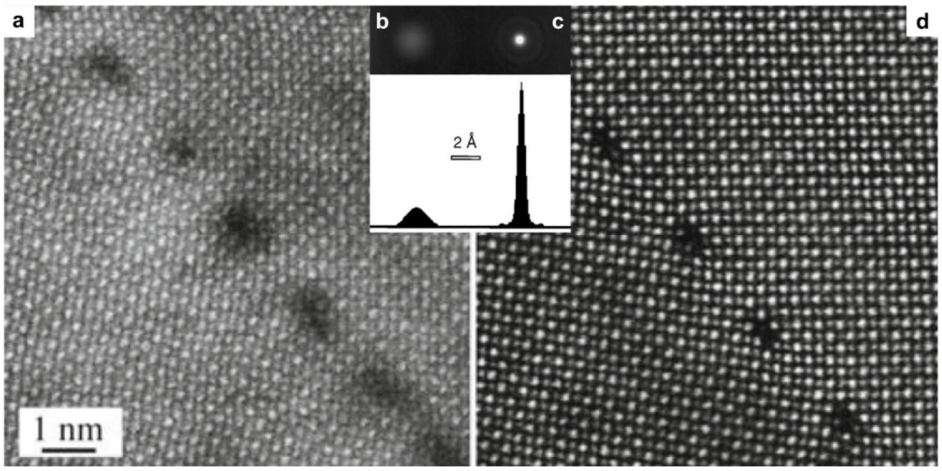

Figure 2.10. STEM Spherical Aberration Correction. (a,d) Comparison of Z-contrast STEM images of dislocation array in $SrTiO_3$ without (a) and with (d) spherical aberration correction. Images adapted from (Williams & Carter, 2008) (b-c) Comparison of STEM probe intensity distributions without (b) and with (c) spherical aberration correction. Top row: shows radially symmetric view parallel to optic axis; bottom row: cross-section view perpendicular to optic axis. Images (b,d) adapted from (Krivanek *et al.*, 1999).

2.3.3 Energy-Dispersive X-Ray Spectroscopy (EDX)

EDX was performed in the TEM and STEM to verify the presence of solutes in ceria solutions, and as part of a procedure to quantify the absolute cation composition off $Ca_xCe_{1-x}O_{2-\delta}$ (Chapter 3). As mentioned previously (see Figure 2.7), when a fast electron scatters inelastically the excited atom may de-excite and emit X-rays isotropically with energy characteristic of the that atom. This chemical sensitivity, combined with the ability to precisely control the position of the primary electron beam has resulted in the widespread application of EDX in scanning and transmission electron microscopy.

The spatial resolution of EDX is defined by the interaction volume in which the primary electrons undergo inelastic scattering. A schematic of the interaction volume for a TEM specimen is provided in Figure 2.11, which indicates that this volume is related to

the specimen thickness because the primary beam broadens as electrons scatter during transmission. For thin specimens, ~tens of nanometers in thickness, the interaction volume in modern aberration-corrected STEM can be on the order of a nanometer, enabling atomic-resolution chemical analysis via EDX. However, X-ray yield drops with decreasing specimen thickness, thus low signal-to-noise ratio can limit sensitivity and spatial resolution. To improve the signal strength for EDX, large-area and/or multi-segment X-ray detectors have been integrated in to TEMs (Pennycook & Nellist, 2011).

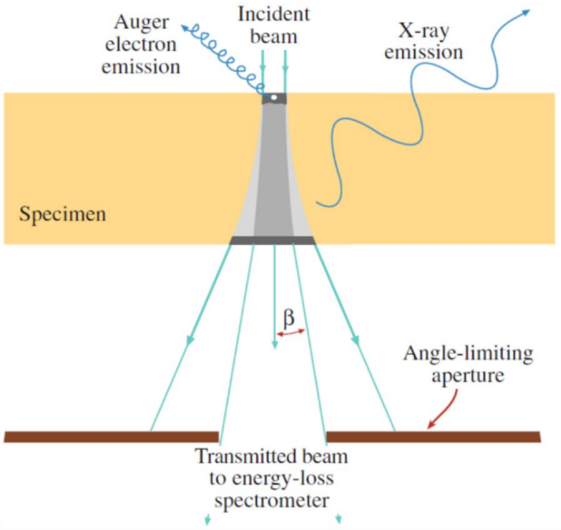

Figure 2.11. Schematic of TEM Interaction Volume. Schematic illustrating the electron-specimen interaction volume and beam path to energy-loss spectrometer. Image from (Williams & Carter, 2008).

2.3.4 Electron Energy-Loss Spectroscopy (EELS)

In this work EELS was employed to measure the spatial distribution of ions, and to assess the electronic structure and valence of cations in particles and in the vicinity of grain boundaries. EELS was used as the primary method of TEM spectroscopic analysis because it enables characterization of local electronic structure in addition to elemental

composition. Furthermore, the bandgap electronic structure of ceria solid solution nanoparticles could be characterized via analysis of the valence-loss region of the energy-loss spectrum.

EELS in the TEM is a powerful technique for probing physical, chemical and optical properties of solids, liquids and gases with high spatial resolution. As the name implies, EELS relies on the quantification of energy lost by incident electrons that are inelastically scattered during transmission through the specimen (Egerton, 2011; Pennycook & Nellist, 2011). The shape of the energy-loss spectrum (described below), and the energy of each loss event can offer detailed knowledge of specimen chemistry and electronic structure of atoms in the specimen, enabling analysis of bonding, local coordination, dielectric properties, thickness, bandgap, etc., much of which is not available via EDX. A chief advantage of the STEM, and indeed one of the motivations for its development, is the ability to couple highly precise positioning of the electron probe with X-ray and energy-loss analysis. In the STEM, where the probe position is known with sub-nanometer precision, the analytical capabilities of EELS (and EDX) are extended down to the length scale of single atoms.

In the TEM, EELS is available in two variants: (1) Broad beam energy-filtered imaging (known as *EFTEM*, or energy-filtered TEM (Crozier, 1995)), whereby a real space image is formed using electrons that have a lost a specified amount of energy. (2) Manual spectral acquisition using a converged or area-selected broad beam, allowing the operator freedom to select the specimen region which will give rise to the spectrum. In STEM EELS,

a spectrum can be acquired at each probe position in a region of interest, enabling pixel-by-pixel spectral acquisition with sub-nanometer spatial resolution.

Less than a decade after construction of the first STEM by von Ardenne, and more than two decades ahead of Crewe's revitalization of the STEM field with the field emission source, it was Hillier who proposed to use "the velocity distribution in the electrons transmitted by thin ... membranes" for microanalysis of "a minute area of the specimen ... irradiated by an electron probe" (Hillier, 1943). In 1966, when Crewe reported his STEM, he also published C K-edge, O K-edge and Al plasmon spectra recorded on his EELS system, giving new motivation to the field of TEM and STEM EELS (Crewe, 1966). The basic operating principle of Crewe's original STEM is shown schematically in Figure 2.12, which includes the field emission source, probe formation and scanning systems, and energy analyzer.

TEM and STEM EELS technique development and studies in biological and physical sciences followed (Colliex, Cosslett, Leapman, & Trebbia, 1976), and spectral processing artifacts and guidelines were elucidated from TEM and STEM EELS (Egerton, 1975; Isaacson & Johnson, 1975). A technological milestone was reached by Krivanek and coworkers when they introduced the parallel EELS detection system, still used widely today (Krivanek, Ahn, & Keeney, 1987). In this system, quadrupole lenses, 'Q_i', are used to focus and magnify the energy-loss spectrum onto a scintillating yttrium aluminum garnet single crystal fiber-optically coupled to a rectangular charge-couple device (CCD). The CCD is employed and detects multiple channels of the energy-loss spectrum

simultaneously, or *in parallel*, the system is sometimes called a parallel detection system, or PEELS.

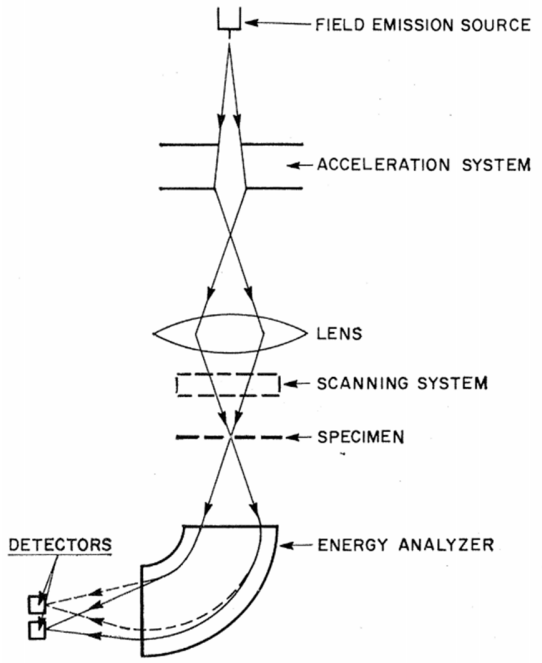

Figure 2.12. Schematic Illustrating Basic Operating Principle of STEM EELS. Image from (Crewe, 1966).

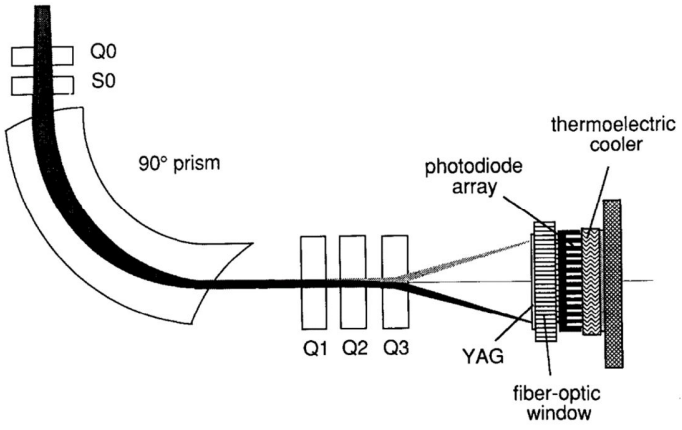

Figure 2.13. Energy-Loss Spectrometer Design Schematic. Schematic illustrating the basic design of a modern energy-loss spectrometer, including the pre-prism alignment/focusing lenses, magnetic prism spectrometer, post-spectrometer lenses and detection system. Image from (Krivanek *et al.*, 1987).

Energy-loss by incident electrons arises from the excitation of core and valence electrons from the occupied bound states of atoms in the specimen to unoccupied states above the Fermi level. This process is illustrated schematically for core-level excitations in Figure 2.14. This schematic uses arrows to indicate electronic excitation from occupied core levels into unoccupied conduction band states in a semiconductor or insulator, whose Fermi level lies in the gap between valence and conduction bands. These ionizations give rise to the indicated core-loss spectrum with energy-loss near edge structure (ELNES) corresponding approximately to the convolution of the initial and final density of states. Modulation of the ELNES within the first several tens of eVs after the edge onset provides information about electronic structure and the bonding environment, which depends on the local crystal structure. The availability of electronic structure information is a key advantage of EELS over EDX. Ionizations into continuum states above the conduction band (i.e. at energy-losses greater than the ELNES) give rise to the extended energy-loss fine structure, sometimes referred to as EXELFS. This region of the ionization edge can provide information regarding the local coordination number and interatomic distances.

To further illustrate the origin of the shape of an EELS ionization edge, a selected example is provided in Figure 2.15, which shows the calculation of the TiO_2 O K edge, and a comparison with an experimentally measured O K edge. From the calculated density of states (Figure 2.15a-c), it is possible to estimate the approximate ionization edge shape via convolution of the initial and final state density under the dipole approximation (Figure 2.15d). In this case, an excellent prediction of the experimentally measured ionization edge is provided. A somewhat similar approach based on the convolution of calculated density

of states is employed in Chapter 5 to model experimental valence-loss EELS data acquired from ceria nanoparticles.

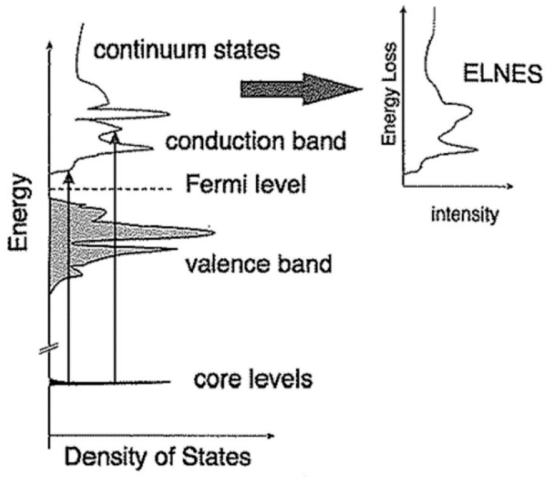

Figure 2.14. Schematic Illustrating Origin of Energy-Loss Spectrum. Schematic illustrating the physical origin of the energy-loss spectrum. Image from Radtke and Botton in (Pennycook & Nellist, 2011).

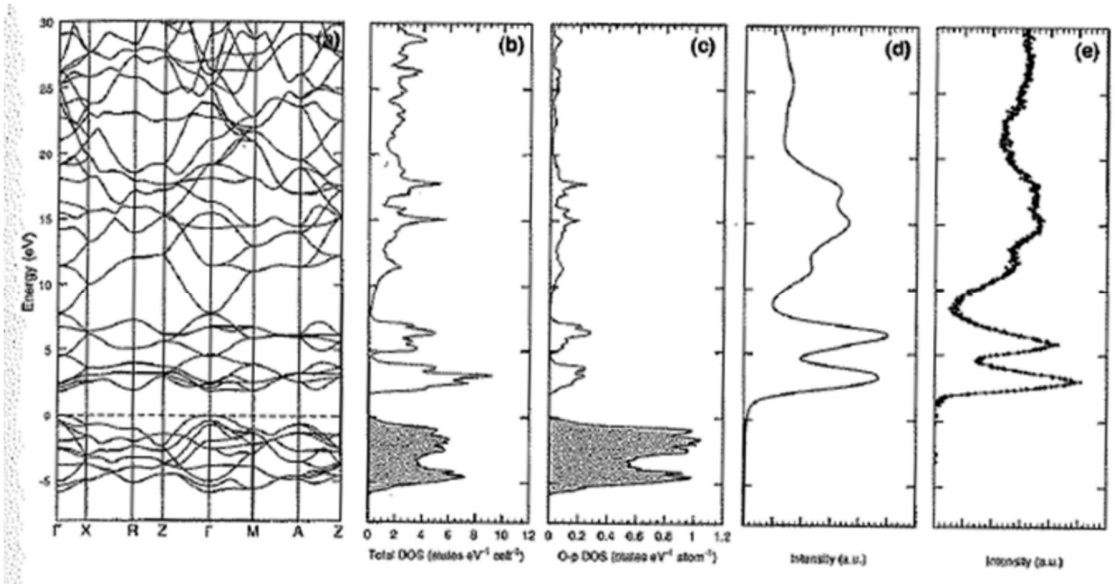

Figure 2.15. First-Principles Calculation of the TiO_2 Electronic Structure. (a) Band structure with energy relative to Fermi level. (b) Total density of states, shaded states are occupied. (c) O *p* projected density of states. (d) O K edge calculated using the dipole approximation. (e) Experimental O K edge. Image from Radtke and Botton in (Pennycook & Nellist, 2011).

To this point, a brief history of the S/TEM EELS technique has been provided, along with a general introduction to the physical processes underlying the measured signal. The discussion below outlines the various EELS spectral components, and provides illustrative examples of some aspects of spectral processing and analyses which yield useful information about the TEM specimen. Subsequent chapters will elaborate considerably on the EELS technique, and will highlight a number of practical aspects related to the discussion in this section.

The energy-loss spectrum comprises three principal features: (1) the zero-loss peak (ZLP), (2) the low energy-loss regime, or low-loss, and (3) the high energy-loss core-loss regime. These energy-loss regimes are indicated in Figure 2.16, which shows a typical energy-loss spectrum from NiO.

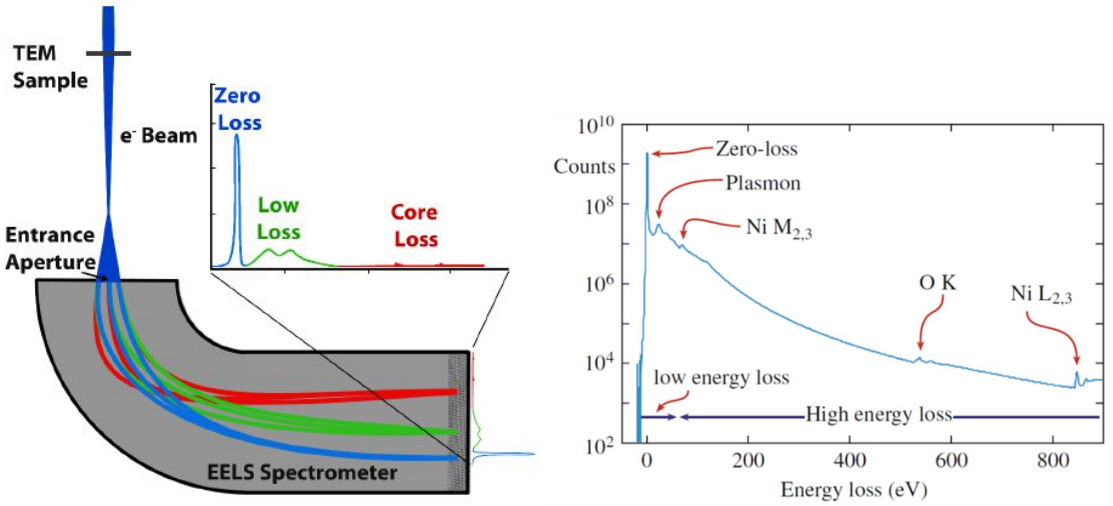

Figure 2.16. EELS Spectrum Acquisition and Features. (a) Schematic illustrating the formation of the energy-loss spectrum using a magnetic prism spectrometer. Colors indicate the relative final energy of electrons in each spectral region. Image from (Crozier & Miller, 2015). (a,b) Spectra comprise three principal regions: the zero-loss peak, low-loss, and high-loss or core-loss. (b) Spectrum (semi-log plot) showing the relative intensity of each region in a measured from NiO (Williams & Carter, 2009).

The ZLP comprises electrons which have been transmitted through the sample without undergoing significant inelastic scattering. The ZLP does not contain spectroscopic information about the specimen, and its tails—which typically extend several eV into the low-loss and degrade the measureable spectral features present in that energy range. Unfortunately, this means that useful spectral information from the near-infrared and visible range is often unobtainable using many microscopes equipped with EELS. While there are not spectroscopic details in the ZLP, it is useful for energy calibration of the loss spectrum, and for determining local thickness as described below.

The width of the ZLP—i.e. the extent of the aforementioned tails—is related to the chromatic incoherence (energy spread) of the incident electron beam, which has been the sharp focus of recent technological progress in the field of high energy resolution EELS. A fundamental limitation on the energy spread of the incident electrons is the energy spread of the electrons emitted by the TEM electron source, which is ca. 0.7 eV for a Schottky emission source, and 0.25 eV for a cold field emission (CFE) source (Krivanek *et al.*, 2014). Using a monochromator, the energy spread of electrons incident on the specimen can be reduced to several hundreds of meV, with the most advanced monochromated instruments giving less than 10 meV. This enables reliable observation of spectral features in the range of 50 meV – 500 meV, like those associated with inter-bandgap states and vibrational excitations.

A monochromator is a series of magnetic prism elements positioned ahead of the specimen which first energy-disperse the incident electrons spatially and then filters them by velocity (i.e. their energy) by passing them through a narrow slit (which transmits a

subset of the electrons according to their energy). This monochromated beam then passes through another magnetic prism or set of prisms which places them back onto the optic axis of the microscope. Figure 2.17 compares ZLPs recorded using a CFE source with and without a monochromator, and indicates the considerable reduction in the width of the ZLP. Application of monochromated EELS to characterize bandgap electronic structure is demonstrated in Figure 5.2.

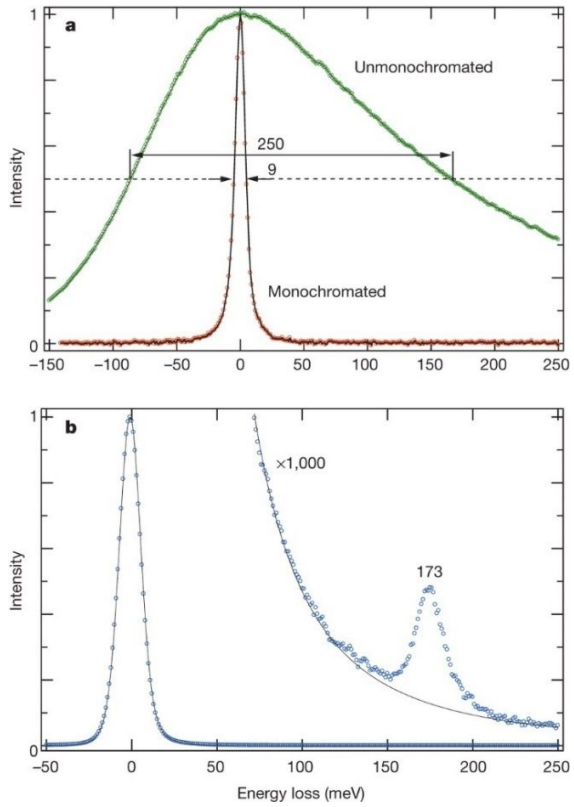

Figure 2.17. Ultra-High Energy Resolution EELS. (a) Comparison of EELS ZLP of CFE source acquired with and without a monochromator. (b) Exemplary vibrational EELS data showing a phonon in BN (173 meV). Image from (Krivanek *et al.*, 2014).

The low-loss, or plasmon, spectrum (losses < 50 eV, typically) is the most intense region of the spectrum aside from the ZLP, and contains information related to the optical properties of the specimen. Plasmons are longitudinal oscillations of the weakly bound

electrons in the valence or conduction bands, and are excited when the fast electron interacts with the specimen. Plasmon oscillations are dampened quickly, with lifetimes on the order 10^{-15} s and localization distance below 10 nm.

The low-loss spectrum also provides a convenient method, described by Egerton (2011), for determining local specimen thickness using EELS. The probability that any one electron undergoes n collisions while passing through the specimen is given by Poisson statistics as

$$P_n = \left(\frac{1}{n!}\right) m^n exp(-m) \tag{2.22}$$

m is the mean number of collision suffered by an electron transmitting the specimen, and is taken as the ratio of the specimen thickness, t, and electron inelastic mean free path (the average distance between inelastic collisions), λ, yielding

$$P_n = \left(\frac{1}{n!}\right)\left(\frac{t}{\lambda}\right)^n exp\left(-\frac{t}{\lambda}\right) \tag{2.23}$$

The probability that an electron travels through the specimen without scattering (i.e. setting $n = 0$ in Equation (2.23)), P_0, relates the total intensity, I_t, with the unscattered intensity (i.e. the ZLP intensity), I_0, by

$$P_0 = \frac{I_0}{I_t} = exp\left(-\frac{t}{\lambda}\right) \tag{2.24}$$

Which gives rise to the useful expression for specimen thickness often referred to as 't-over-lambda ratio':

$$\frac{t}{\lambda} = \ln\left(\frac{I_t}{I_0}\right) \tag{2.25}$$

Figure 2.18a illustrates the influence of specimen thickness (indicated by t/λ) on low-loss and core-loss signals in CeO_2. t/λ was determined using DigitalMicrograph's Log-ratio routine that employs Equation (2.25). I_0, the ZLP, is highlighted in grey, with the effects of increasing specimen thickness is visible as increased plasmon scattering in the low-loss. The core-loss signal (Figure 2.18b) is also affected by plural scattering, with intensity from the Ce M_{45} near edge onset increasingly displaced to higher energy-loss as the specimen thickness increases (Figure 2.18c triangle markers).

The core-loss region includes all losses over 50-100 eV, and arises from interaction of the fast electron with inner shell electrons. In addition to elemental concentrations, core-loss EELS provides chemical information related to electronic structure and bonding, which can be ascertained based on the shape of the spectrum. An example is given in Figure 2.19, which illustrates the evolution of the O K (a,c) and Ce M_{45} (b,d) ionization edges as O ions are removed from a CeO_2 crystal. Sharp peaks are well resolved, with their relative intensities varying systematically with changing O content, an indication in the change in local coordination. The significant intensity modulations in the first several tens of eVs following the ionization edge onset reflects the final state configuration of the electronic transition. The three main peaks in the CeO_2 O K edge are associated with O 1*s* core level excitations into unoccupied Ce levels (Mullins, Overbury, & Huntley, 1998). Two of these peaks (5*d* e_g and 5*d* t_{2g}) arise from the crystal-field splitting of the Ce-O bonding orbitals

of the fluorite structure, and are used in this work to assess loss of long-range order associated with altered coordination at grain boundaries (Hojo *et al.*, 2010; Lei *et al.*, 2002).

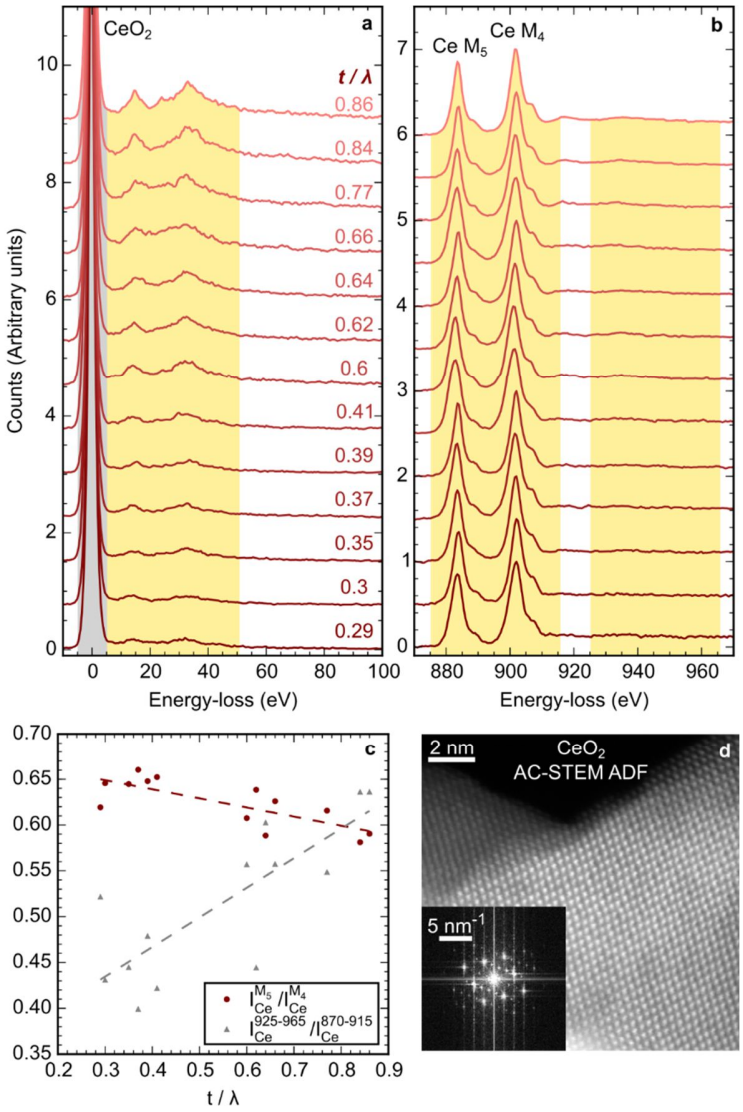

Figure 2.18. Effect of Specimen Thickness on Low-Loss and Core-Loss Signal. (a) ZLP and low-loss spectra from CeO_2 showing the influence of specimen thickness on the low-loss shape and intensity. (b) The influence of specimen thickness on the shape of the background-subtracted Ce M_{45} core-loss spectrum. (c) Relative spectral intensity in the two highlighted integration windows, $I_{Ce}^{870-915}$ and $I_{Ce}^{925-965}$ (triangles). The intensity ratio of the Ce M_4 and M_5 lines, $I_{Ce}^{M_5}/I_{Ce}^{M_4}$, is also presented. (d) AC-STEM ADF image of a CeO_2 crystal used for this measurement. Data from JEOL ARM 200F 200 kV AC-STEM, ASU.

Core-loss spectra are also used in this work as fingerprints to determine cation valence. For example, the peaks in the Ce M_{45} edge are labelled according to their association with the 3+ or 4+ electronic configuration of Ce. The M_{45} multiplet structure (*white lines*) in core-loss spectroscopy of lanthanides results from transitions from 3*d* initial states into unoccupied 4*f* orbitals according to $3d^{10}4f^{n} \rightarrow 3d^{9}4f^{n+1}$, with the relative multiplet intensities and spectral fine structure present in each multiplet indicative of cation valence (Kalkowski, Kaindl, Wortmann, Lentz, & Krause, 1988; Manoubi, Colliex, & Rez, 1990).

Though EELS is readily performed in the STEM using a focused probe (~0.1 nm diameter), the practical spatial resolution depends not only on the probe size, but also the delocalization of the inelastic scattering event responsible for energy loss. Figure 2.20 illustrates the dependence of the delocalization distance on the energy transferred, indicating that the EELS spatial resolution improves with increasing energy-loss. The plotted delocalization distances span about two orders of magnitude, from approximately 10 nm for losses < 5 eV, down ~2 Å for losses > 200 eV. For small energy transfers, on the order of 1 eV or 1 meV, these data suggest that signal delocalization may approach tens of nanometers, which should be a major consideration when characterizing conduction-to-valence band transitions, excitations into inter-bandgap states, or vibrational excitations using EELS.

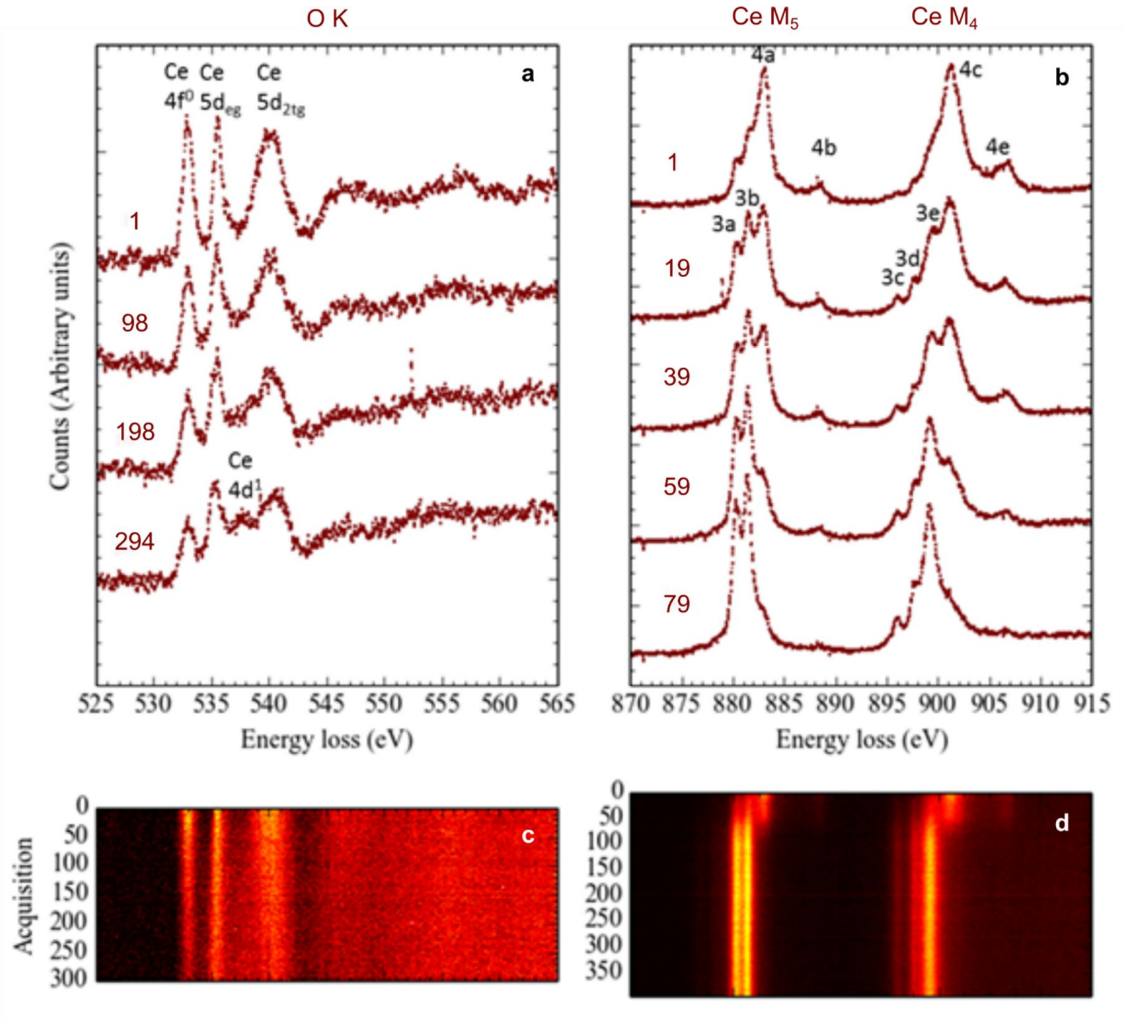

Figure 2.19. EELS Fine Structure Evolution in CeO_2. Evolution of O K and Ce M_{45} core-loss edges during electron beam irradiation in an AC-STEM. O K edge shows increasing oxygen vacancy concentration; Ce M_{45} shows reduction of Ce^{4+} to Ce^{3+}. (a) and (b) share their x-axes with (c) and (d), respectively. 100 kV Nion UltraSTEM100 AC-STEM, ASU.

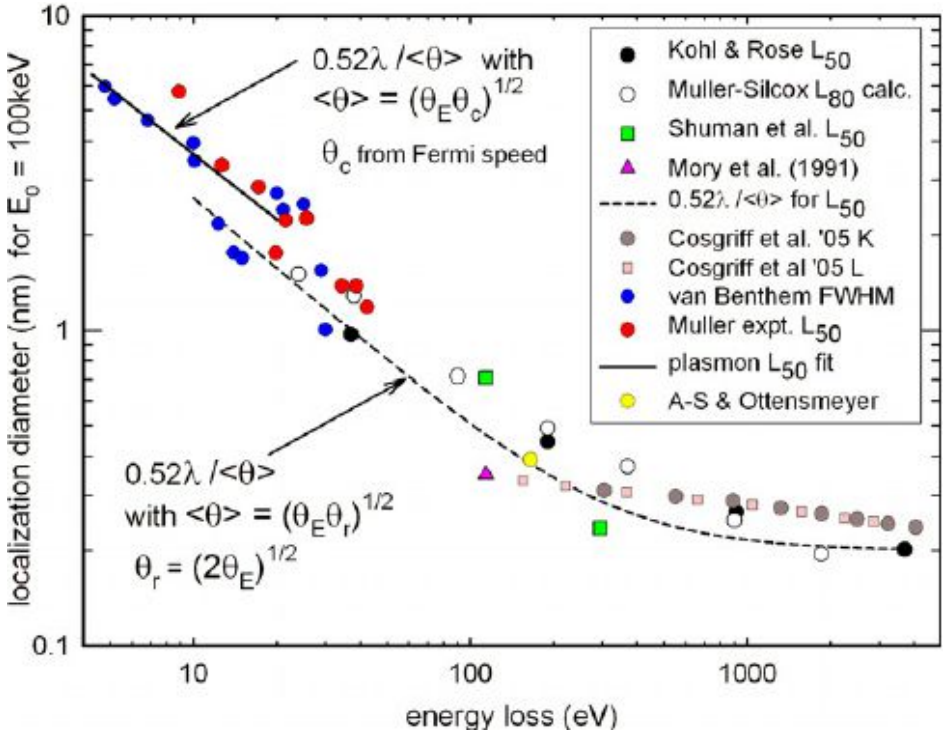

Figure 2.20. EELS Spatial Resolution. The localization diameter (i.e. the spatial resolution) of EELS using 100 keV electrons and 10 mrad. Image from (Egerton, 2011).

Spectral Processing and Quantification

Procedures for quantification of transmission electron energy-loss spectra for elemental analysis, and the factors affecting measurement accuracy were detailed by Egerton (1991), and are summarized here. A typical core-loss spectrum containing the Ca L_{23}, O K and Ce M_{45} ionization edges is shown in Figure 2.21, which is used to illustrate basic spectral processing of raw EELS data. The spectrum is first fit with a background function over a pre-ionization-edge energy window (shaded pink in Figure 2.21). The background fit (grey dashed curve) is extrapolated to higher energy-loss, and subtracted from the raw data over the entire width of the signal integration window (shaded gold). As this technique relies heavily on the extrapolation of the background fitting window, care should be taken when selecting the width and position of the background fitting and signal

integration windows. Increasing the width of the background fitting window reduces error in the parameters of the fitting function, which improves the accuracy of the background extrapolation and signal integration. Similarly, decreasing width of the signal integration window and placing it nearer to the background fitting window will mitigate errors associated with background fit extrapolation. Extrapolation of the background fit becomes increasingly inaccurate ~100 eV beyond the fitting window.

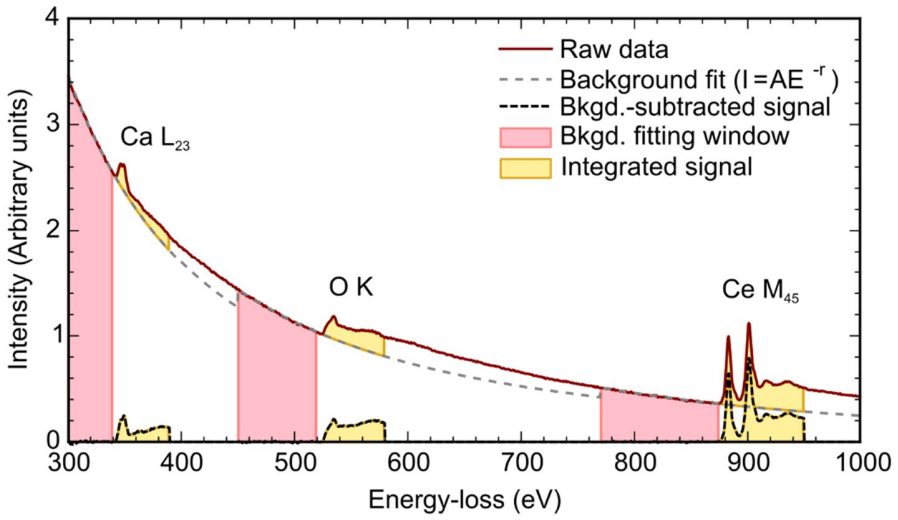

Figure 2.21. Inverse Power Law Background Fit and Subtraction. Process of background fitting, extrapolation and subtraction using an inverse power law background fit.

As will be demonstrated in subsequent chapters, alternative background fitting procedures are applied in some cases to address more complex spectral features such as overlapping ionization edges. For example, as illustrated by Figure 2.22 the Pr M_{45} edge is positioned in the post-edge continuum of the Ce M_{45} edge, making it challenging to fit the background directly ahead of the Pr M_{45} edge onset. To minimize errors in the extrapolation of the background fit to the Pr M_{45} edge, a two-window background fitting procedure is

instead applied based on interpolation of the background fitting function between the two fitting windows on either side of the Pr M_5 peak.

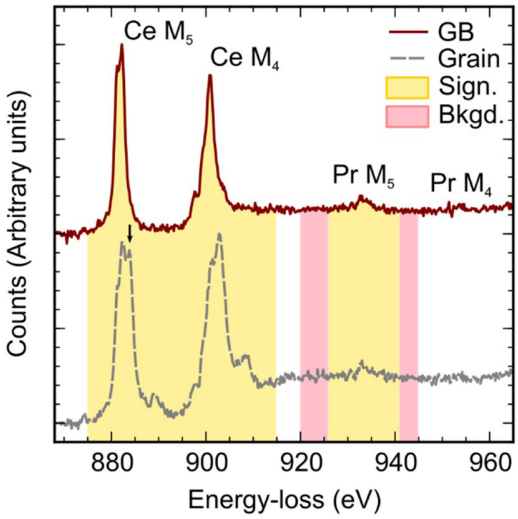

Figure 2.22. Two-Window Background Fitting Procedure Applied to Pr M_5 Peak.

Alternative overlap procedures can be applied if a two-window fitting procedure is not suitable, as demonstrated in Chapter 4 for (Figure 4.7) for the Gd N_{45} edge, which is positioned in the Ce N_{45} post-edge continuum.

Jump Ratio Method

In this procedure, two energy filtered images are generated in spectral regions before and after the ionization edge. The post-edge image is then divided by the pre-edge image to generate the ratio map. The procedure is more sensitive to small changes in the ionization edge intensity and works well for the grain boundary region because it normalizes the effect of variation in mass thickness and diffraction. There is also no background subtraction step, which removes associated errors.

Elemental Quantification

Once the signals from the elements of interest have been extracted from raw data, elemental concentrations can be estimated following the procedure below. The derivation of expressions for elemental concentration summarized below is detailed by Egerton (2011). The background-subtracted intensity of an M edge in the energy-loss spectrum, I_M, is related to the total transmitted intensity, I_T, by the ionization probability, P_M, by

$$\frac{I_M}{I_T} = P_M \tag{2.26}$$

Assuming the electrons responsible for the given edge undergo only one ionization event, the ionization probability can be expressed as

$$P_M = N\sigma_M e^{\left(-\frac{t}{\lambda_M}\right)} \tag{2.27}$$

where N is the areal density (atoms per unit area of a specimen with thickness t) and σ_M is the inelastic scattering cross-section of atoms giving rise to the M edge. As the mean free path for a core-level ionization, λ_M, is typically large relative to the specimen thickness, it is reasonable to assume that the incident electron undergoes only one ionization event while traversing the specimen. This also implies that the exponential term can be approximated as unity and inserting Equation (2.27) into Equation (2.26) yields

$$I_M \approx N\sigma_M I_T \tag{2.28}$$

As the experimentally measured ionization-loss signal, I_M, is determined over a limited energy-loss range, Δ (the signal integration window, see e.g. Figure 2.21), and

scattering collection angle defined by the spectrometer configuration, β, this expression becomes

$$I_M(\beta, \Delta) \approx N \cdot \sigma_M(\beta, \Delta) \cdot I_T(\beta, \Delta) \tag{2.29}$$

Taking the ratio of concentrations of two elements A and B in the specimen, N_A and N_B, yields the expression

$$\frac{N_A}{N_B} = \frac{I_M^A(\beta, \Delta)}{I_M^B(\beta, \Delta)} \cdot \frac{\sigma_M^B(\beta, \Delta)}{\sigma_M^A(\beta, \Delta)} \tag{2.30}$$

If the cross-section ratio is known, perhaps from analysis of a standard specimen, Equation (2.30) can be applied for quantitative microanalysis. The accuracy of determination of cross-sections and cross-section ratios, so-called *k-factors* ($k_{AB}(\beta, \Delta) = \sigma_M^B(\beta, \Delta)/\sigma_M^A(\beta, \Delta)$, discussed further below), can be influenced by several experimental conditions including background subtraction and raw signal intensity (Egerton, 1991; Manoubi *et al.*, 1990). While care was taken to minimize error in k-factor determination, a systematic error of about ≤15 % of the absolute ionic concentration can be expected based on previously reported work (Egerton, 1991; Manoubi *et al.*, 1990). In the work presented here, cross-section ratios were determined using standard specimens (e.g. powders) of known composition, or from reference points within a given specimen where the composition was known (e.g. grains in pellets assumed to have nominal composition). K-factors were assumed to be constant at grains and grain boundaries, enabling elemental quantification at grain boundaries based on knowledge of nominal composition of grains. Relevant k-factors are provided in subsequent chapters.

TEM data were processed using the DigitalMicrograph software suite (Gatan) and the Python Pyzo integrated development environment (open source, www.pyzo.org). Figures were prepared using the Inkscape graphics editor (open source, www.inkscape.org).

Specimen Preparation

TEM powder specimens were prepared by scooping nanoparticles on a lacey C grid supported on a 3 mm Cu grid (Ted Pella). Figure 5.1 shows a TEM powder specimen. Specimens were prepared from pellets using mechanical polishing and Ar^+ ion milling, or Ga^+ focused ion beam (FIB) milling in an SEM equipped with Ga^+ ion column. For mechanical polishing, a specimen is prepared by first cutting a 3 mm diameter disc from a pellet using an ultrasonic disc cutter (Gatan Inc., Pleasanton, CA). The disc is ground to a thickness of approximately 110 μm, and then dimpled to approximately 20 μm with a dimple grinder (Gatan). The dimpled specimen is then ion milled to electron transparency in a PIPS2 ion mill (Gatan) using 4 keV Ar^+ ions with an incidence angle of 8° on top and bottom, followed by 1 – 2 keV Ar^+ ions at 4° top and bottom. Specimens prepared using this method are shown in Figure 3.6 and Figure 4.1. For FIB milling, the standard lift-out technique was employed (Giannuzzi, 2006) using A Nova 200 NanoSEM (FEI Co., Hillsboro, OR) equipped with Ga^+ FIB. This involved first trenching down into the pellet surface using a 30 kV FIB, followed by lift-out/transfer to Cu supporting grid, and final thinning using 5 kV Ga^+ ions. A typical specimen prepared using this method is shown in Figure 6.1a.

2.3.5 X-Ray Diffraction (XRD)

XRD was performed using 0.1541 nm wavelength Cu K_α radiation to verify phase purity and particle size via Scherrer method (Patterson, 1939). Typical diffraction patterns for powders, pellets, and literature are presented in Figure 3.2.

2.3.6 Scanning Electron Microscopy (SEM)

SEM imaging was used to measure the average grain diameter of pellets, and CCO grain boundary character was investigated using EBSD. Prior to imaging, pellet surfaces were polished using lapping film and then heated at 1000 °C in air for 2 h to thermally etch and reveal the grain boundary structure. 10 nm – 15 nm of C or Au was evaporated onto pellet surfaces to mitigate charging during electron beam irradiation.

2.3.7 Electron Backscatter Diffraction (EBSD)

EBSD measurements and data processing was performed in collaboration with Madeleine N. Kelly under the supervision of Gregory S. Rohrer of the Materials Science Department of Carnegie Mellon University. EBSD was employed measure grain boundary character distributions and to assess the relationship between grain boundary character and conductivity in $Ca_xCe_{1-x}O_{2-x-\delta}$. EBSD is an orientation imaging technique performed in the SEM, during which the electron beam is scanned over a region of interest, producing spatially resolved diffraction data (Adams, Wright, & Kunze, 1993). These Kikuchi diffraction patterns are automatically indexed to a library of known patterns from the crystal structure of the material of interest, which identifies the crystallographic orientation

of the material at each position. This process yields a spatial distribution of crystallographic orientation, which changes from grain-to-grain in a polycrystalline material. In this way, a statistical description of the microscopic grain orientations can be developed.

SEM EBSD can readily process misorientation data algorithmically from tens of thousands or hundreds of thousands of grain boundaries, resulting in a statistically robust method of boundary characterization capable of quantifying geometric grain boundary parameters such as misorientation texture and grain boundary plane distribution. A typical EBSD inverse pole figure is presented in Figure 2.23, which indicates the crystallographic orientation of each grain according to the color coded stereographic triangle. Corresponding misorientation angle distributions (MADs, Figure 3.4b,d) are presented which describe the probability of observing particular angles of misorientation between grains (Mackenzie & Thomson, 1957; Mason & Schuh, 2009; Patala, Mason, & Schuh, 2012). Experimental MADs are compared to the analytically determined MAD for randomly oriented cubic crystals (the 'Mackenzie distribution' (Mackenzie, 1958)) to assess the grain boundary character in terms of the deviation from a random distribution. A material whose MAD does not deviate significantly from the Mackenzie distribution is considered to have a random grain boundary distribution, and is not textured.

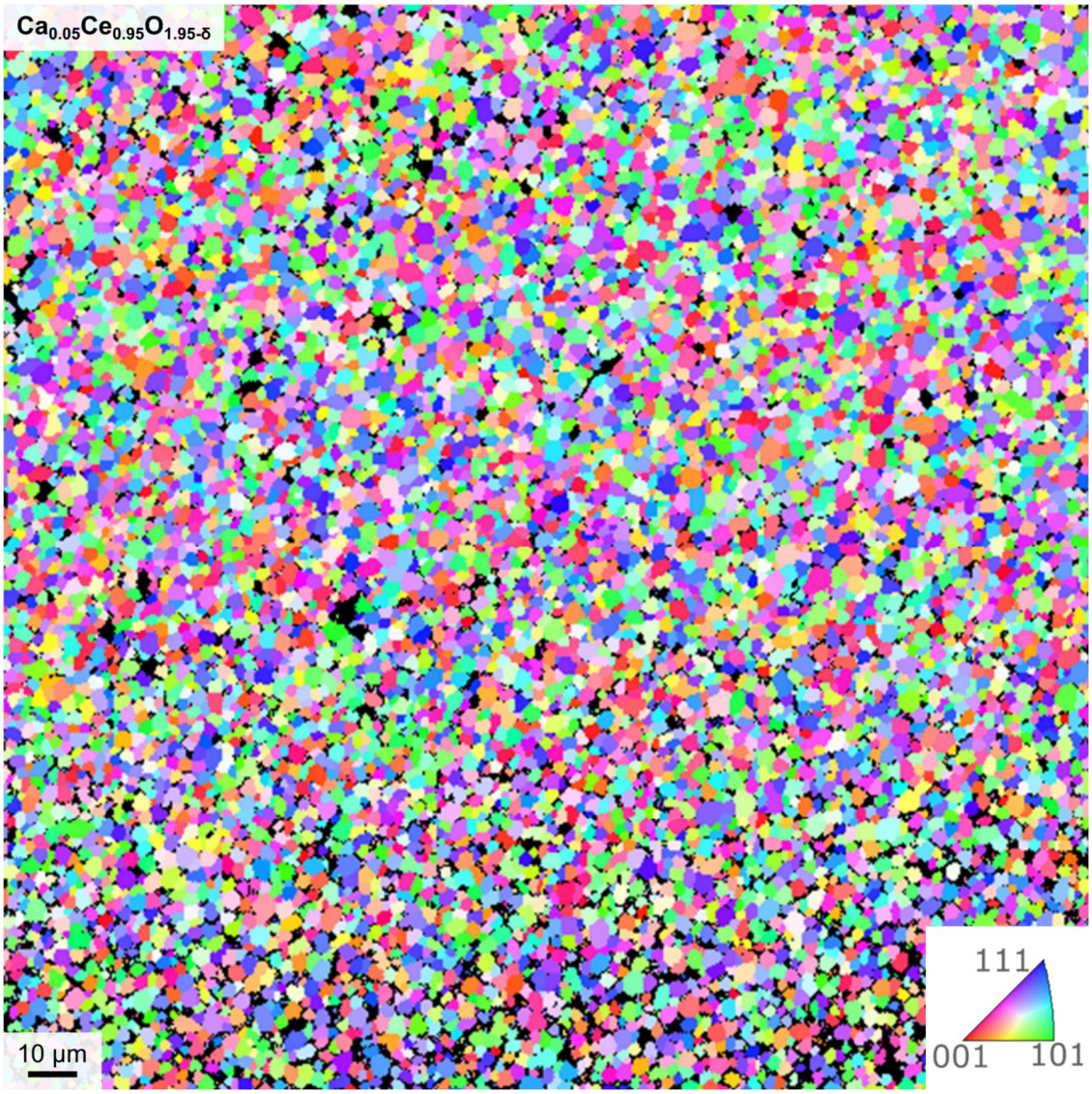

Figure 2.23. EBSD Inverse Pole Figure Showing 5CCO. Data acquired by Madeleine Kelly, Carnegie Mellon University.

The grain boundary plane distribution (GBPD) describes the relative areas of different boundary plane orientations for a given angle of misorientation, providing a richer description of a material's grain boundary character (Helmick *et al.*, 2011; Kelly, Glowinski, Nuhfer, & Rohrer, 2016; Rohrer, 2011; Saylor & Rohrer, 2002). The GBPD is generated by normalizing the areas of various boundary plane orientations determined

experimentally by those of a random, isotropic distribution. Figure 3.5 presents a typical GBPDs.

Pellets were prepared for SEM by surface polishing using a series of diamond suspensions ranging from 9 microns to 0.05 microns. In order to reduce charging effects, the samples' sides and bottoms were coated with Ted Pella, Inc. PELCO® conductive silver paint and subsequently mounted on SEM stubs. An FEI Quanta 200 SEM with EDAX OIM EBSD software, and an FEI Quanta 600 SEM with Oxford Instruments AZtec EBSD software were used for the collection of grain orientation data. SEM imaging was performed at a working distance of 10 mm in low vacuum, with 15 kV accelerating voltage and spot size setting of 5. The sample was tilted 70° and EBSD patterns collected with 4x4 binning, 100 frames/sec and variable gain (depending on the contrast of the sample). Post processing was performed in EDAX TSL software. To remove poorly indexed points in the EBSD scan, data were treated using a grain dilation routine with a minimum grain size of 5 pixels/grain, grain tolerance angle of 5 °, single average orientation per grain, grain confidence index (CI) standardization, and partition of 0.1 CI. Reconstructed grain boundaries were extracted as line segments, and grain boundary character distributions were calculated, independent of misorientation, using five parameter stereological analysis described elsewhere (Saylor & Rohrer, 2002).

2.3.8 Precession-Enhanced Nanodiffraction (PEND)

PEND measurements and data acquisition was performed in collaboration with Amith D. Darbal of AppFive LLC. PEND, like EBSD, is an automated technique for

acquiring spatially resolved electron diffraction patterns in the TEM. The use of precession in electron diffraction was introduced relatively recently by Vincent and Midgley (Vincent & Midgley, 1994), and advantageously achieves a quasi-kinematical condition which reduces dynamical scattering effects because the incident beam is not exactly in a zone-axis orientation (Darbal, Gemmi, Portillo, Rauch, & Nicolopoulos, 2012; Williams & Carter, 2008). Shown in Figure 2.24a, a PEND system double-deflects the incident electron beam using the pre-specimen electron optical elements of the TEM, causing the electrons to undergo precession and form a hollow conical electron probe. During precession, a transmitted electron diffraction pattern is acquired which integrates over the precession cycle. Representative diffraction patterns acquired without and with precession are presented in Figure 2.24, showing that precession results in a higher number of reflections, including those from higher-order Laue zones. The improved data quality helps to mitigate ambiguity in the pattern indexing.

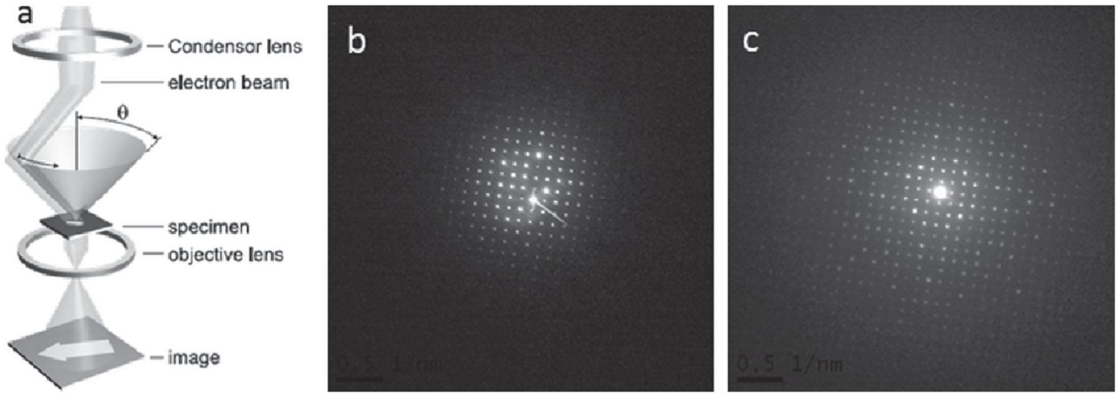

Figure 2.24. Schematic of Precession-Enhanced Nanodiffraction. (a) Schematic illustrating PEND operating principle. Electron diffraction patterns acquired without (b) and with precession (c). Image from (Darbal *et al.*, 2012).

PEND enables automated acquisition and indexing of spatially-resolved diffraction data sets from TEM specimens, allowing statistical quantification of material phase, grain

orientation and grain boundary character (Aebersold, Alexander, & Hébert, 2015; Brons & Thompson, 2014; Darbal *et al.*, 2013). This, combined with targeted S/TEM-based nanocharacterization on the very same specimen offers exciting possibilities to bridge the gap between nanoscale and microscopic characterization techniques such as SEM EBSD. Indeed, a noteworthy drawback to PEND is the necessity of an electron transparent TEM specimen, whose measureable area is typically ~50 μm^2. This results in very few accessible grain boundaries when compared to a typical SEM EBSD sample (~25 mm^2), whose entire surface is accessible for analysis. Although, in lieu of robust counting statistics offered by EBSD, an outstanding advantage of PEND approach is the ability to couple grain boundary character analysis with characterization techniques available in the S/TEM, such as atomic resolution imaging and/or nanospectroscopy.

Spatially-resolved grain orientation data were acquired using a probe aberration corrected JEOL ARM 200F S/TEM equipped with an ASTAR PEND system (NanoMegas USA). A PEND map is presented in Figure 6.1a with corresponding MAD in Figure 6.1b (these data are discussed in detail in the results sections). Serial diffraction patterns were acquired with 5 nm step intervals, and diffraction pattern indexing was performed using TopSpin software (AppFive LLC, USA). PEND data were exported from TopSpin as Euler angles and read into the EDAX TSL OIM5 software for processing and generation of misorientation angle distributions (assuming no correlation relating the orientation of adjacent grains).

3 Grain Boundary Ionic Conductivity Modulated by Local Solute Concentration in $Ca_xCe_{1-x}O_{2-x/2-\delta}$

3.1 Motivation

As discussed in §1.5.1 of the Introduction, efforts to optimize grain boundary ionic conductivity in ceria have focused in part on altering the space charge potential by modifying the concentration and/or species of solute cations deliberately segregated to grain boundaries. Avila-Paredes *et al.* and Litzelman *et al.* showed that grain boundary decoration using divalent transition metal cations could lower the space charge potential in ceria, and Dudek *et al.* demonstrated improved electrolytic performance (i.e. less electronic leakage under reducing conditions) by adding Ca^{2+} to GCO (Avila-Paredes & Kim, 2006; Litzelman *et al.*, 2009; Dudek *et al.*, 2010). Hence, Ca^{2+} was selected as the solute in this work with the aim of elucidating the grain boundary conductivity of a model system $Ca_xCe_{1-x}O_{2-x-\delta}$ (CCO), and to reveal insights for future grain boundary decoration schemes using Ca^{2+} and, more generally, divalent solutes. Moreover, while the role of nominal concentration on grain and total conductivity is established for many ceria solutes, including Ca^{2+} (Avila-Paredes *et al.*, 2009; Bishop *et al.*, 2012; Eguchi *et al.*, 1986), elucidation of the relationship between nominal solute concentration, grain boundary conductivity, and grain boundary composition is still needed to optimize grain boundary transport properties.

In this study described in this chapter, the nominal Ca^{2+} solute concentration was varied in polycrystalline CCO electrolytes to examine systematically for the first time the

influence of the nominal composition on the local grain boundary composition and macroscopic ionic conductivity, measured using AC impedance spectroscopy. Nominally $Ca_{0.02}Ce_{0.98}O_{1.98-\delta}$ (2CCO), $Ca_{0.05}Ce_{0.95}O_{1.95-\delta}$ (5CCO) and $Ca_{0.1}Ce_{0.9}O_{1.9-\delta}$ (10CCO) pellets were fabricated in hope of capturing composition trends commonly observed for ceria solutions with solute concentration below about 15-20 mole%, such as conductivity maxima and/or minima in effective migration activation energy. Change in grain boundary ionic conductivity by several orders of magnitude was observed over the composition range investigated here, with the CCO grain boundary conductivity reaching that of state-of-the-art 10GCO, making it a promising candidate for selective grain boundary decoration schemes to optimize ionic conductivity.

The origin of this conductivity variation was probed across length scales, with the local atomic structure and composition analyzed down to the atomic scale using AC-STEM EELS. Conductivity and chemical data were interpreted in light of grain boundary character probed at the microscale using SEM EBSD, which highlighted the critical interplay between macroscopic grain boundary conductivity and local grain boundary composition. The local solute concentration and grain boundary conductivity were found to be correlated, with each being sensitive to the nominal Ca^{2+} concentration at low nominal solute concentration, before saturating above ~5 mole% Ca^{2+}. This correlated analysis provided insights into fundamental grain boundary science in CCO, yielded valuable guidelines for bottom-up design and optimization of grain boundaries in ceria-based oxygen electrolytes, and should be considered in the development of future theoretical models for electroceramic grain boundaries.

3.2 Experimental

Nominally $Ca_{0.02}Ce_{0.98}O_{1.98-\delta}$ (2CCO), $Ca_{0.05}Ce_{0.95}O_{1.95-\delta}$ (5CCO) and $Ca_{0.1}Ce_{0.9}O_{1.9-\delta}$ (10CCO) nanoparticles were synthesized using spray drying, and calcined to yield ~30 nm nanoparticles, estimated using XRD Scherrer analysis (Patterson, 1939). Following the procedure described in the Methods chapter, particles were compacted uniaxially and sintered at 1400 °C for 24 h with 2.5 °C/min heating rate to produce dense polycrystalline solids. XRD was used to analyze the phase purity of calcined nanoparticles and pellets, with the average grain size of each pellet determined from inspection of SEM images using the average grain intercept method. See Table 3.3 for summary of microstructural data. AC impedance spectroscopy was used to measure the grain and grain boundary conductivity of each pellet, and EBSD was performed on the 2CCO and 5CCO pellets following the procedures outlined in the Methods chapter. Commercial 10GCO powder (Fuel Cell Materials) was also used to prepare a pellet to which CCO conductivity could be compared.

Specimens were prepared for TEM and STEM by mechanical dimpling followed by Ar^+ ion milling as described in the Methods chapter. Phase contrast TEM images were acquired using a 200 kV JEOL 2010F TEM to verify that grain boundaries were free of intergranular amorphous phases. A 200 kV JEOL ARM200F AC-STEM with a Gatan Enfina spectrometer was used for EELS analysis and ADF imaging of grain boundaries. The convergence and collection angles, and spectrometer dispersion were 20 mrad, 42 mrad, 250 meV/channel, respectively. Energy-loss spectra were calibrated by shifting the Ce M_5 peak maximum to 883 eV; the background fitting/subtraction procedures

employed to ionization edge are specified in Table 3.1. Signal integration windows were greater than 50 eV to minimize quantification artifacts associated with plural scattering (see Methods §2.3.4). Elemental maps were generated from EELS spectrum images using the jump ratio method described in the Methods.

Table 3.1. EELS Spectral Processing Windows

EELS edge	Background fitting procedure	Background fitting window(s) (eV)	Signal integration window (eV)	k-factor
Ca L_{23}	Two-window inverse power-law interpolation	325 – 335, 510 – 520	338 – 388	$k_{CaCe} = 0.54 \pm 0.1$
O K	Inverse power-law extrapolation	470 – 520	525 – 575	$k_{OCe} = 3.04 \pm 0.27$
Ce M_{45}	Inverse power-law extrapolation	790 – 870	875 – 955	

Ion concentrations were estimated using the k-factor method, with O:Ce and Ca:Ce k-factors determined as follows. The O:Ce k-factor, i.e. k_{OCe} in Equation (2.30), was determined using fragments of a CeO_2 pellet which was crushed between two glass microscope slides as a standard. These crystalline fragments were heated to 700 °C in air prior to EELS measurements to achieve oxygen stoichiometry. k_{OCe} was found to be 3.04 ± 0.27 (mean value ± standard deviation) from 15 measurements, and is in good agreement with that published by Manoubi, Colliex and Rez (1990), who reported 3.08 ± 0.19. The mean k_{CaCe} was determined to be 0.54 ± 0.10 from 16 measurements of different grains in the 10CCO pellet TEM specimen, wherein the nominal Ca:Ce

concentration ratio was assumed within the grains. The standard deviation of 0.10 corresponds to a 19 % error in the absolute Ca concentration derived from this method (e.g. an estimate of 10 mole% Ca has ±2 mole% uncertainty). The grain boundary composition of 2CCO was determined from eight individual lines scans across four different boundaries. In 5CCO and 10CCO, six line scans of one boundary, and eight line scans of four boundaries were used, respectively. Each grain boundary concentration measurement is provided in Figure 3.9 to illustrate the scatter in the data, with error bars used to indicate the aforementioned error in determining absolute concentration of 19 %.

3.3 Results and Discussion

3.3.1 Microstructure and Phase Purity

The microstructure of the CCO pellets is shown in Figure 3.1. The average grain size (Table 3.2) decreased with increasing total solute concentration, consistent with previous observations of Gd^{3+}-ceria solid solutions (Rupp, Infortuna, & Gauckler, 2006). XRD was used to verify that fluorite structured solid solutions were successfully synthesized, and that CaO_x second phases were not formed in the pellets during sintering. Figure 3.2 presents XRD patterns from CCO particles and pellets confirming that CaO_x second phases were not detected. An expanded view shows that the 10CCO pattern does not feature CaO_x peaks, indicating that Ca^{2+} is in solid solution in CCO.

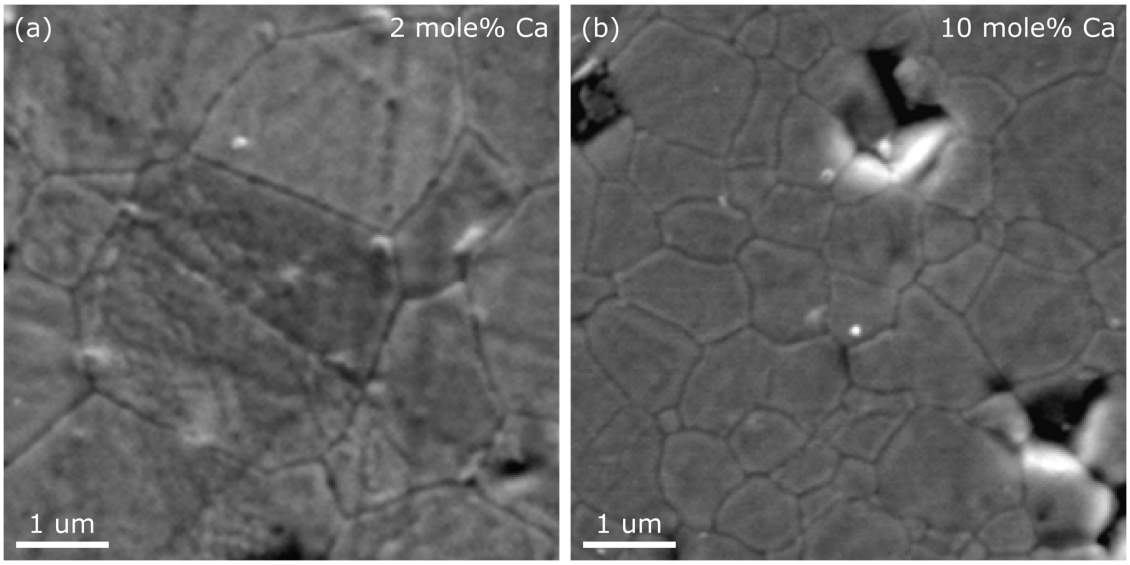

Figure 3.1. CCO Pellet Microstructure. SEM images of (a) 2CCO and (b) 10CCO pellets following sintering, polishing and thermal etching at 1100 °C for 2 h. FEI FEG XL30, ASU.

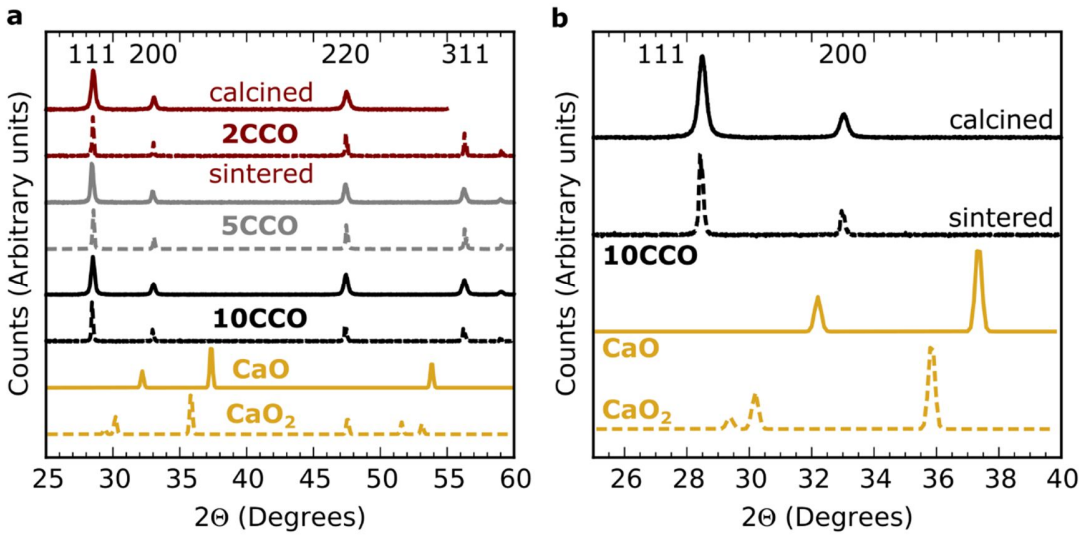

Figure 3.2. XRD of CCO. (a) XRD patterns of calcined CCO powders (dashed curves) and fragments of crushed pellets ('sintered', solid curves). Bold labels refer to nominal Ca concentration; CaO_x peaks were not visible. Reference patterns for CaO and CaO_2 are from (Shen, Liu, Lin, & Huang, 2001) and (Kotov & Reichstein, 1941), respectively. (b) Expanded view of 10CCO and CaO_x reference spectra.

Table 3.2. CCO Particle and Pellet Grain Size

	d_{Powder} (nm)	d_{Grain} (μm)
2CCO	30.0 ± 6.6	7.6 ± 1.0
5CCO	32.0 ± 7.7	2.3 ± 0.2
10CCO	29.1 ± 6.8	1.4 ± 0.3

3.3.2 Ionic Conductivity

Representative Nyquist plots from 10CCO are presented in Figure 3.3a-b, showing the influence of temperature on the impedance response. It can be seen that the overall impedance response collapses towards the origin, indicating a decrease in grain, grain boundary and total electrolyte resistance with increasing temperature. Nyquist plots typically exhibited two or three arcs, which were attributed to the grain, grain boundary and electrode impedance responses according to the brink-layer model (see Methods chapter), and the comparison of the capacitance values associated with each arc with literature (see measured values in Table 3.3). Details on fitting are provided in the Appendix. Conductivities reported here are assumed to be ionic, as the electrolytic domain (wherein ionic transference is unity) of CCO at 800 °C has been shown to extend to oxygen partial pressures of approximately 10^{-9} atm for 10CCO and 10^{-16} atm for 50CCO, many decades lower than that of air—the measurement atmosphere used in this work (Blumenthal *et al.*, 1973; Arai, Kunisaki, Shimizu, & Seiyama, 1986).

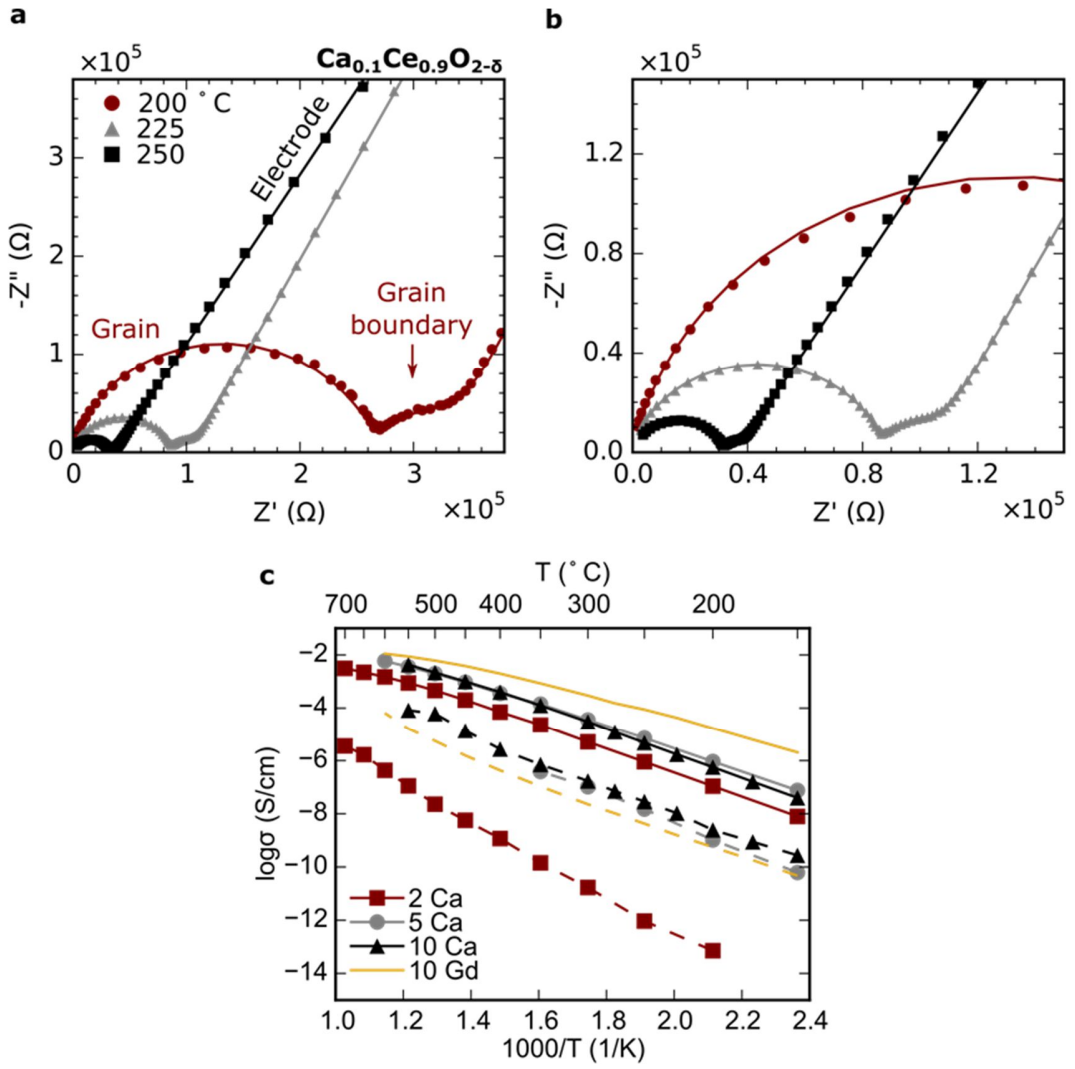

Figure 3.3. Impedance Analysis of CCO. (a,b) Nyquist plots show discernable arcs corresponding to the impedance responses of grain and grain boundary. Solid lines show fits to the equivalent circuit model (Figure 2.4). (c), Arrhenius plots of grain (solid connecting lines) and grain boundary (dashed lines) conductivity for CCO and, for comparison, 10GCO ('10 Gd'). σ_{GB} was calculated using the mean grain size measured using SEM (

Table 3.2) and mean grain boundary chemical width from STEM EELS (Table 3.4) according to Equation (2.13).

Figure 3.3c presents σ_{Grain} and σ_{GB} measured for CCO, and for comparison, 10GCO—a state-of-the-art ceria electrolyte. The marked difference between σ_{Grain} and

σ_{GB} for each composition is apparent, with σ_{Grain} typically exceeding σ_{GB} by four to seven orders of magnitude depending on Ca^{2+} concentration and temperature. There is a pronounced difference between σ_{GB} of 2CCO and that of 5CCO and 10CCO over the temperature range (e.g. a factor of $10^3 - 10^4$ at 300 °C). Also noteworthy is that σ_{GB} in 5CCO and 10CCO is comparable to 10GCO, which is consistent with published results indicating that Ca^{2+} can be added to GCO without degrading σ_{GB} (Dudek *et al.*, 2010). While there is relatively little influence of nominal composition on E_a^{Grain}, E_a^{GB} decreases significantly with increasing Ca content, which suggests reduction of the grain boundary space charge potential (Avila-Paredes *et al.*, 2009; Avila-Paredes & Kim, 2006; Dudek *et al.*, 2010). As discussed in the Introduction, above some threshold temperature there is an apparent oxygen vacancy order-to-disorder transition which liberates mobile vacancies (Kilner & Waters, 1982). Thus, E_a^{Grain} was determined separately for T < 450 °C and T ≥ 450 °C.

Table 3.3. Summary of CCO Electrical Data

	$C_{Grain}^{250\,°C}$ (pF)	$C_{GB}^{250\,°C}$ (nF)	E_a^{Grain} T < 450 °C (eV)	E_a^{Grain} T ≥ 450 °C (eV)	E_a^{GB} (eV)
2CCO	37	48	0.93 ± 0.01	0.70 ± 0.01	1.48 ± 0.13
5CCO	36	15	0.88 ± 0.02	0.73 ± 0.02	1.06 ± 0.09
10CCO	19	23	0.96 ± 0.01	0.81 ± 0.01	1.03 ± 0.08

3.3.3 Grain Boundary Character

The addition of Ca^{2+} significantly enhanced σ_{GB} up to ~5 mole% Ca^{2+}, with the effect saturating beyond that nominal concentration (see Figure 3.9). Understanding the origin of the marked difference in σ_{GB} between 2CCO and 5CCO could help point the way forward to future design and optimization of high-conductivity grain boundaries. It is known that changes in nominal composition could affect the local composition at grain boundaries—which influences grain boundary resistivity (Avila-Paredes & Kim, 2006), and/or grain boundary character defined by the relative orientation of adjacent grains (Rohrer *et al.*, 2004). And because grain boundary resistivity of oxide bicrystals can vary solely due to differences in grain orientation (i.e. grain boundary character), independent of nominal composition (Ye et al., 2014), it is reasonable to hypothesize that the large difference between σ_{GB} in 2CCO and 5CCO could stem from variations in *both* grain boundary character and local composition.

To test this hypothesis, SEM EBSD was used to compare the grain boundary character of 2CCO and 5CCO, two materials with vastly different σ_{GB}. Grain boundary misorientation angle distributions (MADs) and plane distributions (GBPDs) were computed from two-dimensional grain orientation data with misorientation information from ~$7 \cdot 10^4$ and ~$12 \cdot 10^4$ grain boundary segments in 2CCO and 5CCO, respectively. Figure 3.4a,c presents inverse pole figure maps indicating the crystallographic orientation of grains in 2CCO and 5CCO. The inset stereographic triangle is color coded to indicate the crystallographic direction normal to the sample surface in each grain. Figure 3.4b,d provides the computed MADs for both samples, showing the number fraction of grain

boundaries of various misorientation angles. The MADs are essentially identical, and exhibit only minor deviations from the Mackenzie distribution, which is the analytically derived distribution for a randomly oriented cubic system (Mackenzie, 1958; Mason & Schuh, 2009). This indicates that both materials exhibit random grain boundary distributions without significant misorientation texture.

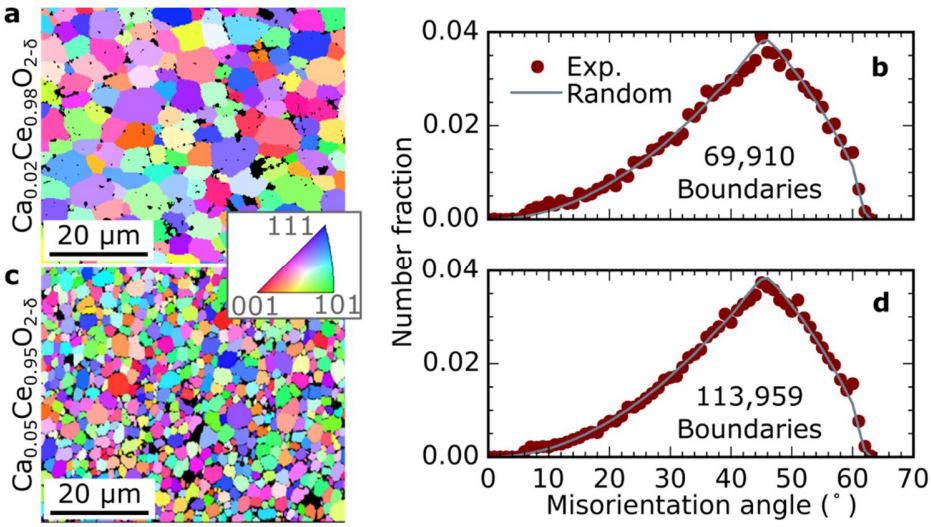

Figure 3.4. EBSD Inverse Pole Figures of CCO and MADs. (a,c) Inverse pole figures with inset stereographic triangle. (b,d) Computed misorientation angle distributions (MADs) for each sample ('Exp.') are plotted with the Mackenzie distribution (the random distribution for a cubic system). The number of grain boundaries analyzed in each sample is provided.

This result is corroborated by the GBPDs presented in Figure 3.5 that describe the relative areas of different boundary plane orientations, expressed as multiples of the random distribution. These are derived from stereological analysis of EBSD data, by normalizing the areas of various grain boundary plane orientations—determined experimentally—by those of a random, isotropic distribution. For both 2CCO and 5CCO the GBPDs are approximately unity; the approximately flat GBPDs indicate a random grain orientation distribution in both samples. (Peaks of ± 0.1 in the multiples of random distribution are not intense enough to be statistically significant.)

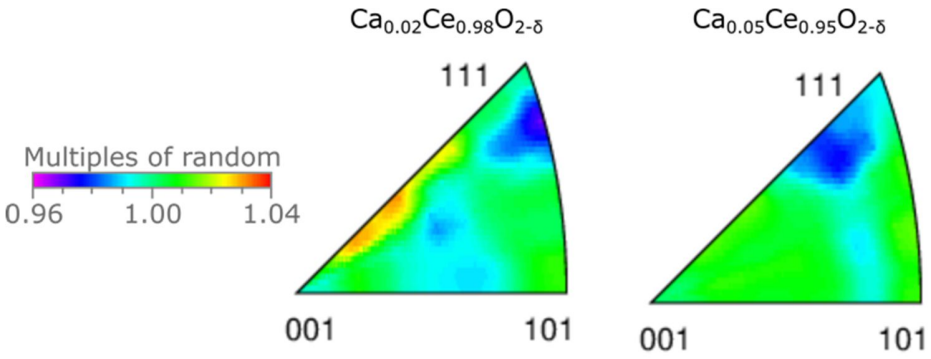

Figure 3.5. CCO Grain Boundary Plane Distributions. Courtesy M.N. Kelly for data acquisition and processing.

This statistically illustrates that from a microscopic viewpoint, the two samples' grain boundary character is indistinguishable, and points to the local grain boundary composition as the principal effect governing the difference in conductivity in this case.

3.3.4 Nanocharacterization

To investigate local grain boundary properties such as atomic structure, composition, and chemistry, atomic-resolution ADF STEM imaging and spatially resolved STEM EELS were performed. Ionic concentrations were estimated using EELS of the Ca L_{23}, O K and Ce M_{45} ionization edges, and nanoscale chemistry was probed via near-edge fine structure (see Methods chapter).

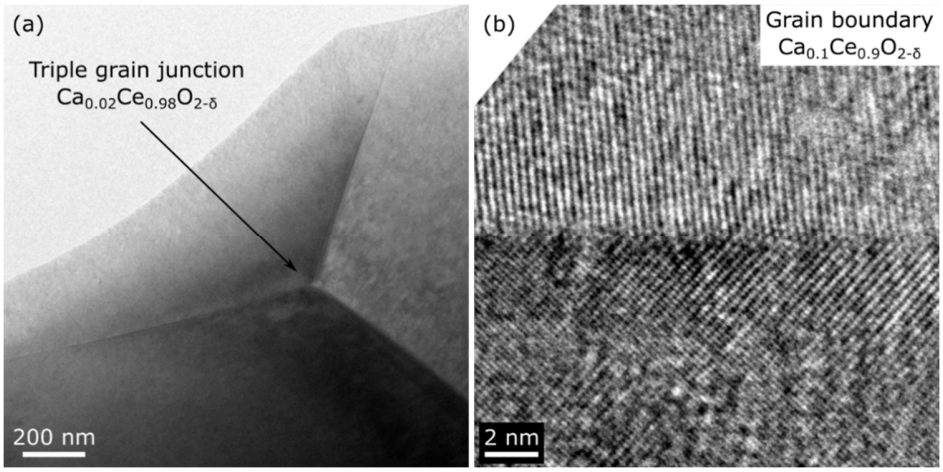

Figure 3.6. Phase Contrast TEM Images of CCO Grain Boundaries. Bright field TEM micrographs of (a) triple grain junction and (b) grain boundary in CCO. 200 kV JEOL 2010F TEM, ASU.

Background-subtracted EELS data from 10CCO are presented in Figure 3.7a, showing the very considerable differences in ionization edge shape and intensity typically observed at grains ('Off GB') and grain boundaries ('On GB'). Strong enhancement of the Ca L_{23} edge intensity was accompanied by a considerable decrease in the Ce M_{45} signal, indicative of an enrichment of Ca ions and depletion of Ce ions in the grain boundary vicinity. Changes in the O K edge were also observed at grain boundaries, indicating a considerable perturbation of the O bonding environment at the grain boundary interface (Browning *et al.*, 2004; Lei *et al.*, 2002). The three main peaks in the O K edge (visible in the grain) are associated with O 1*s* core level excitations into unoccupied Ce levels (Mullins *et al.*, 1998), and were typically not well resolved at grain boundaries. Two of these peaks (5*d* e_g and 5*d* t_{2g}) arise from the crystal-field splitting of the Ce-O bonding orbitals of the fluorite structure, thus smearing of the O K edge at grain boundaries indicates a loss of long-range order associated with altered coordination at the grain boundary (Hojo *et al.*, 2010; Lei *et al.*, 2002). This is likely the combined effect of oxygen deficiency which

accommodates grain boundary structural incoherence (S. Kim *et al.*, 2010), and the presence of mobile O vacancies associated with Ca^{2+} solutes. Furthermore, reduction of the Ce M_4:M_5 peak intensity ratio was observed at grain boundaries, indicating of the presence of Ce^{3+} (Hojo *et al.*, 2010; Mullins *et al.*, 1998), and providing further evidence for structural oxygen deficiency and elevated mobile O vacancy concentration at grain boundaries.

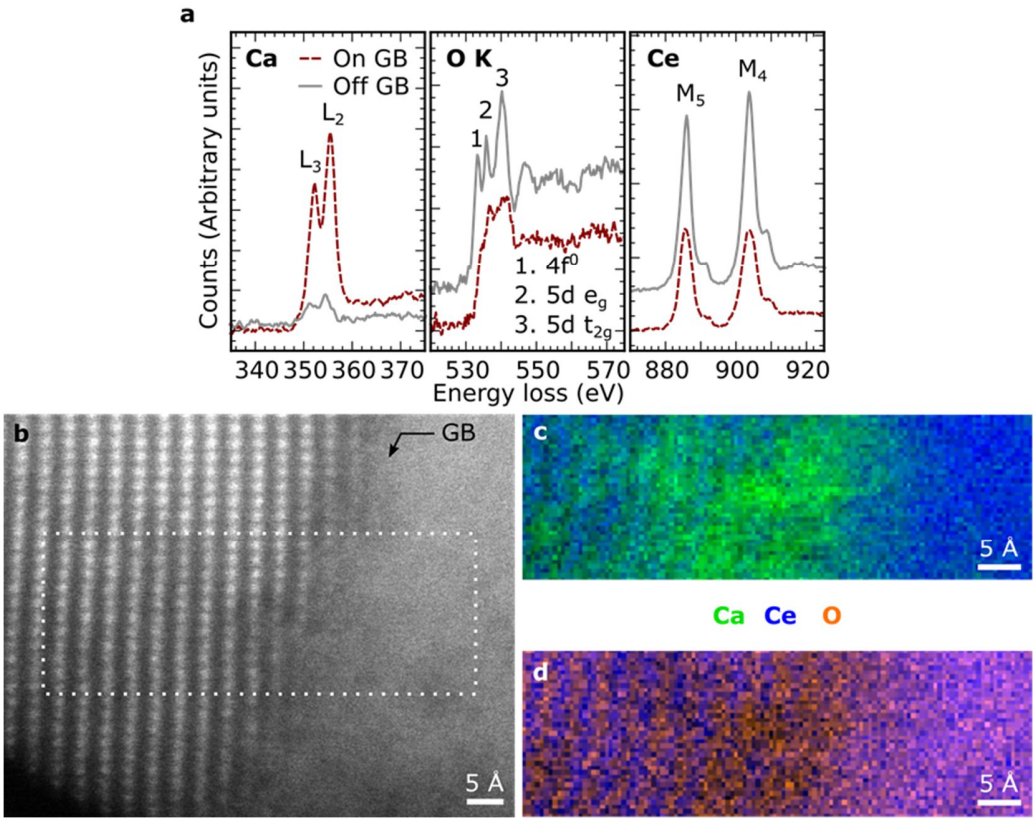

Figure 3.7. Grain Boundary STEM EELS of 10CCO. (a) Comparison of ionization edges typically observed in 10CCO. O K and Ce M edges labelled 'Off GB' have been shifted vertically for clarity (visible as vertical offset in pre-edge intensity). The peaks labelled '1-3' in the O K edge arise from excitations from the O 1*s* core level into the Ce levels indicated in the subplot legend (Mullins *et al.*, 1998). (b) Atomic-resolution ADF STEM image of 10CCO grain boundary. (c,d) Grain boundary EELS elemental maps acquired in the region of (b) highlighted with a dashed box. The EELS mapping pixel size was 0.05 nm; bending distortions visible in the atomic columns result from specimen drift during data acquisition.

From inspection of atomic-resolution ADF images, e.g. Figure 3.7b, and EELS elemental maps, e.g. Figure 3.7c-d, it was possible to correlate atomic-level structural features with local changes in ionic concentration. From the Ca-Ce elemental map (Figure 3.7c) it is clear that the Ca concentration increases dramatically in the several nanometers adjacent to the grain boundary, with the region of highest Ca concentration coinciding with the grain boundary interface. A corresponding decrease in the ADF image intensity (Figure 3.7a) at the grain boundary is also visible, consistent with the reduction of high-angle electron scattering associated with the more open interfacial atomic structure, and the increased concentration of relatively lighter Ca cations (i.e. the image exhibits atomic number (Z) contrast).

The cation columns appear as bright spots due to Z-contrast in the well oriented grain on the left-hand side of Figure 3.7a. Further comparison of this image with the Ca-Ce elemental map reveals that in the several nanometers directly adjacent to the grain boundary, there is a reduction in the contrast of the cation columns correlated with regions of increased Ca EELS signal. This indicates that there are a substantial number of Ca ions substituting for Ce in the fluorite lattice ($Ca_{Ce}^{//}$). Similar nanoscale domains of heterogeneous image contrast have been identified previously in ceria solutions using TEM as point defect clusters involving the ordering of oxygen vacancies (Ou *et al.*, 2006; Ye, Mori, Ou, Zou, & Drennan, 2009). In contrast with the Ce signal, the Ca signal appears diffuse and ill-defined, often appearing *between* the cation columns. This observation is consistent with Ca ions occupying interstitial sites, or alternatively with the report of Chen *et al.*, who—based on a combination of spectroscopic techniques including STEM EELS and extended X-ray absorption fine structure analyses—have proposed a cationic

substitution mechanism in $Sm_xCe_{1-x}O_{2-\delta}$ whereby substitutional Sm ions can assume interstitial positions adjacent to vacant Ce sites (Chen, Chen, Lee, Dong, & Gloter, 2014). These atomic-level observations of the cation distribution suggest that Ca solute ions are located at both interstitial and substitutional sites in the vicinity of the grain boundary. This qualitative result is corroborated below via quantification of the grain boundary cation concentration and comparison with the known solubility limit of Ca^{2+} in CCO.

Figure 3.8a presents an atomic-resolution ADF STEM image of a 5CCO grain boundary, with corresponding EELS elemental map. Like Figure 3.8b, cation columns are identified as bright spots in both grains, with the ADF image contrast decreasing considerably at the grain boundary interface. The elemental map confirms very substantial local Ca enrichment in the 1 nm – 2 nm adjacent the grain boundary interface. Again the image exhibits Z-contrast, and high grain boundary Ca concentration is assumed to decrease the high-angle scattering of the incident electrons from the relatively lighter Ca cations.

From spatially-resolved EELS data it was possible to estimate the mean local grain boundary cation concentration for each sample. Results are summarized in Figure 3.9, and show that the 2CCO specimen exhibited considerably lower grain boundary solute concentration than did 5CCO and 10CCO. The measured grain boundary Ca concentration in 2CCO is approximately 17 mole%, whereas Ca concentrations in 5CCO and 10CCO is ca. 40 mole% – 50 mole%. Interestingly, the average Ca concentration in 5CCO and 10CCO exceeds the bulk Ca solubility limit in CCO of approximately 23 mole% (Arai *et al.*, 1986; Eguchi *et al.*, 1986). This quantitative observation suggests that the grain

boundaries in the 5CCO and 10CCO investigated here facilitate localized solute super-saturation, likely involving the formation of interstitial Ca^{2+} point defects (i.e. $Ca_i^{\bullet\bullet}$).

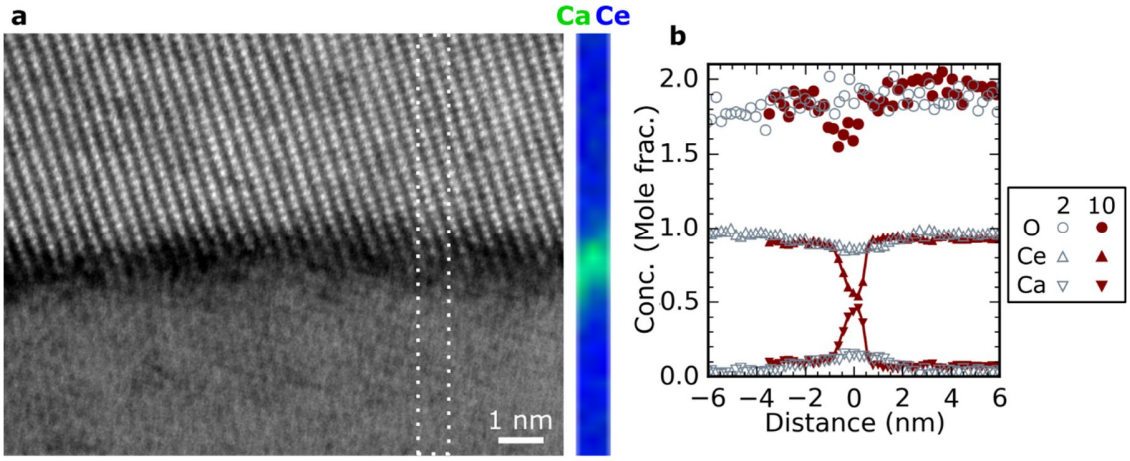

Figure 3.8. Grain Boundary STEM EELS of 5CCO and Line Scans. (a) Atomic-resolution Z-contrast ADF STEM image of 5CCO grain boundary with associated EELS elemental map acquired in the region highlighted with a dashed box. The EELS mapping pixel size was 0.25 nm. (b) Grain boundary ionic concentration profiles (centered at 0 nm) of 2CCO and 10CCO.

Grain-to-grain compositional heterogeneity in the CCO was only observed in one EELS line scan of 10CCO in which the difference in the grain Ca concentration was ~2 mole%. This effect is expected to be approximately one order of magnitude less than the grain boundary concentration variation.

The CaO-CeO_2 equilibrium phase diagram indicates that a bulk solid solution should persist up to at least 1700 °C (Longo & Podda, 1978)—well above the sintering temperature employed here; and it has been demonstrated using XRD that the lattice constant of CCO increases monotonically with Ca content up to 23 mole% (Arai *et al.*, 1986; Eguchi *et al.*, 1986). This suggests that the Ca super-saturated phase observed here at grain boundaries in 5CCO and 10CCO may not correspond to an equilibrium bulk phase,

but rather a nanolayer type Dillon-Harmer grain boundary complexion—a distinct grain boundary phase with thickness on the order of one or two nanometers (Dillon *et al.*, 2007; Cantwell *et al.*, 2014).

Table 3.4. CCO Grain Boundary Composition from STEM EELS. Grain boundary cation concentrations and chemical widths (FWHM) measured using AC-STEM EELS. The mean values from all measurements are provided with the standard deviation.

	Mean $[Ca]^{GB}$ ± Std. dev. (Mole %)	Mean $[Ce]^{Grain}$ ± Std. dev. (Mole %)	Mean chemical width ± Std. dev. (nm)
2CCO	17 ± 4	83 ± 5	3.1 ± 0.4
5CCO	47 ± 5	53 ± 5	3.2 ± 0.4
10CCO	40 ± 7	60 ± 7	3.0 ± 1.0

3.3.5 Grain Boundary Composition and Conductivity

Figure 3.9 summarizes the results of conductivity measurements and STEM characterization by comparing the influence of the nominal Ca^{2+} concentration on grain boundary ionic conductivity and local Ca^{2+} concentration. In both cases there appears to be a threshold nominal Ca^{2+} concentration of ~5 mole% above which the effect of additional Ca^{2+} on grain boundary conductivity and concentration is minimal or negligible. This case indicates that the upper limit to enhancement of grain boundary ionic conductivity may coincide with the nominal solute concentration corresponding to local solute saturation of the grain boundaries. The correlation between macroscopic conductivity and nanoscale composition is a seminal finding of this work, and represents a valuable guideline for design of grain boundaries for optimal ionic conductivity in CCO and other ceria solutions.

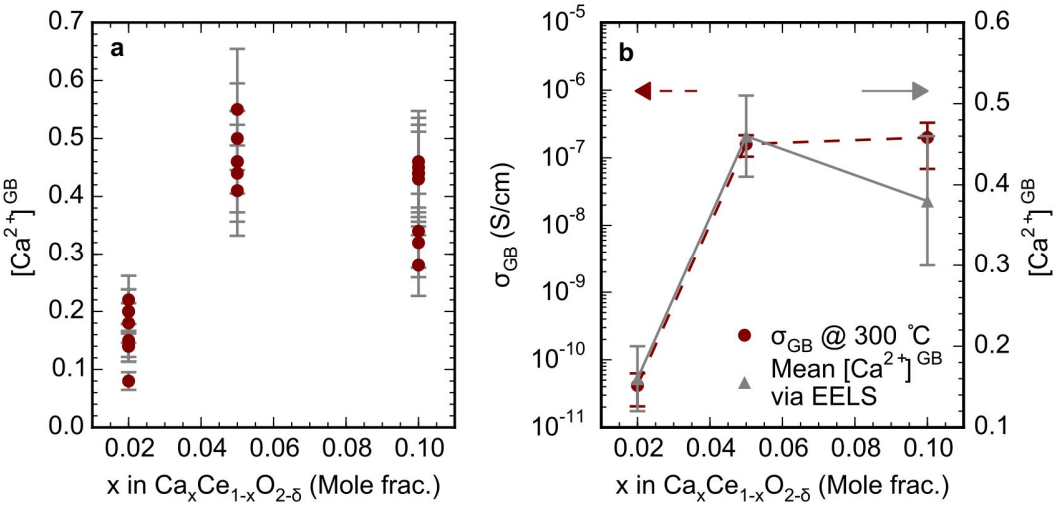

Figure 3.9. CCO Grain Boundary Conductivity and Composition. (a) Effect of nominal Ca concentration, x, on the local grain boundary Ca concentration $[Ca^{2+}]^{GB}$. All measurements are displayed, with error bars indicating the propagated error stemming from determining k_{CaCe}. (b) Comparison of CCO grain boundary ionic conductivity, σ_{GB}, measured at 300 °C and mean grain boundary Ca^{2+} concentration. Error bars indicate standard deviation in measured concentration, and uncertainty in σ_{GB} from equivalent circuit model fitting.

The notion that σ_{GB} is correlated with local solute concentration, which can be several times greater than the nominal solute concentration (e.g. this work and (Lei *et al.*, 2002; Bowman *et al.*, 2015)), may also be apparent in past observations. For instance, Avila-Paredes *et al.* showed that σ_{GB} in $Gd_xCe_{1-x}O_{2-x/2}$ is highly sensitive to nominal Gd^{3+} concentration below ca. 6 mole%, before gradually plateauing around 15 mole% Gd^{3+} (Avila-Paredes *et al.*, 2009). Based on the present study, one could attribute this high sensitivity at low nominal Gd^{3+} concentration and subsequent plateau of σ_{GB} to nanoscale GB saturation of Gd^{3+} (Lei *et al.*, 2002; Bowman *et al.*, 2015; Diercks *et al.*, 2016).

Alternatively, in cases where synthesis conditions are not amicable to strong solute segregation from grains to grain boundaries, such as intermediate temperature thin film deposition processes like pulsed laser deposition, knowledge of the ideal grain boundary

solute concentration should be helpful in guiding post-deposition processing. As mentioned in the motivation section of this chapter, Litzelman *et al.* employed post-deposition in-diffusion of Ni^{2+} and Gd^{3+} cations along grain boundaries in columnar grained ceria thin films (Litzelman *et al.*, 2009); knowledge of optimal grain boundary solute cation concentrations should guide further exploration and optimization of such post-deposition treatments.

3.4 Summary

The electrical, microstructural and chemical properties of grain boundaries were correlated across length scales in the oxygen electrolyte CCO, elucidating the interplay between nominal composition, grain boundary conductivity, microscopic grain boundary character and local grain boundary composition determined at the sub-nanometer level. AC impedance spectroscopy of pellets was used to demonstrate that the grain boundary conductivity increases with nominal Ca^{2+} concentration before reaching a plateau at approximately 5 mole%. Similar saturation-type behavior is observed in the local concentration of Ca^{2+} measured using AC-STEM EELS at the nanoscale and atomic level. The intimate relationship between grain boundary conductivity—determined macroscopically, and local grain boundary composition is reinforced via quantification of microscale grain boundary character determined using stereological analysis of SEM EBSD data. In doing so, a grain boundary solute saturation limit in the CCO system is estimated to be around 45 mole%, thus demonstrating a critical optimization parameter for grain boundary electrical properties and theoretical modelling of grain boundaries in polycrystalline oxide solutions. Furthermore, when compared to state-of-the-art oxygen

electrolyte $Gd_{0.1}Ce_{0.9}O_{1.95-\delta}$, the grain boundary conductivity of 5CCO and 10CCO is found to be comparable, presenting Ca^{2+} as a candidate cation for potential conductivity optimization schemes based on modulating local grain boundary composition.

4 Conductivity and Composition of $Pr_{0.04}Gd_{0.11}Ce_{0.85}O_{1.95-\delta}$

4.1 Motivation

The previous chapter illustrated the vital role of solute segregation on the transport properties of grain boundaries in the model system CCO. In this chapter, the interplay between macroscopic grain boundary conductivity and nanoscale chemical properties is explored in a more technologically relevant ceria solution. As described in §1.4.2 of the Introduction, Gd^{3+} ceria solutions have emerged as some of the most conductive oxide electrolytes for low and intermediate temperatures. DFT studies have predicted ideal dual-solute combinations to further optimize ionic conductivity in ceria solution via lowering the effective activation energy for oxygen ion migration, primarily by reducing solute-vacancy association energies (Andersson *et al.*, 2006; Dholabhai *et al.*, 2011). Following the suggestions of Andersson *et al.* and Dholabhai *et al.*, a combination of Gd^{3+} and Pr^{3+} solutes was employed here in hopes of confirming their predictions of enhanced ionic conductivity relative to ceria with *only* Gd^{3+}, and to explore the influence of Pr solute on grain boundary properties.

Indeed, comparison of grain and grain boundary electrical properties measured using AC impedance spectroscopy showed that the grain conductivity in the quaternary oxide $Pr_{0.04}Gd_{0.11}Ce_{0.85}O_{2-\delta}$ (PGCO) slightly exceeded that of $Gd_{0.2}Ce_{0.8}O_{1.9-\delta}$ (20GCO). Interestingly and unexpectedly, grain boundaries in the PGCO sample were on average almost 100 times more conducting than those in the 20GCO system.

The seminal finding of this work and its principal contribution to the field of electroceramics stems from STEM EELS nanocharacterization of grain boundary composition and chemistry: It was concluded that the enhanced grain boundary conductivity may result from strong Pr segregation to grain boundaries, which activated an alternative transport mechanism to that dominant in grains. This suggested that an electronic conduction mechanism based on Pr polaron hopping may be active at grain boundaries during AC impedance spectroscopy, a surprising finding which has in part motivated the work presented in the subsequent chapters of this dissertation. Much of the work reported in this chapter has been published in the journal Solid State Ionics (Bowman *et al.*, 2015).

4.2 Experimental

4.2.1 Material Synthesis and Sample Fabrication

$Gd_{0.2}Ce_{0.8}O_{2-\delta}$ (20GCO) and $Pr_{0.04}Gd_{0.11}Ce_{0.85}O_{2-\delta}$ (PGCO) nanoparticles were synthesized via spray drying, and pellets were fabrication from powder compacts sintered at 1350 °C for 18 h with 2.5 °C/min heating rate. AC impedance spectroscopy samples were prepared and measurements performed as described in the Methods chapter.

4.2.2 TEM

The 20GCO specimen was prepared by mechanical dimpling followed by Ar^+ ion milling, and the PGCO specimen was prepared via standard focused ion beam lift-out techniques, described in the Methods chapter. TEM and STEM images were used to

estimate grain size; EDX and EELS were used to characterize microscale compositional homogeneity, and nanoscale composition and chemistry of grain boundaries. Measurements were performed using a 200 kV Phillips CM200 FEG S/TEM, 400 kV JEOL 4000EX TEM, 200 kV JEOL 2010F S/TEM and a 200 kV JEOL ARM200F AC-S/TEM. EELS background fitting procedures and integration windows are specified in Table 4.1, with clarifying details provided below.

Table 4.1. EELS Spectral Processing Windows

	Background fitting procedure	Background fitting window(s) (eV)	Signal integration window (eV)	k-factor
Ce N_{45}	Inverse power-law extrapolation	70 – 95	115 – 135	
Gd N_{45}	Inverse power-law extrapolation + overlap correction	70 – 95	144 – 184	$k^{N}_{GdCe} = 0.32 \pm 0.03$
Ce M_{45}	Inverse power-law extrapolation	830 – 875	880 – 920	
Pr M_{45}	Inverse power-law two-window interpolation	920 – 930, 1150 – 1170	930 – 970	$k^{M}_{GdCe} = 0.85 \pm 0.21$
Gd M_{45}	Inverse power-law extrapolation + overlap correction	1120 – 1175	1185 – 1230	$k^{M}_{GdCe} = 2.12 \pm 0.34$

4.3 Results and Discussion

As evidenced by Figure 4.1, pellets had a dense polycrystalline microstructure. Electron diffraction patterns from 20GCO (Figure 4.8a inset) and PGCO (Figure 4.5 inset) confirmed the fluorite structure.

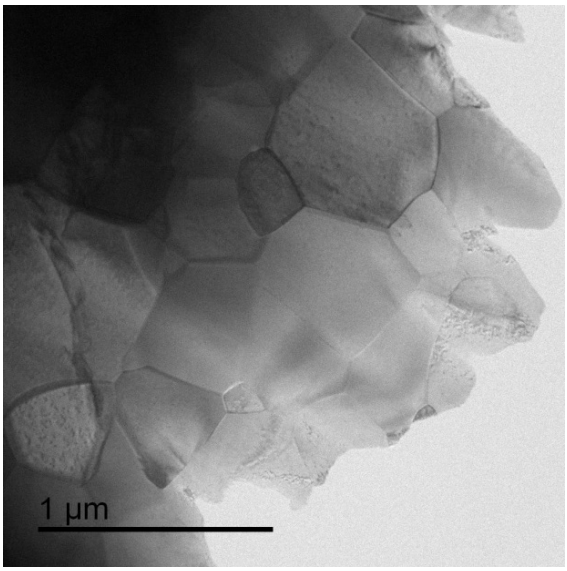

Figure 4.1. Microstructure of PGCO. Bright field TEM image of PGCO pellet. 200 keV JEOL ARM200F, ASU.

4.3.1 Electrical Characterization

Figure 4.2 presents representative Nyquist plots acquired at 200 °C from GCO (a,b) and PGCO (c,d) pellets. Impedance spectra exhibit two arcs corresponding to the grain and grain boundary polarizations, which were differentiated based on the brick-layer model, and their capacitance values which were compared with literature. A good fit to the Nyquist plots was achieved using an equivalent circuit model with subcircuits corresponding to grain and grain boundary arcs. subcircuits. Impedance data from PGCO are provided in the Appendix §8.2 showing also the fits to the measured data.

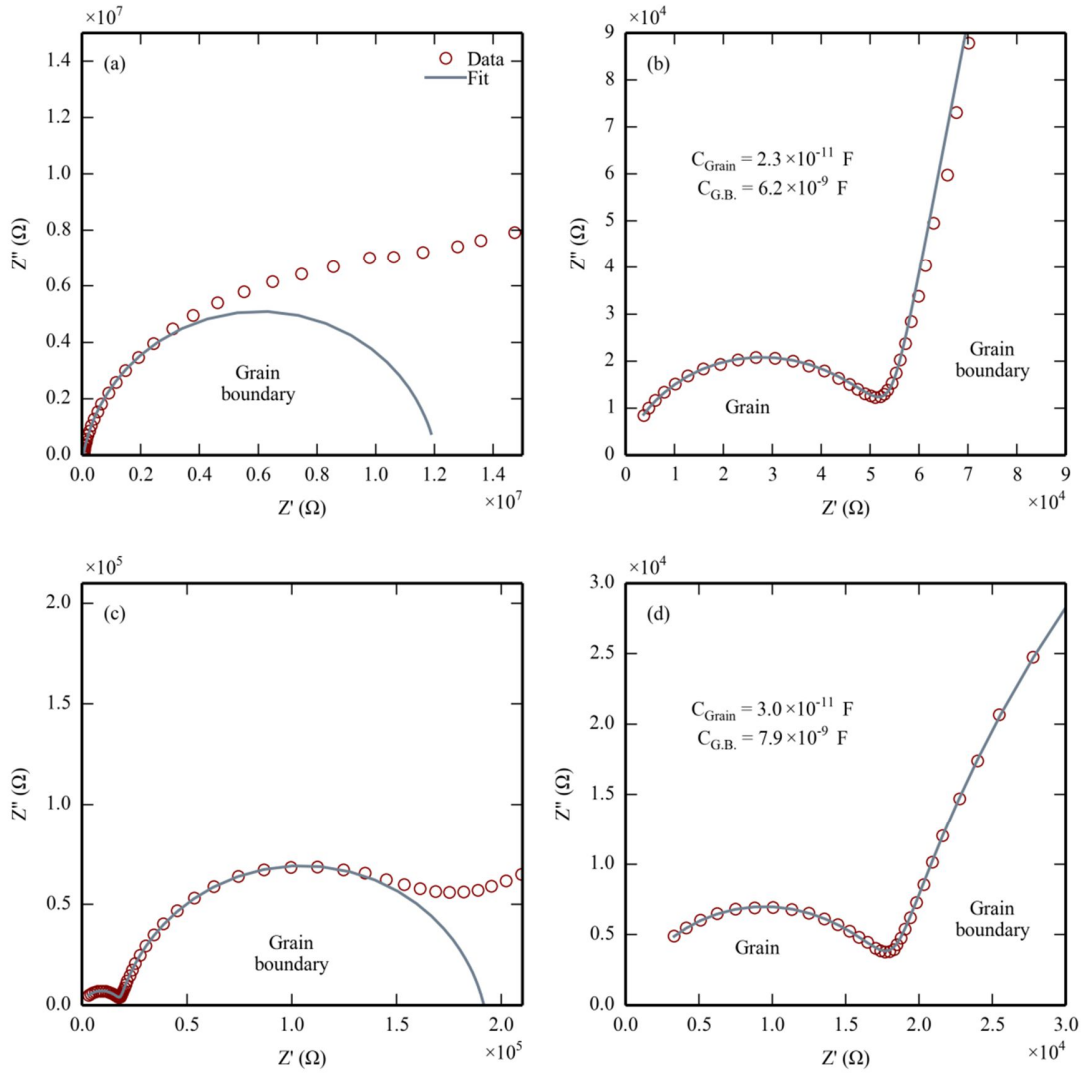

Figure 4.2. Nyquist Data from 20GCO and PGCO. Nyquist plots from (a,b) 20GCO and (c,d) PGCO acquired at 200 °C. Spectra (b) and (d) show the high frequency portions of spectra (a) and (c), as well as the corresponding grain and grain boundary capacitance values determined from fitting parameters using Equation (2.7).

Figure 4.3 shows Arrhenius plots of the grain and grain boundary electrical conductivities for PGCO and 20GCO. The 20GCO conductivities are assumed to be ionic under the measurement conditions used here (Waldhäusl, Preis, & Sitte, 2012), and the measured grain conductivity of 20GCO is in good agreement with literature (Avila-Paredes

et al., 2009; Jasper *et al.*, 2008; Zhang, Ma, Cheng, & Chan, 2006). The grain conductivity of 20GCO measured at 300 °C is (1.5 ± 0.05) · 10^{-4} S·cm^{-1}, which agrees with the value measured by Avila-Paredes *et al.* of approximately 1 · 10^{-4} S·cm^{-1} at 300 °C (Avila-Paredes *et al.*, 2009). At 200 °C the grain boundary conductivity is (7 ± 2) · 10^{-11} S·cm^{-1}, approximately 10 times less than that of Avila-Paredes *et al.* Figure 4.3 shows that the grain boundary conductivity at 200 °C is 5 · 10^{4} times lower than the grain conductivity in 20GCO, clearly demonstrating the deleterious effect of grain boundaries on ionic conductivity, especially at low temperatures.

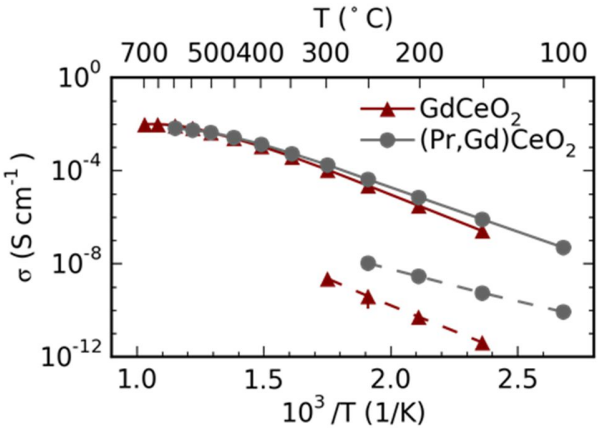

Figure 4.3. Conductivity of 20GCO and PGCO. Arrhenius plots of grain (solid connecting lines) and grain boundary (dashed lines) electrical conductivity for 20GCO ('$GdCeO_2$') and PGCO ('$(Pr,Gd)CeO_2$').

The grain conductivity of PGCO at 300 °C was measured to be (2.1 ± 0.05) · 10^{-4} S·cm^{-1}, approximately 40 % higher than that of 20GCO. The higher grain conductivity of PGCO relative to 20GCO is in agreement with the theoretical predictions of Dholabhai *et al.* described in the Introduction chapter (Dholabhai *et al.*, 2011). This is also reasonable considering that 10GCO (approximately the Gd concentration of PGCO) has been shown experimentally to exhibit higher grain ionic conductivity than 20GCO (Avila-Paredes *et*

al., 2009). While the observations reported here agree with these findings qualitatively, without knowledge of the oxygen partial pressure dependence of total conductivity (see Introduction), the exact transport mechanisms responsible of increased grain conductivity due to Pr doping remains ambiguous at this time. It is assumed, however, that within in the temperature range and oxygen partial pressure (air) used here, oxygen ions are the majority carrier species in PGCO grains, whose Pr concentration is assumed to be 4 mole% (Lubke & Wiemhofer, 1999; Kharton *et al.*, 2002; Schmale *et al.*, 2011; Bishop *et al.*, 2012).

Comparing the grain boundary conductivities of the two materials at 200 °C, one finds that the PGCO grain boundary conductivity is $(3 \pm 1) \cdot 10^{-9}$ S·cm^{-1}, approximately 50 times that of 20GCO ($(6 \pm 1) \cdot 10^{-11}$ S·cm^{-1}). This result suggests a significant effect on the grain boundary electrical properties due to the addition of Pr, and is particularly surprising considering that Avila-Paredes *et al.* found that the grain boundary conductivity in 10GCO—the approximate Gd concentration of our PGCO, was approximately five times lower than that of 20GCO (Avila-Paredes *et al.*, 2009). One possible explanation for the higher grain boundary conductivity in PGCO here is that it is the effect of Pr segregation to grain boundaries, discussed below.

As discussed in the Introduction chapter, the effective activation energy for ionic migration in oxides can decrease at elevated temperatures, where the effect of solute-vacancy association may not be appreciable. Like CCO, E_a^{Grain} was determined separately for T < 450 °C and T ≥ 450 °C. E_a^{GB} was determined only from measurements performed below 300 °C. Results are tabulated in Table 4.2. For 20GCO, E_a^{Grain} and E_a^{GB} are comparable with previous works (Avila-Paredes *et al.*, 2009; Lubke & Wiemhofer, 1999).

For PGCO, E_a^{Grain} at T < 450 °C is slightly lower than that of 20GCO, which is consistent with the aforementioned theoretical predictions (Andersson *et al.*, 2006; Dholabhai *et al.*, 2011), and the observation of higher σ_{Grain}. Interestingly, the PGCO E_a^{GB} is significantly lower than E_a^{Grain}, which may stem from polaron electronic conduction induced in the grain boundary region as a result of very significant local enrichment of Pr (Bishop *et al.*, 2011, 2012), discussed below.

Table 4.2. Summary of Data for 20GCO and PGCO

Sample name (Nominal composition)	Mean grain size (nm)	E_a^{Grain} T < 450 °C (eV)	E_a^{Grain} T ≥ 450 °C (eV)	E_a^{GB} (eV)
20GCO ($Gd_{0.2}Ce_{0.8}O_{1.9-\delta}$)	750 ± 31	0.87 ± 0.02	0.42 ± 0.04	0.92 ± 0.20
PGCO ($Pr_{0.04}Gd_{0.11}Ce_{0.85}O_{2-\delta}$)	450 ± 18	0.78 ± 0.01	0.39 ± 0.04	0.58 ± 0.10

4.3.2 Nanocharacterization

20GCO

EELS and EDX data were collected from 20GCO and PGCO grains to probe the distribution of solute cations. Figure 4.4a shows typical energy-loss spectra from 20GCO and PGCO, with the Gd M_{45} edge confirming the presence of Gd in both samples, and the Pr M_{45} edge indicating presence of Pr in PGCO.

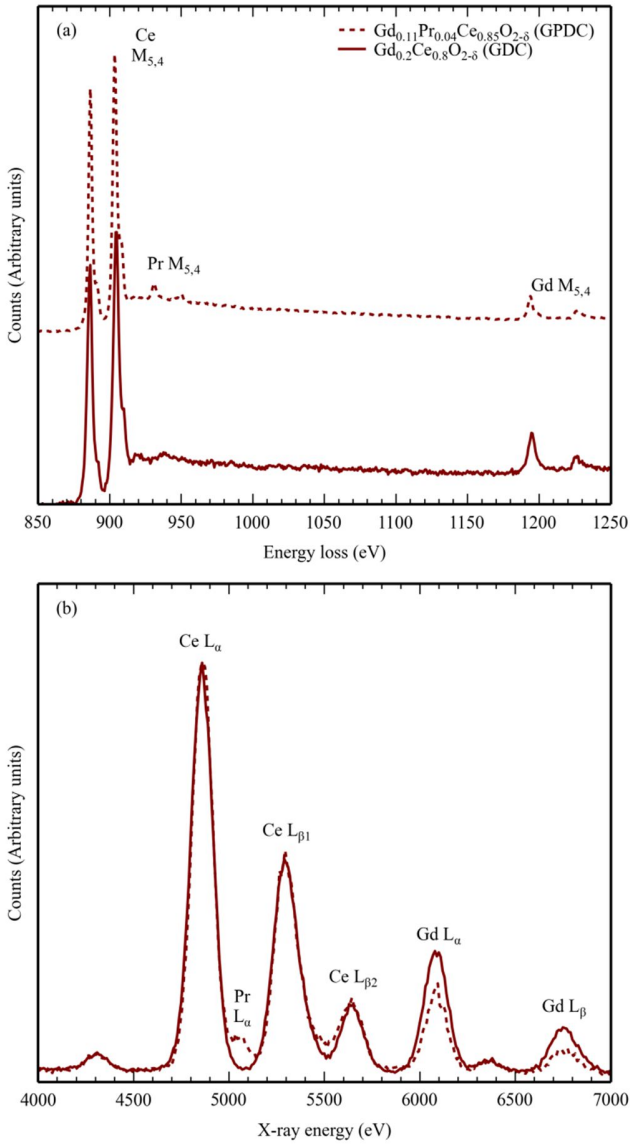

Figure 4.4. Spectroscopic Data from 20GCO and PGCO. (a) EELS and (b) EDX spectra from 20GCO and PGCO. 200 kV Phillips CM200, ASU.

Figure 4.4b compares typical 20GCO and PGCO EDX spectra (normalized to the Ce L_α line). The Pr L_α line visible in the PGCO spectrum was used to verify the presence of Pr. EELS and EDX showed that Gd and Pr were present in all grains analyzed in the PGCO confirming the effectiveness of the spray drying approach to produce polycrystalline quaternary rare-earth oxides. All grain boundaries, like those shown in

Figure 4.5 for PGCO and Figure 4.6 for 20GCO, appeared to be structurally abrupt and free of amorphous intergranular phases in phase contrast images.

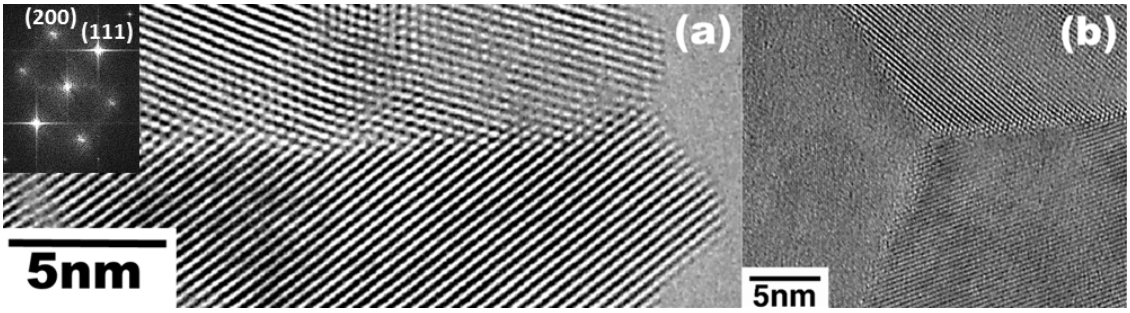

Figure 4.5. TEM Images of 20GCO Grain Boundaries. Typical bright field phase contrast TEM micrograph of a PGCO (a) grain boundary with $[0\bar{1}1]$ zone axis diffractogram inset, and (b) triple grain junction. 400 keV JEOL 4000EX TEM, ASU.

Figure 4.6a shows a TEM image of a grain boundary which is slightly tilted. Diffraction contrast variation is visible in the two adjacent grains, indicating that the right grain is in a stronger electron diffracting condition than the left. Figure 4.6b shows an ADF STEM image of the same grain boundary; the dotted line indicates the scan path of the STEM EELS line scan in (d). There is visible contrast variation caused by misorientation between adjacent grains, as well as dark contrast at the grain boundary interface. The dark contrast visible at this grain boundary interface is believed to be the result of the more open interfacial atomic structure scattering fewer electrons to the annular detector, thus resulting in a less intense signal at the grain boundary interface relative to the adjacent grains.

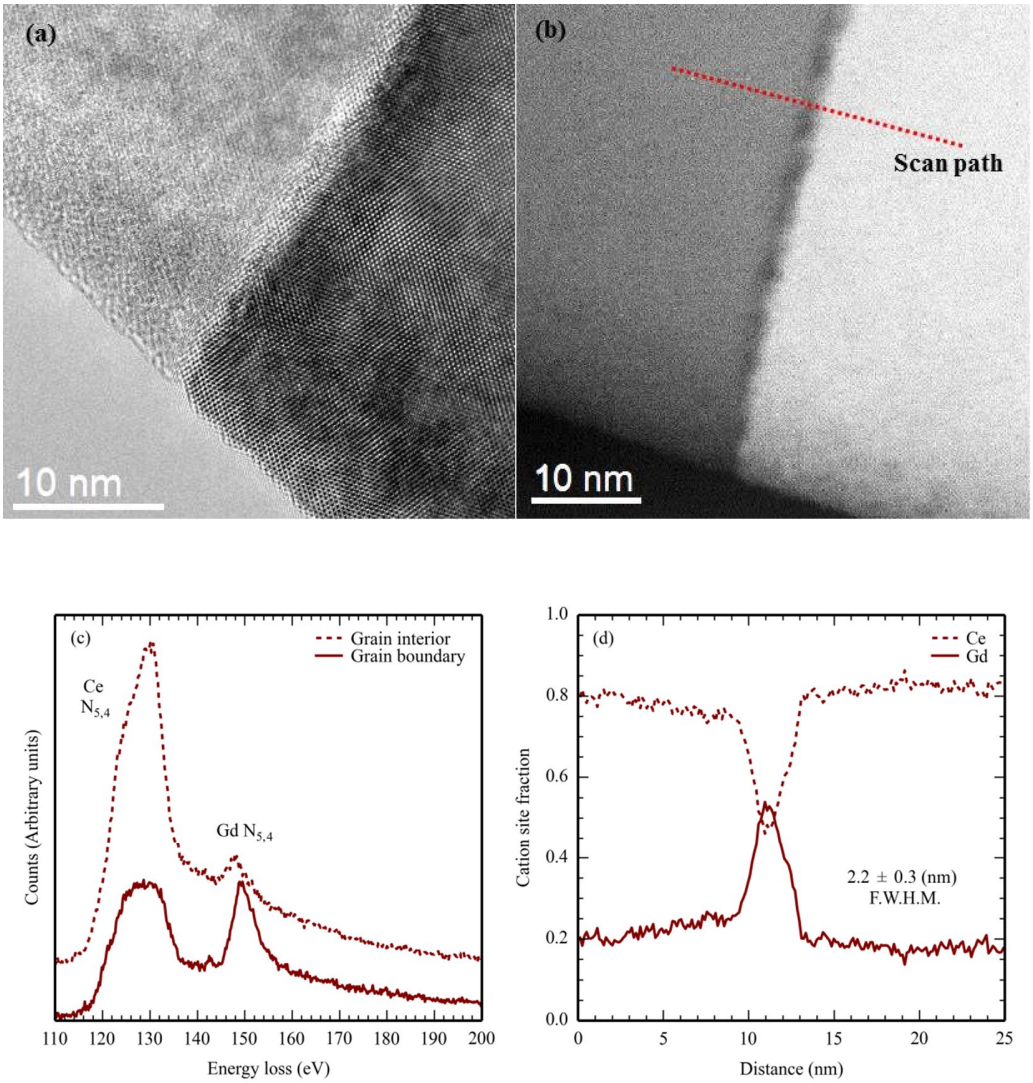

Figure 4.6. Grain Boundary STEM EELS of 20GCO. (a) BF TEM and (b) ADF STEM micrographs of a typical grain boundary in 20GCO. (c) Electron-energy loss spectra from 20GCO grain and grain boundary shown in (b). (d) Ce and Gd composition profiles corresponding to the scan path in (b). The STEM probe size was ≈ 0.2 nm. 200 keV JEOL 2010F TEM, ASU.

Figure 4.6c compares energy-loss spectra acquired from the grain and the grain boundary. There is a marked increase in the Gd:Ce N_{45} edge intensity ratio at the grain boundary, indicating considerable enhancement of the Gd concentration. The spectra also

show that the Ce edge is much more rounded at the grain boundary indicating that a significant change in local Ce bonding has taken place in the grain boundary interface.

Figure 4.7 shows a typical N_{45} EELS edge of 20GCO plotted with a CeO_2 reference spectrum (normalized to the Gd N_{45} maxima), and highlighted integration windows used for edge overlap correction and spectral quantification. Because the tail of the Ce N_{45} edge overlaps the Gd N_{45} edge onset in the energy loss range 144 eV – 184 eV (see Figure 4.7 windows A_2 and A_3), quantification of 20GCO energy-loss spectra like those in Figure 4.6c required a correction procedure.

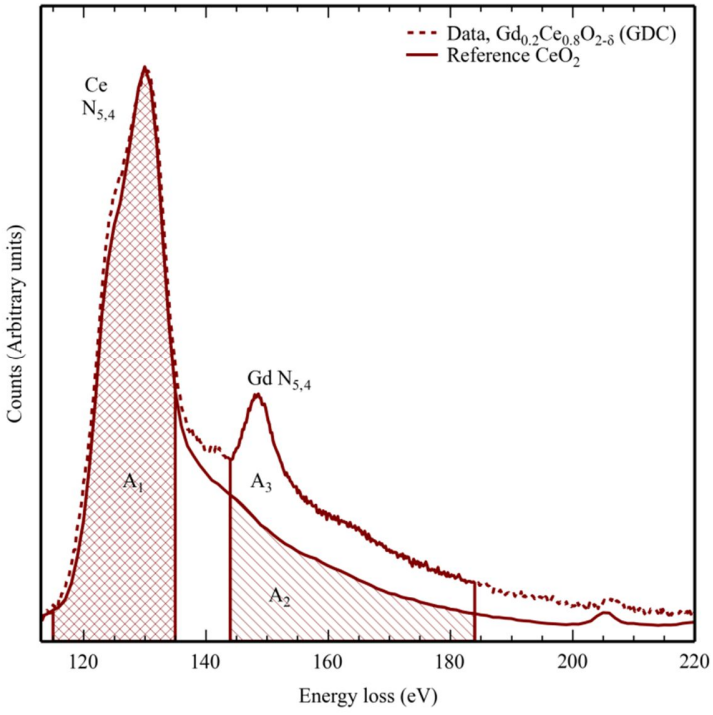

Figure 4.7. EELS Overlap Correction in 20GCO. Background-subtracted experimental 20GCO and reference CeO_2 (Ahn & Krivanek, 1983) energy loss spectra with highlighted integration windows used for edge overlap correction. The spectra are normalized to the Gd N_{45} edge maxima. JEOL 2010F.

The ratio of integrated intensity in window A_1 (115 eV to 135 eV) to that in A_2 was assumed constant so that the contribution of the Ce N_{45} edge tail to the in energy loss range 144 eV to 184 eV (i.e. A_2) could be subtracted, leaving only intensity from the Gd N_{45} (i.e. A_3). In other words, the goal of the quantification process was to isolate the Gd N_{45} integrated intensity (A_3) from the combined Ce + Gd N_{45} signal ($A_2 + A_3$) in the 144 eV to 184 eV energy loss window. The intensity in the Gd N_{45} signal, I_{Gd}, in the energy loss spectra from 20GCO can be expressed as

$$I_{Gd}^{20GCO\ exp.} = A_3 = (A_2 + A_3)^{20GCO\ exp.} - {A_1}^{20GCO\ exp.} \left(\frac{A_2}{A_1}\right)^{CeO_2\ Ref.} \qquad (4.1)$$

The quantity $(A_2/A_1)^{CeO_2\ Ref.}$ is the integrated intensity ratio of the Ce N_{45} tail to the Ce N_{45} edge determined from the CeO_2 reference spectrum. This quantity was multiplied by the measured Ce N_{45} edge intensity, ${A_1}^{20GCO\ exp.}$, to approximate the Ce tail contribution (${A_2}^{20GCO\ exp.}$) to the total signal in the Gd-$N_{4,5}$ energy loss window, $(A_2 + A_3)^{20GCO\ exp.}$. Knowledge of the Gd-$N_{45}$ signal, I_{Gd}, enabled estimation of the $[Gd]/[Ce]$ concentration ratio using the k-factor method. The Gd:Ce k factor (k_{GdCe}) was determined to be 0.32 ± 0.03 using average cation signal intensity ratios acquired in grains.

Figure 4.6d shows the cation concentration along the highlighted scan path in Figure 4.6b. The composition was found to vary significantly along the scan path, from approximately $Gd_{0.2}Ce_{0.8}O_{1.9-\delta}$ in the grain to approximately $Gd_{0.55}Ce_{0.45}O_{1.7-\delta}$ at the grain boundary interface. The FWHM of the peak in Gd^{3+} enhancement profile was estimated to be 2.2 ± 0.3 nm.

A triple grain junction in 20GCO was also investigated using STEM EELS 2D composition mapping. This made it possible to visualize the spatial extent of cation concentration fluctuations along grain boundaries and in the vicinity of the triple grain junction. Figure 4.8a shows a TEM image of one such junction in 20GCO with the corresponding composition map in Figure 4.8b. The slight distortion in the grain boundary shape visible in the map is due to specimen drift during the STEM EELS data acquisition. The average Gd^{3+} concentration at the grain boundary is approximately 55 mole%, similar to the grain boundary line scan in Figure 4.6b. Though, in some regions there does appear to be considerable non-uniformity in the Gd distribution, with the Gd concentration ranging from 40 mole% to 70 mole%. Like the CCO system described in the last section, it is conceivable that some degree of super saturation may have been detected at the grain boundaries in this system.

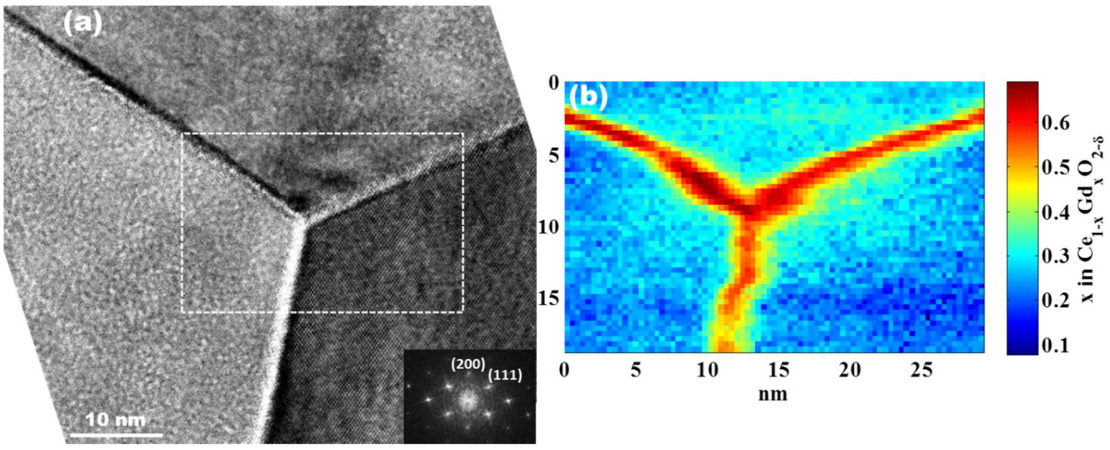

Figure 4.8. STEM EELS Maping at 20GCO Triple Junction. (a) BF TEM micrograph of a triple grain junction in 20GCO with $[0\bar{1}1]$ zone axis diffractogram inset on the corresponding grain. (b) STEM EELS 2D composition map indicating the distribution of Gd^{3+} in the region of the junction. STEM probe size was ≈ 0.2 nm. 200 kV JEOL 2010F S/TEM, ASU.

The average grain boundary Gd^{3+} concentration in 20GCO was estimated to be 62 ± 3 mole%, which is comparable with previous work of Lei *et al.* who measured grain boundary composition of $Gd_{0.41\pm0.04}Ce_{0.59\pm0.04}O_{1.24\pm0.17}$ in nominally 20GCO (Lei *et al.*, 2002). They also measured the peak width of the Gd^{3+} segregation profile (i.e. the compositional grain boundary) to be approximately 2 nm – 2.5 nm, which is consistent with the 2.2 ± 0.3 nm compositional grain boundary width observed here. Lee *et al.* also reported Gd^{3+} segregation profile width approximately 3 nm – 4 nm at grain boundaries in 30GCO thin films using STEM EDS (W. Lee *et al.*, 2012).

PGCO

As discussed above, the grain boundary conductivity of PGCO is approximately 50 times that of 20GCO at 200 °C. This result was particularly interesting considering the work of Avila-Paredes and coworkers (2009), who, when varying the nominal Gd^{3+} concentration of GCO from 1 mole% to 20 mole%, found σ_{GB} of 20GCO to be approximately five times greater than that of 10GCO at approximately 200 °C. Considering that here the sample containing 11 mole% Gd (PGCO) exhibited higher σ_{GB} than the 20GCO, it was concluded that the higher σ_{GB} in PGCO is correlated with Pr addition.

Spatially resolved STEM EELS was thus employed to characterize the Pr distribution and Ce oxidation state at grain boundaries in PGCO. Figure 4.9a illustrates the effect of the grain boundary on the M_{45} edges of Ce, Pr and Gd. Each background-subtracted spectrum is labeled $A \rightarrow K$ and represents the sum of spectra in each row of the spectrum image inset in Figure 4.9b, also labeled $A \rightarrow K$ and highlighted with a rectangular box. M_{45} edges were used for this measurement because all three elements' edges are

visible in a single spectrum, and the Ce M_{45} edge contains readily obtainable information on Ce valence. The integration (I_{Ce}, I_{Pr} and I_{Gd}) and background fitting (B_{Pr} and B_{Gd}) windows used for spectrum quantification are highlighted with solid and dashed boxes, respectively in Figure 4.9a. Though omitted for clarity, a 45 eV wide background fitting window positioned 5 eV to the left of the Ce M_{45} integration window was used. Due to the close proximity of the Pr and Ce edge onsets, a two window background fitting procedure was used to extract the Pr signal with one narrow window just in front of the Pr M_{45} edge and a second just before the Gd M_{45} edge.

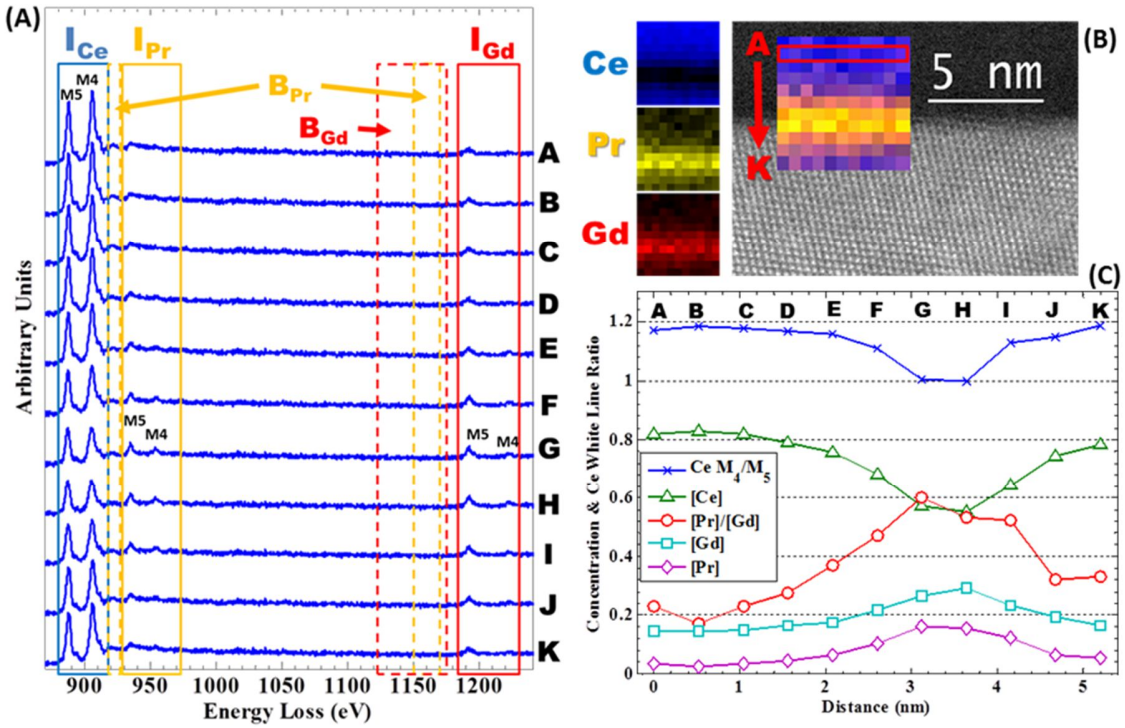

Figure 4.9. STEM EELS Mapping at PGCO Grain Boundary. (a) Background-subtracted energy loss spectra acquired from PGCO showing variations in the Ce, Pr and Gd M_{45} edges across the grain boundary in (b). (b) AC-STEM ADF image of a grain boundary with inset color map illustrating the cation distribution in the interfacial region; constituent color maps are provided. (c) Profiles of estimated cation fraction and the Ce M_4/M_5 white line ratio—an indicator of the Ce oxidation state. STEM probe size was ≈ 0.1 nm and step size ≈ 0.5 nm. 200 kV JEOL ARM200F AC-STEM, ASU.

Figure 4.9b shows an ADF AC-STEM image of a PGCO grain boundary with an inset false-colored spectrum image. The spectrum image is false colored by overlaying the individual color maps (left of STEM image) derived from integrating the M_{45} signal for each cation at every pixel. Figure 4.9c displays variations in the estimated cation concentration, the relative solute concentration, and the Ce M_4/M_5 white line ratio, which is an indication of the oxidation state of the Ce ion (Mullins *et al.*, 1998; Hojo *et al.*, 2010; Turner *et al.*, 2011). The data points are separated by approximately 5.2 Å and labeled $A \rightarrow K$ to indicate the row in the spectrum image from which they were derived. From inspection of these figures, position *H* is taken to be the approximate position of the grain boundary interface.

Figure 4.9a shows significant variation in the cation concentration and the Ce oxidation state with position in the grain boundary region. Distinct increases in the I_{Pr}:I_{Ce} and I_{Gd}:I_{Ce} signal intensity ratios are clearly visible, indicating an enhancement of the Pr and Gd concentrations relative to Ce. Like the 20GCO, this enhancement is attributed to solute segregation during pellet sintering. Also visible is a decrease in the Ce M_4/M_5 white line ratio from $M_4/M_5 \approx 1.2$ at grain s to $M_4/M_5 \approx 1.0$ at the boundary interface. This change is characteristic of the reduction of Ce^{4+} to $Ce^{(4-y)+}$ ($0 \leq y \leq 1$), and indicates the presence oxygen deficiency stemming from the incoherent grain boundary atomic structure (Lei *et al.*, 2002; Browning *et al.*, 2004).

The solute segregation profiles are approximately 1.8 ± 0.3 nm wide, a figure similar to that of our 20GCO. Ce, Pr and Gd cation concentrations were estimated using the k-factor method to be 55 mole%, 16 mole% and 29 mole% at the grain boundary

interface, respectively. Interestingly, the relative solute concentration ratio ([Pr]:[Gd]) was found to vary between approximately 0.28 at grains and 0.55 at the grain boundary, indicating that a greater fraction of Pr segregates to the boundary compared to Gd, possibly caused by different segregation kinetics related to valence and/or ionic radii. The peak FWHM of the white line ratio profile is approximately 0.8 nm, consistent with the *structural* width of grain boundaries visible in high resolution images herein, again indicating that the reduced ceria is associated with the oxygen deficient grain boundary structure.

Enhancements in both ionic and electronic conductivity may play a role in the enhanced grain and grain boundary conductivities of PGCO relative to 20GCO, though the dominant charge transport mechanisms have not been determined in these samples. Like the grain, the enhanced PGCO grain boundary conductivity could stem from an increase in ionic conductivity due to lower effective activation energy caused by Pr enrichment (Andersson *et al.*, 2006; Dholabhai *et al.*, 2011). More likely, however, based on the surprisingly low grain boundary effective activation energy (0.58 eV) and strong Pr enrichment it is hypothesized that $Pr^{3+/4+}$ small polaron (see Introduction) conduction in the vicinity of grain boundaries is giving rise to considerable electronic current during AC impedance spectroscopy. (This mechanism is discussed in detail in Chapter 6, following the presentation of additional data on Pr grain boundary segregation.) It was shown using $Sm_{0.15}Ce_{0.85}O_{1.93-\delta}$ that Nyquist arcs exhibit a tear drop shape under conditions of mixed ionic-electronic conductivity, which was not observed in the grain boundary arcs of PGCO (see Appendix §8.2). Rather, it is thought that the conduction mechanism in the PGCO grain boundary is dominated by a single conduction mechanism—polaron hopping—

during AC impedance spectroscopy because both arcs in the Nyquist plot could be fit with a depressed semi-circle using a constant phase element.

In $Pr_xCe_{1-x}O_{2-\delta}$ (PCO) the Pr *4f* states are positioned in the bandgap of CeO_2 (Figure 4.10), and form an impurity band at sufficiently high Pr concentrations when the discreet energy levels of the Pr solutes overlap (Lubke & Wiemhofer, 1999; Stefanik & Tuller, 2001, 2004). Electron density localized on a Pr^{3+} ion, i.e. a Pr small polaron resulting from oxygen release, may transfer via thermally activated polaron hopping to an adjacent Pr^{4+} ion, with the probability of hopping influenced by the spatial separation of adjacent +3 and +4 Pr ions. This conduction mechanism is maximum when there is an equal concentration of tri- and tetravalent Pr ions. This Pr polaron hopping mechanism is thus sensitive to Pr concentration, and experimental evidence indicates that this mechanism becomes considerable if $x > 0.1$ in $Pr_xCe_{1-x}O_{2-\delta}$ (Bishop *et al.*, 2011, 2012), which is thought to be the case in the vicinity of grain boundaries in PGCO (see Figure 4.9c).

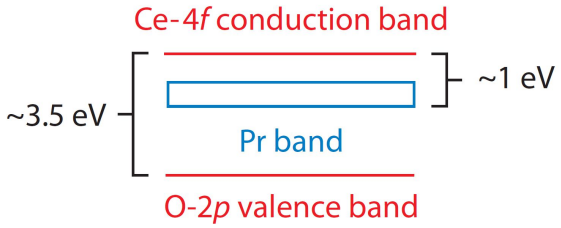

Figure 4.10. Proposed Band Diagram for PCO. Image from (Tuller & Bishop, 2011).

4.4 Summary

PGCO and 20GCO starting powders were successfully synthesized with spray drying, and used to fabricate sintered pellets for macroscopic electrical characterization by

ACIS performed from 150 °C to 700 °C. Electrical conductivity in 20GCO was interpreted as ionic conductivity and was in reasonable agreement with previous reports. The grain and grain boundary conductivities of the PGCO were higher than GCO by up to 1 and 2.5 orders of magnitude depending on the measurement temperature. Interestingly, the PGCO grain boundary migration activation energy was found to be 0.58 ± 0.1 eV, considerably lower than that of the grain which was measured to be 0.92 ± 0.2 eV.

Specimens were analyzed via S/TEM imaging, EDX and EELS. TEM indicated that 20GCO and PGCO microstructures were consistent with those in the literature. EDX and EELS confirmed the presence of appropriate solutes throughout both samples, thus highlighting the efficacy of the spray drying approach to quaternary oxides used to produce pellets with uniform grain composition. Grain boundaries were free of glassy intergranular phases, and significant solute concentration enhancement was observed. The grain boundary interface composition was estimated from EELS to be $Gd_{0.62}Ce_{0.38}O_{2-\delta}$, and $Gd_{0.29}Pr_{0.16}Ce_{0.55}O_{2-\delta}$ for 20GCO and PGCO, respectively. Such a large enhancement in Pr concentration at the PGCO grain boundary, along with the significant reduction in grain boundary effective migration activation energy suggested possible enhancement in ionic conductivity and the likely existence of Pr polaron electronic conduction at grain boundaries. In PGCO, the relative solute concentration ([Pr]:[Gd]) varied as well in the grain boundary region. Lastly, the oxidation state of the Ce host cation was found to decrease in the grain boundary, likely the result of oxygen deficient grain boundary atomic structure.

5 Monochromated STEM EELS of Bandgap States in $Pr_{0.1}Ce_{0.9}O_{2-\delta}$

5.1 Motivation

As described in Chapter 4, substantial enhancement in the electrical conductivity of grain boundaries in PGCO was accompanied by a factor four enrichment in the Pr concentration at grain boundaries. It was speculated that electronic conductivity via Pr^{3+} polaron hopping at Pr-enriched grain boundaries was the origin of the measured conductivity enhancement; however, spectroscopic evidence was not provided for the existence of a Pr polaron conduction band. Thus, an appropriate measurement technique capable of detecting this inter-bandgap state with high spatial resolution is desired to elucidate the aforementioned alteration of grain boundary transport in Pr-containing ceria solid solutions. This chapter focuses on the development of such a technique, and illustrates that the Pr impurity band can be detected in nanoparticles of $Pr_{0.1}Ce_{0.9}O_{2-\delta}$ (10PCO) using ultra-high energy resolution STEM EELS. The occupancy of the band is determined by the oxidation state of Pr ions which can also be determined with EELS. In the future, this technique will be applied to polycrystalline 10PCO specimen, a study for which the work in this chapter lays the foundation using this new ultra-high energy resolution EELS capability.

In general, describing how variations in nanoscale structure and composition affect local electronic and optical properties is critical to developing a fundamental understanding of atomic, nanoscale and mesoscale properties of condensed matter. Experimental methods to explore these relationships require a correlative approach to atomic resolution imaging

and spectroscopy, and high spatial resolution should allow electronic states associated with nanoparticles and defects such as dislocations or grain boundaries to be mapped and correlated with defect atomic structure (Batson, Kavanagh, Woodall, & Mayer, 1986; Lazar, Botton, Wu, Tichelaar, & Zandbergen, 2003). For insulators, the defects often give rise to states within the bandgap which may often control charge transport properties as well as optical properties. Correlating these states with local structure and composition is the key to understanding and controlling the material properties.

Recent developments in monochromated EELS in the AC-STEM offer new opportunities for local nanoscale probing of bandgap states, and correlation with structure and chemistry at the 0.1 nm level. The ability to now correlate atomic structure with loss features down to hundreds of meV in the energy-loss spectrum represents a powerful tool for characterizing electronic and optical properties of materials, especially semiconductors and insulators. Here the energy, width and relative intensity of the density of states within the bandgap that are created when solute Pr ions are added to CeO_2 nanoparticles is quantified.

The PCO system shows mixed ionic-electronic conduction at intermediate temperatures making it a candidate for applications demanding counter diffusion of electrons and oxygen ions (Bishop *et al.*, 2011; Tuller & Bishop, 2011). A monochromated AC-STEM was employed which combines sub-nanometer electron probe diameter and EELS with ultra-high energy resolution of 15 meV. This first-of-its-kind instrument offers entirely new STEM EELS capability, and novel techniques and applications are currently being pioneered (Krivanek *et al.*, 2014; Rez *et al.*, 2016; Liu, March, & Crozier, 2016;

Crozier, Aoki, & Liu, 2016). Here, EELS allows the width and energy position of the state to be determined with respect to the top of the valence band, while optical observations of chemically-induced color changes are employed to provide further information on the energy shift of the inter-bandgap state when the Pr oxidation state is changed. The work in this chapter has been published in the peer reviewed journal Ultramicroscopy (Bowman *et al.*, 2016).

5.2 Experimental

5.2.1 Material Synthesis and Fabrication

10PCO nanoparticles approximately 30 nm in diameter, shown in Figure 5.1, were synthesized via spray drying. The as-synthesized particles were calcined in air at 900 °C for 3 h to achieve full oxygen stoichiometry before EELS analysis.

5.2.2 TEM

A Nion UltraSTEM100 STEM operating at 60 kV accelerating voltage was used to acquire valence-loss EELS data under monochromated condition, using a dispersion of 3 meV/channel. Under this condition, the ZLP FWHM was typically 18 meV to 25 meV to provide reasonable signal-to-noise; the beam current at the specimen was approximately 1 pA. The convergence and collection angles were 30 mrad and 50 mrad, respectively. Core-loss EELS data were acquired from Ce M_{45} and Pr M_{45} edges using a dispersion of 100 meV/channel under non-monochromated conditions, under which the ZLP FWHM was approximately 250 meV—the energy spread of the instrument's cold field-emission

gun. Eight valence-loss spectra were acquired from particles and particle clusters in random orientations. The spectra were similar suggesting that orientational effects were not prominent in part because of the large convergence and collection angles employed.

A typical ADF STEM image obtained with the monochromated probe is shown in Figure 5.1b. It is possible to achieve a probe diameter of 0.3 nm with the monochromator slit adjusted to give 20 meV spectral resolution; however, to achieve higher beam current the probe size was slightly larger than 0.7 nm for the conditions employed here. The high spatial resolution allows the spectra to be correlated with sub-nanometer features in the sample. However, the spatial resolution of the energy loss spectra is determined not by the probe size, but by delocalization effects as predicted by dielectric theory, which are likely to be 5 nm or more in this case. Spectra were recorded in both transmission and aloof beam mode (with the beam positioned a few nanometers outside of the particles). No significant difference was observed in the shape of the intensity within the bandgap region, suggesting that radiation damage effects were minimal at the monochromated beam current used. The spectra shown here were recorded in transmission mode.

5.3 Results and Discussion

5.3.1 EELS

Valence-loss EELS of 10PCO, shown in Figure 5.2a, revealed an inter-band feature with rising onset and extended plateau ahead of the conduction band onset. An inverse power law function was fit to the ZLP tail such that the background intensity was

approximately zero ahead of the plateau onset. The Cherenkov condition for 60 kV electrons (i.e. refractive index of medium, *n*, must exceed 2.3) propagating through 10PCO is unlikely to be satisfied (refractive indices for lanthanide-CeO_2 solid solutions ($La_{0.15}Ce_{0.85}O_{2-\delta}$, La = lanthanide ion) range from 1.65 to 1.95 (Hartridge, Krishna, & Bhattacharya, 1998). Typical reported values of n for pure CeO_2—about 1.8 to 2.5 for photon energies below approximately 2.7 eV (Bueno, Martinez-Duart, Hernandez-Velez, & Vazquez, 1997; Goubin *et al.*, 2004; Hass, Ramsey, & Thun, 1958; Mansilla, 2009; Özer, 2001; Patsalas, Logothetidis, & Metaxa, 2002; Wiktorczyk, Biegański, & Zielony, 2012), are in some cases sufficiently great to satisfy the Cherenkov condition. However, for the 10PCO particles, radiation would likely be suppressed as the 30 nm particle size in this work is significantly less than the emitted photon wavelength (Erni & Browning, 2008; Rivacoba, Zabala, & Aizpurua, 2000; Stöger-Pollach *et al.*, 2006)Thus no correction for Cherenkov effects was performed during background removal.

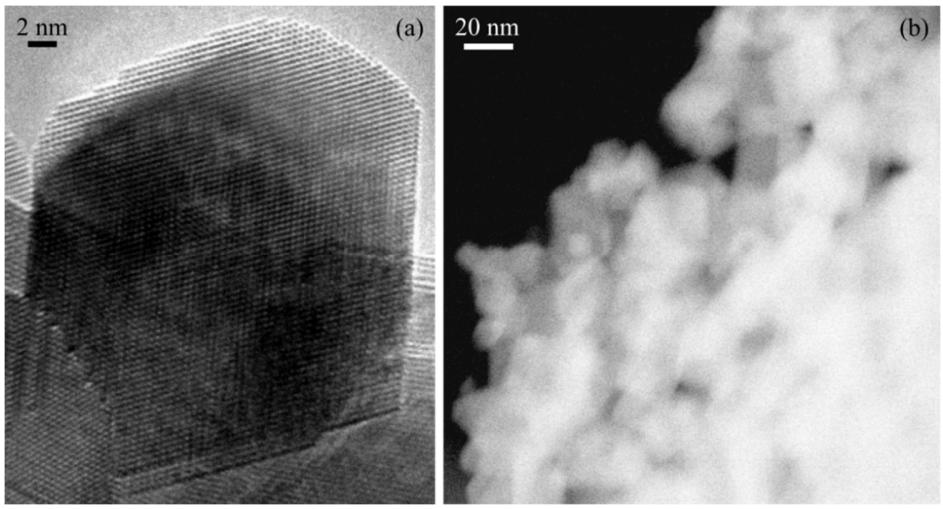

Figure 5.1. TEM and STEM Images of 10PCO Particles. (a) HRTEM image of a typical 10PCO particle. 200 kV JEOL 2010F TEM, ASU. (b) Monochromated ADF STEM image of 10PCO particle cluster. 60 kV Nion UltraSTEM100, ASU.

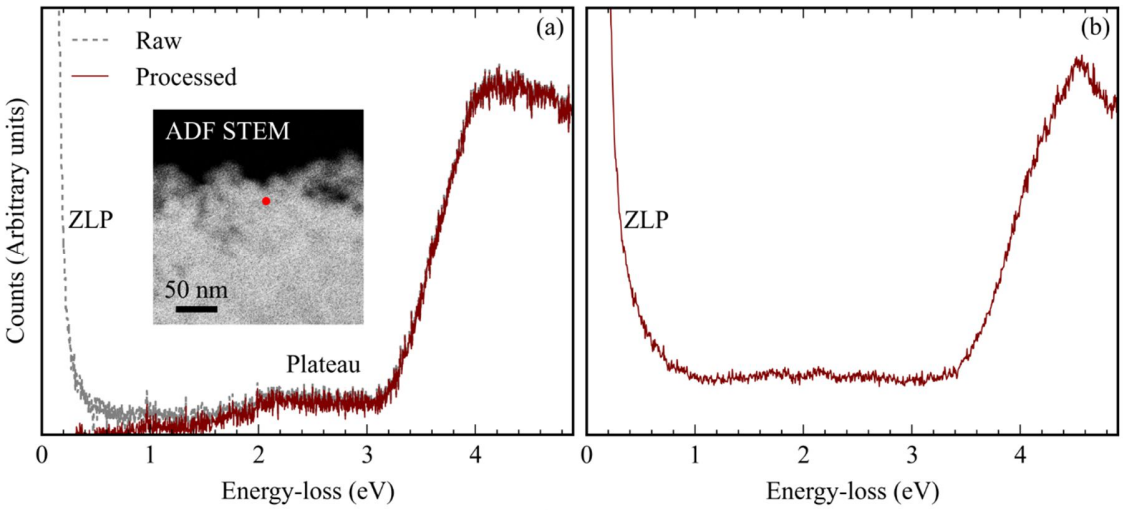

Figure 5.2. Valence-Loss EELS from 10PCO and CeO_2. Typical valence-loss spectra from (a) oxidized 10PCO—showing ZLP, inter-band plateau feature and conduction band onset, and (b) fragment of bulk CeO_2. The beam position during 10PCO spectra acquisition is indicated in the monochromated ADF STEM image inset in (a). Nion UltraSTEM100, ASU.

For reference, valence-loss spectra were acquired from fragments of a crushed CeO_2 sintered pellet. These data, shown in Figure 5.2b, revealed constant intensity within the bandgap attributed to Cherenkov radiation. The Cherenkov intensity is higher in this specimen in part due to the relatively large fragments (greater than several hundred nanometers) that were analyzed. The propagating wave of Cherenkov radiation is only established when the particle size is greater than the radiation wavelength. There is no evidence for a significant plateau in the bandgap region from pure CeO_2.

The 10PCO conduction band onset was measured to be 3.2 ± 0.1 eV (error is one standard deviation)—taken as the intercept of the energy-loss axis with the linear extrapolation of the conduction band onset, and is consistent with that of our reference CeO_2 (3.2 eV – 3.4 eV), and literature (3.0 eV – 3.2 eV (Goubin *et al.*, 2004; Marabelli & Wachter, 1987)). The valence-to-conduction band excitation in CeO_2 is attributed to

transitions from occupied levels at the O 2*p* valence band maximum into unoccupied Ce 4*f* states at the conduction band minimum, which are dipole-allowed due to strong covalent hybridization between occupied O 2*p* states and Ce 4*f* states, and unoccupied O 2*p* states and Ce 5*d* states in CeO_2 (Wuilloud, Delley, Schneider, & Baer, 1984; Marabelli & Wachter, 1987; Mullins *et al.*, 1998; Goubin *et al.*, 2004; Niu *et al.*, 2014). The pre-plateau rise spanned the energy range of approximately 1.4 eV – 2.4 eV with the plateau extending from 2.4 eV to the conduction band edge (~3.2 eV). The inter-band feature was attributed to a Pr impurity band, facilitating electronic transitions from the O 2*p* valence band into unoccupied Pr 4*f* levels lying below the Ce 4*f* levels of the CeO_2 conduction band (J. J. Kim *et al.*, 2012, 2014), stemming presumably from hybridization between O 2*p* and Pr 4*f* levels. The plateau onset energy, 1.4 ± 0.3 eV, was taken to be the position of the Pr impurity band.

The occupancy of the Pr inter-band state (i.e. the Pr valence) was shown to influence the absorption of 10PCO, with absorption strength increasing with the number of tetravalent Pr ions present (J. J. Kim *et al.*, 2012, 2014). Thus to investigate the relative amounts of Pr^{3+} and Pr^{4+}, the Ce/Pr M_{45} edge core-loss spectra was probed in an attempt to detect core-level excitations into unoccupied Pr 4*f* levels associated with Pr^{4+} ions. The separation between the Ce and Pr M_5 white lines was monitored under various acquisition conditions to verify that Pr^{4+} ions were present in the specimen. This approach was employed successfully by López-Cartes *et al.*, who demonstrated that during sequential heating of $Pr_{0.2}Ce_{0.9}O_{2-\delta}$ (20PCO) under gaseous H_2, the reduction of Pr^{4+} to Pr^{3+} was initiated at a significantly lower temperature than was the reduction of Ce^{4+}, and was accompanied by a 1.4 eV contraction in the separation between Ce and Pr M_5 EELS white

lines relative to the initial Ce^{4+}/Pr^{4+} separation (López-Cartes *et al.*, 2003). This result was later corroborated by precise defect analysis of 10PCO by Bishop *et al.* who employed DC conductivity measurements and thermogravimetric analysis to show that the Pr redox couple is active under significantly less reducing conditions than that of Ce (Bishop *et al.*, 2011).

As a first step to detecting tetravalent Pr in the specimen, Ce and Pr M_{45} core-loss spectra, shown in Figure 5.3, were acquired serially with a static electron probe to ensure reduction of Pr^{4+} to Pr^{3+} via electron beam-induced ionization. The Ce and Pr M_{45} multiplet structures are well-characterized under +3 and +4 valence conditions, and it is thus straightforward to identify spectral features attributable to both tri- and tetravalent cations from comparison with published electron energy-loss (López-Cartes *et al.*, 2003; Turner *et al.*, 2011; Niu *et al.*, 2014) and X-ray absorption spectra (Sugar, Brewer, Kalkowski, Kaindl, & Paparazzo, 1985; Kalkowski *et al.*, 1988; Vavassori, Duo, Chiaia, Qvarford, & Lindau, 1995; Mullins *et al.*, 1998; Heyraud *et al.*, 2013). See Methods chapter and Chapter 4 for further discussion on EELS fine structure.

A representative spectrum is presented in Figure 5.3 ('Reduced'), clearly resolving a low-energy shoulder on the Pr M_4 edge at about 950 eV consistent with trivalent Pr (Sugar *et al.*, 1985). Simultaneously the Ce M_{45} edge exhibits features consistent with mixed +4/+3 valence: The most intense peaks in each multiplet, as well as associated satellite peaks (approximately 5 eV greater in energy) are the primary white line features for Ce^{4+} (Kalkowski *et al.*, 1988); whereas the clearly resolved lower-energy side peaks on the Ce white lines are the primary features of the Ce^{3+} white lines (Sugar *et al.*, 1985).

From this spectrum the M_5 peak separation between Ce^{4+} and Pr^{3+} was measured as 46.2 ± 0.1 eV (from each centroid's most intense channel; cited error is one channel (i.e. the dispersion)). Thus, detection of the Pr M_5 white line at greater than 46.2 eV above the Ce^{4+} peak would confirm the presence of Pr^{4+}.

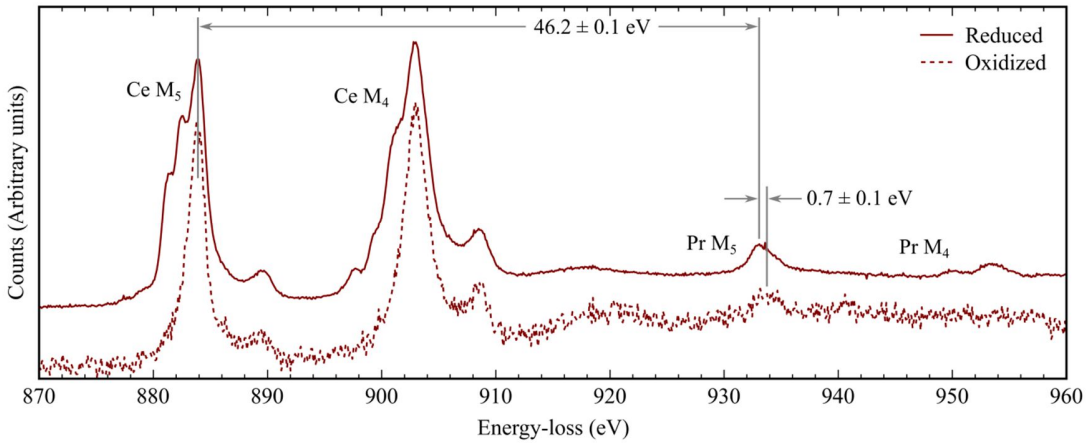

Figure 5.3. Core-Loss EELS from 10PCO. ('Reduced') Sum of 30 Ce/Pr M_{45} core-loss spectra (5 s acquisition) showing mixed-valence Ce and trivalent Pr. ('Oxidized') Single spectrum (10 s acquisition) showing Ce^{4+} and Pr^{y+}, with $4 > y \geq 3$. The 0.7 eV Pr M_5 edge shift verified the presence of Pr^{4+}. 60 kV Nion UltraSTEM100, ASU.

Figure 5.3 also shows a spectrum ('Oxidized') recorded with lower electron dose wherein only Ce^{4+} was present. Despite relatively poor signal-to-noise, the Pr M_5 edge centroid position was readily accessible for measurement in 11 spectra, and it was thus concluded that Pr was predominantly tetravalent in the specimen.

5.3.2 Spectral Modelling

The experimental valence-loss spectrum (Figure 5.2) was characterized following the joint density-of-states (DOS) approximation for the EELS single scattering distribution described by Egerton (2011). This assumes that to a first approximation, the variations in

spectral intensity over a small range of energy-loss are associated with variations in the valence and conduction band DOS. This was employed to determine the location and width of the unoccupied Pr 4*f* inter-band state. The single scattering intensity, $J^1(E)$, a function of energy loss, E, which is related to a solid's band structure via the joint DOS, $N(E)$, according to Equation (5.1). $N(E)$ is the convolution of the initial (occupied) projected DOS in the valence band, $\rho_{VB}(E)$ with the final (unoccupied) projected DOS in the conduction band, $\rho_{CB}(E)$ as

$$J^1(E) \propto N(E) \propto \rho_{VB}(E) * \rho_{CB}(E) \tag{5.1}$$

For EELS collection angles employed here, the convolution is dominated by contributions that follow the dipole selection rule between initial and final states. The single scattering distribution approximates the intensity variation around the bandgap region of the EELS spectrum because particles analyzed were thinner than the electron inelastic mean free path for a 60 kV electron in CeO_2 of ~45 nm. This value was estimated from Equation (5.2) in (Egerton, 2011) assuming a mean atomic number for CeO_2 of 24. (This is likely a slight overestimate, as the mean free path increases to ~55 nm if the value of the empirical parameter E_m used in the calculation is taken to be closer to that of the other oxides (Al_2O_3, NiO, SiO_2) listed in Table (5.2) of the same text.) Furthermore, the valence-to-conduction band excitations responsible for the conduction band onset in the energy-loss spectrum are not significantly affected by plural scattering. We assumed electronic transitions into the unoccupied Pr 4*f* level were dipole-allowed in the same manner as transitions into Ce 4*f* final states.

Figure 5.4a shows symmetry-projected DOS for CeO_2 calculated by Dholabhai *et al.* (2010), and adapted by shifting the unoccupied DOS to higher energy to match the band gap measurement described in Figure 5.2. To model the PCO single-scattering distribution, an unoccupied inter-band Pr 4*f* state was included. This inter-band state was approximated as Gaussian, with the centroid position and width (FWHM) varied until principal features in the single-scattering distribution matched the experimental spectrum. In particular, the inter-band plateau onset energy, plateau width, conduction band onset energy and slope were used as optimization parameters.

Figure 5.4b presents the convolution of the projected DOS in Figure 5.4a, and illustrates that electronic transitions from occupied *p*- and *d*-type valence band levels into the unoccupied Pr 4*f* impurity band produce an inter-band plateau. The single-scattering distribution is the sum of the convolved projected DOS, convolved again with a 25 meV (FWHM) Gaussian broadening function representing the instrument response function.

The simulated spectra for CeO_2 and PCO are plotted with the experimental 10PCO spectrum in Figure 5.4c. The model CeO_2 distribution lacks the inter-band plateau, instead exhibiting a sharp intensity increase at approximately 3.2 eV, corresponding to the conduction band onset energy of CeO_2 (Marabelli & Wachter, 1987; Bueno *et al.*, 1997; Goubin *et al.*, 2004). (In this approach we ignore excitonic interactions but Figure 5.4 suggests they are not a large effect for this case.) The model PCO distribution tracks the plateau and conduction band onset in the experimental 10PCO EELS data closely, showing that the Pr impurity DOS is a sharp Gaussian function with energy approximately 1.4 eV above the top of the valence band edge, and approximate width of 0.1 eV (FWHM).

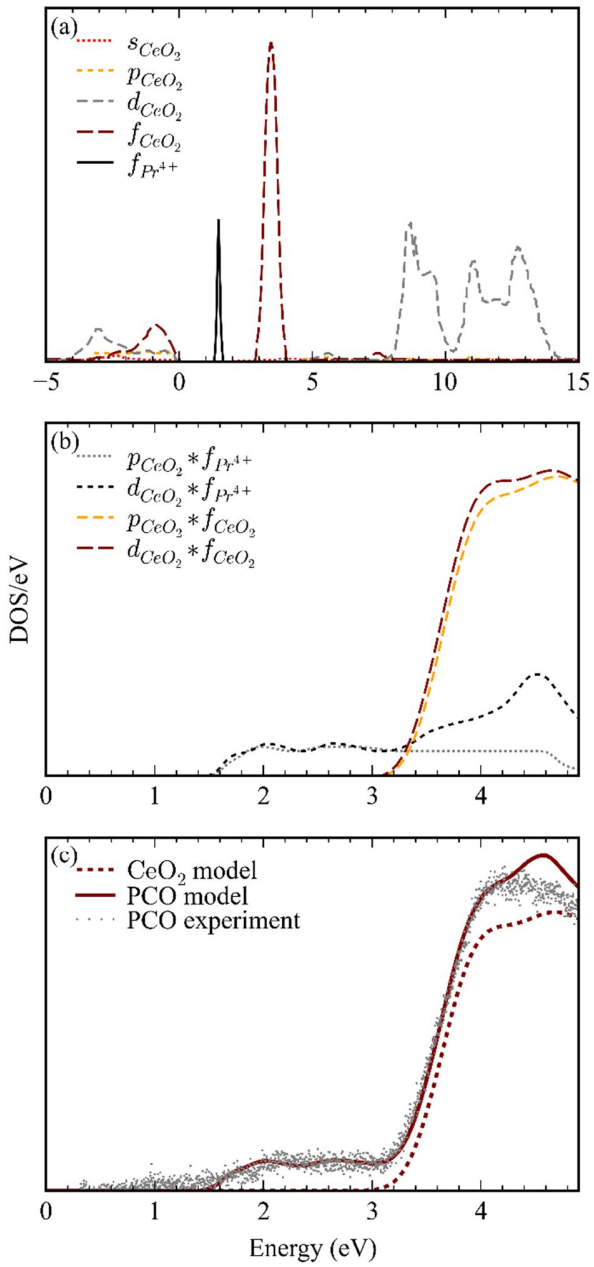

Figure 5.4. DOS Modeling of 10PCO. (a) Symmetry-projected DOS for CeO_2 (Dholabhai *et al.*, 2010) with unoccupied states shifted to match experimental bandgap measurement, and additional unoccupied Pr 4*f* inter-band state. (0 eV represents the valence band maximum.) (b) Convolution of projected DOS. (c) Single-scattering distributions calculated of model CeO_2 and PCO with overlaid 10PCO EELS.

Furthermore, the ratio of integrated Pr and Ce 4*f* DOS, ($Pr\ 4f_{DOS}/Ce\ 4f_{DOS}$), is 0.10—approximately the solid's nominal cation composition ratio, $C_{Pr}/C_{Ce} = 0.11$, suggesting that the spectral intensity of the interband state may vary linearly with Pr concentration in this particular case; this is under current investigation. A summary of the experimentally determined PCO electronic structure and model fitting parameters is given in Figure 5.5. Changes in the optical properties of 10PCO with oxidation state changes are also shown in Figure 5.5. As shown in the inset of Figure 5.5a, stoichiometric 10PCO with the Pr 4*f* impurity band unoccupied results in a deep red solid due to strong absorption via optical excitation into the Pr impurity band. The color is consistent with transition from the valence band into the Pr^{4+} state determined by EELS (energy difference 1.4 ± 0.3 eV as seen in Figure 5.5).

Immediately following reduction under flowing H_2, the 10PCO nanoparticles appeared orange in color due to the presence of Pr^{3+}, which results from charge transfer resulting from oxygen vacancy formation. This yields a partially filled Pr 4*f* impurity level (shown partially shaded), and color change implying an increase of approximately 0.3 eV in the energy of the Pr 4*f* state. The energy increase results from the increase nuclear screening of the 4*f* level due to the additional electron density associated with the Pr^{3+} cation. (Direct EELS measurements were not performed on the reduced sample because it re-oxidized rapidly following exposure to atmosphere at room temperature.) Our analysis is consistent with reports of the 10PCO optical band gap derived from optical transmission measurements and defect analysis (Bishop *et al.*, 2011; J. J. Kim *et al.*, 2012, 2014).

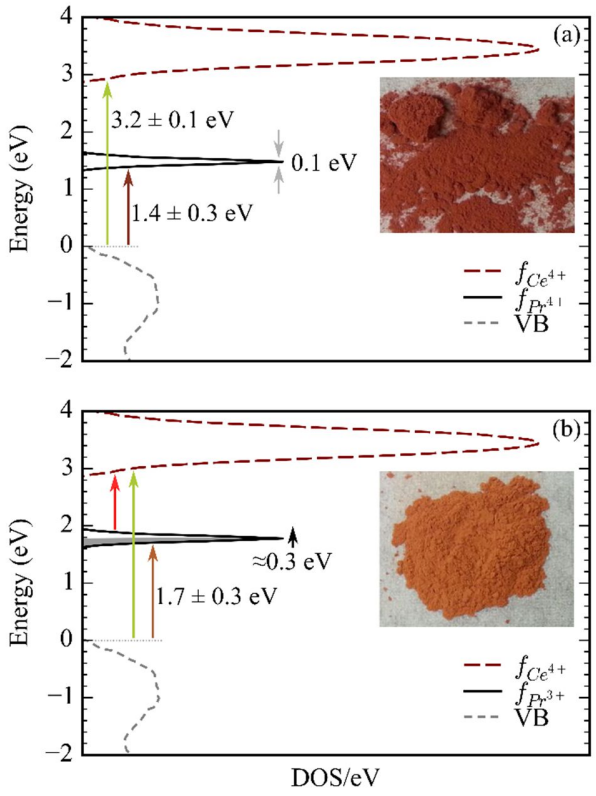

Figure 5.5. Proposed DOS for Oxidized and Reduced 10PCO. (a) DOS of oxidized PCO showing valence-to-conduction and valence-to-impurity transitions (labelled arrows). Inset is an image of 10PCO following heating in air, wherein particles are assumed stoichiometric, with Pr 4*f* impurity band unoccupied (both Ce and Pr are tetravalent). The valence band ('VB') is the sum of occupied symmetry-projected DOS (Figure 5.4a). (b) Analogous to (a) for reduced PCO wherein Ce is +4 and Pr is a mix of Pr^{4+} and Pr^{3+}. Transitions from Pr impurity into Ce conduction band are optically forbidden (red arrow) *f-f* transitions (Bishop *et al.*, 2011; J. J. Kim *et al.*, 2014). Inset image of reduced 10PCO particles following heating in H_2. An approximately + 0.3 eV shift (black arrow) is assumed from the observed color change upon Pr^{4+} reduction.

5.4 Summary

High spatial and energy resolution monochromated EELS has been employed to detect a state within the bandgap of ~30 nm nanoparticles of 10PCO. Quantitative analysis of the spectra showed that the inter-band state is associated with Pr^{4+} 4*f* levels, has a width of about 0.1 eV, and is located 1.4 eV above the top of the valence band. The strength of

the Pr 4*f* DOS relative to the Ce 4*f* DOS scales with the Pr/Ce concentration and is about 0.1. Population and de-population of this state gives rise to color changes in the material attributed to an energy level shift of the impurity state upon population of about +0.3 eV. The ultra-high energy resolution STEM EELS allows interband states to be probed with high spatial resolution and should be applicable to other systems where nanocharacterization is required such as grain boundaries, dislocations and precipitates.

The application of this technique to grain boundaries in a sintered solid solution is the subject of an ongoing study, and will not be included in this dissertation. The subsequent chapter describes an alternative method for accessing the charge transport properties of PGCO grain boundaries based on the cation compositional variability of grain boundaries in PGCO, and correlation with electrical conductivity.

6 The Distribution of Grain Boundary Composition and Conductivity

6.1 Motivation

The mean grain boundary Pr concentration PGCO was estimated in Chapter 4 to be 16 mole%, a factor of four increase in Pr content relative to the grain. Strong grain boundary Pr enrichment, and low migration activation energy, led to speculation that Pr-enriched grain boundaries were facilitating electronic conduction via Pr polaron hopping. This analysis has been extended using a novel correlated STEM approach described below.

Given the rich diversity in grain boundary types (e.g. Figure 1.15), and the complex interplay between atomic structure, composition, and chemistry at the atomic and nanoscale, there is very considerable opportunity to elucidate fundamental science and performance optimization of grain boundaries. Hence, studies should rely on grain boundary datasets correlated across many length scales, with the aim of generalizing high spatial resolution observations to an entire grain boundary population. This should facilitate bottom-up design of grain boundaries with optimized properties, which remains a considerable challenge. By combining suitable modelling approaches with experimental measurement over different length scales, it becomes possible to extend estimates of the electrical properties of individual grain boundaries to the entire population.

Here a novel correlated approach was employed combining precession-enhanced nanodiffraction (PEND) orientation imaging and EELS in an AC-STEM to elucidate the grain boundary transport properties in the PGCO system described in Chapter 4. An outstanding advantage of PEND is the ability to directly couple grain boundary character

analysis with atomic and nanoscale S/TEM characterization techniques, such as imaging and/or spectroscopy. In this chapter, grain boundary transport properties characterized in Chapter 4 are interpreted based on extended AC-STEM EELS characterization of solute segregation. These measurements were generalized to the entire PGCO grain boundary population based on the microscopic grain boundary character determined using PEND orientation imaging. Experimental data were simulated using a thermodynamic modeling framework developed for concentrated ceria solutions. The parameters in the model were adjusted to match the experimentally determined cation distribution and the model then allows the oxygen vacancy distribution and space charge potential of the grain boundary population to be determined. By combining the oxygen vacancy distribution with a composition dependent migration enthalpy, it should be possible to estimate the conductivity variation between different grain boundaries.

6.2 Experimental

The PGCO TEM specimen described in Chapter 4 was used for this work; specimen preparation is described in §4.2.

6.2.1 Precession-enhanced nanodiffraction (PEND)

The PGCO grain boundary character was assessed via misorientation angle distribution (MAD), which was computed from grain orientation data acquired in the TEM using a 200 kV JEOL ARM200F equipped with an ASTAR PEND system (NanoMegas, USA). PEND is detailed in §2.3.8. Serial diffraction patterns were acquired at 5 nm

distance intervals, and pattern indexing to fluorite CeO_2 ($Fm\bar{3}m$) was performed using AppFive TopSpin software. PEND data were exported from TopSpin as Euler angles and read into the EDAX TSL OIM5 software for processing and generation of misorientation angle and coincident site lattice distributions.

6.2.2 TEM

The microscope mentioned in the previous section was also used to perform line scans across grain boundaries to access local composition and chemistry variations. Three or four measurements were typically performed at each grain boundary, from which the mean grain boundary cation concentrations (and standard deviations) could be determined. To avoid specimen tilt artifacts, only grain boundaries deemed to be nearly parallel to the optic axis were analyzed. The convergence and collection angles were 20 mrad and 42 mrad, respectively, and spectrometer dispersions of 250 meV/channel or 500 meV/channel were used. Ce, Pr and Gd M_{45} energy-loss spectra were acquired and processed using the background fitting windows and background subtraction procedures specified below in

Table 6.1. In this case an overlap correction was made for the Gd M_{45} edge, which overlaps the Ce M_3 peak at 1185 eV. Using the symbols in Figure 4.7, the correction factor, $(A_2/A_1)^{CeO_2\ Ref.}$, in Equation (4.1) was 0.08, and A_1 is integrated intensity in Ce M_{45} window, and A_2 is the integrated intensity in the Gd M_{45} window.

Table 6.1. EELS Spectral Processing Windows. K-factors given in Table 4.1

EELS edge	Background fitting procedure	Background fitting window(s) (eV)	Signal integration window (eV)
Ce M_{45}	Inverse power-law extrapolation	795 – 870	870 – 920
Pr M_{45}	Inverse power-law two-window interpolation	920 – 925, 1150 – 1170	925 – 965
Gd M_{45}	Inverse power-law extrapolation + overlap correction	1070 – 1160	1170 – 1225

6.3 Results & Discussion

6.3.1 Grain Boundary Character

Misorientation data acquired from approximately 150 grain boundaries in the TEM specimen were used to generate a grain boundary misorientation angle distribution (MAD). Figure 6.1a shows a TEM image of the specimen with grain orientation data (inverse pole figure) overlaid. Each grain is colored to indicate the crystallographic direction parallel to the electron optic axis according to the inset color coded stereographic triangle. Four such orientation maps were acquired in total. The MAD is presented in Figure 6.1b, plotted with the Mackenzian distribution (described in §3.3.3). Considerable scatter in the data is attributed to poor counting statistics, though the experimental MAD fits reasonably well to

the Mackenzian distribution, suggesting that the PGCO here exhibits a random grain orientation distribution. This is consistent with the $Ca_xCe_{1-x}O_{2-x-\delta}$ system described in Chapter 3, as well as previous SEM EBSD work on zirconia solutions with similar thermal history (Helmick *et al.*, 2011).

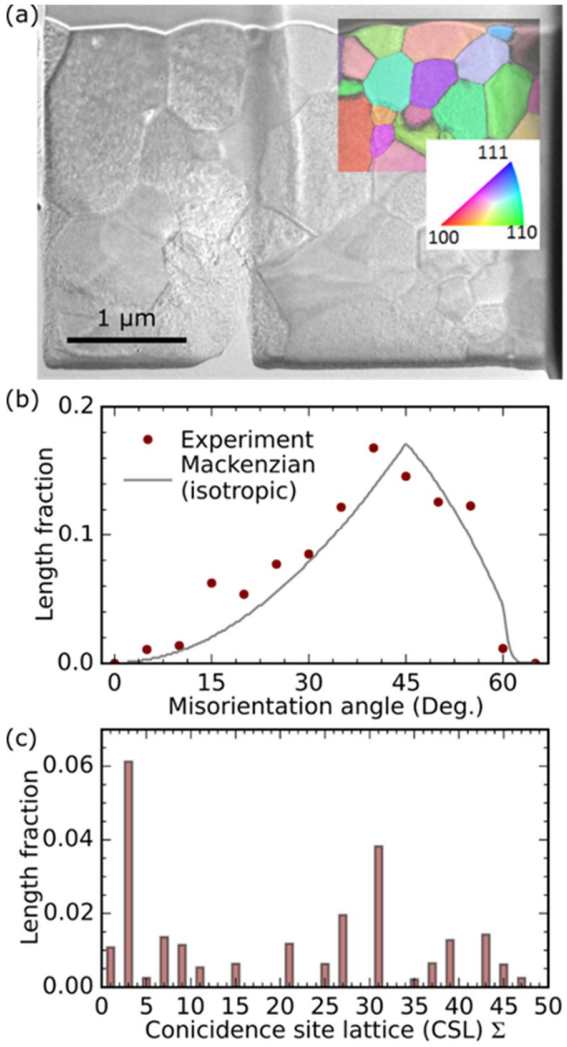

Figure 6.1. Grain Boundary Character Analysis of PGCO. (a) Bright field TEM image of PGCO with overlaid inverse pole figure; grain orientation is indicated via color code corresponding to inset stereographic triangle. (b) Misorientation angle distribution and Mackenzian distribution. (c) Length fraction distribution of coincident site lattice grain boundaries. 200 kV JEOL ARM200F S/TEM with ASTAR, ASU.

Figure 6.1c shows the length fraction of various coincidence site lattice (CSL) grain boundaries (Brandon, 1966; King & Shekhar, 2006). Though Σ3 grain boundaries are the most prevalent, representing about 6 % of the total length, it is strongly emphasized that overall, only about 23 % of the total length was associated with CSL-type grain boundaries. This suggests that in this case, high spatial resolution grain boundary studies should focus predominantly on *non CSL-type* boundaries if they are to be more applicable to polycrystalline materials with random grain orientation.

6.3.2 Grain Boundary Composition via Targeted STEM EELS

With knowledge of the misorientation angle of each grain boundary, 12 were selected for compositional analysis based on their misorientation angle. The grain boundaries in this system were assumed to be free of intergranular amorphous phases based on the results of Chapter 4. In a few cases CSL type boundaries were observed, and the crystal structure of each grain was clearly visible within Ångstroms of the grain boundary. In these instances, there was no evidence for an intergranular amorphous material.

Figure 6.2d-f presents spatially resolved EELS data corresponding to those in Figure 6.2a-c. Spectra acquired at grain boundaries show a decrease in the Ce edge intensity with corresponding increase in both Pr and Gd edges. In some cases, e.g. Figure 6.2d, the relative peak intensity of the Ce M_4 and M_5 peaks was found to change, indicative of the commonly observed valence change of Ce^{4+} to Ce^{3+} at many ceria grain boundaries (Browning *et al.*, 2004; Bowman *et al.*, 2015). This valence change is associated with oxygen deficiency caused by lattice discontinuity at the grain boundary (S. Kim *et al.*,

2010). Variability in the chemical properties of grain boundaries reiterates the need to characterize a representative number of grain boundaries to assess their influence on macroscopic properties. Grain boundary cation concentration profiles are presented in Figure 6.2g-i. The mean width of the concentration profiles was determined to be 2.1 ± 0.6 nm (FWHM), consistent with widths measured in Chapters 3 and 4, as well as previous experimental and theoretical studies (Browning *et al.*, 2004; H. B. Lee, Prinz, & Cai, 2013).

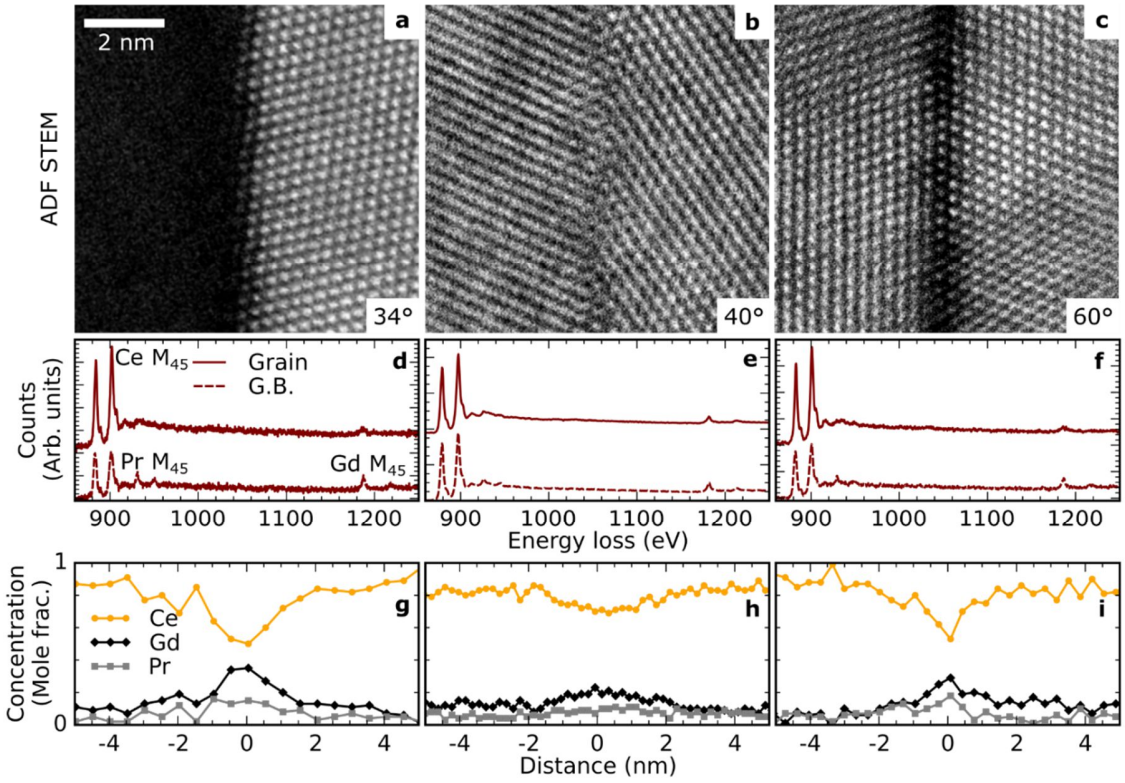

Figure 6.2. AC-STEM and EELS of PGCO. (a-c) AC-STEM ADF images of various PGCO grain boundaries. (d-f) EELS acquired in grains (> 5 nm from grain boundary) and at the grain boundary ('G.B.') corresponding to a-c. (g-i) Cation concentration profiles determined from EELS of grain boundaries in a-c; the grain boundary is located at 0 nm. 200 kV JEOL ARM200F STEM, ASU.

6.3.3 Correlating Grain Boundary Character and Composition

The cation concentration of each grain boundary is plotted as a function of misorientation angle in Figure 6.3a. The grain concentration is approximately the nominal value for all misorientation angles (see Table 6.2). All grain boundaries are solute-enriched and Ce-deficient, with the degree of solute segregation increasing with misorientation angle. Solute segregation to grain boundaries is thought to minimize their high energy relative to adjacent grains (Browning *et al.*, 2004), and there is evidence from thermal groove measurements indicating that grain boundary energy tends to increase with misorientation angle (Saylor, Morawiec, Adams, & Rohrer, 2000). This lends credence to the notion that the observed solute segregation—which increases with misorientation angle, is associated with minimization of the grain boundary energy. Hence, the misorientation angle may represent a tunable parameter influencing grain boundary composition, and presumably properties. To generalize these targeted composition data to the entire grain boundary population, a linear function—the so-called cation concentration function (CCF), was fit to the measured grain boundary concentrations in Figure 6.3a. The CCF was related to the length fraction distribution in Figure 6.1b (a.k.a. the misorientation angle distribution (MAD)) via misorientation angle to yield the concentration length fraction distribution (CLFD) which describes the length fraction of grain boundaries with a particular cation concentration. This is presented in Figure 6.3b as a bar chart, with grain boundary length binned according to cation concentration. The distribution for each cation is peaked and skewed slightly, resembling the shape of the MAD. For example, this approach predicts that grain boundaries with 10 – 15 mole% Pr are the most prevalent in PGCO (see the tallest shaded bar in Figure 6.3b).

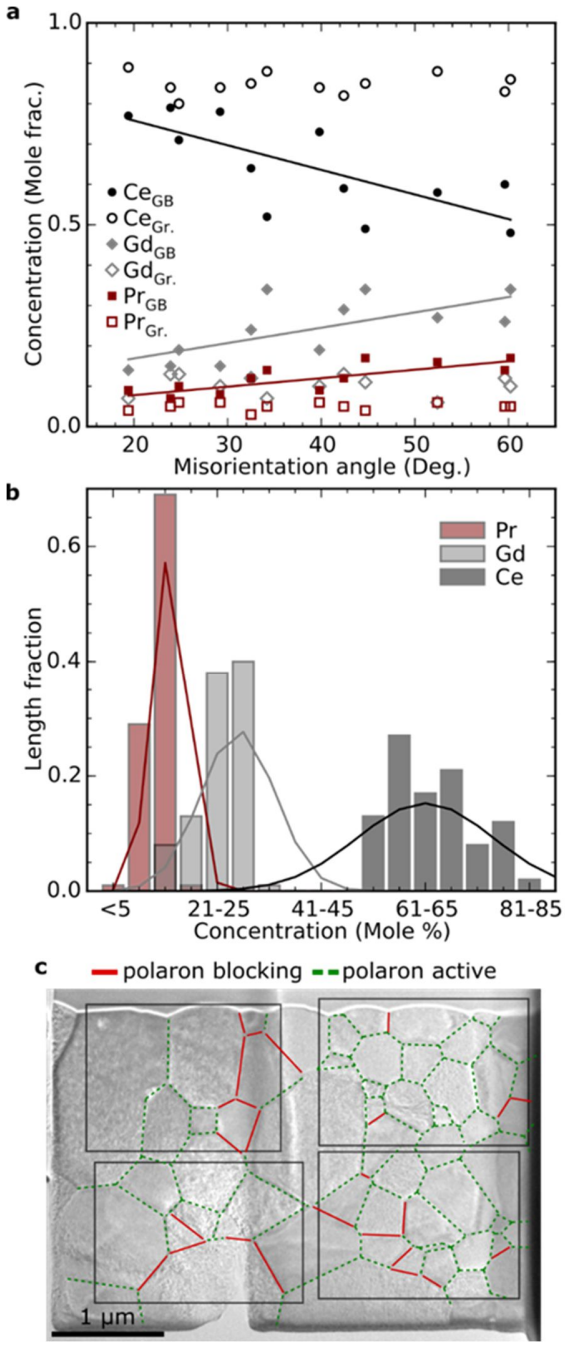

Figure 6.3. Compositional Distribution of PGCO Grain Boundaries. (a) Grain ('Gr.') and grain boundary ('GB') cation concentrations, with linear fits (see Table 6.2 for linear coefficients). (b) Concentration length fraction distributions (CLFD; bar chart) overlaid by solid curves showing CLFDs computed assuming a normal distribution in grain boundary composition. (c) Bright field TEM image of PGCO with regions analyzed using PEND outlined. Grain boundary segments are highlighted to indicate predicted polaron transport behavior based on their Pr concentration: 'Polaron active' grain boundaries have [Pr] ≥ 10 mole%, and 'polaron blocking boundaries have [Pr] < 10 mole%.

This novel approach offers a significant improvement in the understanding of the grain boundary composition distribution compared to random sampling, which assumes a normal distribution in the grain boundary concentration. Random sampling omits any influence of the grain boundary character on composition, and predicts a symmetric CLFD (or pseudo-symmetric, depending on the composition range used for binning). This is shown in Figure 6.3b, in which CLFDs generated assuming a normal distribution are overlaid; mean values and standard deviations are in Table 6.2.

Table 6.2. Grain and Grain Boundary Composition Data for PGCO. Grain and grain boundary cation concentrations assuming normal distribution, and linear coefficients describing the dependence of grain boundary cation concentration on misorientation angle according to $[Cation]_{GB} = A \cdot (Misorientation\ angle) + B$. Mean concentration and standard deviation were determined from 12 grain boundaries.

	Ce	Gd	Pr
Nominal concentration (mole%)	85	11	4
Grain concentration (mole%)	85 ± 3	10 ± 3	5 ± 1
Grain boundary concentration *Normal distribution (mole%)	62 ± 10	26 ± 7	13 ± 3
Linear coefficient A $\times 10^{-3}$ (Mole fraction/degree)	-6.1	3.8	2.1
Linear coefficient B $\times 10^{-2}$ (Mole fraction)	88	9.3	3.6

6.3.4 Grain Boundary Polaron Hopping and Ionic Conductivity

According to Figure 6.3b about 70 % of the grain boundary length exhibits Pr concentration greater than 10 mole%, which is the concentration threshold for activating Pr polaron hopping in ceria (Bishop *et al.*, 2012). Figure 6.3c illustrates this in real space, showing polaron-active and polaron-blocking grain boundary segments, which should aid in development of future percolation transport models. Furthermore, localization of polaron conduction at grain boundaries presents interesting possibilities to engineer microstructures to tune the overall transport mechanism and macroscopic electrical properties of polycrystalline Pr-ceria solutions.

It is likely that Pr-enriched grain boundaries undergo dynamic chemical polarizations under alternating bias (e.g. during AC impedance spectroscopy), during which Pr polarons redistribute within the *compositionally relevant region* of the grain boundary (the region with Pr concentration sufficient to facilitate polaron hopping). This dynamic polaron redistribution is illustrated schematically in Figure 6.4 and gives rise to higher grain boundary conductivity and lower effective migration activation energy (see Chapter 4). However, Pr concentration decreases quickly moving into the grain (Figure 6.2g-i), and the compositional requirement for Pr polaron hopping is thus not satisfied. Under DC conditions—those technically relevant for solid oxide cells and oxygen conduction membranes, Pr polaron conduction is not expected to persist following the initial grain boundary chemical polarization (shown in. Figure 6.4). Polaron conduction could occur via percolation along Pr-enriched grain boundaries; however, as grain boundary conductivity is several orders of magnitude lower than grain conductivity, this

conduction pathway is likely negligible, as discussed in §2.2.1 (Haile *et al.*, 1998). Rather, under DC conditions, oxygen ionic conductivity is expected to be the dominant conduction mechanism, with grain boundary conductivity thus governed by space charge effects (§1.5.2).

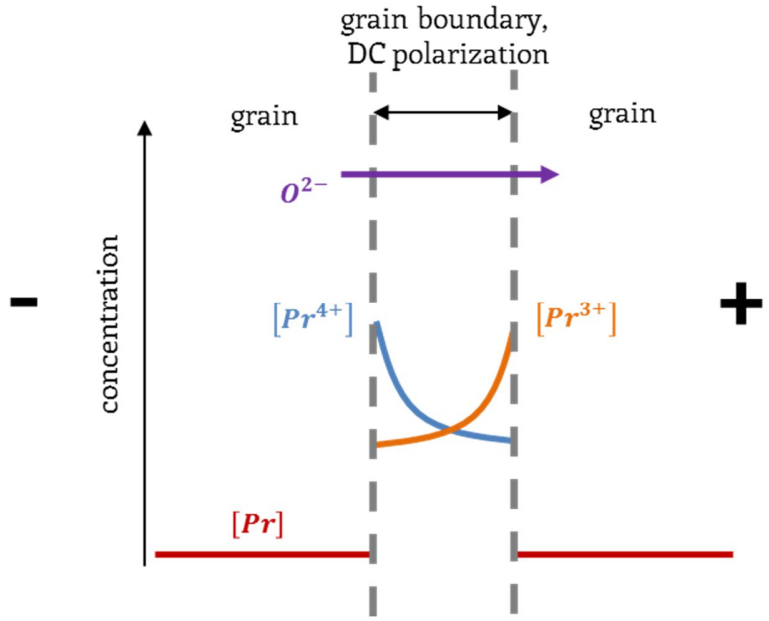

Figure 6.4. Schematic Illustrating Grain Boundary Chemical Polarization. Under an applied electric field Pr^{3+} polarons (Pr'_{Pr}) redistribute within the grain boundary, but are blocked by grains that cannot facilitate polaron hopping due to insufficient Pr concentration.

As described in the introduction, conventional grain boundary space charge theory relies on the assumption of dilute solute concentrations (i.e. < 1 mole%), enabling the use of ideal solution thermodynamic models incorporating non-interacting point defects, as in Equation (1.8) (S. Kim & Maier, 2002; Tuller & Bishop, 2011). However, typical ceria solutions in the literature contain 5 – 20 mole% solute (Esposito and Traversa 2008; Avila-Paredes *et al.* 2009; Rupp *et al.* 2014). Hence, as was discussed in the Introduction §1.5.2, Mebane and De Souza have recently developed a so-called Poisson-Cahn computational

framework to predict point defect distributions in both dilute and concentrated $Gd_xCe_{1-x}O_{2-x/2-\delta}$ (Mebane & De Souza, 2015). In an effort to investigate the variability in ionic conductivity of grain boundaries in PGCO, this computational framework was employed following minor modifications to include Pr solutes and grain boundary misorientation effects. The framework uses an adaptive finite-element solver to compute the effective electrochemical potentials in Equation (1.20), and generates a solute concentration profile, a space charge potential profile and an oxygen vacancy concentration profile. The framework was implemented in MatLab using the code provided in supplementary information by the origin authors.

The goal of the simulation was to replicate grain boundary solute distributions measured using EELS, while simultaneous predicting the distribution of space charge potential and oxygen vacancy concentration profiles. The physical and energetic constants reported in their work (for $Gd_xCe_{1-x}O_{2-x/2-\delta}$) corresponding to the terms in Equation (1.20) were used for this simulation, with several constants adjusted manually to ensure that the width of the simulated solute segregation profiles matched those determined experimentally. Following the approach of the original authors, values of the solute-vacancy interaction energy, f_{av}, oxygen vacancy segregation energy, f_v^{GB}, oxygen vacancy gradient energy coefficient, β_v, and the solute gradient energy coefficient, β_a, were adjusted to give the best experimental fit, and are provided in Table 6.3 along with the original published values. In fact, regarding f_{av}, in order to verify their model, the authors mention that they had to use a value that was *less negative* than one calculated using DFT (by a factor of ~4), so it is not unreasonable to use a *more negative* value than they, as has been done here.

Table 6.3. Constants Used for Poisson-Cahn Simulation. The effect of varying each of these parameter is provided in the table below.

Symbol (unit)	Mebane and De Souza	This work	Name: *Effect of increasing this constant*
f_{av} (J mole^{-1})	$-7 \cdot 10^3$	$-41 \cdot 10^3$	Solute-vacancy interaction energy: *Increases the maximum of solute segregation profile*
f_v^{GB} (J mole^{-1})	$-2 \cdot 10^5$	$-2.2 \cdot 10^5$	Vacancy segregation energy: *Lowers vacancy profile minimum*
β_v (J mole^{-1}-m^{-1})	10^{-9}	$0.5 \cdot 10^{-9}$	Vacancy gradient energy coefficient: *Decreases the maximum of space charge potential*
β_a (J mole^{-1}-m^{-1})	10^{-8}	$0.6 \cdot 10^{-8}$	Vacancy gradient energy coefficient: *Increases the width of segregation profile*
N_{GB} (mole m^{-2})	$2.6 \cdot 10^{-5}$ *Twice the CeO_2 (111) termination*	$\leq 2.6 \cdot 10^{-5}$	Specific oxygen site density: *Increases the maximum of solute segregation*

The variability in grain boundary misorientation angle was simulated by systematically changing the value of the input parameter corresponding to the area-specific site density of oxygen ions at the grain boundary, N_{GB}. This value defines the number of oxygen lattice positions at the grain boundary, and was taken by Mebane and De Souza to be twice that of the FCC close-packed (111) plane (i.e. in CeO_2). As this physically represents the maximum number of possible interfacial sites, the influence of misorientation angle was simulated by systematically *decreasing* N_{GB}. Lacking knowledge of a more sophisticated functional relationship, N_{GB} was assumed to be proportional to misorientation angle, though it is unlikely that the dependence is truly linear.

The electrochemical potential used in this framework is temperature dependent according to Equation (1.19), so a simulation temperature was required. Because the defect distribution measured with EELS reflects the result of sintering, the solute concentration profiles detected should be those frozen during cooling. According to linear shrinkage data for $Gd_{0.1}Ce_{0.9}O_{1.95-\delta}$ sintered in air, there is negligible sintering via mass diffusion below about 700 °C (Ni *et al.*, 2015), thus the solute concentration detected here using EELS is assumed to be that which existed in the material at a temperature just above 700 °C, when it was frozen in. Hence the simulation temperature was selected to be 800 °C.

As the framework was developed for ceria solutions with trivalent Gd solutes, the input parameter that defines the nominal solute concentration, and thus oxygen vacancy concentration (via charge neutrality) had to be adjusted to reflect the presence of tetravalent Pr ions in solution (Pr is a mixed-valence solute). PGCO has a nominal Pr concentration of 4 mole%, and it is known based on the fact that polaron conductivity was measured at grain boundaries that Pr must exist in solution as a mix of tri- and tetravalent Pr. Small polaron hopping requires nearby Pr^{3+} and Pr^{4+} ions, and is maximum when the concentrations of tri- and tetravalent Pr are equal (§4.3.2, (Bishop *et al.*, 2011)). Hence, it was assumed that the concentration of trivalent Pr ions was half of the nominal concentration, thus the overall nominal concentration of trivalent solutes was assumed to be 13 mole% for the simulation (11 mole% from Gd^{3+} and 2 mole% from Pr^{3+}).

Figure 6.5a shows the predicted grain boundary solute segregation profiles, which exhibit a good fit to experimental data. The simulated area-specific oxygen site density, $N_{GB}^{Simulated}$, is expressed in terms of S, via $N_{GB}^{Simulated} = S \cdot N_{GB}$, which is the scalar

multiple applied to the site density of the CeO_2 close-packed plane, N_{GB} in Table 6.3. The widths (at half maximum) of the simulated profiles are provided in the legend, and are consistent with that measured using EELS. Experimental data are overlaid to demonstrate the fairly good fit of the model. The simulation captures the entire range of measured grain boundary solute concentrations and profile widths: At low angles the grain boundaries have an average solute concentration (Pr plus Gd) of ~25 mole%, which rises to ~40 mole% for the grain boundaries with high angles.

Figure 6.5b shows the oxygen vacancy distribution associated with each solute profile in Figure 6.5a, and indicates (inset) that the minimum in the vacancy profile varies with the grain boundary solute concentration ('$[A^{3+}]_{GB}$'). The vacancy profile shapes are consistent with those reported by Mebane and De Souza, and exhibit an asymptote-like feature at the grain boundary associated with the intrinsic oxygen deficiency of grain boundaries. A vacancy depletion region directly adjacent to the grain boundary interface is visible, with the minimum taken as the concentration indicated in the inset. Beyond that, there is an enrichment of vacancies.

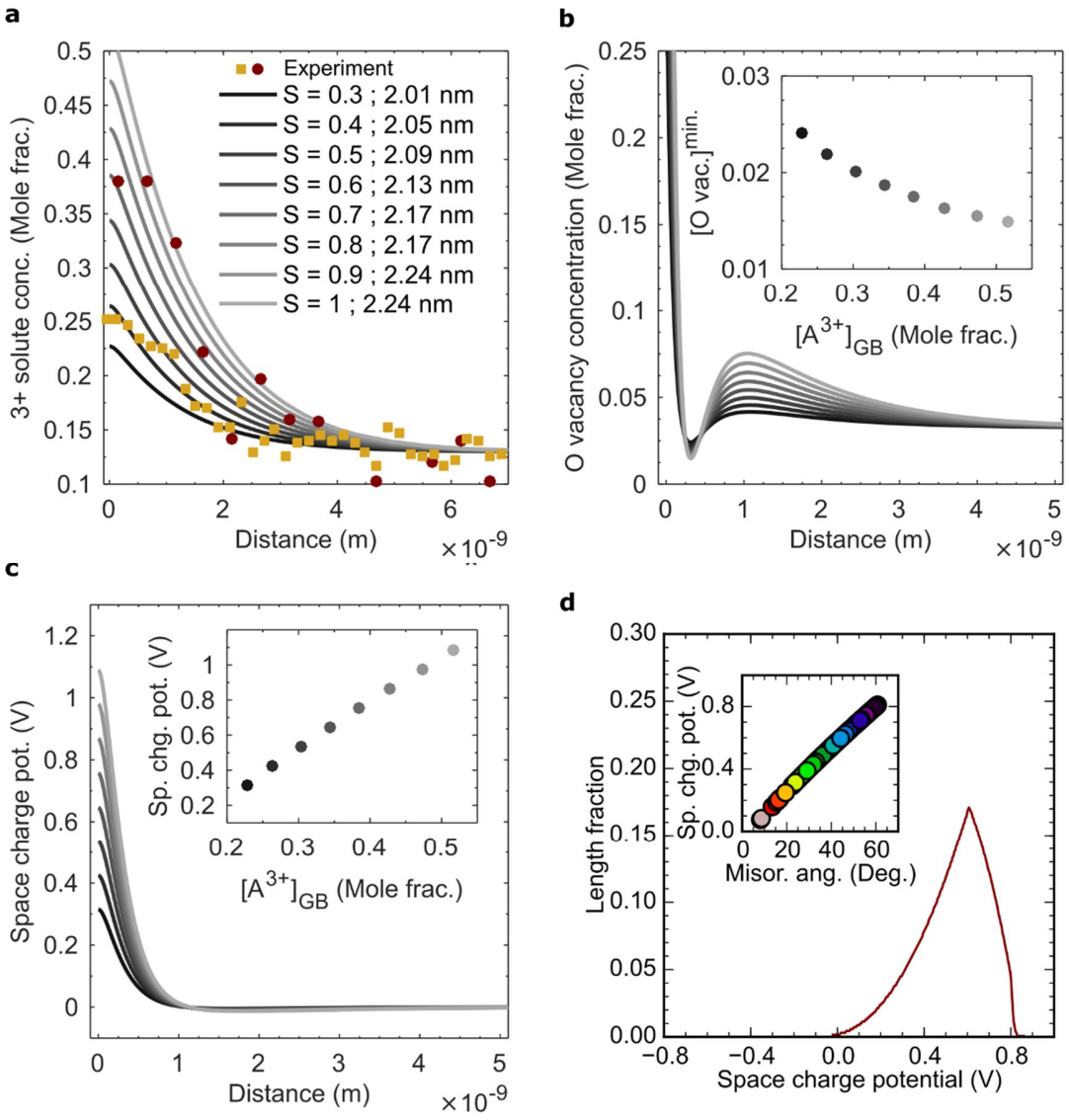

Figure 6.5. Grain Boundary Solute Segregation Simulation Results. (a) Simulated and experimentally measured grain boundary solute segregation profiles. The quantity S is the scalar by which N_{GB} (in Table 6.3) was multiplied for each simulation. (b) Oxygen vacancy distributions associated with solute distributions in (a). Inset are the minima in the oxygen vacancy concentration profiles for each solute concentration maximum in (a). (c) Grain boundary space charge potential distributions associated with (a) and (b); inset shows the relationship between space charge potential and grain boundary solute concentration. (d) Space charge potential distribution with inset showing the relationship between potential and misorientation angle. Inset marker colors correspond to the scale bar in Figure 6.6b.

Figure 6.5c shows the associated space charge potential profiles, with the inset indicating the relationship between space charge potential and solute segregation

maximum. The space charge potential (inset) was fit to a third order polynomial function of the solute concentration so it could be related to the misorientation angle distribution. The polynomial coefficients are provided in Table 6.4 The space charge potentials corresponding to the misorientation angles measured here vary from 0.0 V – 0.8 V, as shown in the space charge potential distribution in Figure 6.5d. The distribution is peaked around 0.6 V, indicating that about 60 % of grain boundaries exhibit this or lower space charge potentials. The space charge potential of polycrystalline Gd-ceria, determined using impedance spectroscopy, is often reported to be 0.2 – 0.9 V (Avila-Paredes *et al.*, 2009; Avila-Paredes & Kim, 2006; Tschöpe, Kilassonia, & Birringer, 2004). This may indicate that the grain boundary conductivity measured using impedance spectroscopy—a volume averaged measurement—may predominantly reflect the transport behavior of grain boundaries with the lowest space charge potential (i.e. the most conducting) in a given material.

Table 6.4. Polynomial Coefficients for Fits of Grain Boundary Properties. A third order polynomial was used to fit grain boundary potential and conductivity (relative to grain conductivity) according to $Y = A * [A_{GB}^{3+}]^3 + B * [A_{GB}^{3+}]^2 + C * [A_{GB}^{3+}] + D$.

Y	A	B	C	D
Space charge potential (V)	1.46	-2.54	3.92	$-4.62 \cdot 10^{-1}$
Grain boundary E_a (eV)	-10	7.71	0.17	0.63
$\frac{\sigma_v^{GB}}{\sigma_v^{Grain}}$	87.2	-65.7	-3.53	1.51

From knowledge of the grain boundary oxygen vacancy concentration, n_v (termed $[O\ vac.]^{min.}$ in Figure 6.5b), it was then possible to estimate the grain boundary ionic/vacancy conductivity, σ_v, defined as

$$\sigma_v = n_v \left[\frac{\sigma_0}{T}\right] exp\left(\frac{-E_a^v}{kT}\right) \tag{6.1}$$

Here the σ_0 is the conductivity pre-exponential, and is assumed to be constant. The solute-concentration-dependent activation energy for ionic migration (Figure 6.6a) was taken from literature on ionic conductivity derived from measurements of grain conductivity in $Sm_xCe_{1-x}O_{2-x/2-\delta}$ (Zhan *et al.*, 2001) and $Gd_xCe_{1-x}O_{2-x/2-\delta}$ (Kudo & Obayashi, 1976). Equation (6.2) relates the grain boundary and grain ionic conductivity

$$\frac{\sigma_v^{GB}}{\sigma_v^{Grain}} = \frac{n_v^{GB} exp\left(\frac{-E_a^{GB}}{kT}\right)}{n_v^{Grain} exp\left(\frac{-E_a^{Grain}}{kT}\right)} \tag{6.2}$$

where n_v^{GB} is the oxygen vacancy concentration derived from modeling EELS solute profiles (termed $[O\ vac.]^{min.}$ in Figure 6.5b), E_a^{GB} is the concentration-dependent activation energy from literature (Figure 6.6a), n_v^{Grain} is the nominal oxygen vacancy concentration of grains (fixed assuming charge neutrality), and E_a^{Grain} is the activation energy for ionic conductivity in the grain, which was measured using AC impedance spectroscopy (see Table 4.2). The conductivity ratio is plotted in Figure 6.6a, and indicates that the grain boundary conductivity decreases exponentially with grain boundary solute concentration.

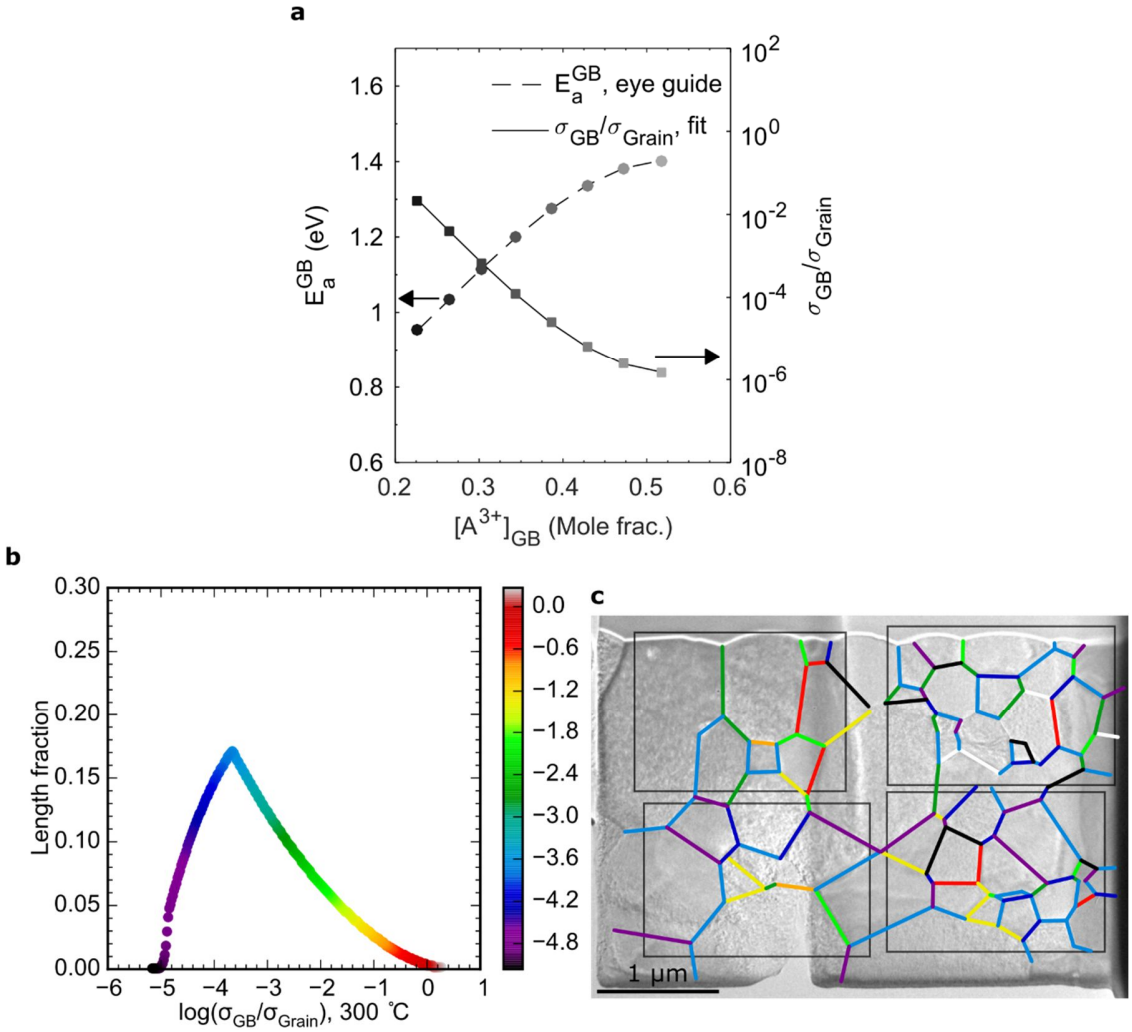

Figure 6.6. Grain Boundary Ionic Conductivity Distribution. (a) Effective migration activation energies, 'E_a^{GB}', taken from literature that were used to calculate $\sigma_{GB}/\sigma_{Grain}$. Ionic conductivity ratios calculated as a function of trivalent solute concentration at the grain boundary using Equation (6.2). (b) Grain boundary ionic conductivity distribution color-coded according to the associated scale bar at right, which gives the exponent given along the x-axis. (c) Bright field TEM image with grain boundary segments color-coded to indicate ionic conductivity in accordance with scale bar at left.

Again, a polynomial was used to fit the conductivity ratio with a function of solute concentration (see Table 6.4), making it possible to relate it to misorientation angle. A grain boundary ionic conductivity distribution that indicates the prevalence of grain boundaries of a given ionic conductivity could then be generated, Figure 6.6b. The peak of the

distribution is located around 10^{-4}, indicating that the plurality of grain boundaries exhibits ionic conductivity that is four orders of magnitude lower than that of grains. This distribution is represented in real space via color-coded grain boundary segments overlaid on a bright field TEM image of the PGCO TEM specimen in Figure 6.6c.

The average value of the grain boundary conductivity divided by the grain conductivity is reasonable, but the trend in grain boundary conductivity with grain boundary solute concentration is not consistent with experimental observation. Figure 6.6a suggests that the grain boundary activation energy increases with increasing solute concentration. However, the work in chapter 4 with Ca solutes shows the opposite behavior—namely that the grain boundary activation energy falls with increasing solute concentration at the grain boundary. Other experimental work on the variation in grain boundary activation energy with nominal solute concentration also implies that the grain boundary activation energy decreases with grain boundary solute concentration (Avila-Paredes *et al.*, 2009). This suggests that the trend in activation energy and solute concentration for oxygen migration across the grain boundary cannot be determined from the trend observed for the grain. This may be reasonable since the detailed bonding configuration at the interface may be very different from the bonding in the grain. This will be explored further in future work.

A key finding of this work is that the shape of the material's misorientation angle distribution (i.e. its character) is imparted on the space charge potential and ionic conductivity distributions. This is a result of the proportionality of the solute concentration to the grain boundary misorientation angle, and more complex MADs and relationships

between concentration and character should facilitate more complex transport property distributions. If one knows the relationship between the material's MAD, and the local grain boundary solute concentration, the transport property distributions may be extracted, giving insight into the optimization of grain boundaries.

6.4 Summary

A novel correlated AC-STEM approach combining STEM orientation imaging and EELS was used to extend nanoscale grain boundary composition measurements to the entire grain boundary population in PGCO. It was concluded that approximately 70 % of the grain boundary length exhibits enhanced conductivity via local Pr polaron hopping under AC impedance spectroscopy measurement conditions. To predict DC ionic transport properties, measured solute segregation profiles were modeled to yield grain boundary space charge potentials and oxygen vacancy concentrations for each grain boundary in the population. The resultant distributions reflect the material's grain boundary character, adopting the form of the misorientation angle distribution. The space charge potential distribution is peaked at 0.6 V in this case, suggesting that space charge potentials derived from AC impedance spectroscopy (published in literature) may reflect transport properties of only the most conductive grain boundaries. The oxygen ionic conductivity distribution was calculated from vacancy concentrations derived from modeling measured solute profiles, and migration activation energies from literature. This distribution indicates that the most common grain boundaries exhibit four orders of magnitude lower ionic conductivity than the grains.

By incorporating the influence of grain boundary character on measured and predicted properties, an improvement in the understanding of the grain boundary population when compared with conventional grain boundary nanoscale analysis by random sampling was demonstrated. This correlated approach produces real-space maps of grain boundary physical and transport properties, and should be considered when developing future studies and models of polycrystalline materials. By explicitly correlating physical and transport properties across length scales, the potential for bottom-up grain boundary design and optimization via control of grain boundary character and microstructure is highlighted.

7 Conclusions and Outlook

This research program explored the complex, and still not well understood interplay between local composition and electronic structure, microscopic character, and macroscopic electrical conductivity of grain boundaries in ceria solutions. Macroscopic electrical transport measurements, a range of electron microscopic characterization techniques, and novel experimental approaches to correlate grain boundary properties across length scales were developed and applied. The objective of this work was to apply advanced TEM techniques and experimental approaches to model and technologically-relevant systems in order to guide the optimization of grain boundary transport properties in anion conducting oxides.

The nominal Ca^{2+} solute concentration was varied in polycrystalline CCO electrolytes to examine systematically for the first time the influence of the nominal composition on the local grain boundary composition and macroscopic ionic conductivity, measured using AC impedance spectroscopy. Nominally $Ca_{0.02}Ce_{0.98}O_{1.98-\delta}$ (2CCO), $Ca_{0.05}Ce_{0.95}O_{1.95-\delta}$ (5CCO) and $Ca_{0.1}Ce_{0.9}O_{1.9-\delta}$ (10CCO) pellets were fabricated to capture composition trends commonly observed for ceria solutions with solute concentration below about 15-20 mole%, such as conductivity maxima and/or minima in effective migration activation energy. Change in grain boundary ionic conductivity by several orders of magnitude was observed over the composition range investigated here, with the CCO grain boundary conductivity reaching that of state-of-the-art 10GCO, making it a promising candidate for selective grain boundary decoration schemes to optimize ionic conductivity.

The origin of this conductivity variation was probed across length scales, with the local structure and composition analyzed down to the atomic scale using AC-STEM EELS. Conductivity and chemical data were interpreted in light of grain boundary character probed at the microscale using SEM EBSD, which highlighted the critical interplay between macroscopic grain boundary conductivity and local grain boundary composition. The local solute concentration and grain boundary conductivity were found to be correlated, with each being sensitive to the nominal Ca^{2+} concentration at low nominal solute concentration, before saturating above ~5 mole% Ca^{2+}. This correlated analysis provided insights into fundamental grain boundary science in CCO, and should be considered in the development of future theoretical models for electroceramic grain boundaries.

Following the suggestions of Andersson *et al.* and Dholabhai *et al.*, a combination of Gd^{3+} and Pr^{3+} solutes was also employed in hopes of confirming their predictions of enhanced ionic conductivity relative to ceria with *only* Gd^{3+}, and to explore the influence of Pr solute on grain boundary properties. Indeed, comparison of grain and grain boundary electrical properties measured using AC impedance spectroscopy showed that the grain conductivity in the quaternary oxide $Pr_{0.04}Gd_{0.11}Ce_{0.85}O_{2-\delta}$ (PGCO) slightly exceeded that of $Gd_{0.2}Ce_{0.8}O_{1.9-\delta}$ (20GCO). Interestingly and unexpectedly, grain boundaries in the PGCO sample were on average almost 100 times more conducting than those in the 20GCO system. Based on STEM EELS characterization of grain boundary composition and chemistry, it was concluded that the enhanced grain boundary conductivity results from strong Pr segregation to grain boundaries, which activated an alternative transport mechanism to that dominant in grains. This analysis suggested that an electronic

conduction mechanism based on Pr polaron hopping may be active at grain boundaries during AC impedance spectroscopy, a surprising finding which has in part motivated the work presented in the subsequent chapters of this dissertation.

High spatial and energy resolution monochromated EELS has been employed to detect a state within the bandgap of ~30 nm nanoparticles of 10PCO. Quantitative analysis of the spectra showed that the inter-band state is associated with Pr^{4+} 4*f* levels, has a width of about 0.1 eV, and is located 1.4 eV above the top of the valence band. The strength of the Pr 4*f* DOS relative to the Ce 4*f* DOS scales with the Pr/Ce concentration and is about 0.1. Population and de-population of this state gives rise to color changes in the material attributed to an energy level shift of the impurity state upon population of about +0.3 eV. The ultra-high energy resolution STEM EELS allows interband states to be probed with high spatial resolution and should be applicable to other systems where nanocharacterization is required such as grain boundaries, dislocations and precipitates.

Finally, a novel correlated AC-STEM approach combining precession enhanced nanodiffraction orientation imaging and EELS was used to extend nanoscale grain boundary composition measurements to the entire PGCO grain boundary population, thus elucidating macroscopic conductivity measurements. We concluded that approximately 70 % of the grain boundary length exhibits enhanced conductivity via local Pr polaron hopping under AC impedance spectroscopy measurement conditions. To predict DC ionic transport properties, measured solute segregation profiles were modeled to yield grain boundary space charge potentials for each grain boundary in the population. This distribution in the grain boundary space charge potential adopts the form of the material's

misorientation angle distribution, and is peaked at 0.6 V, suggesting that potentials derived from impedance spectroscopy may reflect transport properties of the most conductive grain boundaries. The model also generated oxygen vacancy concentration profiles, which allowed the calculation of the grain boundary ionic conductivity of every grain boundary. This distribution in grain boundary ionic conductivity also adopted the form of the grain boundary misorientation angle distribution, and indicated that the plurality of grain boundaries exhibit conductivity that the four orders of magnitude lower than that of the grains.

By incorporating the influence of grain boundary character on measured and predicted properties, we demonstrate an improvement in the understanding of the grain boundary population when compared with conventional grain boundary nanoscale analysis by random sampling. This correlated approach produces real space maps of grain boundary physical and transport properties, and should be considered when developing future studies and models of polycrystalline materials. By explicitly correlating physical and transport properties across length scales, we demonstrate the potential for bottom-up grain boundary design and optimization via control of grain boundary character and microstructure.

Future areas of study may include:

- Heterogeneous solute segregation of Ca^{2+} to grain boundaries in fast oxygen ion conductors such as $Gd_xCe_{1-x}O_{2-x/2-\delta}$. to lower electronic leakage under reducing conditions.

- A systematic correlation of local grain boundary solute concentration, and macroscopic grain boundary conductivity to establish segregation-properties relationships. This could help explain *decrease* in E_a^{GB} with increasing local solute concentration. This is the opposite trend of E_a^{Grain}, and may be related the change in oxygen vacancy formation energy when solutes segregate to the GB. Experimental E_a^{GB}data are provided here for Ca^{2+}, and measured $E_a^{GB}$for Gd^{3+} are previously reported by Avila-Paredes *et al.* (2009).

- Collecting valence-loss spectra in ceria and ceria and PCO as a function of particle size to probe its role on Cerenkov intensity in the bandgap.

- Characterizing the grain boundary conductivity of a polycrystalline material as a function of grain boundary character, possibly via in-situ EBSD and impedance spectroscopy.

- Extending the correlation of grain boundary character and nanoscale properties using the grain boundary plane distribution (i.e. a five parameter character description), rather than misorientation angle.

8 Appendix

8.1 Dielectric Data for Relevant Oxides

Table 8.1. Dielectric Constants Derived from Refractive Index. Refractive indices from (Shannon, Shannon, Medenbach, & Fischer, 2002)

	Refractive index n	Dielectric constant $\varepsilon_r\ (= n^2)$
CeO_2	2.33	4.38
Gd_2O_3	1.92	3.68
CaO	1.81	3.28
Pr_2O_3	1.88	3.53

8.2 Impedance Data

2CCO

In some cases, the grain and grain boundary arcs could not both be fit. For instance, below the grain arc ('Gr') was fit with a [R-RQ^{Gr}] model, rather than an [R-RQ^{Gr}-RQ^{GB}] model, because the grain boundary ('GB') arc could not be fit. The model is specified by name in the bottom-right corner of each Nyquist plot and the file name is in the bottom-left. The lone R is used to account for system resistance, or in the case when the grain arc is not visible it gives the grain resistance (assuming that grain in RC). The fit for each Nyquist plot is indicated in the bottom right of the image. If the GB resistance could not be determined, as in this case, only the grain conductivity could be deduced.


80.00 Mohm
60.00 Mohm
40.00 Mohm
20.00 Mohm
0.000 ohm
-Zmag (ohm)
GB
150 °C
Gr
0.000 ohm
100.0 Mohm
Zreal (ohm)
ZCURVE (1403025_CaDC2_100-400c LN 1M-_#27.1Hz 50mV)
Fit 1 [R-RQ]

In the below case the Gr and GB arc are both included in the model [R-RQ-RQ].

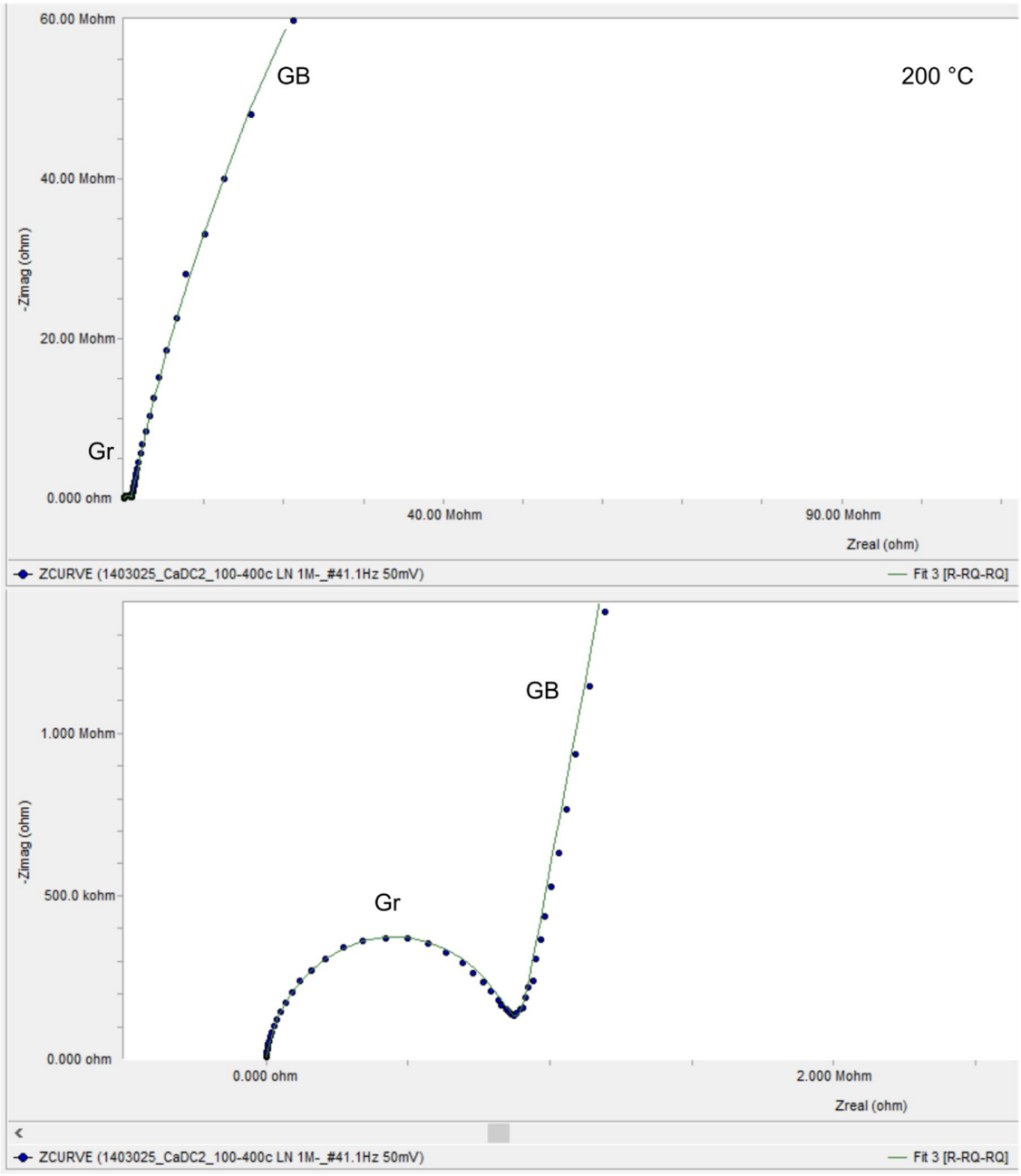

In some cases, the grain boundary arc model deviated from the data. In these cases, the data were fit using the higher frequency data points, and the fit quality was assessed via extrapolation of high frequency side of the electrode arc to the x-axis (see e.g. 400 °C).

In cases where the GB arc fitting was particularly uncertain, several fitting iterations were attempted until the grain boundary resistance derived from fits provided a smooth interpolation between measurement temperatures with more certain fits. This relies on the assumption that the resistance varies with temperature in a predictable manner in the temperature range of interpolation, i.e. the slope of resistivity or conductivity vs. inverse temperature is linear in that temperature range. This is a reasonable expectation considering the Arrhenius slope of grain conductivity is typically constant below ~500 °C, and change in slope of the grain boundary conductivity was not observed. This lack of slope change indicates that defect association effects are dominant, and is reasonable considering defect association effects dominate with solute concentration is high, as is the case at grain boundaries. Thus the aforementioned Nyquist plot processing procedure is not expected to produce slope changes in conductivity plots.

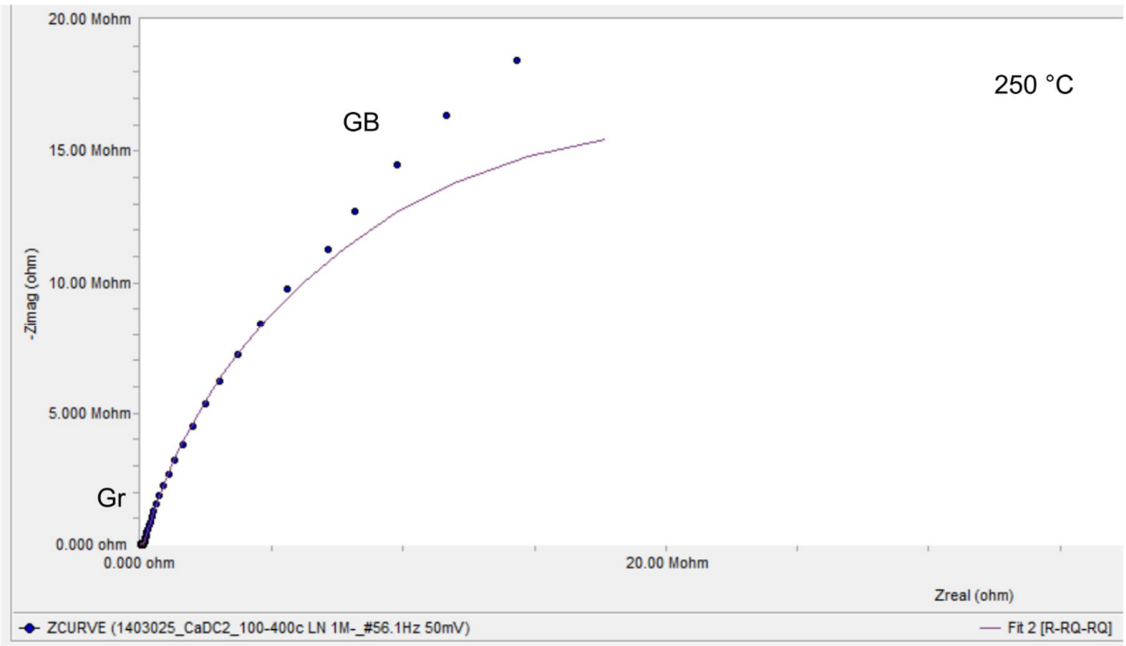
20.00 Mohm
15.00 Mohm
10.00 Mohm
5.000 Mohm
0.000 ohm
-Zimag (ohm)
250 °C
GB
Gr
0.000 ohm
20.00 Mohm
Zreal (ohm)
ZCURVE (1403025_CaDC2_100-400c LN 1M-_#56.1Hz 50mV)
Fit 2 [R-RQ-RQ]

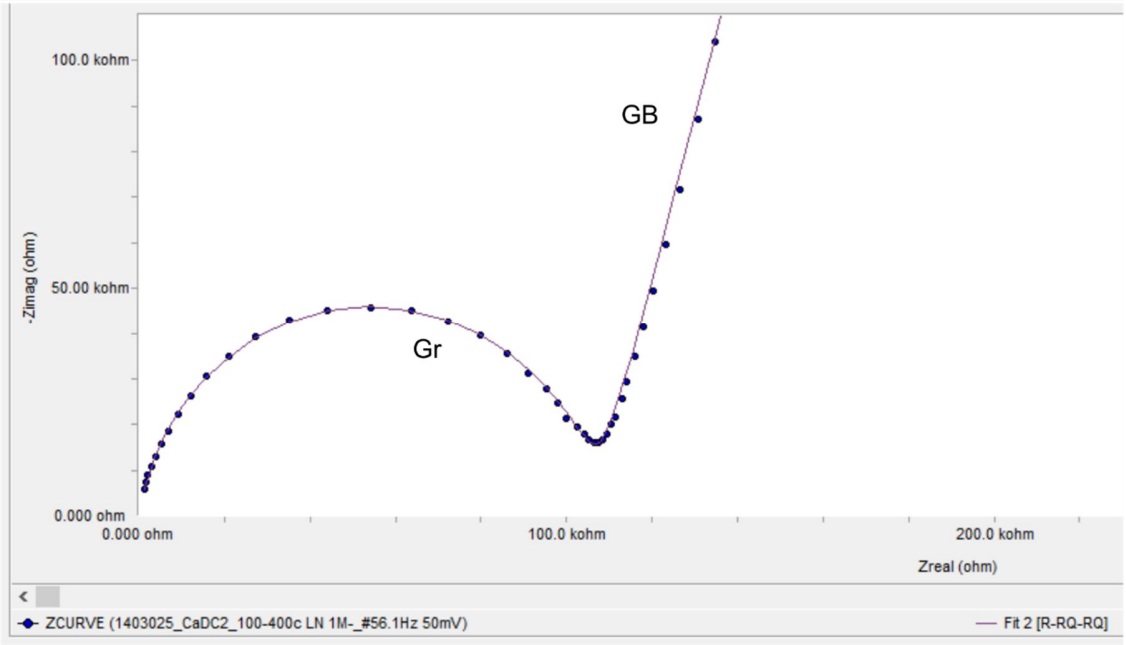
100.0 kohm
50.00 kohm
0.000 ohm
-Zimag (ohm)
GB
Gr
0.000 ohm
100.0 kohm
200.0 kohm
Zreal (ohm)
ZCURVE (1403025_CaDC2_100-400c LN 1M-_#56.1Hz 50mV)
Fit 2 [R-RQ-RQ]

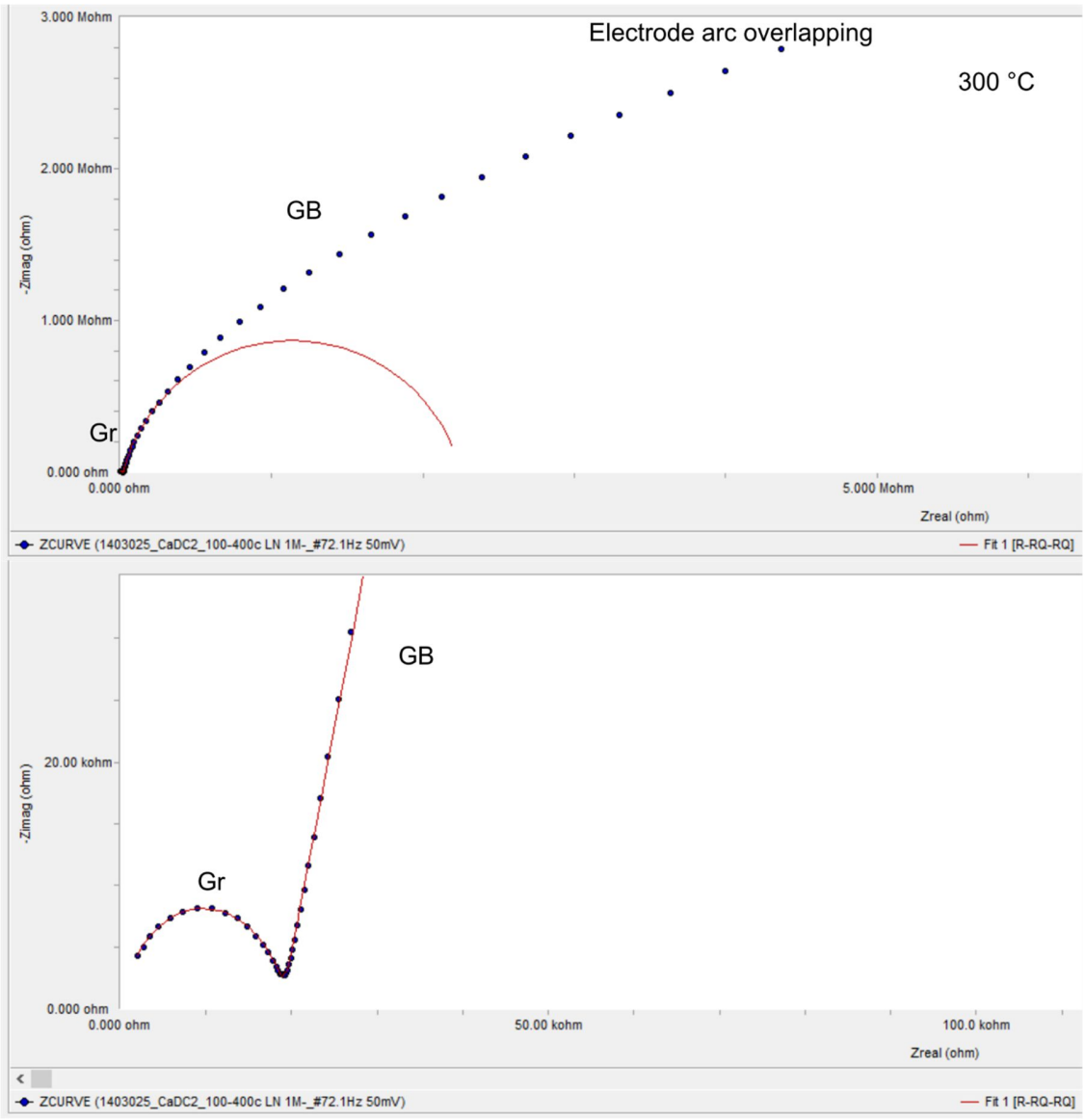
3.000 Mohm
2.000 Mohm
1.000 Mohm
0.000 ohm
-Zimag (ohm)
Electrode arc overlapping
300 °C
GB
Gr
0.000 ohm
5.000 Mohm
Zreal (ohm)
ZCURVE (1403025_CaDC2_100-400c LN 1M-_#72.1Hz 50mV)
Fit 1 [R-RQ-RQ]
20.00 kohm
0.000 ohm
-Zimag (ohm)
GB
Gr
0.000 ohm
50.00 kohm
100.0 kohm
Zreal (ohm)
ZCURVE (1403025_CaDC2_100-400c LN 1M-_#72.1Hz 50mV)
Fit 1 [R-RQ-RQ]

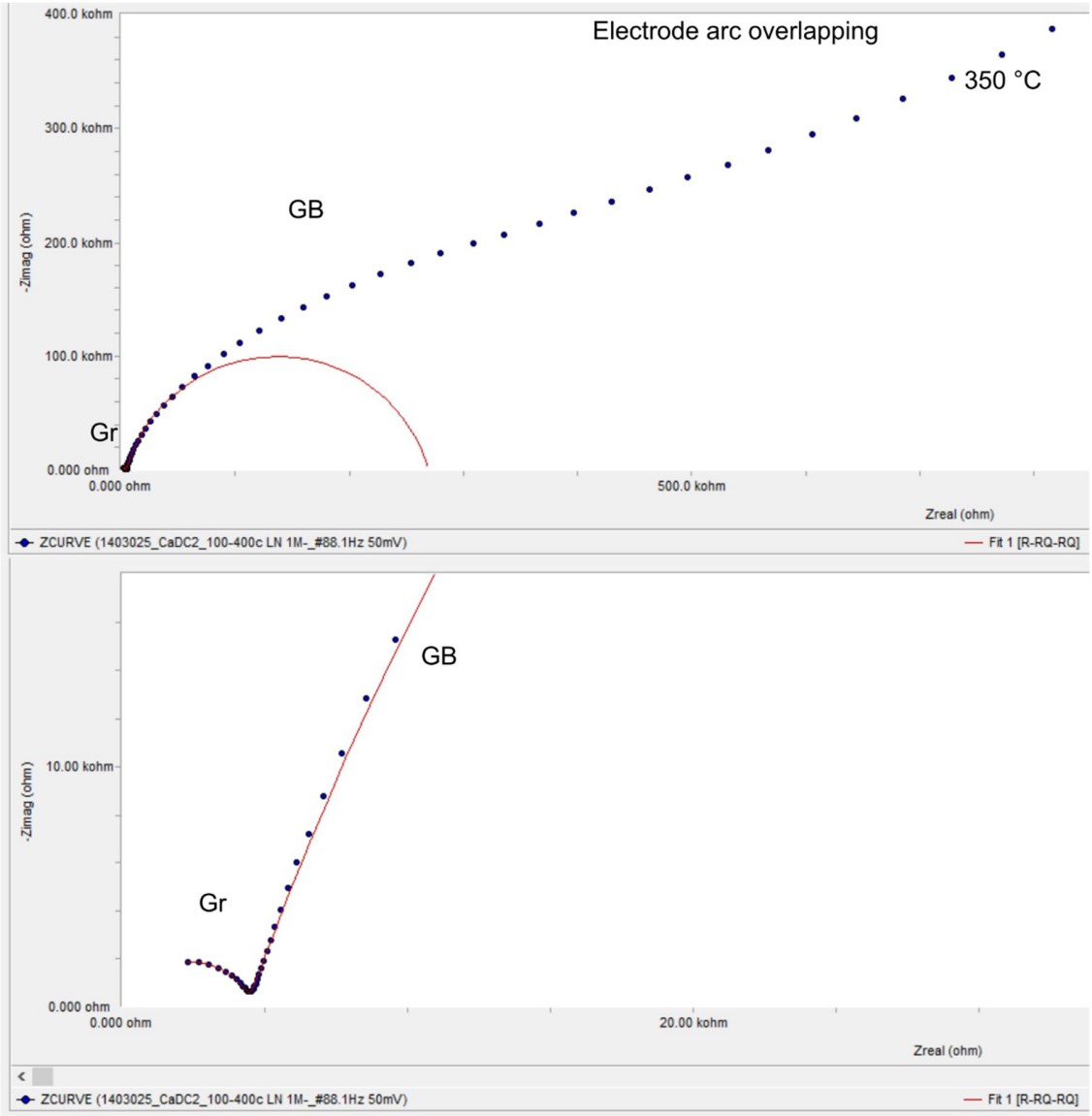
400.0 kohm
300.0 kohm
200.0 kohm
100.0 kohm
0.000 ohm
-Zimag (ohm)
Electrode arc overlapping
350 °C
GB
Gr
0.000 ohm
500.0 kohm
Zreal (ohm)
ZCURVE (1403025_CaDC2_100-400c LN 1M-_#88.1Hz 50mV)
Fit 1 [R-RQ-RQ]
10.00 kohm
0.000 ohm
-Zimag (ohm)
GB
Gr
0.000 ohm
20.00 kohm
Zreal (ohm)
ZCURVE (1403025_CaDC2_100-400c LN 1M-_#88.1Hz 50mV)
Fit 1 [R-RQ-RQ]

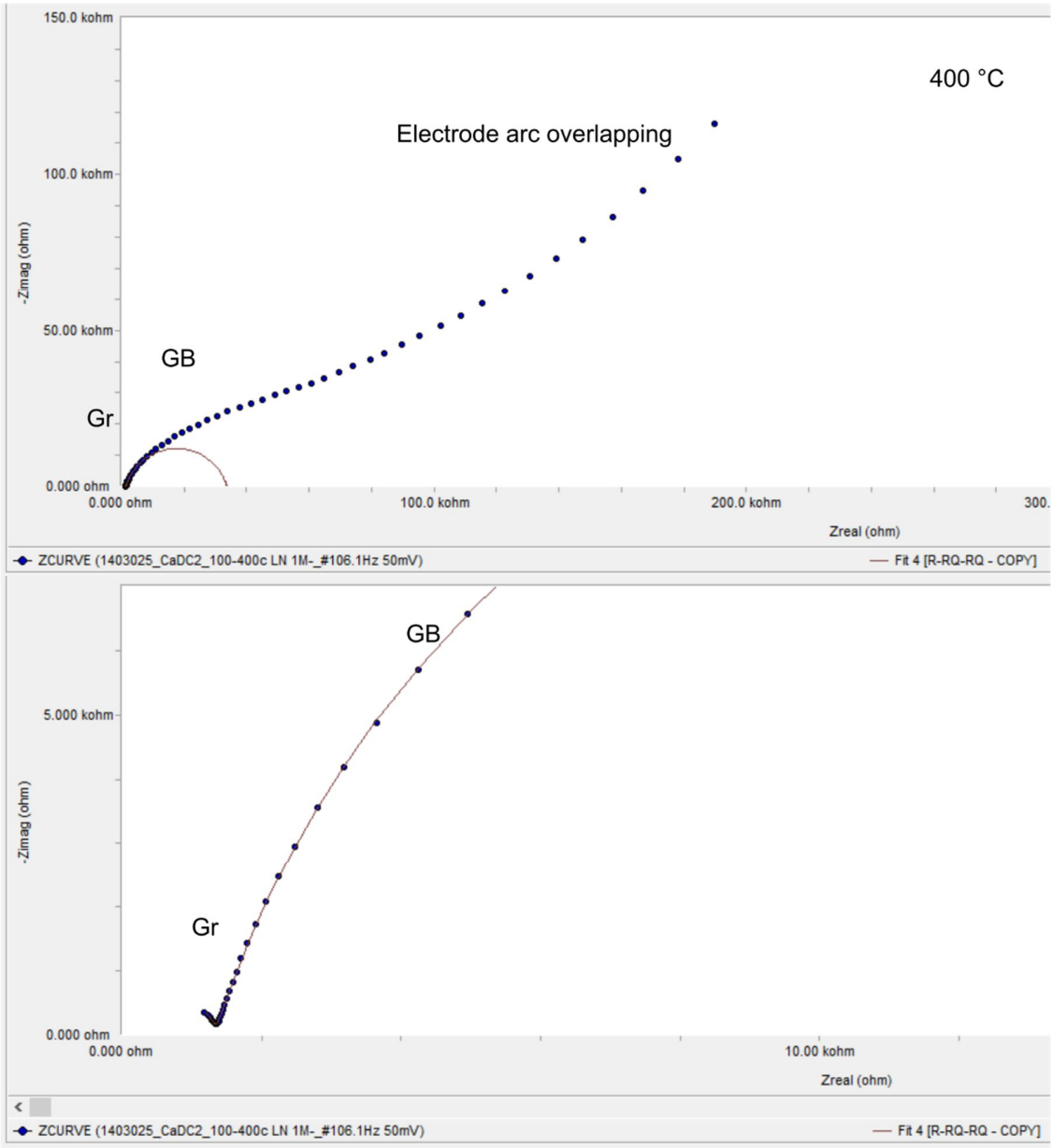

At higher measurement temperatures the electrode arc split into two distinct arcs, indicating that two electrochemical processes were occurring. It is possible that the oxygen dissociation and absorption processes have been detected on the electrode.

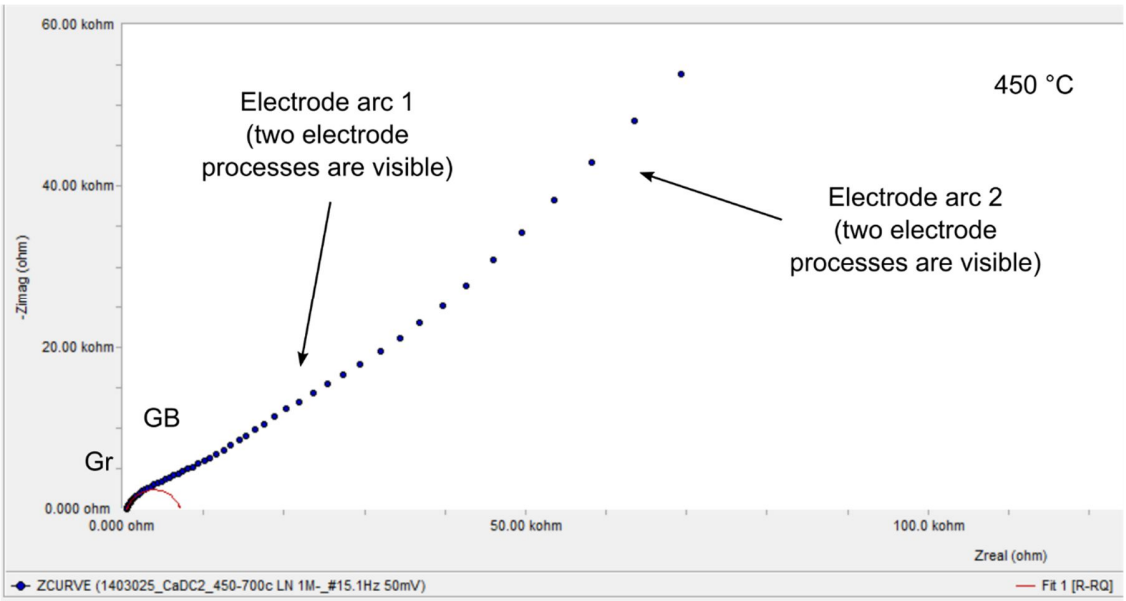
60.00 kohm
40.00 kohm
20.00 kohm
0.000 ohm
-Zmag (ohm)
450 °C
Electrode arc 1
(two electrode
processes are visible)
Electrode arc 2
(two electrode
processes are visible)
GB
Gr
0.000 ohm
50.00 kohm
100.0 kohm
Zreal (ohm)
ZCURVE (1403025_CaDC2_450-700c LN 1M-_#15.1Hz 50mV)
Fit 1 [R-RQ]

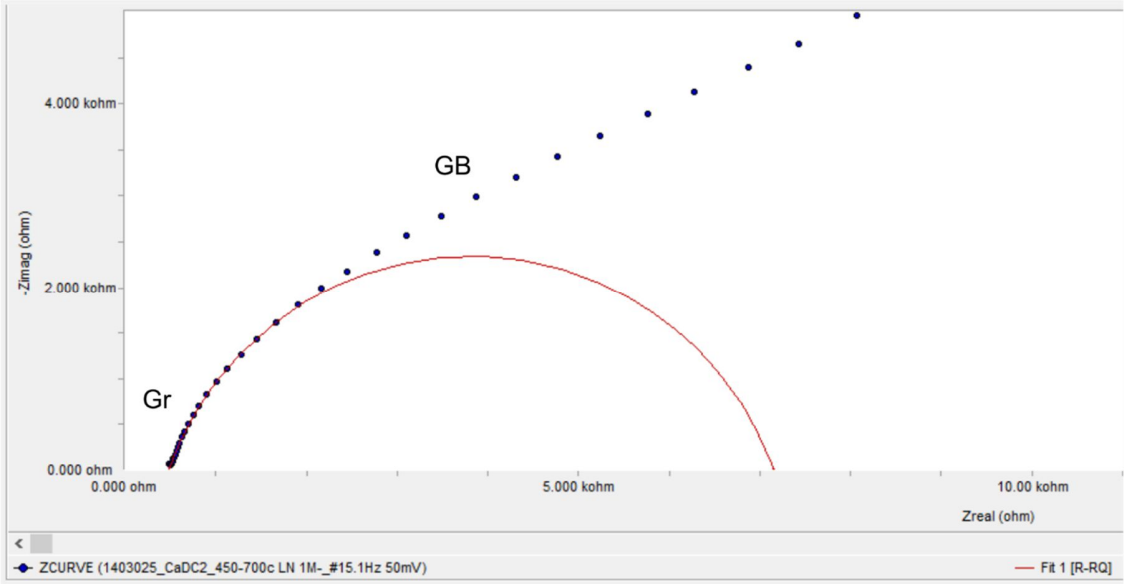
4.000 kohm
2.000 kohm
0.000 ohm
-Zmag (ohm)
GB
Gr
0.000 ohm
5.000 kohm
10.00 kohm
Zreal (ohm)
ZCURVE (1403025_CaDC2_450-700c LN 1M-_#15.1Hz 50mV)
Fit 1 [R-RQ]

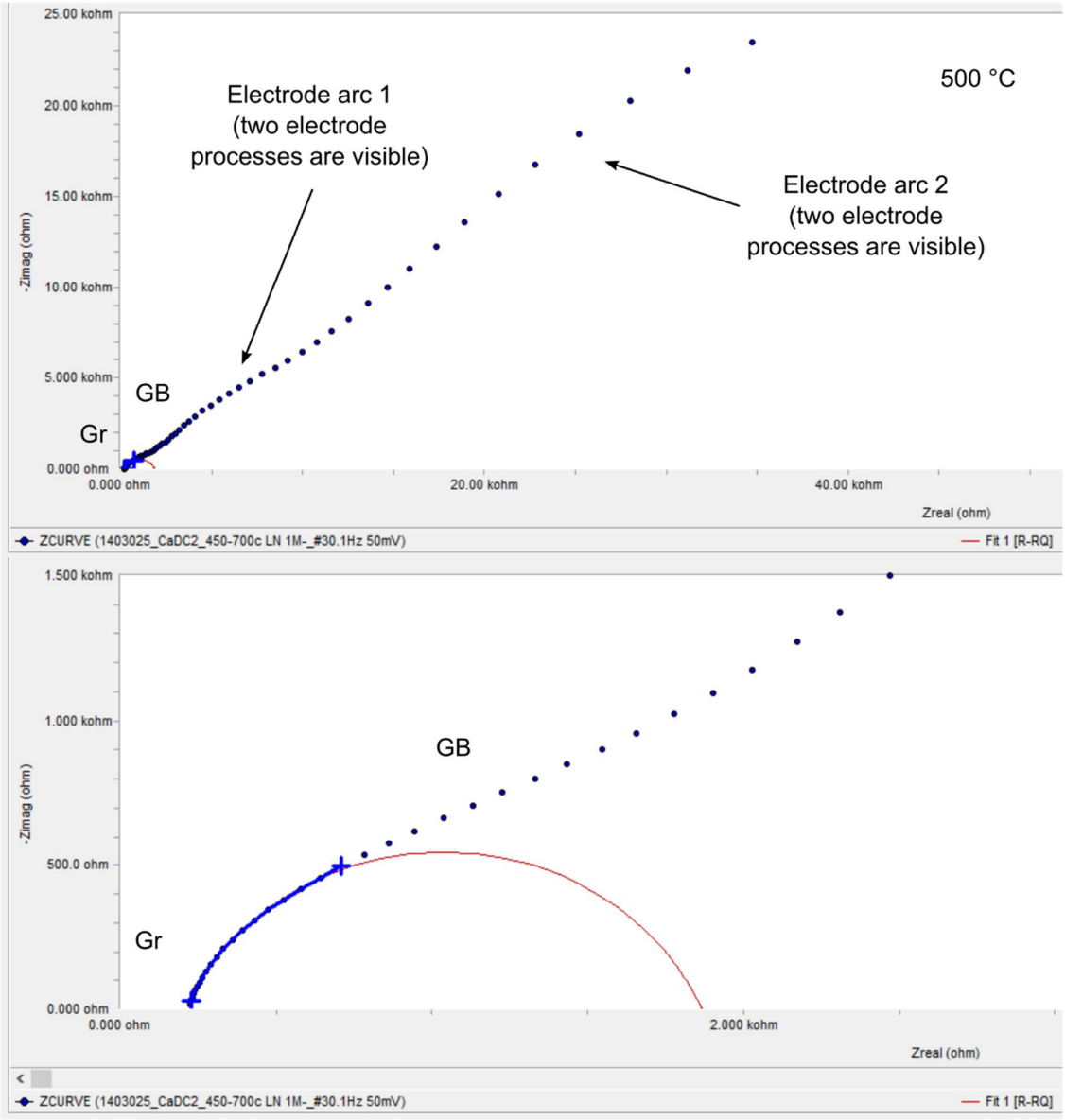
25.00 kohm
20.00 kohm
15.00 kohm
10.00 kohm
5.000 kohm
0.000 ohm
-Zimag (ohm)
0.000 ohm
20.00 kohm
40.00 kohm
Zreal (ohm)
500 °C
Electrode arc 1
(two electrode
processes are visible)
Electrode arc 2
(two electrode
processes are visible)
GB
Gr
ZCURVE (1403025_CaDC2_450-700c LN 1M-_#30.1Hz 50mV)
Fit 1 [R-RQ]
1.500 kohm
1.000 kohm
500.0 ohm
0.000 ohm
-Zimag (ohm)
0.000 ohm
2.000 kohm
Zreal (ohm)
GB
Gr
ZCURVE (1403025_CaDC2_450-700c LN 1M-_#30.1Hz 50mV)
Fit 1 [R-RQ]

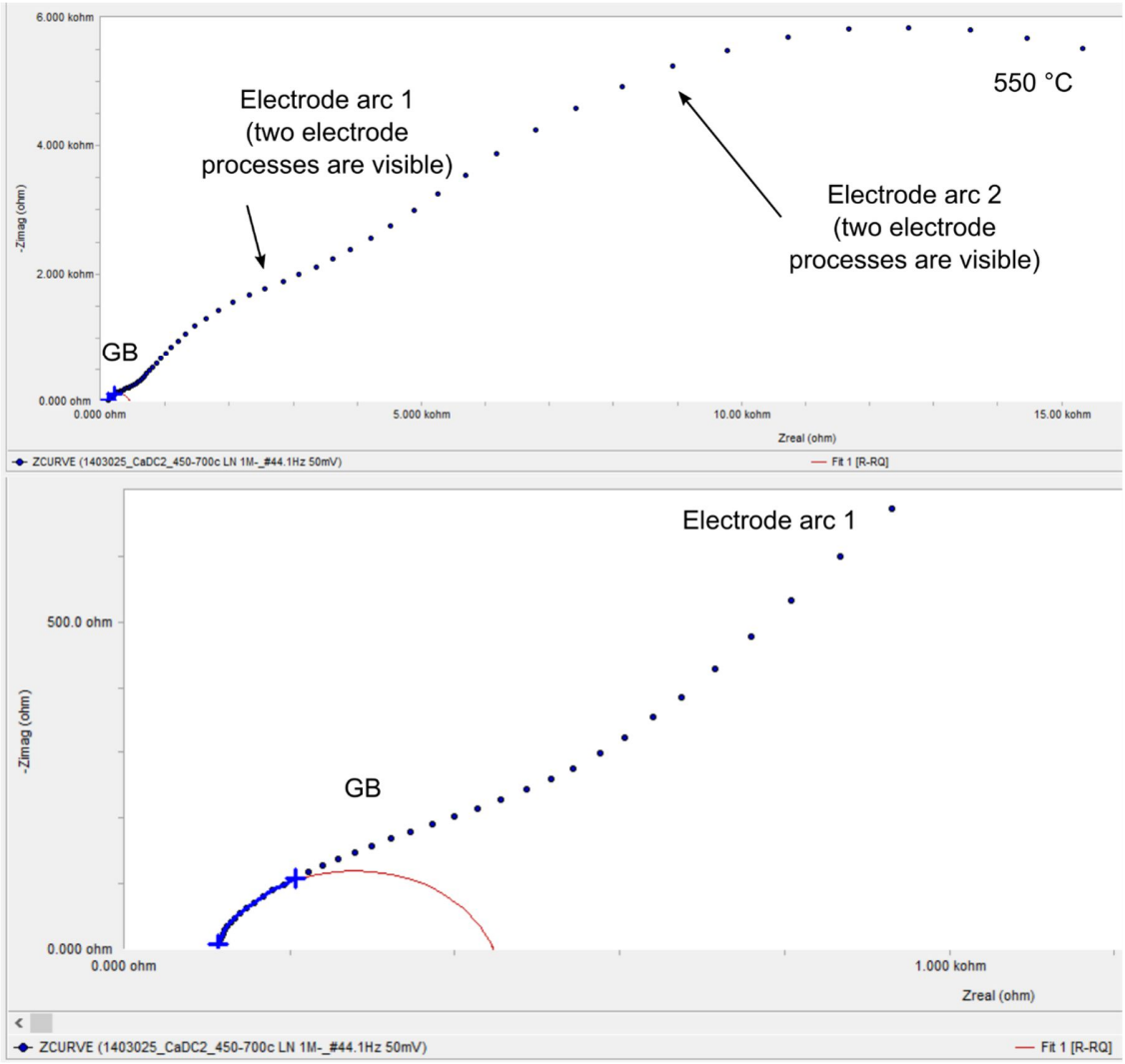
6.000 kohm
4.000 kohm
2.000 kohm
0.000 ohm
-Zmag (ohm)
Electrode arc 1
(two electrode
processes are visible)
550 °C
Electrode arc 2
(two electrode
processes are visible)
GB
0.000 ohm
5.000 kohm
10.00 kohm
15.00 kohm
Zreal (ohm)
ZCURVE (1403025_CaDC2_450-700c LN 1M-_#44.1Hz 50mV)
Fit 1 [R-RQ]
Electrode arc 1
500.0 ohm
-Zmag (ohm)
GB
0.000 ohm
0.000 ohm
1.000 kohm
Zreal (ohm)
ZCURVE (1403025_CaDC2_450-700c LN 1M-_#44.1Hz 50mV)
Fit 1 [R-RQ]

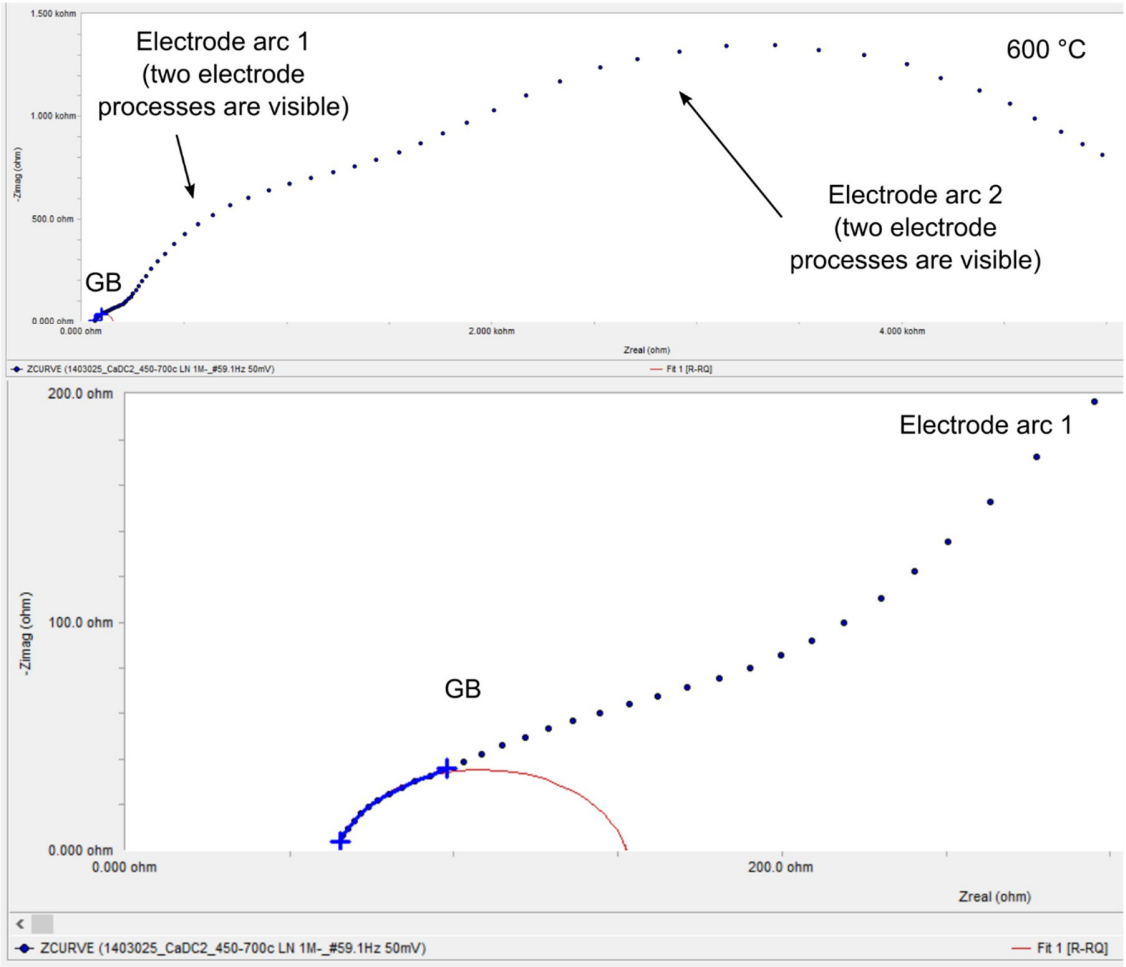
Electrode arc 1
(two electrode
processes are visible)
600 °C
Electrode arc 2
(two electrode
processes are visible)
GB
1.500 kohm
1.000 kohm
500.0 ohm
0.000 ohm
-Zimag (ohm)
0.000 ohm
2.000 kohm
4.000 kohm
Zreal (ohm)
ZCURVE (1403025_CaDC2_450-700c LN 1M-_#59.1Hz 50mV)
Fit 1 [R-RQ]
200.0 ohm
100.0 ohm
0.000 ohm
-Zimag (ohm)
Electrode arc 1
GB
0.000 ohm
200.0 ohm
Zreal (ohm)
ZCURVE (1403025_CaDC2_450-700c LN 1M-_#59.1Hz 50mV)
Fit 1 [R-RQ]

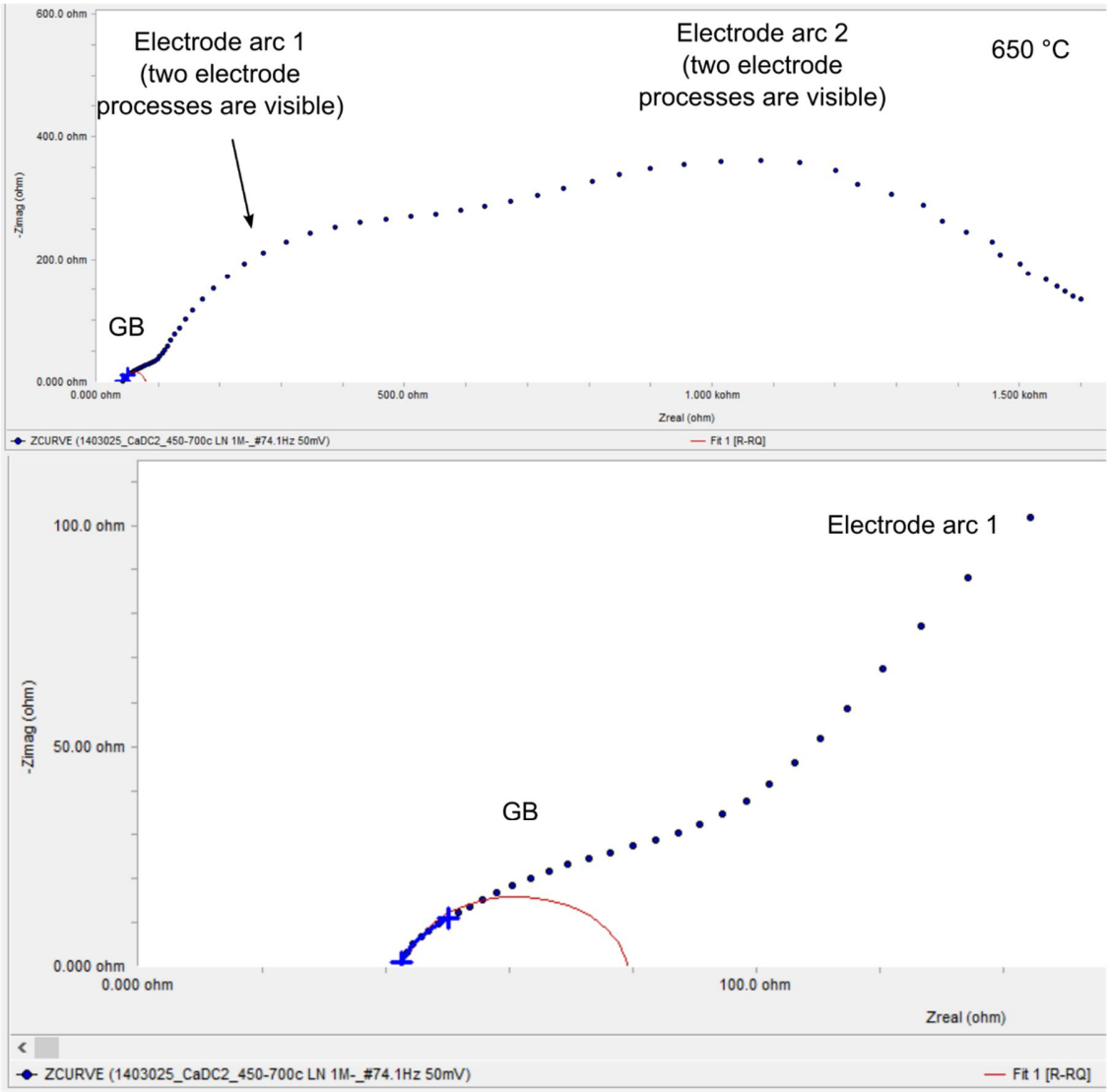
600.0 ohm
400.0 ohm
200.0 ohm
0.000 ohm
-Zimag (ohm)
Electrode arc 1
(two electrode
processes are visible)
Electrode arc 2
(two electrode
processes are visible)
650 °C
GB
0.000 ohm
500.0 ohm
1.000 kohm
1.500 kohm
Zreal (ohm)
ZCURVE (1403025_CaDC2_450-700c LN 1M-_#74.1Hz 50mV)
Fit 1 [R-RQ]
100.0 ohm
50.00 ohm
0.000 ohm
-Zimag (ohm)
Electrode arc 1
GB
0.000 ohm
100.0 ohm
Zreal (ohm)
ZCURVE (1403025_CaDC2_450-700c LN 1M-_#74.1Hz 50mV)
Fit 1 [R-RQ]

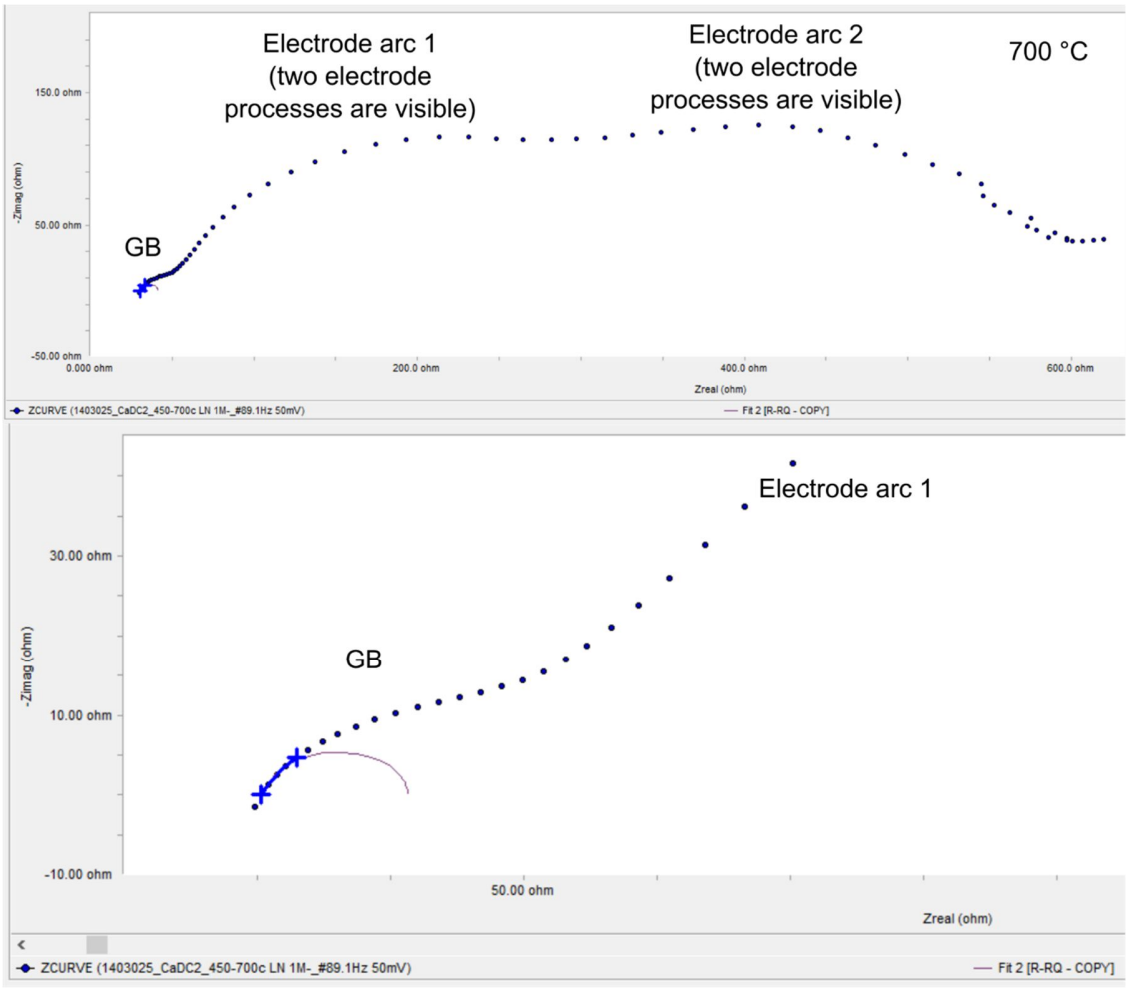
Electrode arc 1
(two electrode
processes are visible)
Electrode arc 2
(two electrode
processes are visible)
700 °C
GB
150.0 ohm
50.00 ohm
-50.00 ohm
-Zimag (ohm)
0.000 ohm
200.0 ohm
400.0 ohm
600.0 ohm
Zreal (ohm)
ZCURVE (1403025_CaDC2_450-700c LN 1M-_#89.1Hz 50mV)
Fit 2 [R-RQ - COPY]
Electrode arc 1
GB
30.00 ohm
10.00 ohm
-10.00 ohm
-Zimag (ohm)
50.00 ohm
Zreal (ohm)
ZCURVE (1403025_CaDC2_450-700c LN 1M-_#89.1Hz 50mV)
Fit 2 [R-RQ - COPY]

PGCO

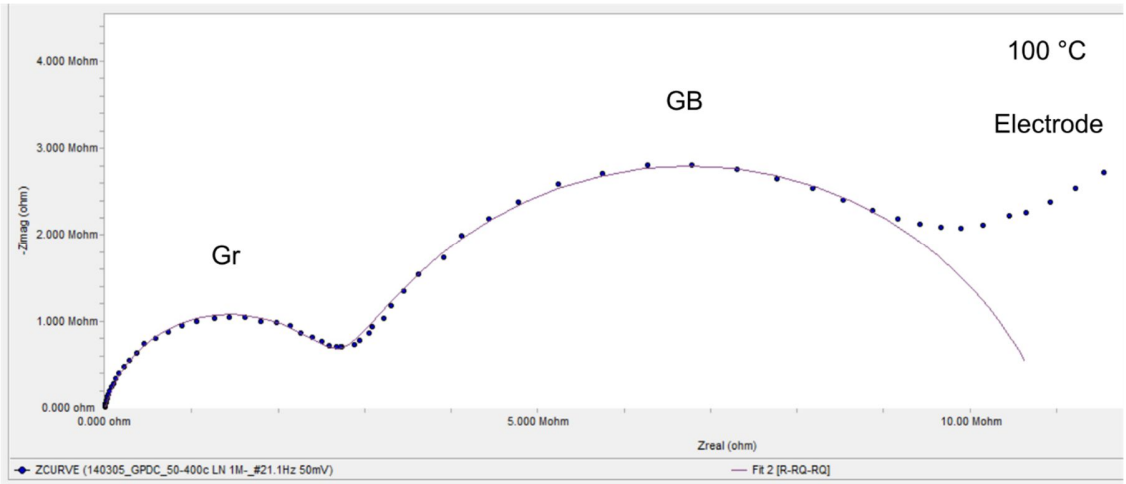
100 °C
GB
Electrode
Gr
4.000 Mohm
3.000 Mohm
2.000 Mohm
1.000 Mohm
0.000 ohm
-Zimag (ohm)
0.000 ohm
5.000 Mohm
10.00 Mohm
Zreal (ohm)
ZCURVE (140305_GPDC_50-400c LN 1M-_#21.1Hz 50mV)
Fit 2 [R-RQ-RQ]

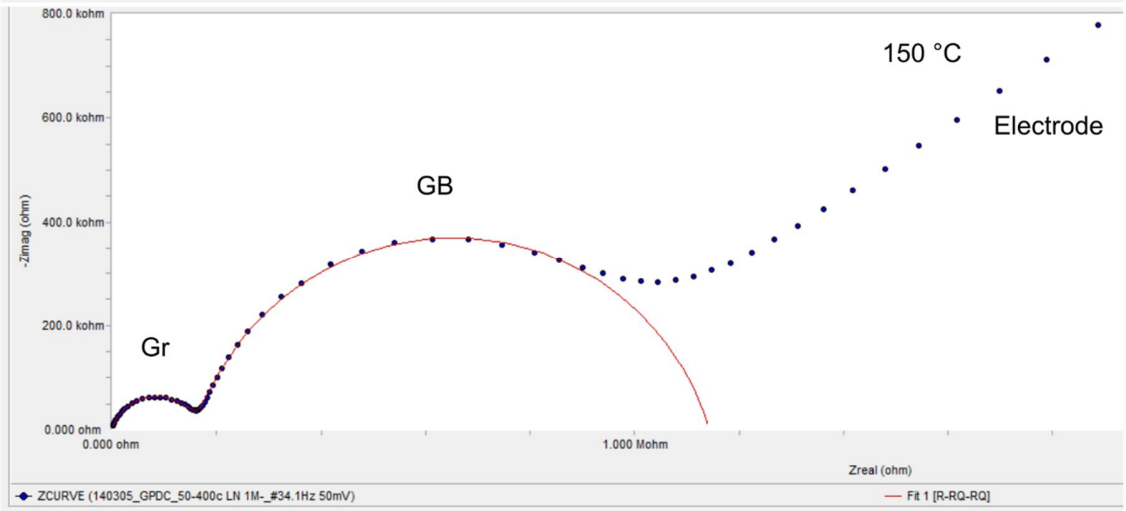
150 °C
Electrode
GB
Gr
800.0 kohm
600.0 kohm
400.0 kohm
200.0 kohm
0.000 ohm
-Zimag (ohm)
0.000 ohm
1.000 Mohm
Zreal (ohm)
ZCURVE (140305_GPDC_50-400c LN 1M-_#34.1Hz 50mV)
Fit 1 [R-RQ-RQ]

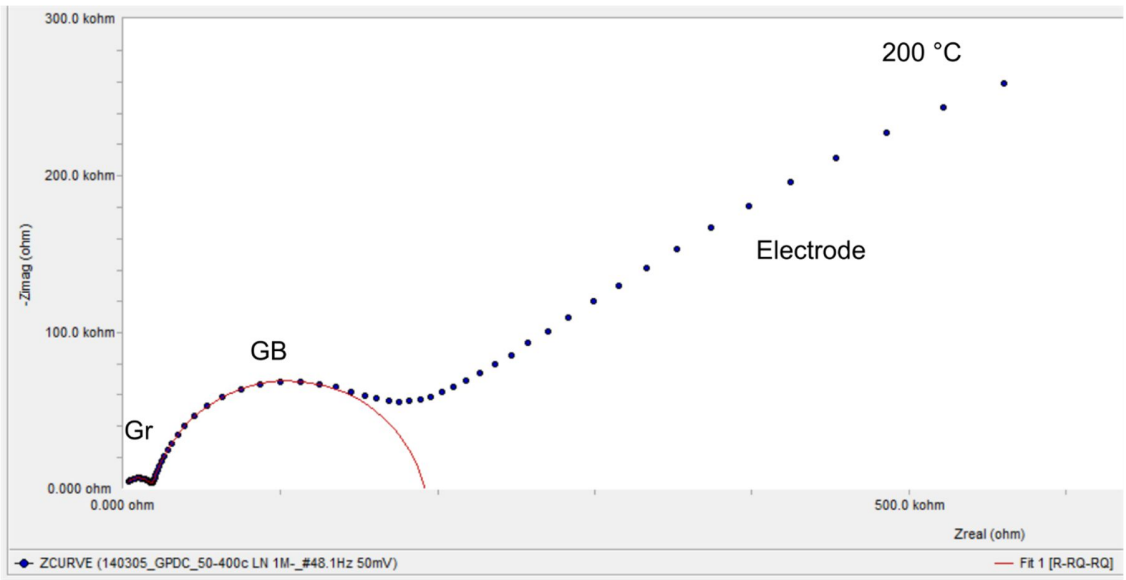
200 °C
Electrode
GB
Gr
300.0 kohm
200.0 kohm
100.0 kohm
0.000 ohm
-Zimag (ohm)
0.000 ohm
500.0 kohm
Zreal (ohm)
ZCURVE (140305_GPDC_50-400c LN 1M-_#48.1Hz 50mV)
Fit 1 [R-RQ-RQ]

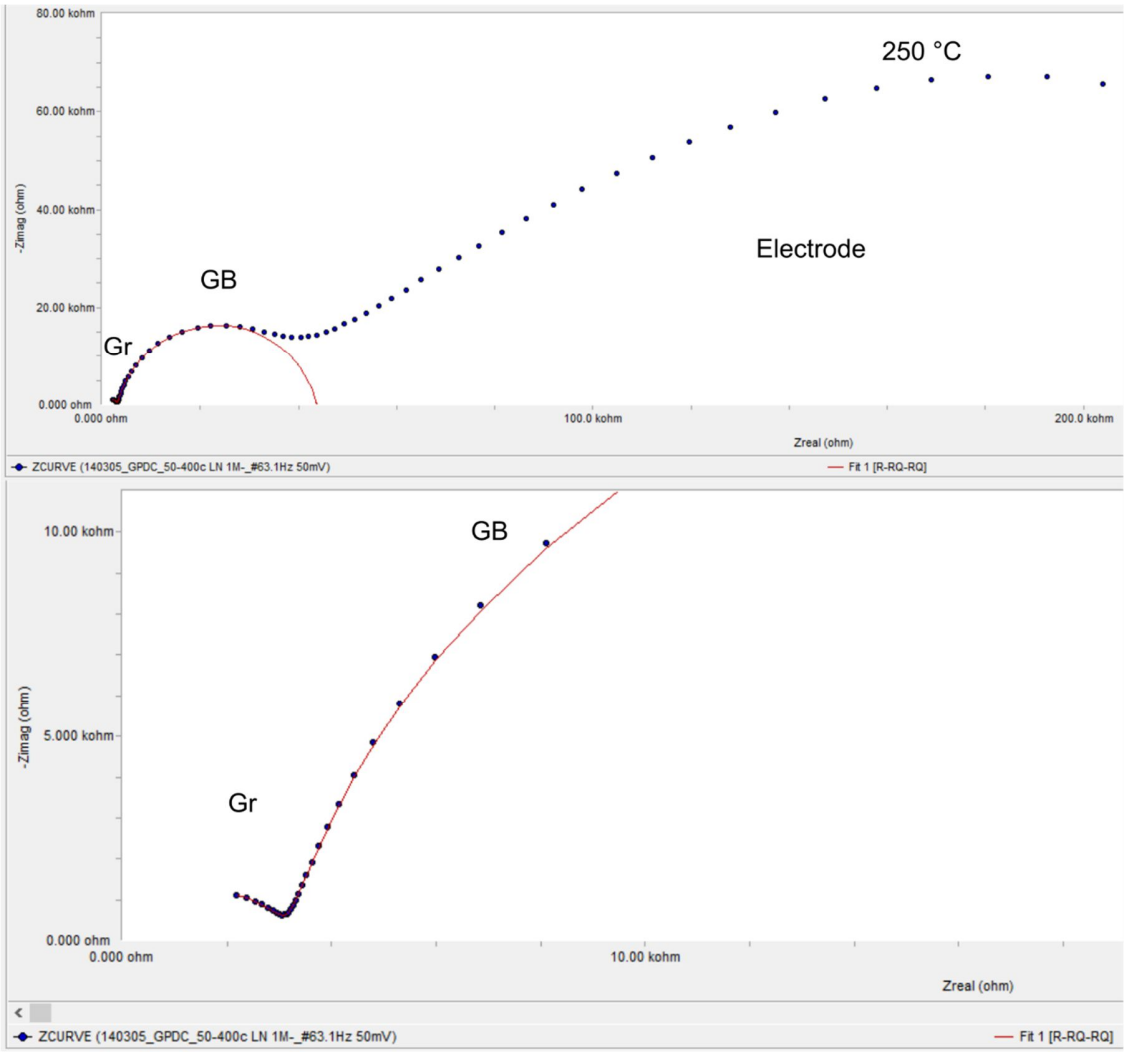
80.00 kohm
60.00 kohm
40.00 kohm
20.00 kohm
0.000 ohm
-Zmag (ohm)
250 °C
Electrode
GB
Gr
0.000 ohm
100.0 kohm
200.0 kohm
Zreal (ohm)
ZCURVE (140305_GPDC_50-400c LN 1M-_#63.1Hz 50mV)
Fit 1 [R-RQ-RQ]
10.00 kohm
5.000 kohm
0.000 ohm
-Zmag (ohm)
GB
Gr
0.000 ohm
10.00 kohm
Zreal (ohm)
ZCURVE (140305_GPDC_50-400c LN 1M-_#63.1Hz 50mV)
Fit 1 [R-RQ-RQ]

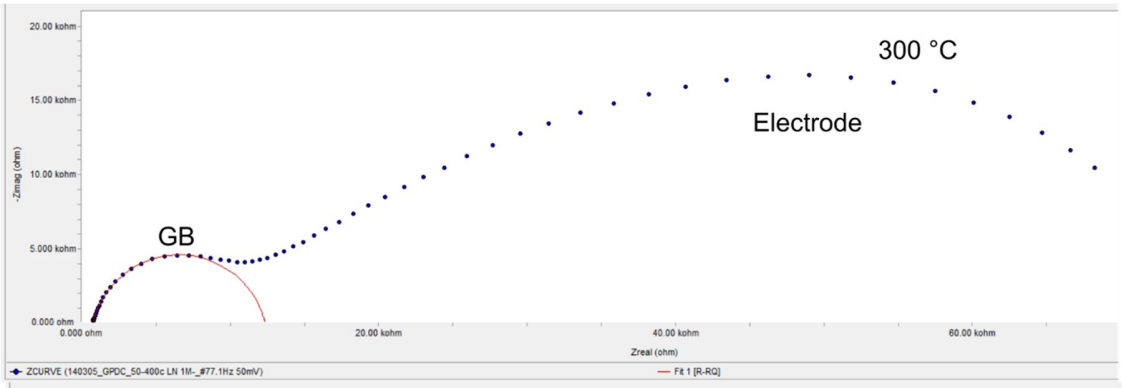
300 °C
Electrode
GB
20.00 kohm
15.00 kohm
10.00 kohm
5.000 kohm
0.000 ohm
-Zimag (ohm)
0.000 ohm
20.00 kohm
40.00 kohm
60.00 kohm
Zreal (ohm)
ZCURVE (140305_GPDC_50-400c LN 1M-_#77.1Hz 50mV)
Fit 1 [R-RQ]

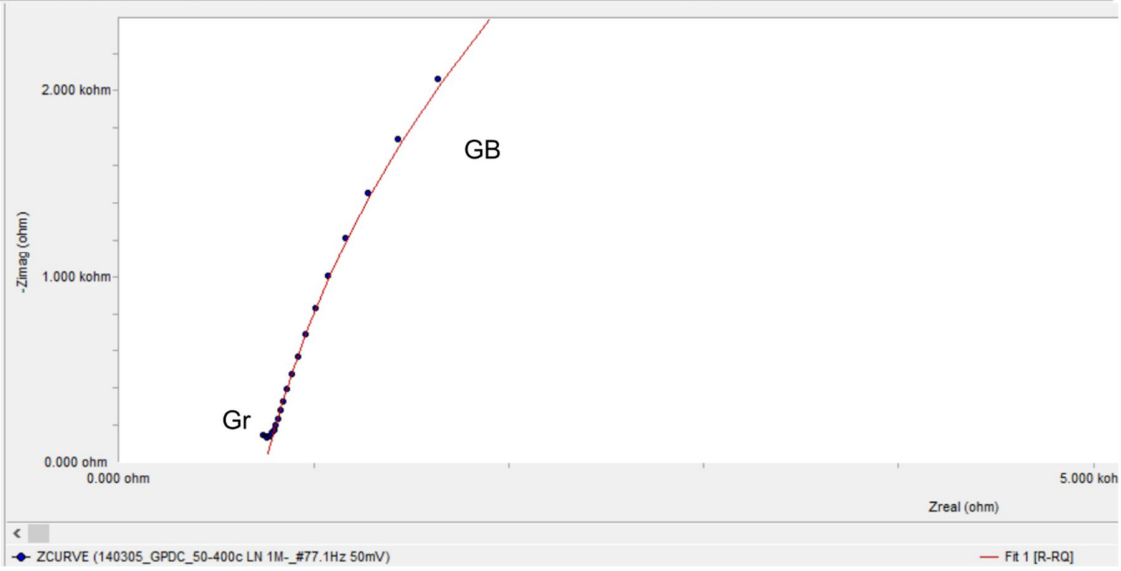
GB
Gr
2.000 kohm
1.000 kohm
0.000 ohm
-Zimag (ohm)
0.000 ohm
5.000 koh
Zreal (ohm)
ZCURVE (140305_GPDC_50-400c LN 1M-_#77.1Hz 50mV)
Fit 1 [R-RQ]

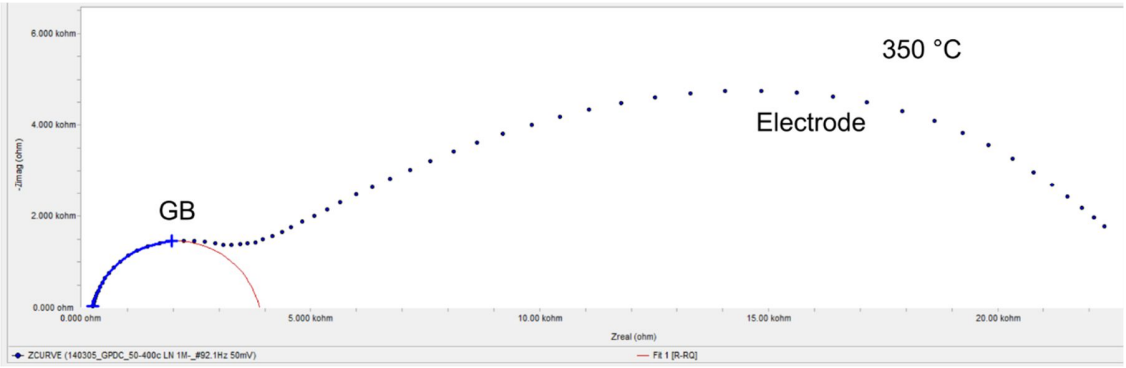
350 °C
Electrode
GB
6.000 kohm
4.000 kohm
2.000 kohm
0.000 ohm
-Zimag (ohm)
0.000 ohm
5.000 kohm
10.00 kohm
15.00 kohm
20.00 kohm
Zreal (ohm)
ZCURVE (140305_GPDC_50-400c LN 1M-_#92.1Hz 50mV)
Fit 1 [R-RQ]

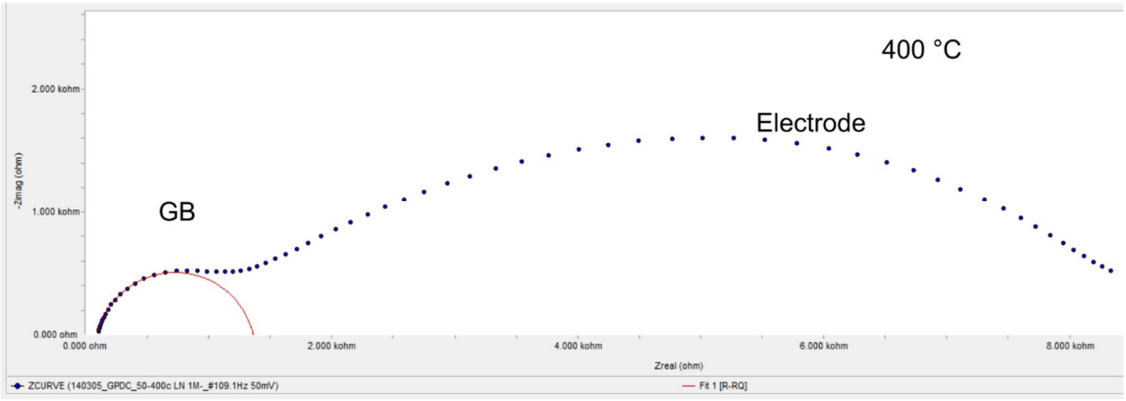
400 °C
Electrode
GB
2.000 kohm
1.000 kohm
0.000 ohm
-Zimag (ohm)
0.000 ohm
2.000 kohm
4.000 kohm
6.000 kohm
8.000 kohm
Zreal (ohm)
ZCURVE (140305_GPDC_50-400c LN 1M-_#109.1Hz 50mV)
Fit 1 [R-RQ]

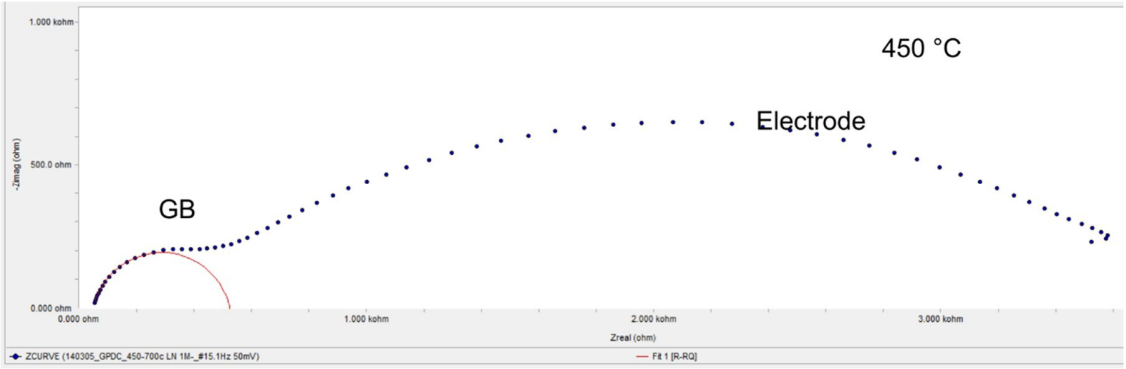
450 °C
Electrode
GB
1.000 kohm
500.0 ohm
0.000 ohm
-Zimag (ohm)
0.000 ohm
1.000 kohm
2.000 kohm
3.000 kohm
Zreal (ohm)
ZCURVE (140305_GPDC_450-700c LN 1M-_#15.1Hz 50mV)
Fit 1 [R-RQ]

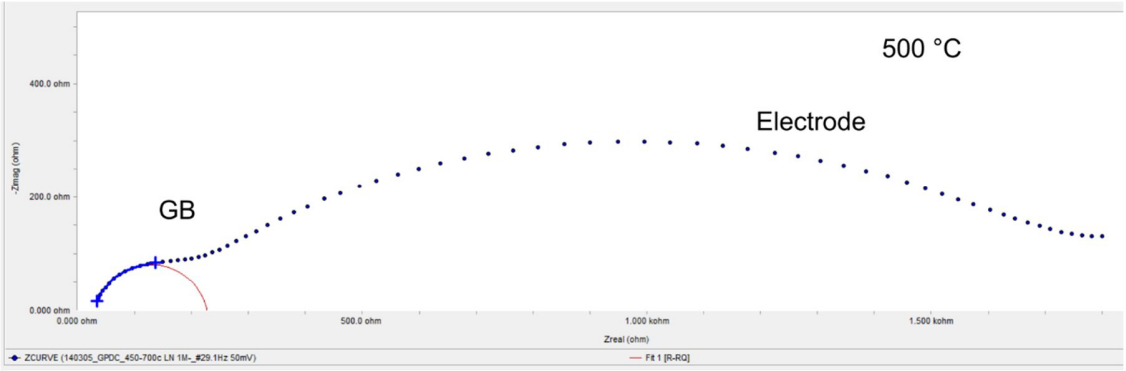
500 °C
Electrode
GB
400.0 ohm
200.0 ohm
0.000 ohm
-Zimag (ohm)
0.000 ohm
500.0 ohm
1.000 kohm
1.500 kohm
Zreal (ohm)
ZCURVE (140305_GPDC_450-700c LN 1M-_#29.1Hz 50mV)
Fit 1 [R-RQ]

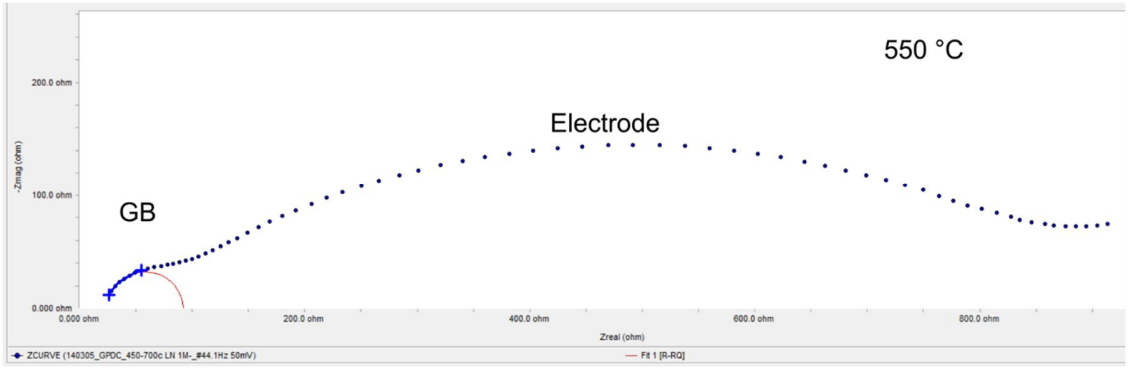

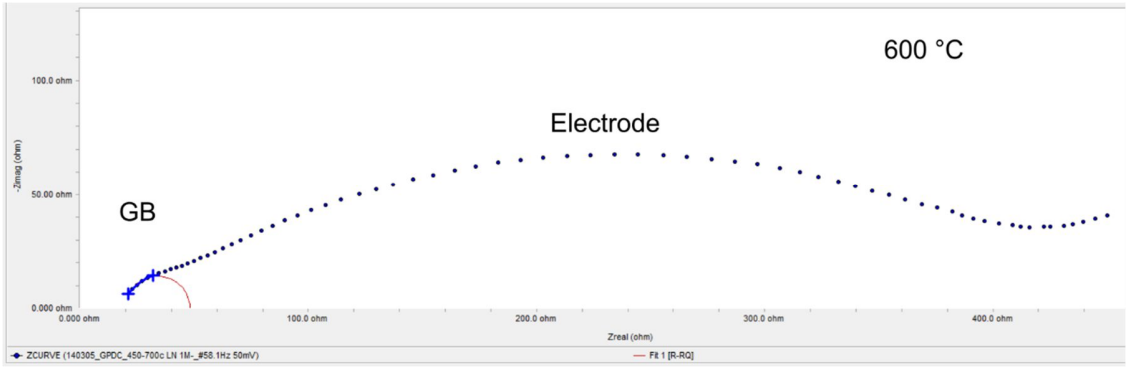

8.3 Comparing Calculation Methods for Conductivity

As discussed at the end of §2.2.1, it is possible to calculate conductivity using two methods: (1) From knowledge of the grain size, G, and grain boundary width, g; and (2) from knowledge of the capacitances of the grain and grain boundary extracted from Nyquist plot fitting (C_{Grain} and C_{GB}, respectively). The latter method relies on the assumption that the dielectric constants of the two media are approximately equal, and thus the ratio of geometric capacitances of the grain and grain boundary ($C_i = (A/L_i) \cdot \varepsilon_i \varepsilon_0$) can be approximated as the grain size and grain boundary width, respectively, as in Equation (2.17).

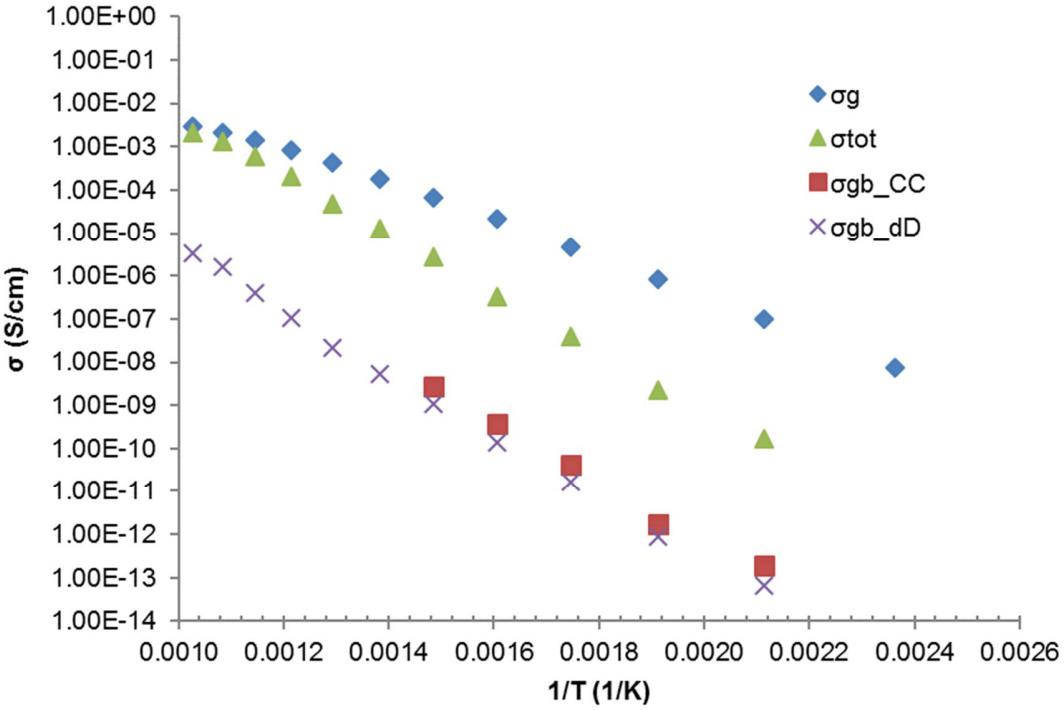

Figure 8.1. Comparison of Conductivity Calculation Methods. 2CCO conductivity with grain boundary conductivity determined from grain size method ('dD') and capacitance method ('CC').

The two methods, so-called 'grain size' and 'capacitance' methods are compared in Figure 8.1 and Table 8.2, which show the grain boundary conductivity for 2CCO, and effective migration activation energies for CCO, respectively. These methods yield a small difference in the absolute conductivity, (factor of ~5), with the resultant migration activation energies varying absolutely by <10 %. However, the trend in the variation of activation energy with nominal composition is apparent in both methods.

Table 8.2. Grain Size vs. Capacitance Method

	2CCO	5CCO	10COO
$E_a^{GB}, \frac{g}{G}$ (eV)	1.48	1.06	1.03
$E_a^{GB}, \frac{C_1}{C_2}$ (eV)	1.39	1.05	0.94

9 References

Acharya, S. A., Singh, K., & Bhoga, S. S. (2010). Synthesis and Characterization of Nanosized Dy-Doped of Ceria Developed by Microwave Assisted Combustion Route. *Integrated Ferroelectrics*, *121*(1), 13–23. https://doi.org/10.1080/10584587.2010.504129

Adams, B. L., Wright, S. I., & Kunze, K. (1993). Orientation Imaging: The Emergence of a New Microscopy. *Metallurgical Transactions, A*, *24A*, 819–831.

Aebersold, A. B., Alexander, D. T. L., & Hébert, C. (2015). Height-resolved quantification of microstructure and texture in polycrystalline thin films using TEM orientation mapping. *Ultramicroscopy*, *159*, 112–123. https://doi.org/10.1016/j.ultramic.2015.08.005

Agullo-Lopez, F., Catlow, C. R. A., & Townsend, P. D. (1988). *Point Defects in Materials*. Academic Press Limitd.

Ahn, C. C., & Krivanek, O. L. (1983). *EELS Atlas*. Gatan Inc.

An, J., Park, J. S., Koh, A. L., Lee, H. B., Jung, H. J., Schoonman, J., … Prinz, F. B. (2013). Atomic Scale Verification of Oxide-Ion Vacancy Distribution near a Single Grain Boundary in YSZ. *Scientific Reports*, *3*. https://doi.org/10.1038/srep02680

Andersson, D. A., Simak, S. I., Skorodumova, N. V., Abrikosov, I. A., & Johansson, B. (2006). Optimization of ionic conductivity in doped ceria. *Proceedings of the National Academy of Sciences of the United States of America*, *103*(10), 3518–3521.

Arai, H., Kunisaki, T., Shimizu, Y., & Seiyama, T. (1986). Electrical Properties of Calcia-Doped Ceria with Oxygen Ion Conduction. *Solid State Ionics*, *20*, 241–248.

Avila-Paredes, H. J., Choi, K., Chen, C.-T., & Kim, S. (2009). Dopant-concentration dependence of grain-boundary conductivity in ceria: A space-charge analysis. *Journal of Materials Chemistry*, *19*(27), 4837. https://doi.org/10.1039/b904583j

Avila-Paredes, H. J., & Kim, S. (2006). The effect of segregated transition metal ions on the grain boundary resistivity of gadolinium doped ceria: Alteration of the space charge potential. *Solid State Ionics*, *177*(35–36), 3075–3080. https://doi.org/10.1016/j.ssi.2006.08.017

Bae, H., Choi, J., & Choi, G. M. (2013). Electrical conductivity of Gd-doped ceria film fabricated by aerosol deposition method. *Solid State Ionics*, *236*, 16–21. https://doi.org/10.1016/j.ssi.2013.01.022

Batson, P. E., Kavanagh, K. L., Woodall, J. M., & Mayer, J. W. (1986). Electron-energy-loss scattering near a single misfit dislocation at the GaAs/GaInAs interface. *Physical Review Letters*, *57*(21), 2729.

Bauerle, J. E. (1969). Study of Solid Electrolyte Polarization by a Complex Admittance Method. *Journal of Physics and Chemistry of Solids*, *30*, 2657–2670.

Bauerle, J. E., & Hrizo, J. (1969). Interpretation of the resistivity temperature dependence of high purity (ZrO 2) 0.90 (Y 2 O 3) 0.10. *Journal of Physics and Chemistry of Solids*, *30*(3), 565–570.

Bevan, D. J. M. (1955). Ordered intermediate phases in the system CeO2-Ce2O3. *Journal of Inorganic and Nuclear Chemistry*, *1*(1), 49–59. https://doi.org/10.1016/0022-1902(55)80067-X

Bishop, S. R., Stefanik, T. S., & Tuller, H. L. (2011). Electrical conductivity and defect equilibria of Pr0.1Ce0.9O2−δ. *Physical Chemistry Chemical Physics*, *13*(21), 10165. https://doi.org/10.1039/c0cp02920c

Bishop, S. R., Stefanik, T. S., & Tuller, H. L. (2012). Defects and transport in Prx Ce1−x O2−δ: Composition trends. *Journal of Materials Research*, *27*(15), 2009–2016. https://doi.org/10.1557/jmr.2012.130

Blennow, P., Chen, W., Lundberg, M., & Menon, M. (2009). Characterization of Ce0.9Gd0.1O1.95 powders synthesized by spray drying. *Ceramics International*, *35*(7), 2959–2963. https://doi.org/10.1016/j.ceramint.2009.04.003

Blumenthal, R. N., Brugner, F. S., & Garnier, J. E. (1973). The Electrical Conductivity of CaO-Doped Nonstoichiometric Cerium Dioxide from 700° to 1500° C. *Journal of the Electrochemical Society*, *120*(9), 1230–1237.

Boaro, M., Modafferi, V., Pappacena, A., Llorca, J., Baglio, V., Frusteri, F., … Antonucci, P. L. (2010). Comparison between Ni–Rh/gadolinia doped ceria catalysts in reforming of propane for anode implementations in intermediate solid oxide fuel cells. *Journal of Power Sources*, *195*(2), 649–661. https://doi.org/10.1016/j.jpowsour.2009.08.006

Bonanos, N., Steele, B. C. H., & Butler, E. P. (2005). Impedance spectroscopy: theory, experiment, and applications. In E. Barsoukov & M. J. Ross (Eds.), *Impedance Spectroscopy* (2nd ed., pp. 205–264). John Wiley & Sons.

Bowman, W. J., March, K., Hernandez, C. A., & Crozier, P. A. (2016). Measuring bandgap states in individual non-stoichiometric oxide nanoparticles using monochromated STEM EELS: The Praseodymium–ceria case. *Ultramicroscopy*, *167*, 5–10. https://doi.org/10.1016/j.ultramic.2016.04.009

Bowman, W. J., Zhu, J., Sharma, R., & Crozier, P. A. (2015). Electrical conductivity and grain boundary composition of Gd-doped and Gd/Pr co-doped ceria. *Solid State Ionics*, *272*, 9–17. https://doi.org/10.1016/j.ssi.2014.12.006

Brandon, D. G. (1966). The Structure of High-Angle Grain Boundaries. *Acta Metallurgica*, *14*, 1479–1484.

Brons, J. G., & Thompson, G. B. (2014). Abnormalities associated with grain growth in solid solution Cu(Ni) thin films. *Thin Solid Films*, *558*, 170–175. https://doi.org/10.1016/j.tsf.2014.03.009

Browning, N. D., Klie, R. F., & Lei, Y. (2004). Vacancy Segregation at Grain Boundaries in Ceramic Oxides. In *Mixed Ionic Electronic Conducting Perovskites for Advanced Energy Systems* (pp. 15–25). Kluwer.

Bueno, R. M., Martinez-Duart, J. M., Hernandez-Velez, M., & Vazquez, L. (1997). Optical and structural characterization of rf sputtered CeO2 thin films. *Journal of Materials Science*, *32*(7), 1861–1865.

Cantwell, P. R., Tang, M., Dillon, S. J., Luo, J., Rohrer, G. S., & Harmer, M. P. (2014). Grain boundary complexions. *Acta Materialia*, *62*, 1–48. https://doi.org/10.1016/j.actamat.2013.07.037

Chao, C.-C., Hsu, C.-M., Cui, Y., & Prinz, F. B. (2011). Improved Solid Oxide Fuel Cell Performance with Nanostructured Electrolytes. *ACS Nano*, *5*(7), 5692–5696. https://doi.org/10.1021/nn201354p

Chen, S.-Y., Chen, R.-J., Lee, W., Dong, C.-L., & Gloter, A. (2014). Spectromicroscopic evidence of interstitial and substitutional dopants in association with oxygen vacancies in Sm-doped ceria nanoparticles. *Physical Chemistry Chemical Physics*, *16*(7), 3274. https://doi.org/10.1039/c3cp54613f

Cho, P.-S., Lee, S. B., Cho, Y. H., Kim, D.-Y., Park, H.-M., & Lee, J.-H. (2008). Effect of CaO concentration on enhancement of grain-boundary conduction in gadolinia-doped ceria. *Journal of Power Sources*, *183*(2), 518–523. https://doi.org/10.1016/j.jpowsour.2008.05.041

Cho, P.-S., Lee, S. B., Kim, D.-S., Lee, J.-H., Kim, D.-Y., & Park, H.-M. (2006). Improvement of Grain-Boundary Conduction in Gadolinia-Doped Ceria by the Addition of CaO. *Electrochemical and Solid-State Letters*, *9*(9), A399. https://doi.org/10.1149/1.2214235

Cho, Y. H., Cho, P.-S., Auchterlonie, G., Kim, D. K., Lee, J.-H., Kim, D.-Y., … Drennan, J. (2007). Enhancement of grain-boundary conduction in gadolinia-doped ceria by the scavenging of highly resistive siliceous phase. *Acta Materialia*, *55*(14), 4807–4815. https://doi.org/10.1016/j.actamat.2007.05.001

Christie, G. M., & van Berkel, F. P. F. (1996). Microstructure-ionic conductivity relationships in ceria-gadolinia electrolytes. *Solid State Ionics*, *83*, 17–27.

Chueh, W. C., & Haile, S. M. (2010). A thermochemical study of ceria: exploiting an old material for new modes of energy conversion and CO2 mitigation. *Philosophical Transactions of the Royal Society A: Mathematical, Physical and Engineering Sciences*, *368*(1923), 3269–3294. https://doi.org/10.1098/rsta.2010.0114

Colliex, C., Cosslett, V. E., Leapman, R. D., & Trebbia, P. (1976). Contribution of electron energy loss spectroscopy to the development of analytical electron microscopy. *Ultramicroscopy*, *1*(3–4), 301–315.

Cook, J., Nuccitelli, D., Green, S. A., Richardson, M., Winkler, B., Painting, R., … Skuce, A. (2013). Quantifying the consensus on anthropogenic global warming in the scientific literature. *Environmental Research Letters*, *8*(2), 24024. https://doi.org/10.1088/1748-9326/8/2/024024

Costa-Nunes, O., Vohs, J. M., & Gorte, R. J. (2003). A Study of Direct-Conversion SOFC with n-Butane at Higher Fuel Utilization. *Journal of The Electrochemical Society*, *150*(7), A858. https://doi.org/10.1149/1.1574807

Crewe, A. V. (1966). Scanning Electron Microscopes: Is High Resolution Possible? *Science*, *154*(3750), 729–738.

Crewe, A. V., Wall, J., & Langmore, J. (1970). Visibility of Single Atoms. *Science*, *168*(3937), 1338–1340.

Crozier, P. A. (1995). Quantitative elemental mapping of materials by energy-filtered imaging. *Ultramicroscopy*, *58*, 157–174.

Crozier, P. A., Aoki, T., & Liu, Q. (2016). Detection of water and its derivatives on individual nanoparticles using vibrational electron energy-loss spectroscopy. *Ultramicroscopy*, *169*, 30–36. https://doi.org/10.1016/j.ultramic.2016.06.008

Crozier, P. A., & Miller, B. K. (2015). Spectroscopy of Solids, Gases and Liquids in the ETEM. In T. W. Hansen & J. B. Wagner (Eds.), *Controlled Atmosphere Transmission Electron Microscopy*. New York: Springer.

Darbal, A. D., Ganesh, K. J., Liu, X., Lee, S.-B., Ledonne, J., Sun, T., … Barmak, K. (2013). Grain Boundary Character Distribution of Nanocrystalline Cu Thin Films Using Stereological Analysis of Transmission Electron Microscope Orientation Maps. *Microscopy and Microanalysis*, *19*(1), 111–119. https://doi.org/10.1017/S1431927612014055

Darbal, A. D., Gemmi, M., Portillo, J., Rauch, E., & Nicolopoulos, S. (2012). Nanoscale Automated Phase and Orientation Mapping in the TEM. *Microscopy Today*, *20*(6), 38–42. https://doi.org/10.1017/S1551929512000818

Dholabhai, P. P., Adams, J. B., Crozier, P. A., & Sharma, R. (2011). In search of enhanced electrolyte materials: a case study of doubly doped ceria. *Journal of Materials Chemistry*, *21*(47), 18991. https://doi.org/10.1039/c1jm14417k

Dholabhai, P. P., Adams, J. B., Crozier, P., & Sharma, R. (2010). Oxygen vacancy migration in ceria and Pr-doped ceria: A DFT+U study. *The Journal of Chemical Physics*, *132*(9), 94104. https://doi.org/10.1063/1.3327684

Diercks, D. R., Tong, J., Zhu, H., Kee, R., Baure, G., Nino, J. C., … Gorman, B. P. (2016). Three-dimensional quantification of composition and electrostatic potential at individual grain boundaries in doped ceria. *J. Mater. Chem. A*, *4*(14), 5167–5175. https://doi.org/10.1039/C5TA10064J

Dillon, S. J., Tang, M., Carter, W. C., & Harmer, M. P. (2007). Complexion: A new concept for kinetic engineering in materials science. *Acta Materialia*, *55*(18), 6208–6218. https://doi.org/10.1016/j.actamat.2007.07.029

Dimos, D., Chaudhari, P., Mannhart, J., & LeGoues, F. K. (1988). Orientation Dependence of Grain-Boundary Critical Currents in Y Ba 2 Cu 3 O 7- δ Bicrystals. *Physical Review Letters*, *61*(2), 219.

Donald, A. M., & Craven, A. J. (1979). A study of grain boundary segregation in Cu-Bi alloys using STEM. *Philosophical Magazine A*, *39*(1), 1–11. https://doi.org/10.1080/01418617908239271

Dudek, M., Rapacz-Kmita, A., Mroczkowska, M., Mosiałek, M., & Mordarski, G. (2010). Co-doped ceria-based solid solution in the CeO2–M2O3–CaO, M=Sm, Gd system. *Electrochimica Acta*, *55*(14), 4387–4394. https://doi.org/10.1016/j.electacta.2010.01.039

Ebbesen, S. D., & Mogensen, M. (2009). Electrolysis of carbon dioxide in Solid Oxide Electrolysis Cells. *Journal of Power Sources*, *193*(1), 349–358. https://doi.org/10.1016/j.jpowsour.2009.02.093

Egerton, R. F. (1975). Inelastic scattering of 80 keV electrons in amorphous carbon. *Philosophical Magazine*, *31*(1), 199–215.

Egerton, R. F. (1991). Factors affecting the accuracy of elemental analysis by transmission EELS. *Microscopy Microanalysis Microstructures*, *2*(2–3), 203–213. https://doi.org/10.1051/mmm:0199100202-3020300

Egerton, R. F. (2011). *Electron Energy-Loss Spectroscopy in the Electron Microscope* (3rd ed.). New York: Springer.

Eguchi, K., Kunisaki, T., & Arai, H. (1986). Effect of Microstructures on the Ionic Conductivity of Ceria-Calcia Oxides. *Journal of the American Ceramic Society*, *69*(11), c282–c285.

Eguchi, K., Setoguchi, T., Inoue, T., & Arai, H. (1992). Electrical properties of ceria-based oxides and their application to solid oxide fuel cells. *Solid State Ionics*, *52*(1–3), 165–172.

Erni, R., & Browning, N. D. (2008). The impact of surface and retardation losses on valence electron energy-loss spectroscopy. *Ultramicroscopy*, *108*(2), 84–99. https://doi.org/10.1016/j.ultramic.2007.03.005

Esposito, V., & Traversa, E. (2008). Design of Electroceramics for Solid Oxides Fuel Cell Applications: Playing with Ceria. *Journal of the American Ceramic Society*, *91*(4), 1037–1051. https://doi.org/10.1111/j.1551-2916.2008.02347.x

Fergus, J. W. (2007). Materials challenges for solid-oxide fuel cells. *Jom*, *59*(12), 56–62.

Findlay, S. D., Azuma, S., Shibata, N., Okunishi, E., & Ikuhara, Y. (2011). Direct oxygen imaging within a ceramic interface, with some observations upon the dark contrast at the grain boundary. *Ultramicroscopy*, *111*(4), 285–289. https://doi.org/10.1016/j.ultramic.2010.12.022

Franceschetti, D. R. (1981). Local thermodynamic formalism for space charge in ionic crystals. *Solid State Ionics*, *2*(1), 39–42.

Fuel Cell Today. (2013). *The Fuel Cell Industry Review 2013*.

Gaye, A. (2007). Access to energy and human development. *Human Development Report*, *2008*. Retrieved from http://citeseerx.ist.psu.edu/viewdoc/download?doi=10.1.1.422.3937&rep=rep1&type=pdf

Gerhardt, R., Nowick, A. S., Mochel, M. E., & Dumler, I. (1986). Grain-Boundary Effect in Ceria Doped with Trivalent Cations: II, Microstructure and Microanalysis. *Journal of the American Ceramic Society*, *69*(9), 647–651.

Gerhardt-Anderson, R., & Nowick, A. S. (1981). Ionic Conductivity of CeO2 with Trivalent Dopants of Different Ionic Radii. *Solid State Ionics*, *5*, 547–550.

Giannuzzi, L. A. (2006). *Introduction to focused ion beams: instrumentation, theory, techniques and practice*. Springer Science & Business Media.

Goubin, F., Rocquefelte, X., Whangbo, M.-H., Montardi, Y., Brec, R., & Jobic, S. (2004). Experimental and Theoretical Characterization of the Optical Properties of CeO_2, $SrCeO_3$, and Sr_2CeO_4 Containing Ce^{4+} (f^0) Ions. *Chemistry of Materials*, *16*(4), 662–669. https://doi.org/10.1021/cm034618u

Guo, X., & Maier, J. (2001). Grain Boundary Blocking Effect in Zirconia: A Schottky Barrier Analysis. *Journal of The Electrochemical Society*, *148*(3), E121. https://doi.org/10.1149/1.1348267

Guo, X., Sigle, W., & Maier, J. (2003). Blocking Grain Boundaries in Yttria-Doped and Undoped Ceria Ceramics of High Purity. *Journal of the American Ceramic Society*, *86*(1), 77–87.

Guo, X., & Waser, R. (2004). Space charge concept for acceptor-doped zirconia and ceria and experimental evidences. *Solid State Ionics*, *173*(1–4), 63–67. https://doi.org/10.1016/j.ssi.2004.07.053

Haile, S. M. (2003). Fuel cell materials and components. *Acta Materialia*, *51*(19), 5981–6000. https://doi.org/10.1016/j.actamat.2003.08.004

Haile, S. M., West, D. L., & Campbell, J. (1998). The role of microstructure and processing on the proton conducting properties of gadolinium-doped barium cerate. *Journal of Materials Research*, *13*(6), 1576–1595.

Hartridge, A., Krishna, M. G., & Bhattacharya, A. K. (1998). Optical Constants of Nanocrystalline Lanthanide-Doped Ceria Thin Films with the Fluorite Structure. *J. Phys. Chem. Solids*, *59*(6–7), 859–866.

Hass, G., Ramsey, J. B., & Thun, R. (1958). Optical properties and structure of cerium dioxide films. *JOSA*, *48*(5), 324–326.

Helmick, L., Dillon, S. J., Gerdes, K., Gemmen, R., Rohrer, G. S., Seetharaman, S., & Salvador, P. A. (2011). Crystallographic Characteristics of Grain Boundaries in Dense Yttria-Stabilized Zirconia: Crystallography of Grain Boundaries in YSZ. *International Journal of Applied Ceramic Technology*, *8*(5), 1218–1228. https://doi.org/10.1111/j.1744-7402.2010.02567.x

Heyraud, S., Blanchard, P. E. R., Liu, S., Zhou, Q., Kennedy, B. J., Brand, H. E. A., … Hester, J. R. (2013). Structural and magnetic studies of the electron doped manganites $Sr_{0.65}Pr_{0.35-x}Ce_xMnO_3$ ($0.00 \leq x \leq 0.35$). *Journal of Physics: Condensed Matter*, *25*(33), 335401. https://doi.org/10.1088/0953-8984/25/33/335401

Hillier, J. (1943). On microanalysis by electrons. *Physical Review*, *64*(9–10), 318.

Hojo, H., Mizoguchi, T., Ohta, H., Findlay, S. D., Shibata, N., Yamamoto, T., & Ikuhara, Y. (2010). Atomic Structure of a CeO_2 Grain Boundary: The Role of Oxygen Vacancies. *Nano Letters*, *10*(11), 4668–4672. https://doi.org/10.1021/nl1029336

Huang, H., Gür, T. M., Saito, Y., & Prinz, F. (2006). High ionic conductivity in ultrathin nanocrystalline gadolinia-doped ceria films. *Applied Physics Letters*, *89*(14), 143107. https://doi.org/10.1063/1.2358851

Huang, T.-J., & Chen, H.-M. (2010). Hydrogen production via steam reforming of methanol over Cu/(Ce,Gd)O2−x catalysts. *International Journal of Hydrogen Energy*, *35*(12), 6218–6226. https://doi.org/10.1016/j.ijhydene.2010.03.082

International Energy Agency (Ed.). (2014). *Renewable Energy Medium-Term Market Report 2014 Executive Summary*.

Isaacson, M., & Johnson, D. (1975). The microanalysis of light elements using transmitted energy loss electrons. *Ultramicroscopy*, *1*(1), 33–52.

Jang, W. S., Hyun, S. H., & Kim, S. G. (2002). Preparation of YSZ/YDC and YSZ/GDC composite electrolytes by the tape casting and sol-gel dip-drawing coating method for low-temperature SOFC. *Journal of Materials Science*, *37*(12), 2535–2541.

Jasper, A., Kilner, J. A., & McComb, D. W. (2008). TEM and impedance spectroscopy of doped ceria electrolytes. *Solid State Ionics*, *179*(21–26), 904–908. https://doi.org/10.1016/j.ssi.2008.02.001

Jiang, J., Hu, X., Shen, W., Ni, C., & Hertz, J. L. (2013). Improved ionic conductivity in strained yttria-stabilized zirconia thin films. *Applied Physics Letters*, *102*(14), 143901. https://doi.org/10.1063/1.4801649

Kalkowski, G., Kaindl, G., Wortmann, G., Lentz, D., & Krause, S. (1988). 4f-ligand hybridization in CeF 4 and TbF 4 probed by core-level spectroscopies. *Physical Review B*, *37*(3), 1376.

Kang, Z. C., & Eyring, L. (1997). A compositional and structural rationalization of the higher oxides of Ce, Pr, and Tb. *Journal of Alloys and Compounds*, *249*(1), 206–212. https://doi.org/10.1016/S0925-8388(96)02633-3

Kelly, M. N., Glowinski, K., Nuhfer, N. T., & Rohrer, G. S. (2016). The five parameter grain boundary character distribution of α-Ti determined from three-dimensional orientation data. *Acta Materialia*, *111*, 22–30. https://doi.org/10.1016/j.actamat.2016.03.029

Kharton, V. V., Viskup, A. P., Figueiredo, F. M., Naumovich, E. N., Shaulo, A. L., & Marques, F. B. M. (2002). Electrochemical properties of Pr-doped Ce(Gd)O2-d. *Materials Letters*, *53*, 160–164.

Kilner, J. A., & Brook, R. J. (1982). A study of oxygen ion conductivity in doped non-stoichiometric oxides. *Solid State Ionics*, *6*(3), 237–252. https://doi.org/10.1016/0167-2738(82)90045-5

Kilner, J. A., & Waters, C. D. (1982). The effects of dopant cation-oxygen vacancy complexes on the anion transport properties of non-stoichiometric fluorite oxides. *Solid State Ionics*, *6*(3), 253–259.

Kim, J. J., Bishop, S. R., Thompson, N. J., Chen, D., & Tuller, H. L. (2014). Investigation of Nonstoichiometry in Oxide Thin Films by Simultaneous *in Situ* Optical Absorption and Chemical Capacitance Measurements: Pr-Doped Ceria, a

Case Study. *Chemistry of Materials*, *26*(3), 1374–1379. https://doi.org/10.1021/cm403066p

Kim, J. J., Bishop, S. R., Thompson, N., Kuru, Y., & Tuller, H. L. (2012). Optically derived energy band gap states of Pr in ceria. *Solid State Ionics*, *225*, 198–200. https://doi.org/10.1016/j.ssi.2012.03.047

Kim, M., Duscher, G., Browning, N. D., Sohlberg, K., Pantelides, S. T., & Pennycook, S. J. (2001). Nonstoichiometry and the Electrical Activity of Grain Boundaries in SrTiO 3. *Physical Review Letters*, *86*(18), 4056–4059. https://doi.org/10.1103/PhysRevLett.86.4056

Kim, S., Fleig, J., & Maier, J. (2003). Space charge conduction: Simple analytical solutions for ionic and mixed conductors and application to nanocrystalline ceria. *Phys. Chem. Chem. Phys.*, *5*(11), 2268–2273. https://doi.org/10.1039/B300170A

Kim, S., Jain, P., Avila-Paredes, H. J., Thron, A., van Benthem, K., & Sen, S. (2010). Strong immobilization of charge carriers near the surface of a solid oxide electrolyte. *Journal of Materials Chemistry*, *20*(19), 3855. https://doi.org/10.1039/b926664j

Kim, S., Kim, S. K., Khodorov, S., Maier, J., & Lubomirsky, I. (2016). On determining the height of the potential barrier at grain boundaries in ion-conducting oxides. *Phys. Chem. Chem. Phys.*, *18*(4), 3023–3031. https://doi.org/10.1039/C5CP06387F

Kim, S., & Maier, J. (2002). On the Conductivity Mechanism of Nanocrystalline Ceria. *Journal of The Electrochemical Society*, *149*(10), J73. https://doi.org/10.1149/1.1507597

King, A. H., & Shekhar, S. (2006). What does it mean to be special? The significance and application of the Brandon criterion. *Journal of Materials Science*, *41*(23), 7675–7682. https://doi.org/10.1007/s10853-006-0665-8

Kingery, W. D., Bowen, H. K., & Uhlmann, D. R. (1976). *Introduction to Ceramics* (2nd ed.). New York: Wiley-Interscience.

Kliewer, K. L., & Koehler, J. S. (1965). Space charge in ionic crystals. I. General approach with application to NaCl. *Physical Review*, *140*(4A), A1226.

Korte, C., Peters, A., Janek, J., Hesse, D., & Zakharov, N. (2008). Ionic conductivity and activation energy for oxygen ion transport in superlattices—the semicoherent multilayer system YSZ (ZrO2 + 9.5 mol% Y2O3)/Y2O3. *Physical Chemistry Chemical Physics*, *10*(31), 4623. https://doi.org/10.1039/b801675e

Kotov, V., & Reichstein, S. (1941). *Zhurnal Fizicheskoi Khimii*, *15*, 1057–1058.

Krivanek, O. L., Ahn, C. C., & Keeney, R. B. (1987). Parallel detection electron spectrometer using quadrupole lenses. *Ultramicroscopy*, *22*(1–4), 103–115.

Krivanek, O. L., Dellby, N., & Lupini, A. R. (1999). Towards sub-Å electron beams. *Ultramicroscopy*, *78*(1), 1–11.

Krivanek, O. L., Lovejoy, T. C., Dellby, N., Aoki, T., Carpenter, R. W., Rez, P., … Crozier, P. A. (2014). Vibrational spectroscopy in the electron microscope. *Nature*, *514*(7521), 209–212. https://doi.org/10.1038/nature13870

Kröger, F. A., & Vink, H. J. (1956). Relationships between the Concentrations of Imperfections in Crystalline Solids. *Journal of Solid State Physics*, *3*, 307–435.

Kudo, T., & Obayashi, H. (1976). Mixed Electrical Conduction in the Fluorite-Type Ce1-x Gdx O2-x/2. *Journal of The Electrochemical Society*, *123*(3), 415–419.

Lasia, A. (1999). Electrochemical Impedance Spectroscopy and its Applications. In B. E. Conway, J. Bockris, & R. E. White (Eds.), *Modern Aspects of Electrochemistry* (Vol. 32, pp. 143–248). New York: Kluwer.

Lazar, S., Botton, G. A., Wu, M.-Y., Tichelaar, F. D., & Zandbergen, H. W. (2003). Materials science applications of HREELS in near edge structure analysis and low-energy loss spectroscopy. *Ultramicroscopy*, *96*(3–4), 535–546. https://doi.org/10.1016/S0304-3991(03)00114-1

Lee, H. B., Prinz, F. B., & Cai, W. (2013). Atomistic simulations of grain boundary segregation in nanocrystalline yttria-stabilized zirconia and gadolinia-doped ceria solid oxide electrolytes. *Acta Materialia*, *61*(10), 3872–3887. https://doi.org/10.1016/j.actamat.2013.03.027

Lee, K. T., Jung, D. W., Camaratta, M. A., Yoon, H. S., Ahn, J. S., & Wachsman, E. D. (2012). Gd0.1Ce0.9O1.95/Er0.4Bi1.6O3 bilayered electrolytes fabricated by a simple colloidal route using nano-sized Er0.4Bi1.6O3 powders for high performance low temperature solid oxide fuel cells. *Journal of Power Sources*, *205*, 122–128. https://doi.org/10.1016/j.jpowsour.2012.01.040

Lee, W., Jung, H. J., Lee, M. H., Kim, Y.-B., Park, J. S., Sinclair, R., & Prinz, F. B. (2012). Oxygen Surface Exchange at Grain Boundaries of Oxide Ion Conductors. *Advanced Functional Materials*, *22*(5), 965–971. https://doi.org/10.1002/adfm.201101996

Lei, Y., Ito, Y., Browning, N. D., & Mazanec, T. J. (2002). Segregation Effects at Grain Boundaries in Fluorite-Structured Ceramics. *Journal of the American Ceramic Society*, *85*(9), 2359–2363.

Litzelman, S. J., De Souza, R. A., Butz, B., Tuller, H. L., Martin, M., & Gerthsen, D. (2009). Heterogeneously doped nanocrystalline ceria films by grain boundary

diffusion: Impact on transport properties. *Journal of Electroceramics*, *22*(4), 405–415. https://doi.org/10.1007/s10832-008-9445-y

Liu, Q., March, K., & Crozier, P. A. (2016). Nanoscale probing of bandgap states on oxide particles using electron energy-loss spectroscopy. *Ultramicroscopy*. https://doi.org/10.1016/j.ultramic.2016.06.010

Longo, V., & Podda, L. (1978). Phase Equilibrium Diagram of the Ternary System CaO-MgO-CeO2 Between 1700 and 1200 C. *Journal of the American Ceramic Society-Discussions and Notes*, *61*(7–8), 370–371.

López-Cartes, C., Bernal, S., Calvino, J. J., Cauqui, M. A., Blanco, G., Pérez-Omil, J. A., … Hansen, P. L. (2003). In situ transmission electron microscopy investigation of Ce(iv) and Pr(iv) reducibility in a Rh (1%)/Ce0.8Pr0.2O2–x catalyst. *Chemical Communications*, (5), 644–645. https://doi.org/10.1039/b211786j

Lubke, S., & Wiemhofer, H.-D. (1999). Electronic conductivity of Gd-doped ceria with additional Pr-doping. *Solid State Ionics*, *117*, 229–243.

Lundberg, M., Wang, H.-J., Blennow, P., & Menon, M. (2011). Mesoporous high surface area Ce0.9Gd0.1O1.95 synthesized by spray drying. *Ceramics International*, *37*(3), 797–802. https://doi.org/10.1016/j.ceramint.2010.10.024

Ma, C., Chen, K., Liang, C., Nan, C.-W., Ishikawa, R., More, K., & Chi, M. (2014). Atomic-scale origin of the large grain-boundary resistance in perovskite Li-ion-conducting solid electrolytes. *Energy & Environmental Science*, *7*(5), 1638. https://doi.org/10.1039/c4ee00382a

Mackenzie, J. K. (1958). Second Paper on Statistics Associated with the Random Disorientation of Cubes. *Biometrika*, *45*(1/2), 229. https://doi.org/10.2307/2333059

Mackenzie, J. K., & Thomson, M. J. (1957). Some statistics associated with the random disorientation of cubes. *Biometrika*, *44*(1–2), 205–210.

Maier, J. (1986). On the conductivity of polycrystalline materials. *Berichte Der Bunsengesellschaft Für Physikalische Chemie*, *90*(1), 26–33.

Maier, J. (1995). Ionic conduction in space charge regions. *Progress in Solid State Chemistry*, *23*(3), 171–263.

Manoubi, T., Colliex, C., & Rez, P. (1990). Quantitative Electron Energy Loss Spectroscopy on M45 Edges in Rare Earth Oxides. *Journal of Electron Spectroscopy and Related Phenomena*, *50*, 1–18.

Mansilla, C. (2009). Structure, microstructure and optical properties of cerium oxide thin films prepared by electron beam evaporation assisted with ion beams. *Solid State*

Sciences, *11*(8), 1456–1464. https://doi.org/10.1016/j.solidstatesciences.2009.05.001

Marabelli, F., & Wachter, P. (1987). Covalent insulator CeO 2: optical reflectivity measurements. *Physical Review B*, *36*(2), 1238.

Mason, J. K., & Schuh, C. A. (2009). The generalized Mackenzie distribution: Disorientation angle distributions for arbitrary textures. *Acta Materialia*, *57*(14), 4186–4197. https://doi.org/10.1016/j.actamat.2009.05.016

Mebane, D. S., & De Souza, R. A. (2015). A generalised space-charge theory for extended defects in oxygen-ion conducting electrolytes: from dilute to concentrated solid solutions. *Energy Environ. Sci.*, *8*(10), 2935–2940. https://doi.org/10.1039/C5EE02060C

Mermelstein, J., Millan, M., & Brandon, N. (2010). The impact of steam and current density on carbon formation from biomass gasification tar on Ni/YSZ, and Ni/CGO solid oxide fuel cell anodes. *Journal of Power Sources*, *195*(6), 1657–1666. https://doi.org/10.1016/j.jpowsour.2009.09.046

Mogensen, M., Sammes, N. M., & Tompsett, G. A. (2000). Physical, chemical and electrochemical properties of pure and doped ceria. *Solid State Ionics*, *129*(1–4), 63–94. https://doi.org/10.1016/S0167-2738(99)00318-5

Moulson, A. J., & Herbert, J. M. (2003). *Electroceramics: materials, properties, applications* (2nd ed). West Sussex ; New York: Wiley.

Mullins, D. R., Overbury, S. H., & Huntley, D. R. (1998). Electron spectroscopy of single crystal and polycrystalline cerium oxide surfaces. *Surface Science*, *409*, 307–319.

Ni, D. W., Florio, D. Z. de, Marani, D., Kaiser, A., Tinti, V. B., & Esposito, V. (2015). Effect of chemical redox on Gd-doped ceria mass diffusion. *Journal of Materials Chemistry A*, *3*(37), 18835–18838. https://doi.org/10.1039/C5TA05537G

Niu, G., Schubert, M. A., d'Acapito, F., Zoellner, M. H., Schroeder, T., & Boscherini, F. (2014). On the local electronic and atomic structure of Ce1−xPrxO2−δ epitaxial films on Si. *Journal of Applied Physics*, *116*(12), 123515. https://doi.org/10.1063/1.4896590

Nowick, A. S., & Park, D. S. (1976). Fluorite-type oxygen conductors. In *Superionic Conductors* (pp. 395–412). Springer. Retrieved from http://link.springer.com/chapter/10.1007/978-1-4615-8789-7_58

Omar, S., Wachsman, E. D., Jones, J. L., & Nino, J. C. (2009). Crystal Structure-Ionic Conductivity Relationships in Doped Ceria Systems. *Journal of the American Ceramic Society*, *92*(11), 2674–2681. https://doi.org/10.1111/j.1551-2916.2009.03273.x

Omar, S., Wachsman, E., & Nino, J. (2006). A co-doping approach towards enhanced ionic conductivity in fluorite-based electrolytes. *Solid State Ionics*, *177*(35–36), 3199–3203. https://doi.org/10.1016/j.ssi.2006.08.014

Omar, S., Wachsman, E., & Nino, J. (2008). Higher conductivity Sm3+ and Nd3+ co-doped ceria-based electrolyte materials. *Solid State Ionics*, *178*(37–38), 1890–1897. https://doi.org/10.1016/j.ssi.2007.12.069

Ou, D. R., Mori, T., Ye, F., Kobayashi, T., Zou, J., Auchterlonie, G., & Drennan, J. (2006). Oxygen vacancy ordering in heavily rare-earth-doped ceria. *Applied Physics Letters*, *89*(17), 171911. https://doi.org/10.1063/1.2369881

Ou, D. R., Mori, T., Ye, F., Zou, J., Auchterlonie, G., & Drennan, J. (2008). Oxygen-vacancy ordering in lanthanide-doped ceria: Dopant-type dependence and structure model. *Physical Review B*, *77*(2). https://doi.org/10.1103/PhysRevB.77.024108

Ou, D. R., Ye, F., & Mori, T. (2011). Defect clustering and local ordering in rare earth co-doped ceria. *Physical Chemistry Chemical Physics*, *13*(20), 9554. https://doi.org/10.1039/c0cp02174a

Özer, N. (2001). Optical properties and electrochromic characterization of sol–gel deposited ceria films. *Solar Energy Materials and Solar Cells*, *68*(3), 391–400.

Pachauri, R. K., Mayer, L., & Intergovernmental Panel on Climate Change (Eds.). (2015). *Climate change 2014: synthesis report*. Geneva, Switzerland: Intergovernmental Panel on Climate Change.

Park, J.-Y., & Wachsman, E. D. (2006). Stable and high conductivity ceria/bismuth oxide bilayer electrolytes for lower temperature solid oxide fuel cells. *Ionics*, *12*(1), 15–20. https://doi.org/10.1007/s11581-006-0010-x

Patala, S., Mason, J. K., & Schuh, C. A. (2012). Improved representations of misorientation information for grain boundary science and engineering. *Progress in Materials Science*, *57*(8), 1383–1425. https://doi.org/10.1016/j.pmatsci.2012.04.002

Patsalas, P., Logothetidis, S., & Metaxa, C. (2002). Optical performance of nanocrystalline transparent ceria films. *Applied Physics Letters*, *81*(3), 466. https://doi.org/10.1063/1.1494458

Patterson, A. L. (1939). The Scherrer Formula for X-Ray Particle Size Determination. *Physical Review*, *56*, 978–982.

Pennycook, S. J., & Nellist, P. D. (Eds.). (2011). *Scanning Transmission Electron Microscopy: Imaging and Analysis*. New York: Springer.

Pikalova, E. Y., Murashkina, A. A., Maragou, V. I., Demin, A. K., Strekalovsky, V. N., & Tsiakaras, P. E. (2011). CeO2 based materials doped with lanthanides for applications in intermediate temperature electrochemical devices. *International Journal of Hydrogen Energy*, *36*(10), 6175–6183. https://doi.org/10.1016/j.ijhydene.2011.01.132

Rawlence, M., Garbayo, I., Buecheler, S., & Rupp, J. L. M. (2016). On the chemical stability of post-lithiated garnet Al-stabilized Li $_7$ La $_3$ Zr $_2$ O $_{12}$ solid state electrolyte thin films. *Nanoscale*, *8*(31), 14746–14753. https://doi.org/10.1039/C6NR04162K

Rez, P., Aoki, T., March, K., Gur, D., Krivanek, O. L., Dellby, N., … Cohen, H. (2016). Damage-free vibrational spectroscopy of biological materials in the electron microscope. *Nature Communications*, *7*, 10945. https://doi.org/10.1038/ncomms10945

Rivacoba, A., Zabala, N., & Aizpurua, J. (2000). Image potential in scanning transmission electron microscopy. *Progress in Surface Science*, *65*(1), 1–64.

Rohrer, G. S. (2011). Measuring and Interpreting the Structure of Grain-Boundary Networks: Measuring and Interpreting the Structure of Grain-Boundary Networks. *Journal of the American Ceramic Society*, *94*(3), 633–646. https://doi.org/10.1111/j.1551-2916.2011.04384.x

Rohrer, G. S., Saylor, D. M., Dasher, B. E., Adams, B. L., Rollett, A. D., & Wynblatt, P. (2004). The distribution of internal interfaces in polycrystals. *Zeitschrift Für Metallkunde*, *95*(4), 197–214.

Rose, H. (1974). Phase Contrast in Scanning Transmission Electron Microscopy. *Optik*, *39*(4), 416–436.

Rossignol, C., Roman, B., Benetti, G. D., & Djurado, E. (2011). Elaboration of thin and dense CGO films adherent to YSZ by electrostatic spray deposition for IT-SOFC applications. *New Journal of Chemistry*, *35*(3), 716. https://doi.org/10.1039/c0nj00570c

Ruiz-Trejo, E. (2013). The optical band gap of Gd-doped CeO2 thin films as function of temperature and composition. *Journal of Physics and Chemistry of Solids*, *74*(4), 605–610. https://doi.org/10.1016/j.jpcs.2012.12.014

Rupp, J. L. M., Fabbri, E., Marrocchelli, D., Han, J.-W., Chen, D., Traversa, E., … Yildiz, B. (2014). Scalable Oxygen-Ion Transport Kinetics in Metal-Oxide Films: Impact of Thermally Induced Lattice Compaction in Acceptor Doped Ceria Films. *Advanced Functional Materials*, *24*(11), 1562–1574. https://doi.org/10.1002/adfm.201302117

Rupp, J. L. M., & Gauckler, L. (2006). Microstructures and electrical conductivity of nanocrystalline ceria-based thin films. *Solid State Ionics*, *177*(26–32), 2513–2518. https://doi.org/10.1016/j.ssi.2006.07.033

Rupp, J. L. M., Infortuna, A., & Gauckler, L. J. (2006). Microstrain and self-limited grain growth in nanocrystalline ceria ceramics. *Acta Materialia*, *54*(7), 1721–1730. https://doi.org/10.1016/j.actamat.2005.11.032

Ruska, E. (1987). The development of the electron microscope and of electron microscopy. *Reviews of Modern Physics*, *59*(3), 627.

Saylor, D. M., Morawiec, A., Adams, B. L., & Rohrer, G. S. (2000). Misorientation dependence of the grain boundary energy in magnesia. *Interface Science*, *8*(2–3), 131–140.

Saylor, D. M., & Rohrer, G. S. (2002). Determining Crystal Habits from Observations of Planar Sections. *Journal of the American Ceramic Society*, *85*(11), 2799–2804.

Schmale, K., Grünebaum, M., Janssen, M., Baumann, S., Schulze-Küppers, F., & Wiemhöfer, H.-D. (2011). Electronic conductivity of Ce0.8Gd0.2−xPrxO2−δ and influence of added CoO. *Physica Status Solidi (B)*, *248*(2), 314–322. https://doi.org/10.1002/pssb.201046365

Schweiger, S., Kubicek, M., Messerschmitt, F., Murer, C., & Rupp, J. L. M. (2014). A Microdot Multilayer Oxide Device: Let Us Tune the Strain-Ionic Transport Interaction. *ACS Nano*, *8*(5), 5032–5048. https://doi.org/10.1021/nn501128y

Shannon, R. D., Shannon, R. C., Medenbach, O., & Fischer, R. X. (2002). Refractive Index and Dispersion of Fluorides and Oxides. *Journal of Physical and Chemical Reference Data*, *31*(4), 931. https://doi.org/10.1063/1.1497384

Sharma, V., Crozier, P. A., Sharma, R., & Adams, J. B. (2012). Direct observation of hydrogen spillover in Ni-loaded Pr-doped ceria. *Catalysis Today*, *180*(1), 2–8. https://doi.org/10.1016/j.cattod.2011.09.009

Sharma, V., Eberhardt, K. M., Sharma, R., Adams, J. B., & Crozier, P. A. (2010). A spray drying system for synthesis of rare-earth doped cerium oxide nanoparticles. *Chemical Physics Letters*, *495*(4–6), 280–286. https://doi.org/10.1016/j.cplett.2010.06.060

Shelef, M., & McCabe, R. W. (2000). Twenty-five years after introduction of automotive catalysts: what next? *Catalysis Today*, *62*(1), 35–50. https://doi.org/10.1016/S0920-5861(00)00407-7

Shen, C. H., Liu, R. S., Lin, J. G., & Huang, C. Y. (2001). Phase stability study of La 1.2 Ca 1.8 Mn 2 O 7. *Materials Research Bulletin*, *36*(5), 1139–1148.

Shibata, N., Oba, F., Yamamoto, T., & Ikuhara, Y. (2004). Structure, energy and solute segregation behaviour of [110] symmetric tilt grain boundaries in yttria-stabilized cubic zirconia. *Philosophical Magazine*, *84*(23), 2381–2415. https://doi.org/10.1080/14786430410001693463

Steele, B. C. H. (2000). Appraisal of Ce1−yGdyO2−y/2 electrolytes for IT-SOFC operation at 500°C. *Solid State Ionics*, *129*(1–4), 95–110. https://doi.org/10.1016/S0167-2738(99)00319-7

Stefanik, T. S. (2004). *Electrical Properties and Defect Structure of Praseodymium-Cerium Oxide Solid Solutions*. Massachusetts Institute of Technology, Cambridge, MA.

Stefanik, T. S., & Tuller, H. L. (2001). Ceria-based gas sensors. *Journal of the European Ceramic Society*, *21*, 1967–1970.

Stefanik, T. S., & Tuller, H. L. (2004). Nonstoichiometry and defect chemistry in praseodymium-cerium oxide. *Journal of Electroceramics*, *13*(1–3), 799–803.

Stöger-Pollach, M., Franco, H., Schattschneider, P., Lazar, S., Schaffer, B., Grogger, W., & Zandbergen, H. W. (2006). Čerenkov losses: A limit for bandgap determination and Kramers–Kronig analysis. *Micron*, *37*(5), 396–402. https://doi.org/10.1016/j.micron.2006.01.001

Sugar, J., Brewer, W. D., Kalkowski, G., Kaindl, G., & Paparazzo, E. (1985). Photoabsorption by the 3d shell in Ce, Pr, Ho, and Er: Observation and calculations. *Physical Review A*, *32*(4), 2242–2248.

Sun, L., Marrocchelli, D., & Yildiz, B. (2015). Edge dislocation slows down oxide ion diffusion in doped CeO2 by segregation of charged defects. *Nature Communications*, *6*, 6294. https://doi.org/10.1038/ncomms7294

Sunarso, J., Baumann, S., Serra, J. M., Meulenberg, W. A., Liu, S., Lin, Y. S., & Diniz da Costa, J. C. (2008). Mixed ionic–electronic conducting (MIEC) ceramic-based membranes for oxygen separation. *Journal of Membrane Science*, *320*(1–2), 13–41. https://doi.org/10.1016/j.memsci.2008.03.074

Sutton, A. P., & Balluffi, R. W. (1995). *Interfaces in Crystalline Materials*. Clarendon Press.

Timmermann, H., Fouquet, D., Weber, A., Ivers-Tiffée, E., Hennings, U., & Reimert, R. (2006). Internal Reforming of Methane at Ni/YSZ and Ni/CGO SOFC Cermet Anodes. *Fuel Cells*, *6*(3–4), 307–313. https://doi.org/10.1002/fuce.200600002

Tong, W., Yang, H., Moeck, P., Nandasiri, M. I., & Browning, N. D. (2013). General schema for [001] tilt grain boundaries in dense packing cubic crystals. *Acta Materialia*, *61*(9), 3392–3398. https://doi.org/10.1016/j.actamat.2013.02.029

Treacy, M. M. J., Howie, A., & Wilson, C. J. (1978). Z contrast of platinum and palladium catalysts. *Philosophical Magazine A*, *38*(5), 569–585. https://doi.org/10.1080/01418617808239255

Trovarelli, A. (2002). *Catalysis by Ceria and Related Materials*. London: Imperial College Press.

Tschöpe, A. (2001). Grain size-dependent electrical conductivity of polycrystalline cerium oxide II: Space charge model. *Solid State Ionics*, *139*(3), 267–280.

Tschöpe, A., & Birringer, R. (2001). Grain size dependence of electrical conductivity in polycrystalline cerium oxide. *Journal of Electroceramics*, *7*(3), 169–177.

Tschöpe, A., Kilassonia, S., & Birringer, R. (2004). The grain boundary effect in heavily doped cerium oxide. *Solid State Ionics*, *173*(1–4), 57–61. https://doi.org/10.1016/j.ssi.2004.07.052

Tuller, H. L., & Bishop, S. R. (2011). Point Defects in Oxides: Tailoring Materials Through Defect Engineering. *Annual Review of Materials Research*, *41*(1), 369–398. https://doi.org/10.1146/annurev-matsci-062910-100442

Tuller, H. L., & Nowick, A. S. (1975). Doped ceria as a solid oxide electrolyte. *Journal of the Electrochemical Society*, *122*(2), 255–259.

Tuller, H. L., & Nowick, A. S. (1977). Small Polaron Electron Transport in Reduced CeO2 Single Crystal. *Journal of Physics and Chemistry of Solids*, *38*, 859–867.

Tuller, H. L., & Nowick, A. S. (1979). Defect structure and electrical properties of nonstoichiometric CeO2 single crystals. *Journal of The Electrochemical Society*, *126*(2), 209–217.

Turner, S., Lazar, S., Freitag, B., Egoavil, R., Verbeeck, J., Put, S., … Van Tendeloo, G. (2011). High resolution mapping of surface reduction in ceria nanoparticles. *Nanoscale*, *3*(8), 3385. https://doi.org/10.1039/c1nr10510h

Urban, K., Kabius, B., Haider, M., & Rose, H. (1999). A way to higher resolution: spherical-aberration correction in a 200 kV transmission electron microscope. *Journal of Electron Microscopy*, *48*(6), 821–826.

van den Broek, J., Afyon, S., & Rupp, J. L. M. (2016). Interface-Engineered All-Solid-State Li-Ion Batteries Based on Garnet-Type Fast Li $^{+}$ Conductors. *Advanced Energy Materials*, 1600736. https://doi.org/10.1002/aenm.201600736

Van Driessche, I., Schoofs, B., Bruneel, E., & Hoste, S. (2004). The effect of processing conditions on the properties of spray dried Nd1Ba2Cu3Oy/Ag composite superconductors. *Journal of the European Ceramic Society*, *24*(6), 1823–1826. https://doi.org/10.1016/S0955-2219(03)00444-8

Vavassori, P., Duo, L., Chiaia, G., Qvarford, M., & Lindau, I. (1995). Bulk electronic structure of Ce compounds studied by x-ray photoemission and x-ray absorption spectroscopies. *Physical Review B*, *52*(23), 16503.

Vincent, R., & Midgley, P. A. (1994). Double conical beam-rocking system for measurement of integrated electron diffraction intensities. *Ultramicroscopy*, *53*(3), 271–282.

von Ardenne, M. (1938). Das Elektronon-Rastermikroskop. Theoretische Grundlagen. *Zeitschrift Für Physik*, *109*, 553–372.

Wachsman, E. D., & Lee, K. T. (2011). Lowering the Temperature of Solid Oxide Fuel Cells. *Science*, *334*(6058), 935–939. https://doi.org/10.1126/science.1204090

Waldhäusl, J., Preis, W., & Sitte, W. (2012). Electrochemical characterization of gadolinia-doped ceria using impedance spectroscopy and dc-polarization. *Solid State Ionics*, *225*, 453–456. https://doi.org/10.1016/j.ssi.2012.01.016

Wall, J., Langmore, J., Isaacson, M., & Crewe, A. V. (1974). Scanning transmission electron microscopy at high resolution. *Proceedings of the National Academy of Sciences*, *71*(1), 1–5.

Wang, D. Y., & Nowick, A. S. (1980). The "grain-boundary effect" in doped ceria solid electrolytes. *Journal of Solid State Chemistry*, *35*(3), 325–333.

Wiktorczyk, T., Biegański, P., & Zielony, E. (2012). Preparation and optical characterization of e-beam deposited cerium oxide films. *Optical Materials*, *34*(12), 2101–2107. https://doi.org/10.1016/j.optmat.2012.05.027

Williams, D. B., & Carter, C. B. (2008). *Transmission Electron Microscopy: A Textbook for Materials Science* (2nd ed). New York: Springer.

Williams, D. B., & Carter, C. B. (2009). X-ray spectrometry. In *Transmission Electron Microscopy* (pp. 581–603). Springer. Retrieved from http://link.springer.com/chapter/10.1007/978-0-387-76501-3_32

Wu, H. M., Tu, J. P., Yang, Y. Z., & Shi, D. Q. (2006). Spray-drying process for synthesis of nanosized LiMn2O4 cathode. *Journal of Materials Science*, *41*(13), 4247–4250. https://doi.org/10.1007/s10853-006-6129-3

Wuilloud, E., Delley, B., Schneider, W.-D., & Baer, Y. (1984). Spectroscopic Evidence for Localized and Extended f-Symmetry States in Ce O 2. *Physical Review Letters*, *53*(2), 202.

Yahiro, H., Eguchi, K., Arai, H., & others. (1988). Electrical properties and microstructure in the system ceria-alkaline earth oxide. *Journal of Materials Science*, *23*(3), 1036–1041.

Ye, F., Mori, T., Ou, D. R., Zou, J., & Drennan, J. (2009). A structure model of nano-sized domain in Gd-doped ceria. *Solid State Ionics*, *180*(26–27), 1414–1420. https://doi.org/10.1016/j.ssi.2009.08.013

Ye, F., Yin, C. Y., Ou, D. R., & Mori, T. (2014). Relationship between lattice mismatch and ionic conduction of grain boundary in YSZ. *Progress in Natural Science: Materials International*, *24*(1), 83–86. https://doi.org/10.1016/j.pnsc.2014.01.007

Zhan, Z., Wen, T.-L., Tu, H., & Lu, Z.-Y. (2001). AC Impedance Investigation of Samarium-Doped Ceria. *Journal of The Electrochemical Society*, *148*(5), A427. https://doi.org/10.1149/1.1359198

Zhang, T. S., Ma, J., Cheng, H., & Chan, S. H. (2006). Ionic conductivity of high-purity Gd-doped ceria solid solutions. *Materials Research Bulletin*, *41*(3), 563–568. https://doi.org/10.1016/j.materresbull.2005.09.008

Zintl, E., & Croatto, U. (1939). Fluoritgitter mit leeren Anionenplätzen. *Zeitschrift Für Anorganische Und Allgemeine Chemie*, *242*(1), 79–86. https://doi.org/10.1002/zaac.19392420109